

JOURNAL OF THE MYANMAR ACADEMY OF ARTS AND SCIENCE



Physics, Mathematics, Computer Studies

Vol. XXI, No.2, November, 2024

Myanmar Academy of Arts and Science

Edition

2024, November, 200 Copies

Copyright

Ministry of Education

Published by

Dr Maung Kyaw (00322) Vice-President,
Myanmar Academy of Arts and Science

ISSN 2520-0186

LCCN 2003-323143

Printed by

U Tin Soe (00171), Manager

Universities Press, Yangon, Myanmar

FOREWORD

The Myanmar Academy of Arts and Science (MAAS) was constituted on August-16, 1999 with four major fields of endeavour, namely:

- (a) Introduction to Modern Methods of Teaching and Learning
- (b) Promotion of Research Activities through Research Guidelines
- (c) Dissemination of Knowledge and Emerging Technologies
- (d) Motivating New Generation of Experts and Academics

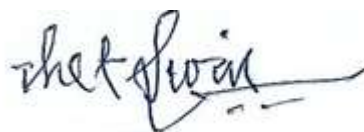
In pursuance of these endeavours, MAAS has, since the year 2001, held Research Conferences and published research papers in the Journal of the Myanmar Academy of Arts and Science.

At the Research Conference held on 19- 21 December 2022, a total of (223) research papers were read and outstanding papers have been published in volume XXI as follows:

- | | |
|----------------|--|
| Vol. XXI, No.1 | Chemistry, Industrial Chemistry |
| Vol. XXI, No.2 | Physics, Mathematics and Computer Studies |
| Vol. XXI, No.3 | Zoology, Botany, Marine Science |
| Vol. XXI, No.4 | Myanmar, Oriental Studies, Archaeology, Anthropology and Library and Information Studies |
| Vol. XXI, No.5 | Geography, History, International Relation, Geology, Statistics, Management Studies, Law, Journalism |
| Vol. XXI, No.6 | Educational Theory and Management, Curriculum and Methodology |
| Vol. XXI, No.7 | Educational Psychology |

The executive committee members of Myanmar Academy of Arts and Science had been reconstituted on 4 August 2022 and again reconstituted on 8 March 2024, by the Ministry of Education with the Approval of the Government of the Union of Myanmar. Accordingly, the Publication Committee along with the Editorial Board have been formed. The primary mission of the academy is to develop and promote Higher Education in preparing future generations to meet the challenges in the 21st century.

The majority of the papers in these issues represent findings of research conducted by aspirants as well as postgraduate candidates in partial or total fulfillment of requirement for these degrees. We, the members of MAAS, do appreciate the editing work done by senior professors and scholars of high standing, these papers would prove useful, and not only for other candidates but also for all those who are interested in the results of systematic research and inquiry.



Dr Thet Lwin
President

The Myanmar Academy of Arts and Science

Editorial Board

Chief Editor - Professor Dr. Maung Kyaw
Editors - Professor Dr Hla Pe

Editors

(Physics, Mathematics, Computer Studies)

Physics

Dr Pho Kaung, Rector (Retd.), University of Yangon
Dr Aung Myat Kyaw, Professor and Head (Retd.), Department of Physics, Dawei University
Dr Kalyar Thwe, Professor and Head (Retd.), Department of Physics, University of Mandalay
Dr Min Maung Maung, Professor, Department of Physics, University of Yangon
Dr Cho Cho Thet, Professor, Department of Physics, University of Yangon
Dr Nyein Thida, Professor, Department of Physics, University of Yangon
Dr San Yu Swe, Professor, Department of Physics, University of Mandalay
Dr Khin Than Tint, Professor, Department of Physics, University of Mandalay
Dr Yin Maung Maung, Professor and Head, Department of Physics, University of Yangon
Dr Nyein Wint Lwin, Professor and Head, Department of Chemistry, Mandalay University

Mathematics

Dr Cho Win, Professor and Head (Retd.), Department of Mathematics, University of Yangon
Dr Aung Moe Khaing, Professor, Department of Mathematics, University of Yangon
Dr Yin Yin Su Win, Professor, Department of Mathematics, University of Yangon
Dr Aung Kyaw, Professor and Head, Department of Mathematics, University of Yangon
Dr Ko Ko Lwin, Professor and Head, Department of Mathematics, University of Mandalay

Computer Studies

Dr Nwe Nwe Win, Professor and Head (Retd.), Department of Computer Studies, University of Yangon
Dr Than Than Win, Deputy Director General, Department of Higher Education
Dr Yi Mon Win, Professor and Head, Department of Computer Studies, Dagon University
Dr Soe Mya Mya Aye Professor and Head, Department of Computer Studies, University of Yangon
Dr Kyaw Moe Min, Professor and Head, Department of Computer Studies, University of Mandalay

Myanmar Academy of Arts and Science and its Editors assume no responsibility
for the statement and opinions advanced by the contributors

Journal of the Myanmar Academy of Arts and Science

Vol. XXI. No.2

Contents

Section (i) Physics

Sr.No	Title	Pages
1	Soe Ko Ko Aung , *Can Endow High Purity Perovskite Phase in Ambient Air? Toward Low-Cost, Scalable, And Vacuum Free Perovskite Solar Cells	1
2	Htaik Nandar Kyaw Evidence of Strangeness -1 Hypernucleus Formation Via Ξ^- Hyperon Capture Point In Nuclear Emulsion	7
3	Shwe Sin Aye , Structural and Thermal Properties of ZnO Modified Bismuth Borate Glasses	17
4	Kham Kham Saing , Synthesis and Characterization of Glass Ceramics Using Rice Husk Ash as Silica Source	25
5	Myat Myo Myo Aye , Study on Optical Properties of Natural Dye Extracted From Rose Flowers	35
6	Myat Thet Mon , Characterization of Structural and Morphological Properties of PbTiO ₃ Powder	41
7	Nyein Nyein Htet , Synthesis and Fabrication of Zinc Oxide on FTO Substrates By Spin Coating Method	49
8	Soe Moe May Me , An Innovative Home Automation System Using Arduino and Bluetooth Module	57
9	Thuzar Hnin , Synthesis and Characterization of Ca Dopant Effect on PbCaTiO ₃ Powders	65
10	May Thwe Soe , Structural Characterization and Electrical Properties of ZnFe ₂ O ₄ Spinel Ferrite	73
11	Pwint Yi Thein , Behavior And Ferroelectric Properties of Lead Titanate Films as a Gate Material	81
12	Yin Min Thant , Investigation on Energy Levels of Bottomonium	91
13	Mono Zaw , Investigation on Electrochemical Properties of Electrochromic Tungsten Trioxide Thin Films	101
14	Nay Min Hla , Evaluation of Band Gaps and Urbach Energies For ZnO Thin Films By Thermal Effect	109
15	May Zin Oo , Assessment of Heavy Metals Concentration in Water Samples from Mandalay City	115

Sr.No	Title	Pages
16	Pyae Wa Maung , Investigation of Nucleon Single-Particle Energy Levels IN ⁹⁰ Zr Using NUMEROV Method	123
17	May Saw Ohn , Lambda Single-Particle Energy Levels In ¹³⁹ _Λ La By Using Numerov Method	133
18	Hnin Thidar Soe , Investigation of Radioactive Elements in Sediments from the Ayeyarwady River Bank at Magway Township	143
19	Aung Zaw Myint , Design and Construction of Four Channels Automatic Bluetooth Control System	151
20	Zin Mar Naing , Calculation of Charge Density Distribution Parameters of Silicon Isotope ³⁰ ₁₄ Si for 3pg-Model	157
21	Zaw Win , Preparation And Characterization of Al ₂ O ₃ /SiO ₂ /Si Tunnel Diode	165
22	Chit Su Aung , Analysis on Modified Ultrasonic Distance Meter using Ultrasonic Sensor, Esp32 And Plx_Daq Software	175
23	Hein Nay Zar Wann , Seasonal Determination of Radon Concentration in Soil Samples From Kalain Gold Mine at Bago Region	185
24	Khin Sandar Lin , Sound-Absorbing Properties of Waste Scraped Tire Rubber Fiber Reinforced Polyvinyl Alcohol Films as Rubber Aerogel	193
25	Khin Myat Thet Wai , The Propagation of A Particle in the One-Dimensional Infinite Square-Well By Using the Path Integral Formalism	203
26	Hnin Hnin Ei , Measurements of Radon Concentrations of Shweku Tanke Pagoda at Pakokku Township in Magway Region, Myanmar	213

Section (ii) Mathematics

Sr.No	Title	Pages
1	Oothan Nweit , *Rainbow Numbers with Independent Cycles in $K_{m,n}$ Depending on Rainbow Bipartite Graphs	223

Section (ii) Computer Studies

Sr.No	Title	Pages
1	Shwe Sin Ei , *Prediction And Visualization Of Mental Health Patterns Using Machine Learning Techniques	231
2	Kyaw Kyaw Min , Exploring The Big Data Analytics Tools for Structured and Unstructured Data	243

CAN ENDOW HIGH PURITY PEROVSKITE PHASE IN AMBIENT AIR? TOWARD LOW-COST, SCALABLE, AND VACUUM FREE PEROVSKITE SOLAR CELLS*

Soe Ko Ko Aung¹, Thae Thinzar Lwin², Lin Zarchi Khaing³, Mono Zaw⁴, San Yu Swe⁵

Abstract

In recent years, lead halide perovskite solar cell efficiency has tremendously reached up to 22.7% due to excellent optoelectronics properties with various fabrication methods. However, stability in ambient air for perovskite solar cells is a lack of effective solution to the problem until now. On the other hand, fabrication processes in a glovebox are strictly limited for large scale production due to high operational costs. Hence, perovskite films are fabricated by two-step deposition method in ambient air relative humidity (RH) of $45 \pm 5\%$ to acquire high quality films and good crystallization. For the first step, 1 M of lead iodide/N, N-dimethylformamide (PbI₂/DMF) solution is deposited on the glass substrate. In a second step, separated amount of 10 to 25 mg of methylammonium iodide (MAI) in 1 ml of isopropanol (IPA) solution is deposited on the PbI₂ film. To optimize the high-purity phase, 1% of N, N-dimethylformamide (DMF) is added to MAI/IPA solution. Meanwhile, residual PbI₂ peaks transform in the final perovskite films indicate that DMF additive increases the full reaction state of perovskite film. Furthermore, three different annealing times (10, 15 and 30 min) are investigated at 110 °C in air. The highest purity phase achieved for 25 mg/ml (MAI/IPA) increases crystalline size up to 51.8 nm from 35.2 nm (10 mg/ml) analyzed by X-ray diffraction (XRD) and ultraviolet–visible (UV–vis) spectrum exhibits higher absorbance intensity in the longer wavelength as well. Thus, solvent additive method facilitates mass production fabricated in an ambient environment due to increase crystalline growth of perovskite films.

Keywords: Perovskite, N, N-dimethylformamide, isopropanol, crystallization, additive

Introduction

Perovskite solar cells (PSCs) are promising candidate in the future photovoltaic power generation due to their outstanding optoelectronics properties and low cost fabrication techniques. The power conversion efficiency of PSCs have greatly achieved from barely 3.8% to 22.7% in 2021 (Jeong et al., 2021). However, stability issues of PSCs are crucial to repair the point defects as vacancies, interstitials, and substitutions as well as degradation of perovskite films occur due to easily decomposed under high temperature or moisture (Kim et al., 2017; Wang et al., 2018). One critical drawback of PSCs is sensitivity to moisture due to organic cation dissolved by water.

In addition, the device performance of PSCs films depend on deposition methods to improve high quality film such as grain size, high phase purity, good crystallization, surface coverage etc (Ansari et al., 2018). Several deposition methods including single-step or sequential deposition, thermal evaporation and vapor processing have been reported (Chen et al., 2020). Among them, one-step and two-step sequential processes are low cost and easiest way to enhance films quality, especially in two-step solution method is essential for morphology of desire outcome film in pinhole free to achieve high efficiencies (Burschka et al., 2013; Im et al., 2014; Ko et al., 2015). To achieve the high quality films, purity phase MAPbI₃ has been prepared in the N₂ filled glove box which increases the equipment costs and limits mass production in the industrial points of views. This barrier may financially prohibit in large-scale manufacture of PSCs. Thus,

¹ Department of Physics, University of Mandalay, 05032, Mandalay, Myanmar

² Department of Physics, University of Mandalay, 05032, Mandalay, Myanmar

³ Department of Physics, University of Mandalay, 05032, Mandalay, Myanmar

⁴ Department of Physics, University of Mandalay, 05032, Mandalay, Myanmar

⁵ Department of Physics, University of Mandalay, 05032, Mandalay, Myanmar

*Best Paper Award Winning Paper in Physics (2022)

fabrication method for perovskite are required in ambient air even under high humidity condition using solvent additive method to achieve the high performance of PSCs.

In this work, we prepared the perovskite films by two-step process using the solvent additive method in ambient relative humidity (RH) of $40 \pm 5\%$. It was found that 1% DMF additive in the optimum solution 25 mg/ml (MAI/IPA) improved the crystallization and absorbance of perovskite film. Our work provides a simple and low cost fabrication approach to achieve high-quality perovskite film under ambient air.

Experimental Section

Materials

lead (II) iodide (PbI_2 , 99.5%), N, N-dimethylformamide (DMF, 99.8%), dimethylsulfoxide (DMSO, 99.8%), methylammonium iodide, $\text{CH}_3\text{NH}_3\text{I}$ (MAI), chlorobenzene (anhydrous, 99.8%) and isopropanol (IPA, ACS reagent, $\geq 99.5\%$) were purchased from Sigma-Aldrich. All purchased chemicals were used without further purification.

Perovskite Preparation Methods

Pure glass ($25 \times 25 \text{ mm}^2$) substrates were ultrasonically cleaned with diluted detergent, deionized water, acetone, ethanol and isopropyl alcohol for 15 min each, then dried in air stream. After being further treated by UV-ozone cleaning at 60°C for 15 min to remove the organic residues and increase the wettability. For perovskite precursor solution, 1M PbI_2 was dissolved in N, N-dimethylformamide (DMF) and then kept at 70°C for 2 h under laboratory type constant magnetic stirrer. And then methylammonium iodide, $\text{CH}_3\text{NH}_3\text{I}$ (MAI) was prepared in 2 propanol solvents with the different concentration ($10\text{--}25 \text{ mg ml}^{-1}$) separately, and then kept for 1 h under magnetic stir. Before perovskite layer deposition, PbI_2 solutions was filtered with $0.45\text{-}\mu\text{m}$ PTEE filters before use. The perovskite films were deposited using two-step in following steps. First, PbI_2 precursor solution was spun on the substrate at 5000 rpm for 20s, and then it was immediately moved to hotplate and dried at 100°C for 30 min. After cooling down at room temperature (RT), MAI/IPA solution was dropped on the PbI_2 substrate and kept for 20 s and spin coated at 3000 rpm for 30s for the final step. Finally, it was transferred on a hotplate and annealed at 110°C for 30 min. For the additive device, 1% DMF is added to MAI concentration varied from 10 to 25 mg in 1ml of IPA. For anti-solvent method, perovskite precursor was prepared by dissolving 1.2 M of PbI_2 and MAI in DMF/DMSO (9/1, v/v) via one step method and deposited at 3000 rpm for 30s. 200 μL chlorobenzene (CB) was dropped on the center of spinning substrate before 10 s prior to the end. All processes were carried out in lab ambient environment.

Characterizations and Measurements

Perovskite films were characterized by X-ray diffractometer (XRD, Shimadzu, Japan) with $\text{Cu K}\alpha$ ($\lambda = 1.5406 \text{ \AA}$) radiation at 40 kV and 30 mA with a range from 10 to 55° scanning parameter in 0.6 s/step at 0.02° (2θ) step size. To analyze the absorption spectra of perovskite films, Ultraviolet-visible (UV-vis) spectrum was recorded on a Hitachi U-4100 spectrophotometer in the wavelength of $250 \text{ nm} - 900 \text{ nm}$.

Results and Discussion

Figure 1 shows the schematic diagram of experimental produces using two step deposition method. In second step, solvent additive method was applied in the sequential deposition which can increase the crystallization of MAPbI₃ perovskite films. Fabrication processes were carried out in the ambient atmosphere.

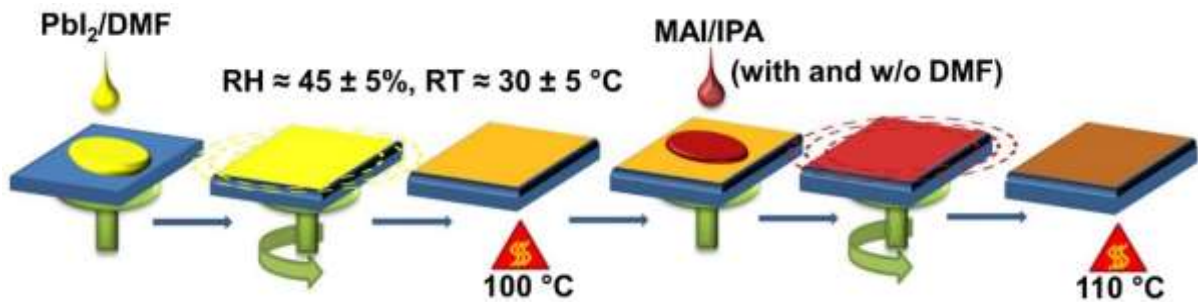


Figure 1 Schematic illustration of prepared with and w/o additive perovskite film by two step deposition method.

Figure 2 shows different PbI₂ molar (M) concentration with and without (w/o) additive films corresponding to the different MAI concentration as shown in Figure 2. In our study, 1% DMF was added into the different amount of MAI/IPA concentration. Comparison results at a PbI₂ concentration, w/o additive film (1M PbI₂) showed high roughness and many pinholes than PbI₂ additive films (1.2 M PbI₂) which increased the films quality likely smooth surface. However, it significantly changed to pale yellow color due to increased PbI₂ concentration. As an alternative, MAI concentrations were varied from 10 mg to 25 mg additive in IPA solution by solvent exchange method. As a result, dark brown and dense perovskite films were achieved when 20 mg and 25 mg/IPA solution were deposited on the 1M PbI₂ films. To confirm the films quality, Ultraviolet-visible (UV-vis) spectrophotometer and X-ray diffractometer (XRD) are further performed to be analyzed.

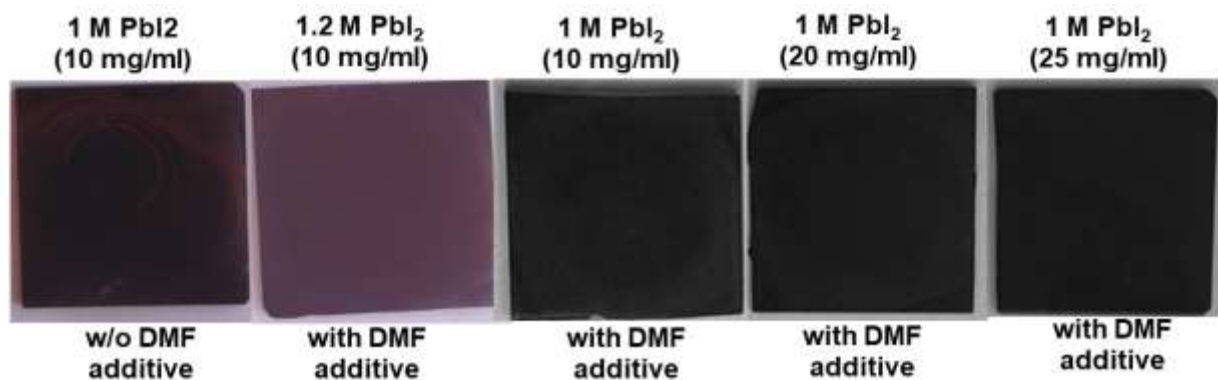


Figure 2 Photographs of different PbI₂ molar concentration with and w/o DMF additive films.

The absorption spectra of w/o additive perovskite films are measured with different annealing time for the concentration of 1M PbI₂ and 10 mg/ml (MAI/IPA) in Figure 3a. Obviously, absorbance spectra of perovskite films were increased during prolonged annealing. Strongest absorption spectrum (25 mg/ml) was observed in the visible region range between 350 nm and 650 nm by annealing at 110 °C for 30 min. Furthermore, UV-vis absorptions of additive films were measured for different MAI concentration plotted in Figure 3b. The film (25 mg/ml) exhibited highest absorption intensity in the range of 500 nm – 850 nm. It is noted that 30 mg/ml (MAI/IPA)

are not taken into further XRD characterization due to lower absorption spectrum than that of 25 mg/ml. Energy gaps were calculated from absorbance spectra using Tauc plot following this equation (Makula et al., 2018): $(\alpha h\nu)^2 = C(h\nu - E_g)$ where α = the absorption coefficient, h = Planck's constant, ν = the frequency of light, E_g = the band gap and C = the proportionality constant. Tauc plot showed the 1.54 eV (10, 25 mg/ml) and 1.56 eV (15, 20, 30 mg/ml) attributed to the similar energy values in Figure 3c. To compare with anti-solvent method (one step), absorption spectra of two step method was higher visible range compared than that of one step method in Figure 3d.

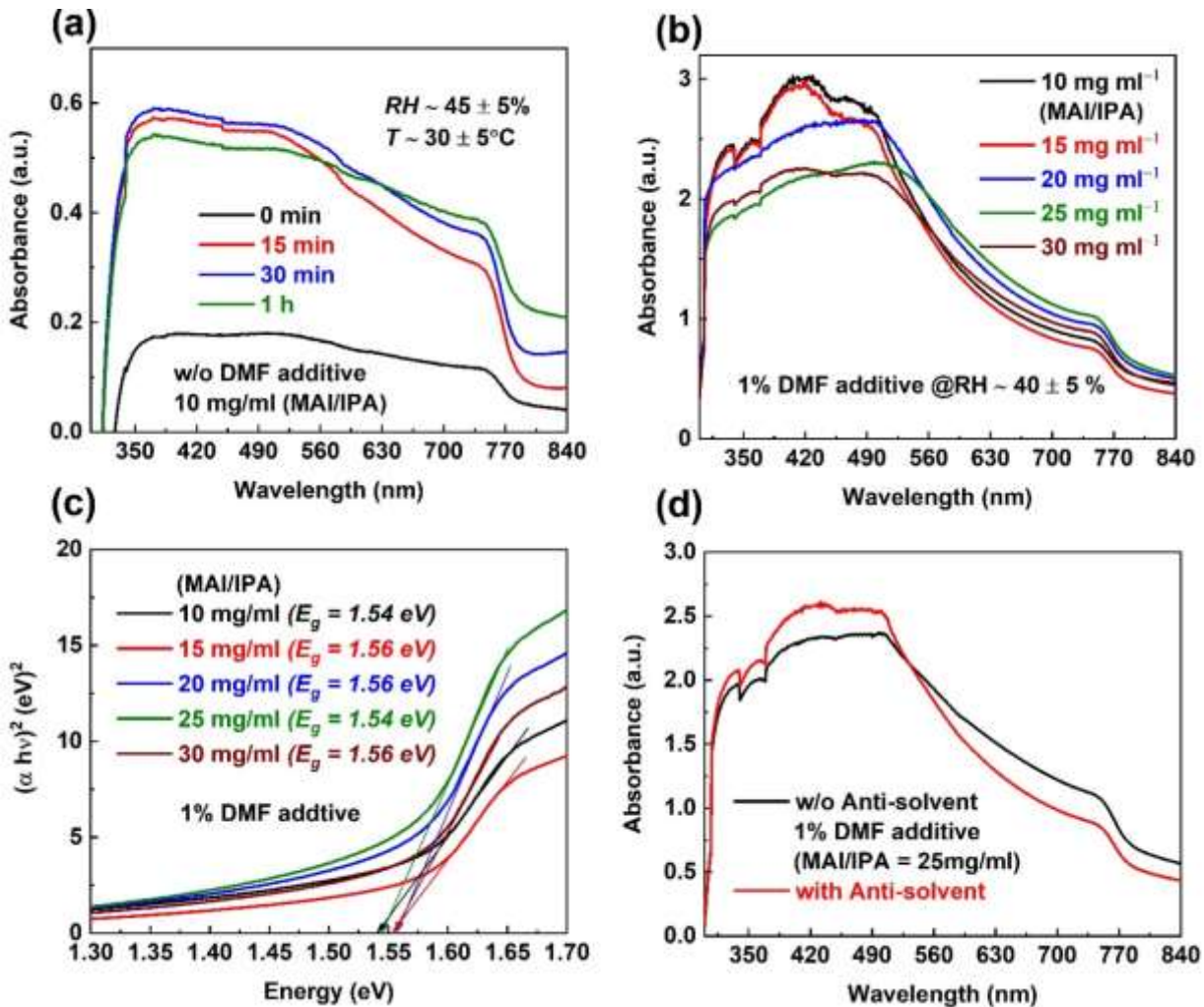


Figure 3 UV-Vis absorption spectra of perovskite films (a) w/o additive films under different annealing time (b) with 1% DMF additive films with different MAI concentration for 30 min each (c) Tauc plots calculated from absorbance spectra of different MAI concentration and (d) two different techniques between one step and two step deposition with and w/o anti-solvent.

First, we compared the X-ray diffraction (XRD) patterns of perovskite films (w/o DMF additive) on different annealing time and ambient atmosphere (Figure 4a-b). Strong diffraction peak (2θ) was 12.56° (PbI_2), corresponding to (001) crystal plane under ambient atmosphere (Guo et al., 2016). Perovskite crystal plane intensity (110) annealed for 30 min was slightly higher than that of 10 min and 15 min indication as an impurity of perovskite (Figure 4a). Similar results were received due to low purity of perovskite (110) crystal plane (figure 4b) after increased

MAI (w/o DMF additive) from 10 mg to 20 mg under RH ~ 60 ± 5%. Compared with crystal planes of PbI₂ (001) and perovskite (110), it can be seen that the content of perovskite decreases, whereas the residual PbI₂ increases. Unreacted PbI₂ was not completely transformed into perovskite film due to leaving a large portion of PbI₂. Hence, low humidity environment (RH ~ 45 ± 5%) is for further optimization. Figure 4c shows the XRD patterns of perovskite additive (1% DMF) films with different amount of MAI/IPA solution. The perovskite peaks at 2θ = 14.02°, 28.36° and 50.27° are corresponding to the (110), (220) and (404) planes of the tetragonal phase (I4/mcm space group)(Chen et al., 2016; Guo et al., 2016). A fraction of PbI₂ (12.56°) was decreased with increasing MAI concentration. As a result, strongest perovskite peak at 2θ (14.02°) was observed when MAI value was increased to in 25 mg. At last, least portion of PbI₂ peak remained in the final perovskite film. We suppose that residual PbI₂ could be beneficial to improve the grain boundaries and defect passivation. This result is good agreement with UV-Vis absorption spectrum corresponding to the higher absorbance in the visible region. The crystallite size of additive perovskite films can be calculated according to the Scherrer's equation: $D = k \lambda / (\beta_{hkl} \cos \theta_{hkl})$, where k = 0.89 (shape factor), λ = 0.15406 nm, β_{hkl} = half-width of the diffraction band (FWHM) θ_{hkl} = Bragg-diffraction angle. As shown in Figure 4d, the full width at half maximum (FWHM) of additive perovskite (110) peaks was highly reduced from 0.228° to 0.155° after increasing the MAI/IPA concentration. The crystallite sizes of perovskite films were increased from 35.18 nm (10 mg), 37.67 (15 mg), 40.17 nm (20 mg) up to 51.77 (25 mg). It is noted that crystallite size was easily controlled for perovskite fabrication in ambient atmosphere.

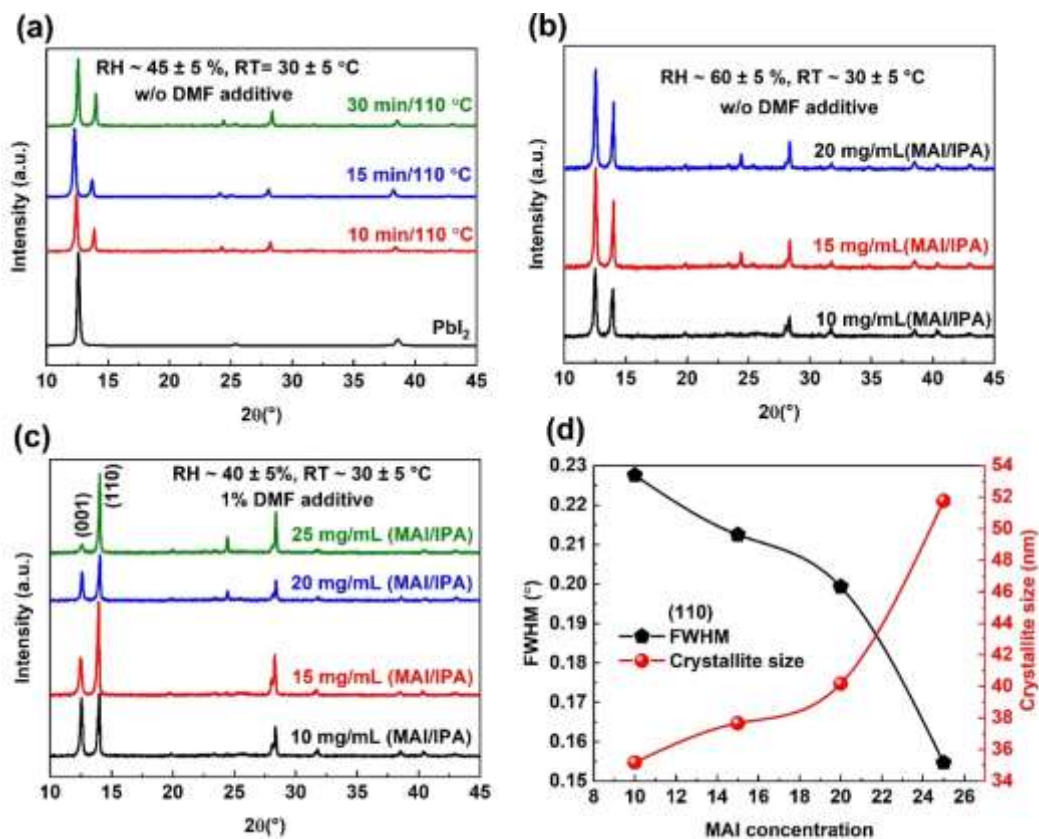


Figure 4 XRD of perovskite films fabricated on different annealing time in relative humidity of (a) RH ~ 45 ± 5% (b) RH ~ 60 ± 5% (c) different MAI concentration (d) Full-width at half maximum (FWHM) and crystallite size of (110) peak of all the samples.

Conclusion

We successfully fabricated that additive solvent method increases the perovskite formation by two-step deposition method in ambient air. Transformation kinetics between PbI_2 and perovskite peak intensities were confirmed by XRD analysis. Moreover, optimum concentration of 25 mg/ml (MAI/IPA) solution correlates to higher absorbance in the visible region confirmed by UV-vis spectroscopy. Both solvent additive and two step methods are essential improving high quality film. This work paves simple, low cost and vacuum free fabrication processes in air for potential application in perovskite solar cells.

Acknowledgements

This work was fully funded by International Science Programme (ISP), Uppsala Univeristy, Grand No. MYA: 01 and department of higher education, Ethical Review Committee (ERC), Univeristy of Mandalay, Project No. 18 (2022-2023). The author thanks to Prof. Dr Nyein Wink Lwin for strongly support.

References

- Ansari, M.I.H., Qurashi, A., Nazeeruddin, M.K., (2018) "Frontiers, Opportunities, and Challenges in Perovskite Solar Cells: A critical review." *J. Photochem. Photobiol. C Photochem. Rev.* vol.35, pp.1–24.
- Burschka, J., Pellet, N., Moon, S.J., Humphry-Baker, R., Gao, P., Nazeeruddin, M.K., Grätzel, M., (2013) "Sequential Deposition as A Route to High-Performance Perovskite-Sensitized Solar Cells." *Nature*, vol.499, pp.316–319.
- Chen, W., Li, X., Li, Yaowen, Li, Yongfang, (2020) "A Review: Crystal Growth for High-Performance All-Inorganic Perovskite Solar Cells." *Energy Environ. Sci.* vol.13, pp.1971–1996.
- Chen, Y., He, M., Peng, J., Sun, Y., Liang, Z., (2016) "Structure and Growth Control of Organic–Inorganic Halide Perovskites for Optoelectronics: From Polycrystalline Films to Single Crystals." *Adv. Sci.* vol.3, pp.1500392.
- Guo, X., McCleese, C., Kolodziej, C., Samia, A.C.S., Zhao, Y., Burda, C., (2016) "Identification and Characterization of the Intermediate Phase in Hybrid Organic-Inorganic MAPbI_3 Perovskite." *Dalt. Trans.* vol.45, pp.3806–3813.
- Im, J.H., Kim, H.S., Park, N.G., (2014) "Morphology-Photovoltaic property correlation in perovskite solar cells: One-step versus two-step deposition of $\text{CH}_3\text{NH}_3\text{PbI}_3$." *APL Mater.* vol.2, pp.081510.
- Jeong, J., Kim, Minjin, Seo, J., Lu, H., Ahlwat, P., Mishra, A., Yang, Y., Hope, M.A., Eickemeyer, F.T., Kim, Maengsuk, Yoon, Y.J., Choi, I.W., Darwich, B.P., Choi, S.J., Jo, Y., Lee, J.H., Walker, B., Zakeeruddin, S.M., Emsley, L., Rothlisberger, U., Hagfeldt, A., Kim, D.S., Grätzel, M., Kim, J.Y., (2021) "Pseudo-Halide Anion Engineering for α -FAPbI₃ Perovskite Solar Cells." *Nature* vol.592, pp.381–385.
- Kim, S., Bae, S., Lee, S.W., Cho, K., Lee, K.D., Kim, H., Park, S., Kwon, G., Ahn, S.W., Lee, H.M., Kang, Y., Lee, H.S., Kim, D., (2017) Relationship Between Ion Migration and Interfacial Degradation of $\text{CH}_3\text{NH}_3\text{PbI}_3$ Perovskite Solar Cells Under Thermal Conditions." *Sci. Rep.* vol.7, pp.1200.
- Ko, H.S., Lee, J.W., Park, N.G., (2015) 15.76% Efficiency Perovskite Solar Cells Prepared Under High Relative Humidity: Importance of PbI_2 Morphology in Two-step Deposition of $\text{CH}_3\text{NH}_3\text{PbI}_3$. *J. Mater. Chem. A* vol.3, pp.8808–8815.
- Makula, P., Pacia, M., Macyk, W., (2018) "How To Correctly Determine the Band Gap Energy of Modified Semiconductor Photocatalysts Based on UV-Vis Spectra." *J. Phys. Chem. Lett.* vol.9, pp.6814–6817.
- Wang, M., Li, B., Yuan, J., Huang, F., Cao, G., Tian, J., (2018) "Repairing Defects of Halide Perovskite Films to enhance Photovoltaic Performance." *ACS Appl. Mater. Interfaces* vol.10, pp.37005–37013.

EVIDENCE OF STRANGENESS -1 HYPERNUCLEUS FORMATION VIA Ξ^- HYPERON CAPTURE POINT IN NUCLEAR EMULSION

Htaik Nandar Kyaw¹, Nyi Nyi Soe², Cho Cho Aung³

Abstract

A strangeness -1 single- Λ hypernucleus event which is detected in nuclear emulsion of hybrid-emulsion experiment KEK-PS E373 is analyzed starting from its decay point. Kinematical analysis is used to perform analysis. The neutral particle emission at point B is checked by two methods and it is observed that the neutral particles are also emitted as the decay products. $+7+9+^7t$; possible decay modes are selected by calculating the energy and momentum of decay products and kinematical analysis is done. Masses and binding energies of possible hypernuclei were calculated. According to the analysis result, the event is assigned to be ${}^7_8\Lambda\text{Li}$ or ${}^{10}_\Lambda\text{Be}$ or ${}_\Lambda{}^{14}\text{C}$. The most probable decay mode is identified as ${}^8_\Lambda\text{Li} \rightarrow d + \text{He}^3 + 3n$ with 7641.4 ± 0.006 MeV/c² mass and 9.65 ± 0.06 MeV binding energy. Our results are consistent with other theoretical and experimental results.

Keywords: nuclear emulsion, strangness-1, single- Λ hypernucleus, neutral particle, kinematical analysis, mass, binding energy

Introduction

In the present research, a single- Λ hypernucleus event which is detected in nuclear emulsion of KEK-PS E373 experiment is analyzed by applying relativistic kinematics. The aim of KEK-PS E373 experiment is searching and studying the strangeness hypernuclei with ten times higher statistics than previous experiment KEK-PS E176 [Nakazawa K,2010].

In this experiment $p(K^-, K^+)\Xi^-$ reaction is used. Beam exposure is done at Japanese High Energy Accelerator Research Organization (KEK) and emulsion scanning is performed by laboratories of collaboration universities. The analyzed event is observed in Nakazawa Laboratory, Gifu University, Japan during the semi-automatic scanning of emulsion plates. In semi-automatic scanning system, Ξ^- hyperon tracks are searched by automatic scanning by using the predicted positions and angles. When Ξ^- hyperon is captured by nuclear emulsion, the scanning result was checked individually by human eyes.

A hypernucleus is a nucleus which consists of protons, neutrons and one or more hyperon (Λ , Σ , Ξ , Ω). A single- Λ hypernucleus is a bound system of nucleons and one Λ hyperon. It is also called strangeness -1 ($S = -1$) hypernucleus. A single- Λ hypernucleus can be seen as an event with two vertex points in nuclear emulsion. A single- Λ hypernucleus is mostly produced via quasifree $p(K^-, K^+)\Xi^-$ reaction in the particle accelerator and $\Xi^- + p \rightarrow \Lambda + \Lambda$ reaction in nuclear emulsion. Nuclear emulsion is the most suitable detector to study hypernuclei events because the hypernuclei events can be recorded and measured the ranges of charged particle tracks precisely. The famous hypernuclei searching experiment KEK-PS E176, E373 and J-PARC E07 experiments are carried out using nuclear emulsion.

For strangeness zero ($S=0$) ordinary nuclear systems 7000 nuclides are naturally observed. Among them 3000 nuclides are unstable nuclei and nearly 300 stable nuclei were observed experimentally. Using the ordinary nuclei, nucleon-nucleon (NN) interaction which is very fundamental for nuclear force has been studied. But after observing the hypernucleus event via cosmic ray interaction with nuclear emulsion, the main door of baryon-baryon (BB) interaction is

¹ Department of Physics, Kyaukse University

² Department of Physics, Defence Services Academy

³ Department of Physics, Panglong University

opened. So, to complete the knowledge of baryon-baryon interaction, nucleon-nucleon interaction can be studied by ordinary nuclei, lambda-nucleon (Λ -N) interaction can be studied by single- Λ hypernuclei and lambda-lambda (Λ - Λ) interaction can be studied by double- Λ hypernuclei.

At present, about 4000 data of NN interaction are already obtained. For the hypernuclei observation, about 50 single Λ -hypernuclei and six double- Λ hypernuclei were found experimentally [Tamura H, 2012]. So, we have very few data of Λ -N and Λ - Λ interaction and observation of more and more hypernuclei is strongly desired to construct the baryon-baryon interaction model. To do so, hypernuclei identification is the most important work and the present research aims to perform kinematical analysis of single- Λ hypernucleus event which is produced by Ξ^- hyperon captured point in nuclear emulsion and to investigate the mass and binding energy of analyzed event. This research also aims to support the identification data to hypernuclear physics groups.

Event Description

The photograph and schematic diagram of analyzed single- Λ hypernucleus event are presented in figure 1.

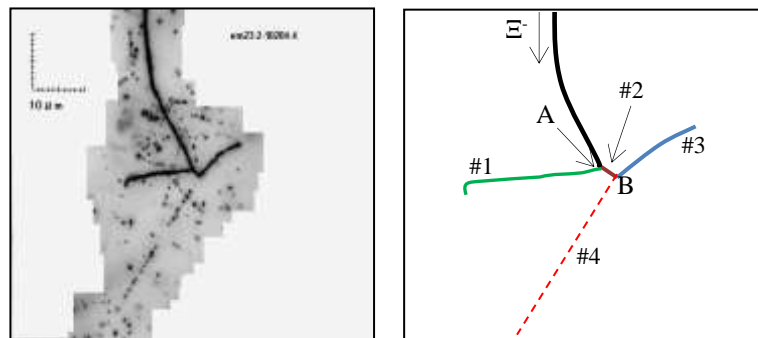


Figure 1 Photograph and schematic diagram of analyzed single- Λ hypernucleus in nuclear emulsion of KEK-PS E373 experiment

In the analyzed event, Ξ^- hyperon is captured by the emulsion nucleus at point A, from which two charged particles track #1 and track #2 are emitted. The particle of track #2 decays again into track #3 and track #4 at point B. So, point A is production vertex and point B is decay vertex of track #2. In the analyzed event, a single- Λ hypernucleus is produced with two charged particles decay products. In this event, there are two vertex points; one production vertex and one decay vertex. Therefore, we decided that a charged particle track #2 is a single- Λ hypernucleus. The experimental data of positions (x,y,z) are measured by Htaik Nandar Kyaw who is one of the collaborators of KEK-PS E373 experiment. The measured ranges and position angles of emitted charged particle tracks are presented in table 1.

Table 1 Measured ranges of hypernucleus track #1 and charged particle decay products

Vertex	Track	Range (μm)	θ (degree)	ϕ (degree)	Remark
A	#1	24.75 \pm 0.001	147.11 \pm 0.48	357.52 \pm 0.28	
	#2	4.27 \pm 0.001	159.52 \pm 0.21	121.03 \pm 0.44	Single- Λ hypernucleus
B	#3	11.99 \pm 0.001	101.17 \pm 0.34	233.11 \pm 0.64	
	#4	1486.80 \pm 0.14	73.18 \pm 1.79	57.15 \pm 2.784	

Identification of a Single- Λ Hypernucleus

In this section the analysis of single- Λ hypernucleus event which is observed via Ξ^- hyperon captured by nuclear emulsion is presented.

Checking the Neutral Particles Emission at Point B

In kinematical analysis, hypernuclei identification work is done by using the decay point of single- Λ hypernucleus event. Therefore, choosing the possible decay mode is the most important. In the analyzed event a single- Λ hypernucleus track #2 decays into two charged particles track #3 and #4. Therefore, it is necessary to check the neutral particle emission in the decay products other than two charged particles.

In our analysis, we checked the neutral particle(s) emission at point B using the unit vector plane checking method which is mentioned in equation 1. If coplanarity is zero, there is no neutral particle emission at the point B. If the coplanarity is not equal zero, there is neutral particle emission at point B. In this method, the unit vectors of charged particle tracks are used as follows.

Coplanarity of three tracks at point B can be calculated by

$$C_B = \hat{U}_A \cdot (\hat{U}_B \times \hat{U}_C) \quad (1)$$

$$\vec{A} = A_x \hat{x} + A_y \hat{y} + A_z \hat{z} \quad (2)$$

$$\vec{B} = B_x \hat{x} + B_y \hat{y} + B_z \hat{z} \quad (3)$$

$$\vec{C} = C_x \hat{x} + C_y \hat{y} + C_z \hat{z} \quad (4)$$

$$\hat{U}_A = \frac{\vec{A}}{|\vec{A}|}, \hat{U}_B = \frac{\vec{B}}{|\vec{B}|}, \hat{U}_C = \frac{\vec{C}}{|\vec{C}|} \quad (5)$$

where, \vec{A} is position vector of track #2, \vec{B} is position vector of track #3 and \vec{C} is position vector of track #4. In equation 5, \hat{U}_A, \hat{U}_B and \hat{U}_C are unit vectors of \vec{A}, \vec{B} and \vec{C} . According to our calculation, the coplanarity of three tracks at point B is 0.269 ± 0.164 . Therefore, neutral particle emission at point B will be considered.

Checking the Neutral Particle Emission at Point B by using the Decay Modes without Neutron

To check the neutron emission at point B, we used another method which is comparing the total kinetic energy and Q-value of no neutron emission decay modes. To do so, the decay modes without neutron emission are firstly considered and (81) decay modes of ${}^4_\Lambda\text{He}$ to ${}^{15}_\Lambda\text{N}$ are obtained. The Q- values of above decay modes are calculated by the formula

$$Q(\text{MeV}) = [\{ M(\#2) - M(\#3) - M(\#4) \} \text{ MeV}/c^2] c^2 \quad (6)$$

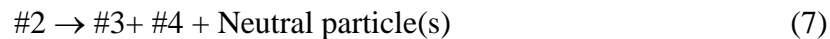
Therefore, possible decay modes of single- Λ hypernucleus track #1 are chosen according to equation 2. Firstly, internal structures of possible single- Λ hypernuclei are considered. Track #1 decays into decay products of three charged particle tracks and neutral particles, the possible hypernucleus must be chosen ${}^4_\Lambda\text{He}$ to ${}^{15}_\Lambda\text{N}$.

The kinetic energy of decay products are calculated by R-E (Range-Energy) relation calculation package supported by Professor Nakazawa who is the spokesperson of KEK-PS E373

experiment [Nakazawa K, 2019]. Then, the total energies which are the sum of kinetic energies of two decay products track #3 and #4 for all decay modes are calculated. Moreover, the calculated Q-values and total energy are compared. If all charged particles are emitted as the decay products, the total energy should be equal to Q-values. According to our calculation, the Q-values are very much greater than total energy for all (81) decay modes. Therefore, the decay modes without neutron are rejected and we can concluded not only two charged particles but also neutral particles are emitted in the decay products for all possible decay modes.

Choosing the Possible Decay Modes at Point B

At point B, a single- Λ hypernucleus track#2 decayed into two charged particle tracks #3 and #4. Due to the coplanar checking we have found that there is neutron emission at point B in addition to two charged particles track #3 and track #4. Therefore the non-mesonic decay modes of single- Λ hypernucleus are considered as follows.



According to non-mesonic decay process which is mentioned in equation (7), the possible (140) decay modes from ${}^4_{\Lambda}\text{He} \rightarrow {}^2_1\text{H} + {}^2_1\text{H} + 2n$ to ${}^{15}_{\Lambda}\text{N} \rightarrow {}^3_2\text{He} + {}^{10}_5\text{B} + 2n$ are obtained. In order to choose the possible decay modes, one neutron emission, two neutrons emission and three neutrons emission cases are considered.

Identification of Single- Λ Hypernucleus Event

A single- Λ hypernucleus is decayed by weak interaction and identification of hypernucleus event is performed by its decay point. In section 3.3, 140 possible decay modes with neutral particles decay products are chosen. In order to check the possible decay modes that we have chosen are allowed or forbidden, Q-values at point B are calculated. If Q-value is positive, the reaction is exoergic and it will be energetically possible. If Q-value is negative, the reaction cannot energetically possible and the energy is needed to supply incident particle. In nuclear emulsion, the decay processes of hypernuclei should be exoergic because the lifetime of hypernucleus is $\sim 10^{-10}$ s and it can decay energetically within 10^{-10} s. According to our calculation, Q-values at point B are positive for all possible decay modes and they all are acceptable to perform analysis.

Then Q-values and total energy of all decay products are compared. The kinetic energy of charged particles which is also defined as visible energy (E_{vis}) is calculated by range-energy relation calculation package [Nakazawa K, 2019]. The kinetic energy of neutral particles is calculated by momentum conservation. The total energy which is the sum of kinetic energy of charged particles and that of neutral particles is also calculated. In order to choose the most probable decay modes, Q-values and total energies are compared. If neutral particles are emitted as the decay products the total energy should be less than Q-value because neutral particles cannot be seen or measured in nuclear emulsion. So, we assumed that the neutral particle or particles emitted as back to back direction with charged particles. At that time we can get minimum kinetic energy and inserting the greater than sign for two or three neutron emission cases. In our research 133 decay modes have greater total energy than Q-value and these decay modes are rejected. Only 7 decay modes are acceptable because their total energies are less than Q-values and the results are presented in table 2 and figure 2.

Table 2 Comparison of Q-values and total energy for all acceptable decay modes at point B

No.	Decay Modes	Q(MeV)	E _{tot} (MeV)	Remark
1	${}^5_{\Lambda}\text{He} \rightarrow {}^1_1\text{H} + {}^3_1\text{H} + \text{n}$	152.14±0.05	127.74±0.003	Acceptable
2	${}^6_{\Lambda}\text{He} \rightarrow {}^2_1\text{H} + {}^3_1\text{H} + \text{n}$	154.21±0.12	138.82±0.003	Acceptable
3	${}^7_{\Lambda}\text{Li} \rightarrow {}^1_1\text{H} + {}^3_2\text{He} + 3\text{n}$	144.72±0.06	>131.74±0.006	Acceptable
4	${}^8_{\Lambda}\text{Li} \rightarrow {}^2_1\text{H} + {}^3_2\text{He} + 3\text{n}$	138.48±0.06	>137.16±0.006	Acceptable
5	${}^9_{\Lambda}\text{Be} \rightarrow {}^7_3\text{Li} + {}^1_1\text{H} + \text{n}$	150.11±0.06	136.80±0.007	Acceptable
6	${}^{10}_{\Lambda}\text{Be} \rightarrow {}^6_3\text{Li} + {}^2_1\text{H} + 2\text{n}$	141.02±0.23	>110.14±0.006	Acceptable
7	${}^{14}_{\Lambda}\text{C} \rightarrow {}^{10}_5\text{B} + {}^1_1\text{H} + 3\text{n}$	128.56±0.33	>103.93±0.012	Acceptable

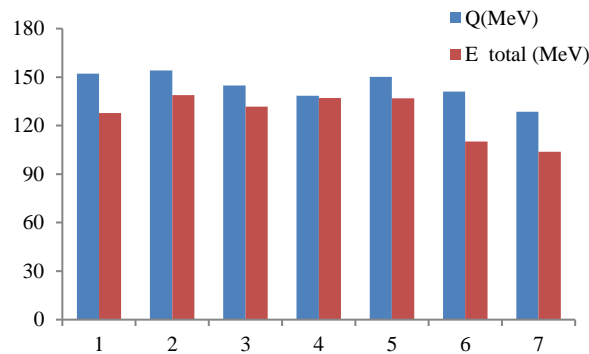


Figure 2 Comparison of Q and E_{tot} for Acceptable Decay Modes

After choosing the seven acceptable decay modes, three decay modes with one neutron emission, one decay mode with two neutrons emission and three decay modes with three neutrons emission are obtained. So, we tried to analyze a single- Λ hypernucleus event by calculating its mass and binding energy for seven acceptable decay modes. The possible masses of single- Λ hypernucleus are calculated by the formulae

$$M({}^{\Lambda}_Z) c^2 = E_3 + E_4 + E_n \tag{8}$$

for one neutron emission case,

$$M({}^{\Lambda}_Z) c^2 = E_3 + E_4 + E_{2n} \tag{9}$$

for two neutrons emission case and

$$M({}^{\Lambda}_Z) c^2 = E_3 + E_4 + E_{3n} \tag{10}$$

for three neutrons emission case.

In the equations 8, 9 and 10,

$M({}^{\Lambda}_Z)$ = mass of single- Λ hypernucleus

E_3 = total energy of charged particle track #3

E_4 = total energy of charged particle track #4

E_n, E_{2n}, E_{3n} = total energy of neutron or neutrons

The binding energy of single- Λ hypernucleus is calculated by the formula,

$$B_{\Lambda} = M(^{A-1}Z) + M_{\Lambda} - M(^A_{\Lambda}Z) \tag{11}$$

where,

B_{Λ} = binding energy of single- Λ hypernucleus,

M_{Λ} = mass of Λ hyperon

$M(^{A-1}Z)$ = mass of core nucleus

The detailed calculated results of mass and binding energy are also presented in table 3.

According to the mass calculation, our results are slightly smaller but consistent with known experimental results as shown in the following graph of figure 3.

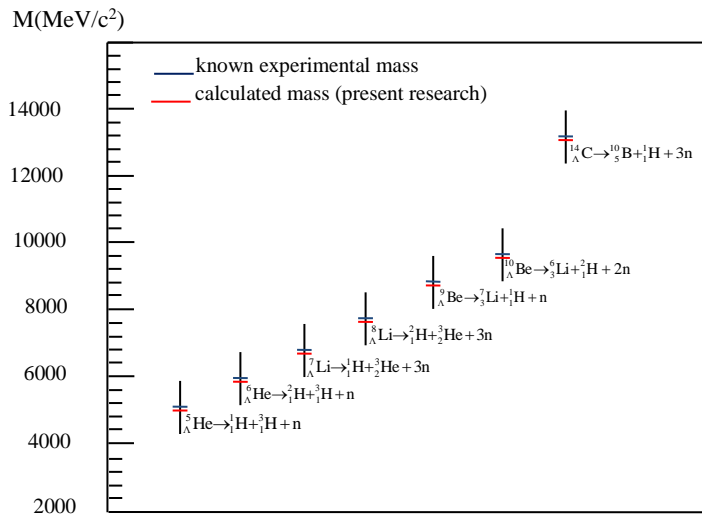


Figure 3 Comparison of known experimental mass and calculated Mass

In figure 3, the blue line represents the known experimental mass of observed single- Λ hypernuclei and the red line represents the calculated mass of present research for all acceptable decay modes. According to the figure 4, it is found that the calculated masses are slightly smaller than known experimental masses for all acceptable decay modes because of neutron contamination in the decay products. In the seven acceptable decay modes of present research, the mass differences between calculate masses and known masses are $\leq 30 \text{ MeV}/c^2$. We compared our calculated results with the previous calculations of two charged particles and one or two or three neutral particles decay products [Htaik Nandar Kyaw, 2020, Takahashi, 2010, Bando, 1990 & Samanta, 2019]. It is found that the results are consistent with the results of previous calculations.

Table 3 Comparison of our Calculated Results of Masses and Binding Energies of Acceptable Single-Λ Hypernuclei and Previous Experimental and Theoretical Values

Decay Modes	Calculated Mass MeV/c ²	Known Mass MeV/c ²	B.E. (MeV)	Known B.E. (MeV)	Remark
${}^5_{\Lambda}\text{He} \rightarrow {}^1_1\text{H} + {}^3_1\text{H} + n$	4815.52 ± 0.003	4839.92 ± 0.05	28.56 ± 0.06	3.12±0.02	Reject
${}^6_{\Lambda}\text{He} \rightarrow {}^2_1\text{H} + {}^3_1\text{H} + n$	5763.94 ± 0.003	5779.33 ± 0.12	20.44 ± 0.15	4.18 ± 0.10	Reject
${}^7_{\Lambda}\text{Li} \rightarrow {}^1_1\text{H} + {}^3_2\text{He} + 3n$	>6698.64 ± 0.01	6711.61 ± 0.06	<20.10± 0.06	5.58 ± 0.03	Acceptable
${}^8_{\Lambda}\text{Li} \rightarrow {}^2_1\text{H} + {}^3_2\text{He} + 3n$	>7641.40 ± 0.01	7642.71 ± 0.06	<9.65 ± 0.06	6.80 ± 0.03	Acceptable
${}^9_{\Lambda}\text{Be} \rightarrow {}^7_3\text{Li} + {}^1_1\text{H} + n$	8550.52 ± 0.01	8563.83 ± 0.06	22.06 ± 0.07	6.71 ± 0.04	Reject
${}^{10}_{\Lambda}\text{Be} \rightarrow {}^6_3\text{Li} + {}^2_1\text{H} + 2n$	>9468.45± 0.01	9499.33 ± 0.06	<42.03± 0.23	9.11 ± 0.22	Acceptable
${}^{14}_{\Lambda}\text{C} \rightarrow {}^{10}_5\text{B} + {}^1_1\text{H} + 3n$	>13188.41± 0.01	13213.03± 0.08	<39.83± 0.34	12.17 ± 0.33	Acceptable

For the binding energy calculation, we used equation 11 and our calculated results are presented in table 3. It is also observed that our calculated results are consistent with the binding energy values of previous theoretical and experimental results [Bando H, 1990 & Samanta C, 2019].

Results and Discussions

A single-Λ hypernucleus event of KEK-PS E373 experiment is kinematically analyzed. Our calculated results are compared with previous calculations and the following four decay modes are most acceptable.

$${}^7_{\Lambda}\text{Li} (\#2) \rightarrow {}^1_1\text{H} (\#3) + {}^3_2\text{He} (\#4) + 3n \tag{12}$$

$${}^8_{\Lambda}\text{Li} (\#2) \rightarrow {}^2_1\text{H} (\#3) + {}^3_2\text{He} (\#4) + 3n \tag{13}$$

$${}^{10}_{\Lambda}\text{Be} (\#2) \rightarrow {}^6_3\text{Li} (\#3) + {}^2_1\text{H} (\#4) + 2n \tag{14}$$

$${}^{14}_{\Lambda}\text{C} (\#2) \rightarrow {}^{10}_5\text{B} (\#3) + {}^1_1\text{H} (\#4) + 3n \tag{15}$$

In the ${}^7_{\Lambda}\text{Li} (\#2) \rightarrow {}^1_1\text{H} (\#3) + {}^3_2\text{He} (\#4) + 3n$ decay mode, the calculated mass is $>6698.64 \pm 0.01 \text{ MeV}/c^2$ and the known experimental mass of ${}^7_{\Lambda}\text{Li}$ is $6711.61 \pm 0.06 \text{ MeV}/c^2$. So, the

mass difference value is $12.97 \pm 0.07 \text{ MeV}/c^2$. The calculated binding energy is $< 20.10 \pm 0.06 \text{ MeV}$ and known binding energy is $5.58 \pm 0.03 \text{ MeV}$. Therefore, this decay mode is acceptable.

In the ${}^8_{\Lambda}\text{Li} (\#2) \rightarrow {}^2\text{H} (\#3) + {}^3\text{He} (\#4) + 3n$ decay mode, the calculated mass is $> 7641.40 \pm 0.01 \text{ MeV}/c^2$ and the known experimental mass of ${}^8_{\Lambda}\text{Li}$ is $7642.71 \pm 0.06 \text{ MeV}/c^2$. So, the mass difference value is $1.31 \pm 0.07 \text{ MeV}/c^2$. The calculated binding energy is $< 9.65 \pm 0.06 \text{ MeV}$ and known binding energy is $6.80 \pm 0.03 \text{ MeV}$. Therefore, this decay mode is acceptable.

In the ${}^{10}_{\Lambda}\text{Be} (\#2) \rightarrow {}^6\text{Li} (\#3) + {}^2\text{H} (\#4) + 2n$ decay mode, the calculated mass is $> 9468.45 \pm 0.01 \text{ MeV}/c^2$ and the known experimental mass of ${}^{10}_{\Lambda}\text{Be}$ is $9499.33 \pm 0.06 \text{ MeV}/c^2$. So, the mass difference value is $30.88 \pm 0.07 \text{ MeV}/c^2$. The calculated binding energy is $< 42.03 \pm 0.23 \text{ MeV}$ and known binding energy is $9.11 \pm 0.22 \text{ MeV}$. Therefore, this decay mode is acceptable.

In the ${}^{14}_{\Lambda}\text{C} (\#2) \rightarrow {}^{10}\text{B} (\#3) + {}^1\text{H} (\#4) + 3n$ decay mode, the calculated mass is $> 13188.41 \pm 0.01 \text{ MeV}/c^2$ and the known experimental mass of ${}^{14}_{\Lambda}\text{C}$ is $13213.33 \pm 0.03 \text{ MeV}/c^2$. So, the mass difference value is $24.62 \pm 0.07 \text{ MeV}/c^2$. The calculated binding energy is $< 39.83 \pm 0.34 \text{ MeV}$ and known binding energy is $12.17 \pm 0.33 \text{ MeV}$. Therefore, this decay mode is acceptable.

According to our analysis, a single- Λ hypernucleus track #2 can be assigned as ${}^7_{\Lambda}\text{Li}$ (or), ${}^8_{\Lambda}\text{Li}$ (or), ${}^{10}_{\Lambda}\text{Be}$ (or) ${}^{14}_{\Lambda}\text{C}$ and the decay particles are p, d, ${}^3\text{He}$, ${}^6\text{Li}$, ${}^{10}\text{B}$ and neutrons. Among the most acceptable four decay modes, ${}^8_{\Lambda}\text{Li} (\#2) \rightarrow {}^2\text{H} (\#3) + {}^3\text{He} (\#4) + 3n$ decay is most probable because its mass difference between calculated mass and known mass is very small value; $1.31 \pm 0.07 \text{ MeV}/c^2$. The binding energy difference is also close to the known value in this decay mode.

Conclusions

The major objectives of nuclear physics are exploring the unknown nuclei to understand the evolution of matter in the universe and studying the origin of nuclear force to understand the formation of atomic nuclei. To fulfill those purposes, the theoretical and experimental investigations have been performed on the nuclear structure, nuclear force and various nuclear properties. Due to those efforts, observation of hypernuclei opens the main door of baryon-baryon interaction to investigate the nuclear forces between hyperon-nucleon (Y-N) and hyperon-hyperon (Y-Y).

At present, hypernuclei are searched via (K^- , K^+) reaction in nuclear emulsion at KEK and J-PARC. In the present research, a single- Λ hypernucleus event which is observed in nuclear emulsion of KEK-PS E373 experiment is analyzed to identify its species and to investigate its mass and binding energy. Kinematical analysis which is based on relativity theory is used to perform present research and it is found that lithium hypernucleus decay is most probable by the emission of deuteron, helion and three neutrons as the decay products.

From our analysis, it can be obtained useful information for Λ -N interaction. Hypernuclear physics is now developing and it is necessary to get more and more information and data on hypernuclear production, decay, life time, mass and binding energy, etc. The present research can support those data to hypernuclear physics group.

Acknowledgements

We would like to thank Professor Nakazawa, Spokesperson of KEK-PS E373 Experiment and Head of Physics Department, Gifu University, and all collaborators of KEK-PS E373 experiment for their discussions, supports and valuable advices to carry out hypernuclear research.

References

- Bando H, Motoba T and Zofka J, "Production, Structure and Decay of Hypernuclei" *International Journal of Modern Physics A*, Vol. 5, 1990, Page 4021-4198.
- Htaik Nandar Kyaw, "Kinematical Analysis of Single- Λ Hypernuclei with Neutral Particle Decay Products in Nuclear Emulsion", *Journal of MAAS*, Vol. XVIII, No. 2C, 2020, Page 479-488.
- Nakazawa K, "Double- Λ Hypernuclei via the Ξ Hyperon Capture at Rest", *Nuclear Physics A 835*, Elsevier Print, ISSN03759474, Netherlands, 2010, Page 207-214.
- Nakazawa K, Private Communication, 2019.
- Samanta C and Schmitt A. T, "Binding, Bonding and Charge Symmetry breaking in Λ -hypernuclei", *AIP Conference Proceedings V*, vol. 2130, 2019. Page 040004.
- Tamura H, "Strangeness Nuclear Physics Experiments at J-PARC", *Progress of Theoretical and Experimental Physics*, vol. 1, Oxford University Press, 2012, page 02B012.
- Takahashi H and Nakazawa K, "Experimental Study of Double- Λ Hypernuclei with Nuclear Emulsion", *Progress of Theoretical Physics Supplement 185*, Oxford University Press, 2010, Page 335-343.

STRUCTURAL AND THERMAL PROPERTIES OF ZnO MODIFIED BISMUTH BORATE GLASSES

Shwe Sin Aye¹, Min Maung Maung², Kham Kham Saing³

Abstract

Borate glasses containing the network modifier oxide ZnO was prepared by melt quenching technique. The structural characterization of these glass samples has been investigated by using X-ray powder diffraction technique (XRD). The morphology of these samples has been determined by using SEM. The transition temperature and crystallization temperature of these glasses were determined by TGA-DTA method. Thermal stability (ΔT) of the glass samples with the different compositions was identified. The FTIR spectroscopy was also used to study the bonding structure of these glasses in the range from 400 to 4000 cm^{-1} . It was found that the Bi^{3+} cations were incorporated in the glass structure as BiO_3 and BiO_6 units and also boron ions were incorporated as BO_3 and BO_4 units.

Keywords melt quenching method, XRD, SEM, DTA, FTIR

Introduction

Glasses are amorphous materials and they have the random periodic arrangement of atoms or ions or molecules [Khanna, A., et al., 2003]. Glasses have been synthesized the main properties such as rapidly freezing or super cooling their melts without crystallization [Pal, M., et al., 2011]. The structures and various properties of glasses depend on the quenching rates and compositions [Pal, M., et al., 2011]. Glasses are accepting significant consideration because of their interesting properties like hardness, good strength, transparency and excellent corrosion resistance [Oprea, I. I., et al., 2004]. There are various glasses in material research, a boric oxide B_2O_3 perform as the popular and brilliant glass formers, flux materials and has get great attention from the person which are study the material science because of its interesting electrical, optical and luminescent properties for various technical applications [Singh, L., et al., 2014].

Nowadays, Bi_2O_3 , TeO_2 and PbO are heavy metal oxide glasses, these oxides have been analysed widely in many applications [Bajaj, A., et al., 2009]. These glasses have several ranges of applications due to their high refractive index, infrared transmission, non-linear properties) low melting temperature and high dielectric constant [Ali, A. A., 2008].

There are two types of glass former in the glass system [Ali, A. A., 2008]. They are conditional glass former and conventional glass former [Ali, A. A., 2008]. B_2O_3 acts as a typical glass former or conventional glass former and Bi_2O_3 performs as a conditional glass former that is perform as well as modifier [Dong, M. G., et al., 2017]. Nevertheless, both network-forming and network modifying positions can applied in Bi_2O_3 depending on its concentration in the glass composition as well as ZnO [Doweidar, H., 2009]. In recent year, many applications such as optical and electronic devices, thermal and mechanical sensors, reflecting windows, radiation-shielding purposes, etc. apply Bi_2O_3 consist of glasses because of its interesting properties [ElBatal, F. H., et al., 2006]. The nature and concentration of constituent oxides are main part of the glass system because of these facts are strongly depended on the glass structure and properties [Radhakrishnan, A. A., 2014].

In this research work, the sample preparation was expressed about the network modifier type of zinc oxide bismuth borate glasses with the different compositions. The structural

¹ Department of Physics, University of Computer Studies (Pinlon)

² Department of Physics, University of Yangon

³ Department of Physics, Technological University (Loikaw)

characterization of these glasses had been measured by using X-ray Diffraction (XRD) and Scanning Electron Microscope (SEM), the thermal properties of these glasses had been determined by using Differential Thermal Analysis (DTA) and the bonding structure of these glasses was also analyzed by Fourier Transform Infrared Spectroscopy (FTIR).

Material and Methods

Sample Preparation

The flowchart of the sample preparation was shown in Figure 1. Borate glasses having the formula $x \text{ZnO} + y \text{Bi}_2\text{O}_3 + (1 - x - y) \text{B}_2\text{O}_3$ (where $x = 0.1, 0.2, 0.3$ and $y = 0.1$) were prepared by using the melt-quenching technique. The reagent grade of the starting materials ZnO , Bi_2O_3 and H_3BO_3 had been mixed thoroughly in a porcelain pestle-mortar for an hour. After being pulverized, it was heated at 300°C for two hours to convert from boric acid (H_3BO_3) to boric oxide (B_2O_3). Then, it was melted at 1100°C for two hours again. The formation of zinc oxide bismuth borate glass (ZBB) molten samples was obtained. The melted homogeneous glass samples were then quenched by pouring it onto the copper plate and cooled down to room temperature. Finally, the brightly yellow of ZBB samples without bubbles were obtained.

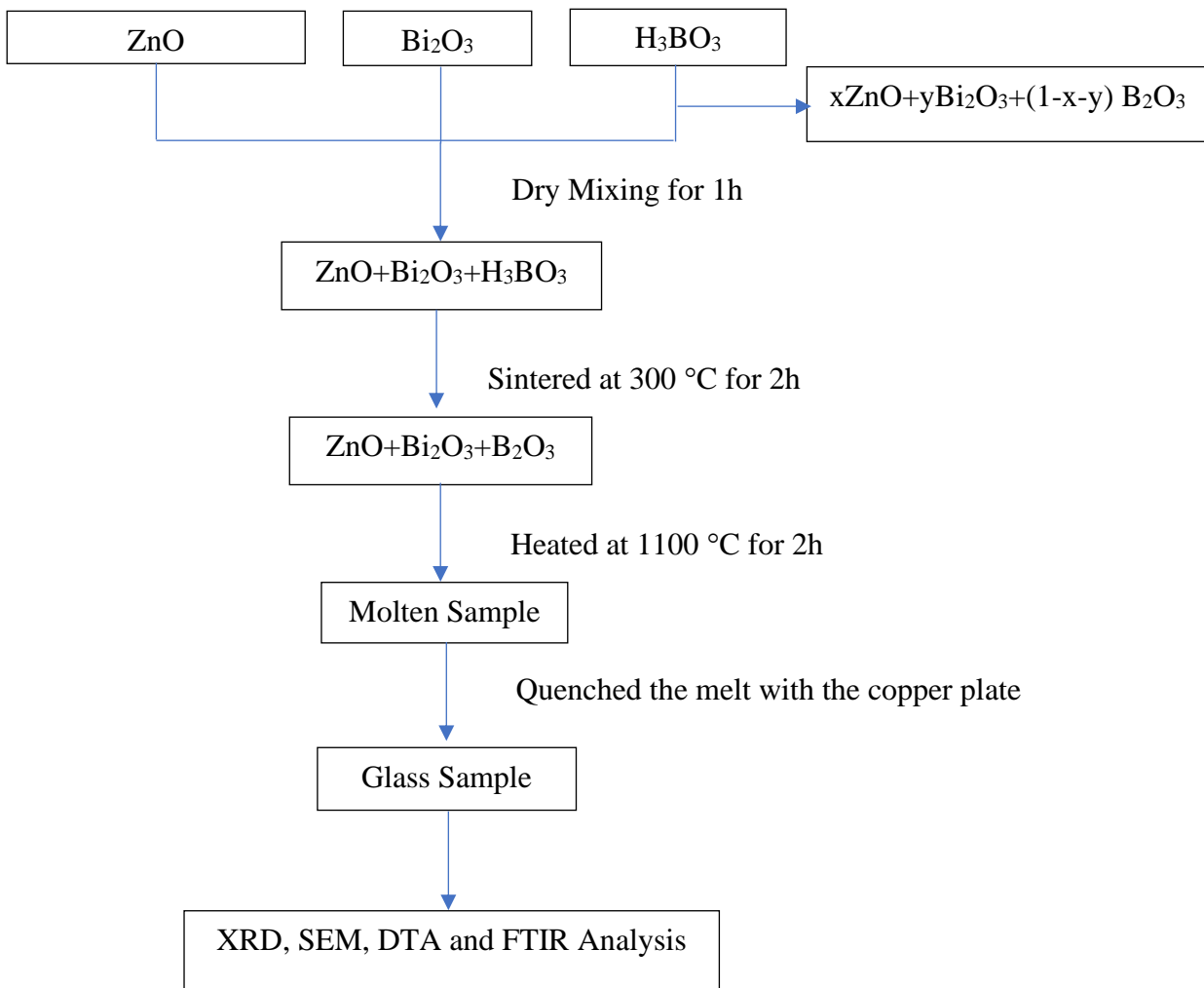


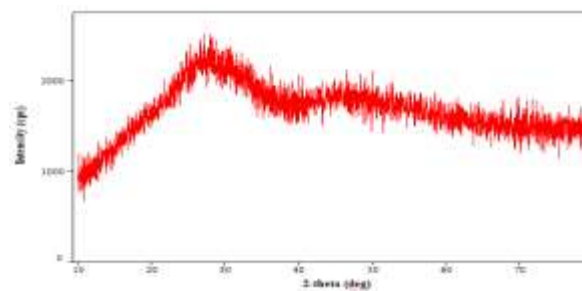
Figure 1 The Flow Diagram Showing the Process of the Sample Preparation

Results and Discussion

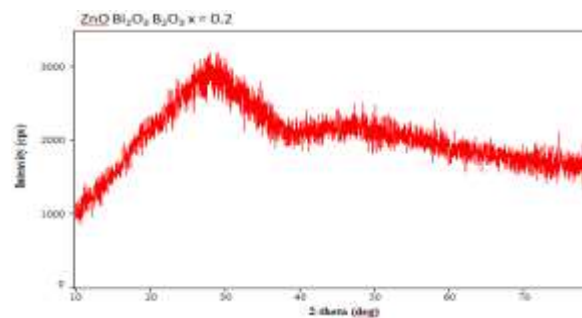
The study of glass structure and thermal properties are important because the properties exhibited by the glasses are both composition and structure sensitive. Network modifier type of zinc oxide based on bismuth borate glasses with the composition of ZnO contents $x = 0.1, 0.2, 0.3$ have been investigated for structural and thermal characterization. Therefore, the XRD, SEM, DTA and FTIR measurements have been employed for the structural and thermal characterization of these glasses.

XRD Analysis

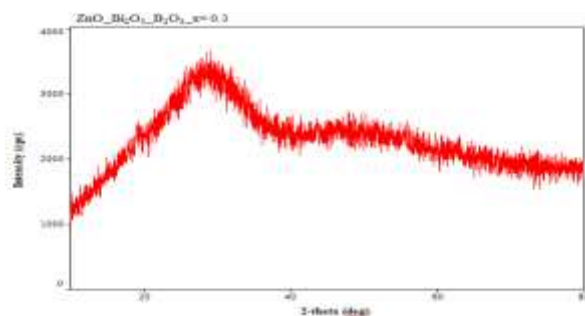
Bismuth borate glass samples could be prepared in the system where in the ZnO varies corresponding to difference x values, $x = 0.1, 0.2$ and 0.3 . The XRD patterns have a broad hump peak at about 20-30 degree, as in generally observed in several oxide glasses with an amorphous structure. The X-ray diffraction pattern of these prepared three glass samples show only few broad diffuse scatterings at angles characteristic of short-range structured disorder, confirming the amorphous nature of the samples in the composition range studies. The formation of homogeneous glass samples was confirmed by XRD is illustrated. The XRD patterns of the various samples with the composition x are shown in Figure 2(a), (b) and (c).



(a)



(b)

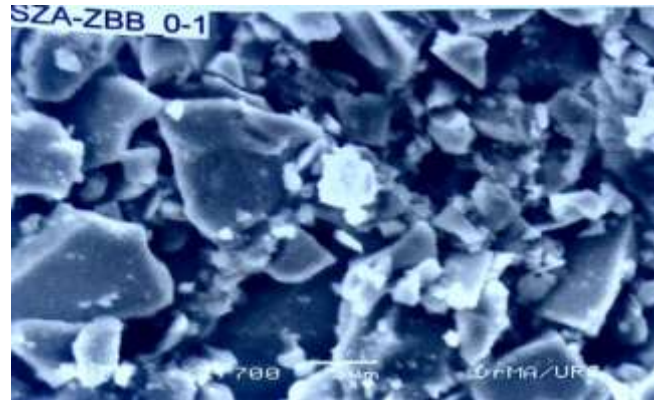


(c)

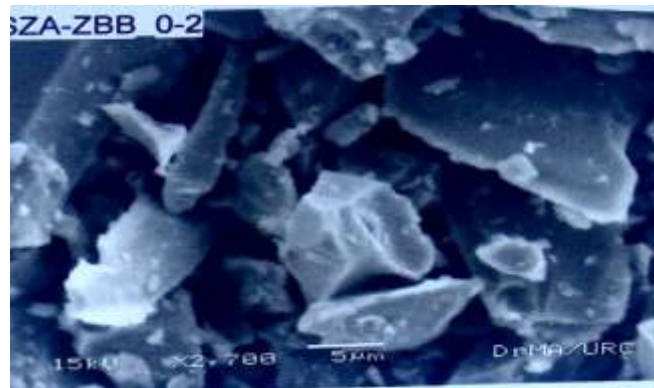
Figure 2 XRD Pattern of x ZnO + y Bi₂O₃ + (1 - x - y) B₂O₃ Glasses for (a) $x = 0.1$ and $y = 0.1$ (b) $x = 0.2$ and $y = 0.1$ (c) $x = 0.3$ and $y = 0.1$

SEM Analysis

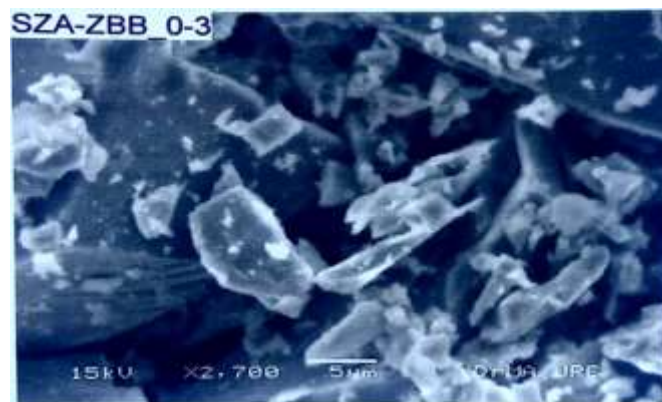
SEM method was used to analyze the morphologies of the zinc bismuth borate glasses with different compositions. Figure 3(a), (b) and (c) illustrate the presence of non-spherical and irregularly shaped particles with sharp edges in all compositions. According to the results, all glasses with different compositions were extremely fine and contained grain sizes of 0.96 μm , 0.92 μm and 0.61 μm which tended to compact producing aggregates.



(a)



(b)

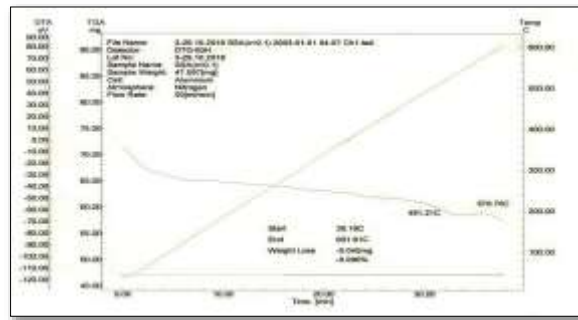


(c)

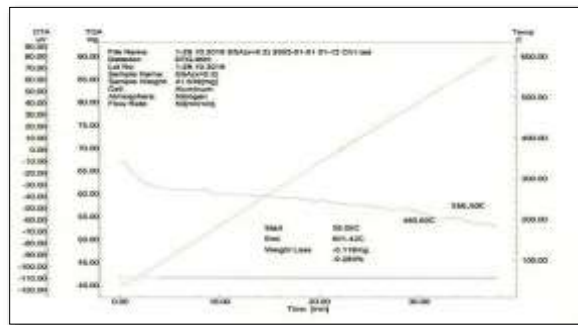
Figure 3 SEM images for ZBB glasses (a) $x = 0.1$ (b) $x = 0.2$ and (c) $x = 0.3$

DTA Analysis

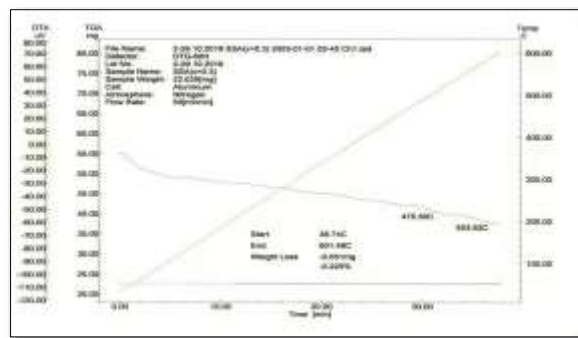
The differential thermal analysis (DTA) studies of modifier oxide ZnO bismuth borate glasses with different composition were shown in Figure 4(a), (b) and (c). From these results, it was found that the transition temperature T_g decreased from 481 °C to 476 °C as the content of ZnO increased. Similarly, the crystallization temperature T_c also decreased from 571 °C to 554 °C as the content of ZnO increased. In the result of DTA analysis, the increasing value of ZnO oxide modifier content, the values of glass transition temperature T_g and crystalline temperature T_c were decreased. It is believed that T_g depending on the strength of chemical bonds in the structure. The increase of non-bridging oxygen suggests the breaking of chemical bonds, which successively decrease the T_g and T_c . The thermal stability ΔT was calculated by the equation $\Delta T = T_c - T_g$. The values of the thermal stability of the glasses were obtained 90 °C, 87 °C and 78 °C with different compositions (ZnO = 0.1, 0.2 and 0.3).



(a)



(b)



(c)

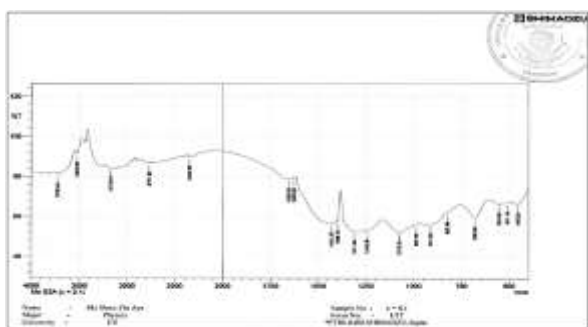
Figure 4 DTA Result of $x \text{ ZnO} + y \text{ Bi}_2\text{O}_3 + (1 - x - y) \text{ B}_2\text{O}_3$ Glasses for (a) $x = 0.1$ and $y = 0.1$ (b) $x = 0.2$ and $y = 0.1$ (c) $x = 0.3$ and $y = 0.1$

FT-IR analysis

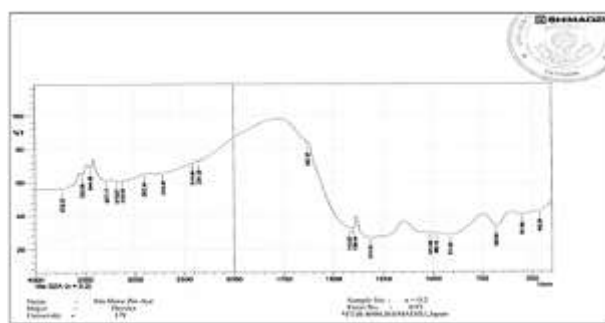
The characteristic absorption band studies of zinc oxide bismuth borate glasses with different composition were shown in Table 1 and Figure 5(a), (b) and (c).

Table 1. The FT-IR Absorption Bands of ZnO - Bi₂O₃ - B₂O₃ Glass with x = 0.1, 0.2, 0.3

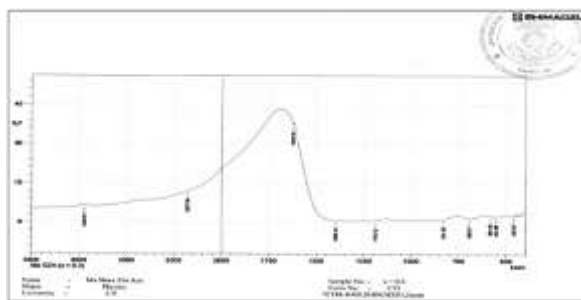
Wavelength(cm ⁻¹)			FTIR Assignment
x = 0.1	x = 0.2	x = 0.3	
455	462	459	Zn-O bond vibrations in tetrahedral ZnO ₄ units.
511	551	584	Stretching vibrations of Bi-O bonds in strongly distorted BiO ₆ octahedral units, B-O-B bond bending vibration.
680	680	692	Symmetric stretching vibrations of Bi-O bonds in pyramidal BiO ₃ units, O ₃ B-O-BO ₃ bending vibrations.
825	914	831	Symmetric stretching vibrations of Bi-O bonds in pyramidal BiO ₃ units, stretching vibrations of B-O bonds in BO ₄ units from diborate groups.
987	1012	1190	Stretching vibrations of B-O bonds in BO ₄ units from tri-, tetra-, and penta-borate groups.
1246	1315	1315	Stretching vibrations of B-O bonds in BO ₃ units from meta- and ortho-borate groups.
1398	1413	1626	Asymmetric stretching vibrations of B-O bonds in BO ₃ units.



(a)



(b)



(c)

Figure 5 FT-IR Spectrum of x ZnO + y Bi₂O₃ + (1 - x - y) B₂O₃ Glasses for (a) x = 0.1 and y = 0.1 (b) x = 0.2 and y = 0.1 (c) x = 0.3 and y = 0.1

Conclusions

In this present work, the glass system $x \text{ ZnO} + y \text{ Bi}_2\text{O}_3 + (1 - x - y) \text{ B}_2\text{O}_3$ with different compositions ($x = 0.1, 0.2$ and 0.3) were prepared by melt quenching method. From XRD results, all patterns of the zinc bismuth borate glasses show no sharp Bragg's peak, but only few broad diffuse humps which confirm that all samples have the amorphous nature.

From SEM result, all samples had irregular shape and grain sizes were smaller with the increasing of ZnO modifier content.

The DTA studies showed that the glass transition temperature T_g decreased with the increasing of the glass modifier content ZnO. ZnO, play the role of a network modifier and non-bridging oxygen increases with the increasing of modifier content. It is shown that the increasing of connectivity due to the increasing of non-bridging oxygen (BO_3 to BO_4) causes the thermal expansion to decrease and viscosity to increase. Therefore, the thermal stabilities also decrease with the increasing of ZnO compositions.

From FT-IR results, Zn-O bond converted to ZnO_4 structure in zinc bismuth borate glasses and Bi^{3+} cations were incorporated in the glass structure as BiO_3 and BiO_6 units and also boron ions were incorporated as BO_3 and BO_4 units. According to the results, the structure link of these glasses was improved with the increasing of the modifier content.

Acknowledgments

The authors would like to express our deepest gratitude to the Department of Physics and Universities' Research Center, University of Yangon, for the supports with research facilities. The authors are grateful to Dr Myint Myint Khing, Pro-rector, University of Computer Studies (Pinlon), for her kind encouragement and permission. We deeply thank the Myanmar Academy of Arts and Science for submission of research paper.

References

- Ali, A. A., and Shaaban, M. H., (2008), "Electrical conductivity of silver bismuth borate tellurite glasses", Phys. B Condens. Matter, vol. 403, no. 13–16, pp. 2461–2467.
- Bajaj, A., Khanna, A., Chen, B., Longstaffe, J., Zwanziger, U., Zwanziger, J.W., Gomez, Y., Gonzalez, F., (2009), "Structural investigation of bismuth borate glasses and crystalline phases", J. Non. Cryst. Solids, vol. 355, no. 1, pp. 45–53.
- Doweidar, H., and Saddeek, Y. B., (2009), "FTIR and ultrasonic investigations on modified bismuth borate glasses", J. Non. Cryst. Solids, vol. 355, no. 6, pp. 348–354.
- Dong, M.G., Sayyed, M.I., Lakshminarayana, G., Ersundu, M. C., Ersundu, A.E., Priyanka Nayar, Mahdi, M.A., (2017), "Investigation of gamma radiation shielding properties of lithium zinc bismuth borate glasses using XCOM program and MCNP5 code", J. Non. Cryst. Solids, vol. 468, no. April, pp. 12–16.
- ElBatal, F. H., Marzouk, S. Y., Nada, N., and Desouky, S. M., (2006), "Gamma-ray interaction with copper-doped bismuth-borate glasses", Phys. B Condens. Matter, vol. 391, no. 1, pp. 88–97.
- Khanna, A., Sawhney, K. J. S., Tiwari, M. K., Bhardwaj, S., and Awasthi, A. M., (2003), "Effects of melt ageing on the density, elastic modulus and glass transition temperature of bismuth borate glasses", J. Phys. Condens. Matter, vol. 15, no. 40, pp. 6659–6670.
- Oprea, I. I., Hesse, H., and Betzler, K., (2004), "Optical properties of bismuth borate glasses", Opt. Mater. (Amst), vol. 26, no. 3, pp. 235–237.
- Pal, M., Roy, B., and Pal, M., (2011), "Structural Characterization of Borate Glasses Containing Zinc and Manganese Oxides", J. Mod. Phys., vol. 2, no. 9, pp. 1062–1066.
- Radhakrishnan, A. A., and Beena, B. B., (2014), "Structural and Optical Absorption Analysis of CuO Nanoparticles", Indian J. Adv. Chem. Sci., vol. 2, no. 2, pp. 158–161.
- Singh, L., Thakur, V., Punia, R., Kundu, R. S., and Singh, A., (2014), "Structural and optical properties of barium titanate modified bismuth borate glasses", Solid State Sci., vol. 37, pp. 64–71.

SYNTHESIS AND CHARACTERIZATION OF GLASS CERAMICS USING RICE HUSK ASH AS SILICA SOURCE

Kham Kham Saing¹, Min Maung Maung², Shwe Sin Aye³

Abstract

In this research, the sodium calcium silicate glass ceramics was prepared via sol-gel method utilizing rice husk ash (RHA). To prepare rice husk ash, the rice husk was treated with dilute hydrochloric acid solution to gain the high percentage silica content and then calcined at 700 °C. The high-quality rice husk ash with acid pretreatment was used as silica source for sodium silica solution to prepare silica gel. The silica gel was prepared by sol gel method with extracted rice husk ash, NaOH and Ca (NO₃)₂·4H₂O. The dried silica gel was calcined at 700 °C and then sintered at 900 °C to obtain glass ceramics. EDXRF was employed to study the chemical purity of the obtained silica. The structure of extracted silica and the phase purity of the prepared samples were identified by X-ray Diffractometer (XRD) analysis and it was found that the sodium calcium silicate phase was appeared. The morphology of the obtained samples was analyzed by Scanning Electron Microscope (SEM) that are depicted as aggregated particles with broad size distribution and the grain size of glass ceramics was 3.6 μm. Fourier Transform Infrared (FTIR) spectroscopy was used to detect the binding groups in the samples and Si-O-Si stretching mode and sodium calcium silicate phase were observed in both calcined glass powder and glass ceramics.

Keywords: glass ceramics, rice husk ash (RHA), sol-gel, EDXRF, XRD, SEM, FTIR

Introduction

Sodium calcium silicate glass ceramics is one of the most important biomaterials because of its bioactive property and the ability to form chemical bond with living bones and help in new bone growth [Kumar, S., 2009]. The glass ceramics has many properties with both glass and more traditional crystalline ceramics [Ravindranadh, K., 2016]. The glass ceramics have been used in different fields such as construction, optical, military, biomedical, electronics and kitchenware [Prakash Nayak, J., 2010]. The bioactive glass ceramics has found in clinical applications as coating for prostheses, bone filler, vertebral substitution and bone substitutes [Tabia, Z., et al., 2019]. Major disadvantage of bioactive glass ceramics is the high cost of fabrication [Leenakul, W., et al., 2015]. For this study, rice husk ash was used as the silica source for sodium silica solution to prepare bioactive glass ceramics. In our country, large amount of agricultural waste materials such as rice husk and rice straw are remained after rice grain milling and rice husk ash contains above 90 % of silica after complete combustion. Using RHA as a precursor can significantly reduce the cost of the bioactive glass ceramics productions and so benefits economical aspect. In this research, the glass ceramics was prepared by sol-gel method with extracted rice husk ash. The obtained samples were characterized by XRD, SEM and FTIR analysis.

¹ Department of Physics, Technological University (Loikaw)

² Department of Physics, University of Yangon

³ Department of Physics, University of Computer Studies (Pinlon)

Materials and methods

Preparation of Glass Ceramics

Glass ceramics in the system of SiO_2 - CaO - Na_2O with composition of 50 mol% SiO_2 -25 mol% Na_2O - 25 mol% CaO was synthesized by acid catalyzed sol-gel method. The required silica was extracted from the rice husk. The raw materials, rice husk, was firstly collected, thoroughly cleaned and then washed with tap water for several times. The cleaned rice husk was treated with 1:10 dilution ratio of HCl solution and was washed with distilled water to become pH-7 level and then dried at room temperature. The dried rice husk was calcined with 700 °C for 6 h to get required rice husk ash. RHA (5 g) as source of silica, NaOH (3.33 g) as source of Na_2O and $\text{Ca}(\text{NO}_3)_2 \cdot 4\text{H}_2\text{O}$ (9.84 g) as source of CaO were weighted by electronic balance. The weighted NaOH and $\text{Ca}(\text{NO}_3)_2 \cdot 4\text{H}_2\text{O}$ were added into 100 ml and 40 ml of deionized water, respectively. The NaOH solution was heated by temperature 70 °C. RHA was added into this warmed NaOH solution and the resultant solution was stirred on a magnetic stirrer with temperature 100 °C. After 1 h and 30 min of boiling, the resultant solution was filtered to obtain sodium silicate solution. 100 ml of $\text{HNO}_3(\text{conc})$ was mixed with $\text{Ca}(\text{NO}_3)_2 \cdot 4\text{H}_2\text{O}$ solution to obtain clear solution. Titration of sodium silicate solution dropped wise very slowly into this clear solution in stirring condition. After complete addition of sodium silicate solution, gelation took 55 min for completion. The resulting gel was left for 3 days with temperature 70 °C for ageing to optimize the glass network formation and it was dried at 150 °C for 2 days. The dried gel was ground by mortar and pestle to obtain fine powder and then calcined at 700 °C for 2 h to remove impurities from gel powder. Finally, the calcined powder was pelletized and sintered at 900 °C for 2 h. The flowchart for the synthesis of bioactive glass ceramics using RHA is shown in Figure 1.

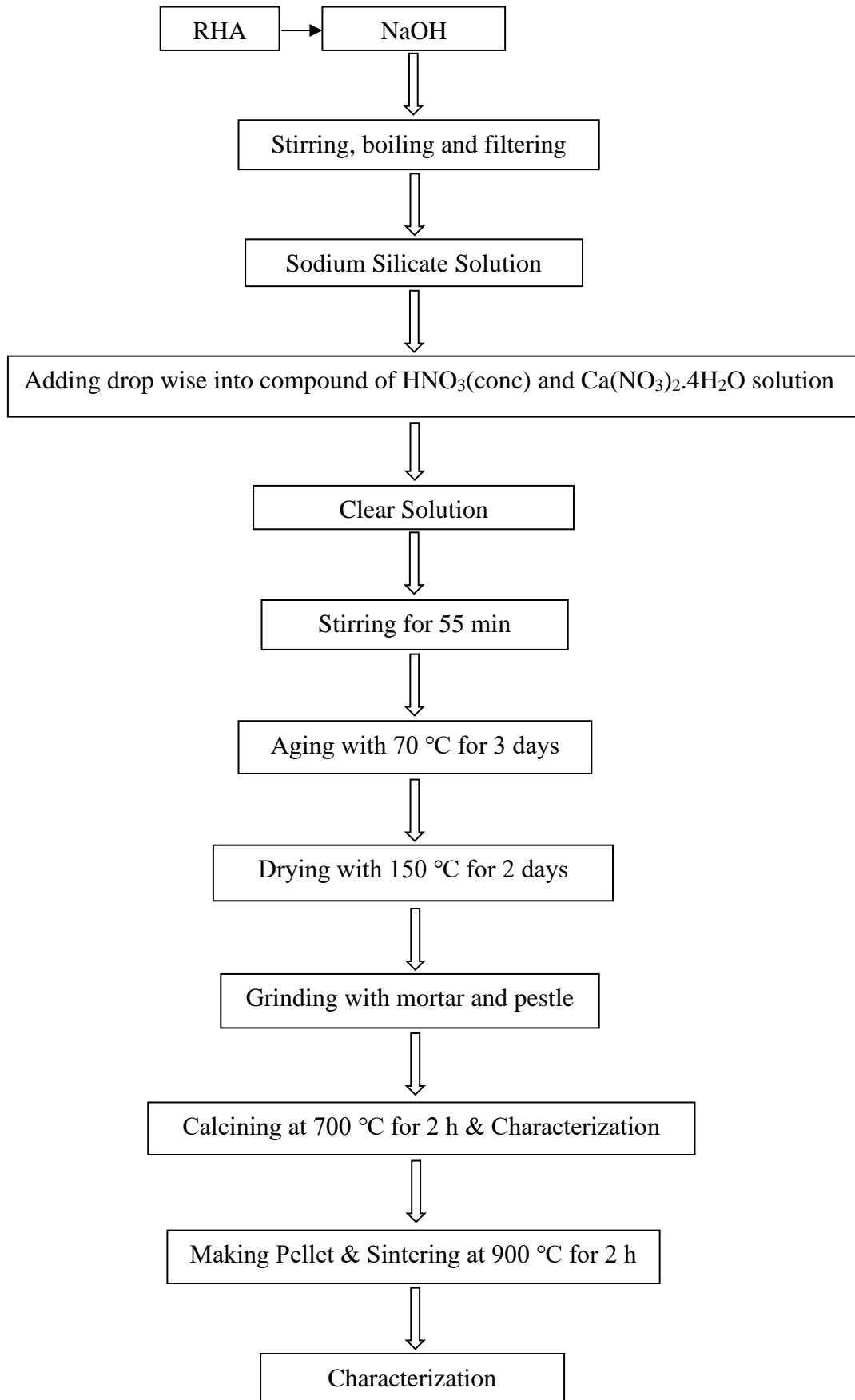


Figure 1 Flow chart for synthesis of glass ceramics using RHA

Results and Discussion

EDXRF Analysis of Rice Husk Ash

The chemical purity of the rice husk ash has been characterized by using EDXRF analysis before preparing glass ceramics. The EDXRF spectrum of rice husk ash is shown in Figure 2. The chemical composition of rice husk ash is summarized in Table 1. The EDXRF results of the rice husk ash confirmed that the main chemical component of the ash was observed as SiO₂.

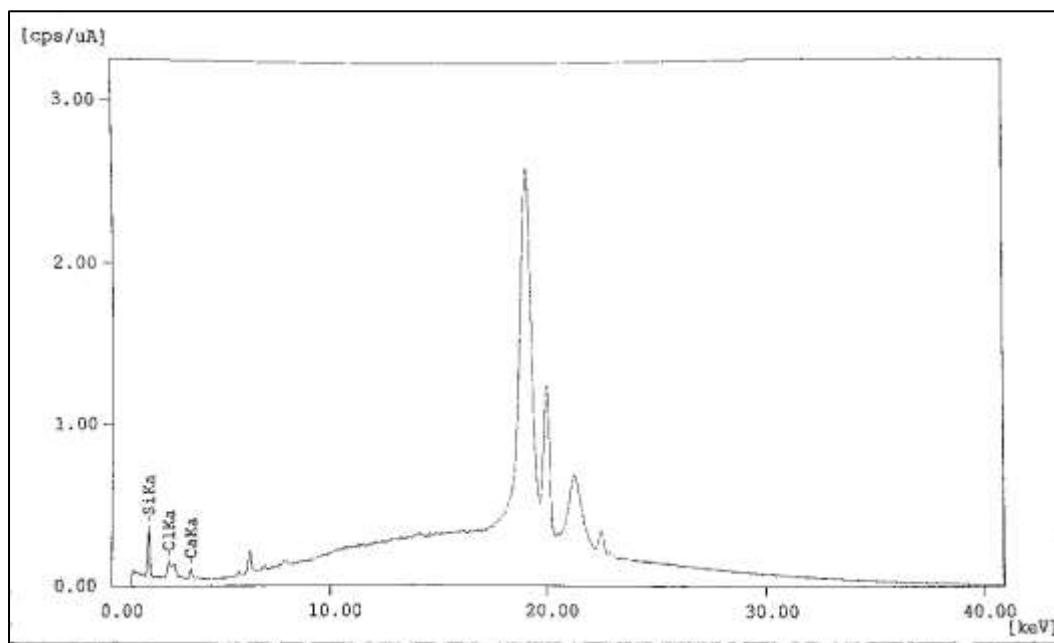


Figure 2 EDXRF spectrum of rice husk ash

Table 1 Chemical Composition of Rice Husk Ash

Compounds	Percentage of weight for Rice Husk ash
SiO ₂	95.561%
Cl	3.869%
CaO	0.570%

XRD Analysis

The amorphous and crystalline form of the resultant ash has been analyzed by XRD characterization. The XRD spectrum of rice husk ash is shown in Figure 3. There is no sharp peak and the broad peak zone centered near $2\theta = 22^\circ$ shows the nature of amorphous silica-based materials. Therefore, the amorphous silica phase was observed in the rice husk ash.

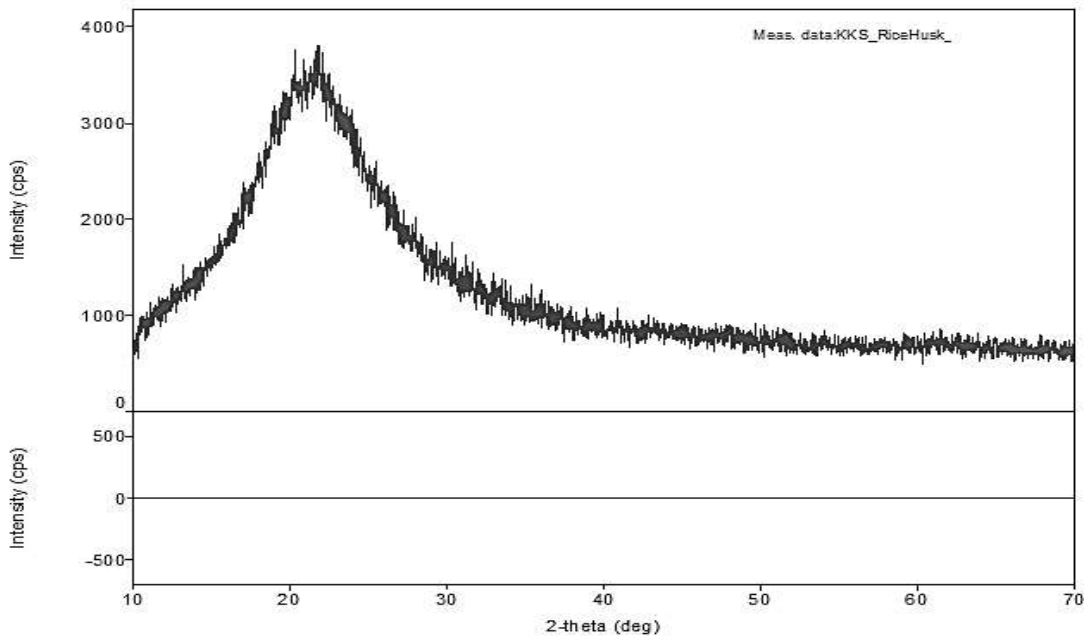


Figure 3 XRD pattern of rice husk ash (RHA)

The XRD spectra of calcined gel powder and glass ceramics are shown in Figure 4(a) and 4(b). The observed XRD profiles were confirmed with International Centre of Diffraction Data (ICDD) library file. From XRD result, sharp peaks of sodium nitrate (NaNO_3) were appeared around $2\theta = 29.2^\circ$, 38.8° , 42.4° and 48° with (104), (113), (202) and (018) planes in calcined gel powder, respectively. The peaks (226) around $2\theta = 32.8^\circ$ and (040) around $2\theta = 34.8^\circ$ were also observed the present of sodium calcium silicate ($\text{Na}_2\text{Ca}_2\text{Si}_2\text{O}_7$) phase.

In XRD spectrum of glass ceramics, it was observed (104), (018) and (113) peaks at $2\theta = 29.2^\circ$, 48° and 38.8° that show the present of sodium nitrate structure. The intensity of peaks for sodium nitrate was decreased due to its decomposition after sintering at 900°C for 2 h. The presence of sodium calcium silicate was shown by the peaks (226) around $2\theta = 32.8^\circ$, (040) around $2\theta = 34.8^\circ$, (0012) around $2\theta = 44.5^\circ$ and (440) around $2\theta = 49^\circ$. The sample pattern of glass ceramics showed that there was the formation of sodium calcium silicate with two different crystalline phases $\text{Na}_6\text{Ca}_3\text{Si}_6\text{O}_{18}$ and $\text{Na}_2\text{Ca}_2\text{Si}_2\text{O}_7$ by two peaks around $2\theta = 33^\circ$ [Prakash Nayak, J., 2010]. As the results, the main crystalline phase of the glass ceramics was the sodium calcium silicate.

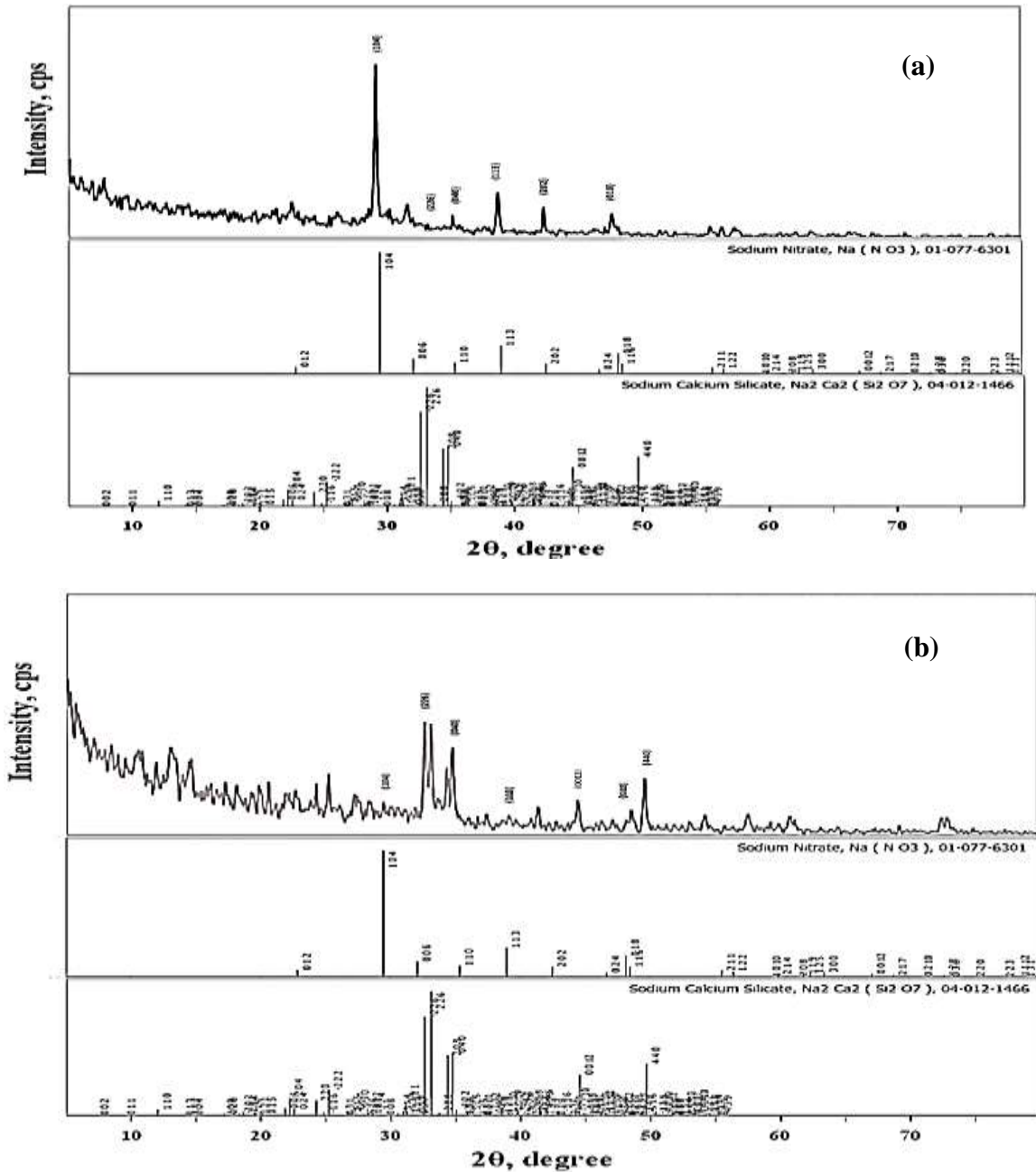


Figure 4 XRD spectrum of (a) calcined gel powder (b) glass ceramics

SEM Analysis

The microstructure and average grain size of the samples were analyzed by using SEM image. Changes in the microstructure of calcined gel powder and glass ceramics were observed in Figure 5(a) and 5(b). The morphology of both samples can be seen as aggregated particles with broad size distribution. The morphology and surface appearance of the calcined gel powder at 700 °C corresponded to irregular agglomerates distributed heterogeneously.

In sintered glass ceramics at 900 °C, one can also see irregular agglomerates but the distribution of grains is homogeneous than the calcined gel powder sample. After the sintering process, it was possible to observe fine grains in the microstructure. Increasing the volume of crystallization after sintering process was observed by the microstructural features of the samples. SEM ruler base on line intercept method was used to determine the average grain size of the glass ceramics sample. From the results, the grain size of the glass ceramics was 3.6 μm .

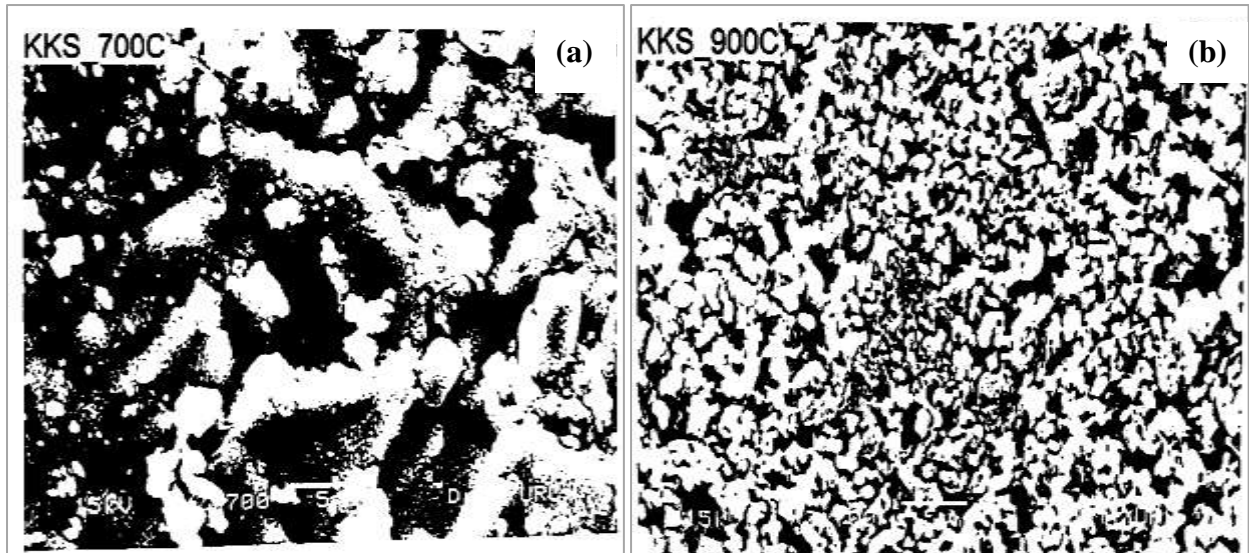


Figure 5 SEM image of (a) calcined gel powder (b) glass ceramics

FTIR Analysis

The FTIR spectrum of the calcined gel powder and glass ceramics were shown in Figure 6(a) and 6(b). The explanations for FTIR transmission bands of samples were shown in Table 2. From FTIR analysis, Si-O-Si bending vibration was strongly found in both samples. The bands at 947.46 cm^{-1} in calcined gel powder and 959.52 cm^{-1} in glass ceramics were indication of Sodium Calcium Silicate phases [Michailova, I., et al., 2015]. C-O stretching mode in both samples was considered to the absorption of carbonate group [Kazeli, K., et al., 2021]. Observing of O-H bond in these samples was associated with the presence of moisture in the samples [Ikotun, B. D., et al., 2014].

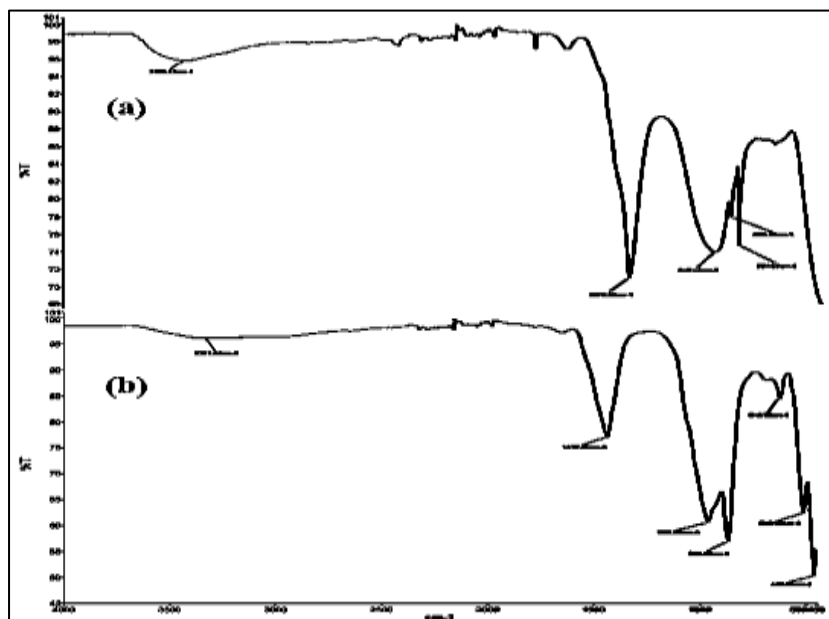


Figure 6 FTIR spectrum of (a) calcined gel powder (b) glass ceramics

Table 2 FTIR Transmission bands of calcined gel powder and glass ceramics sample

Functional Group	Wavenumber (cm ⁻¹)		Explanation
	Calcined gel powder	Glass ceramics	
Si-O-Si bending vibrations	-	458.71, 510.82	confirmed silica strongly found
Si-O vibration	-	619.75	presence of cristobalite phase and most likely arise from sodium calcium silicate phase
Symmetric stretching vibration of Si-O-Si	834	-	confirmed silica strongly found
Stretching vibration of SiO ₄	872.76	864.38	confirmed silica strongly found
Asymmetric stretching vibration of Si-O-Si	947.46	959.52	indication of sodium calcium silicate phase
C-O stretching mode	1348.20	1437.4	absorption of carbonate group
O-H bond	3428.22	3321.66	showed water trapped in sample

Conclusion

The required silica was prepared by combustion of rice husk at 700 °C for 6 h with acid pre-treatment. From the results of EDXRF and XRD analysis, the obtained rice husk ash is suitable to use as silica source for preparation glass ceramics. The silica gel was synthesized by sol-gel method utilizing the extracted silica, sodium hydroxide and calcium nitrate tetrahydrate. The prepared silica gel was calcined at 700 °C for 2 h. The calcined powder was pelletized and sintered at 900 °C for 2 h to prepare sodium calcium silicate glass ceramics.

From XRD results, the peaks of sodium nitrate and sodium calcium silicate were observed in both samples. However, the intensity of peaks for sodium nitrate was decreased due to its decomposition and there was formation of sodium calcium silicate with two different crystalline phases Na₆Ca₃Si₆O₁₈ and Na₂Ca₂Si₂O₇ in glass ceramics.

According to SEM images, both samples corresponded to irregular agglomerates distributed heterogeneously but the particles began to be homogeneous in glass ceramics sample due to sinter. The grain size of the glass ceramics was 3.6 μm.

By FTIR analysis, the peaks for the Si-O-Si group, CO₃²⁻ group and sodium calcium silicate phase were strongly found in both samples. In the prepared samples, the detected peaks for O-H groups indicated that some water molecules were trapped inside both samples. The above results showed that the glass ceramics containing the sodium calcium silicate as main crystalline phase was prepared in this research.

Acknowledgements

The authors would like to express our deepest gratitude to the Department of Physics and Universities' Research Center, University of Yangon, for the supports with research facilities. The authors are grateful to Dr Khaing Zaw Naing, Pro-rector, Technological University (Loikaw), for his kind encouragement and permission. We deeply thank the Myanmar Academy of Arts and Science for submission of research paper.

References

- Ikotun, B. D., Mishra, S., and Fanourakis, G. C., (2014), “*Structural characterization of four south african fly ashes and their structural changes with β -cyclodextrin*”, Part. Sci. Technol., vol. 32, no. 4, pp. 360–365.
- Kazeli, K., Tsamesidis, I., Theocharidou, A., Malletzidou, L., Rhoades, J., Pouroutzidou, G. K., and Lymperaki, E., (2021), “*Synthesis and characterization of novel calcium-silicate nanobioceramics with magnesium: Effect of heat treatment on biological, physical and chemical properties*”, Ceramics, vol. 4, no. 4, pp. 628–651.
- Kumar, S., (2009), “*Sol-gel Synthesis and in Vitro Characterization of Bioactive Glass Ceramics using Rice Husk Ash Waste Material*”, Department of Ceramic Engineering National Institute of Technology, Rourkela.
- Leenakul, W., Tunkasiri, T., Tongsir, N., Pengpat, K., and Ruangsuriya, J., (2015), “*Effect of sintering temperature variations on fabrication of 45S5 bioactive glass-ceramics using rice husk as a source for silica*”, Mater. Sci. Eng. C, vol. 61, pp. 695–704.
- Mihailova, I., Radev, L., Aleksandrova, V., Colova, I., Salvado, I. M., and Fernandes, M. H., (2015), “*Carbonate-apatite forming ability of polyphase glass-ceramics in the CaO-MgO- SiO₂ system*”, Journal of Chemical Technology and Metallurgy, 50 (2015), vol. 50, no. January, pp. 502–511.
- Nayak, J. P., (2010), “*Preparation and Characterization of Bioactive Silica-based Ceramics derived from Rice Husk Ash*”, ProQuest Diss. Theses ProQuest Diss. Theses, no.507,p.160.
- Ravindranadh, K., (2016), “*Bioactive glasses for technological and clinical applications*”, Int. J. Chem. Sci., vol. 14, no. 3, pp. 1339–1348.
- Tabia, Z., El Mabrouk, K., Bricha, M., and Nouneh, K., (2019), “*Mesoporous bioactive glass nanoparticles doped with magnesium : Drug delivery and acellular : In vitro bioactivity*”, RSC Adv., vol. 9, no. 22, pp. 12232–12246.

STUDY ON OPTICAL PROPERTIES OF NATURAL DYE EXTRACTED FROM ROSE FLOWERS

Myat Myo Myo Aye¹, Poe Ei San², Aye Moe Thae³, Pyae Phyko Ko⁴

Abstract

The natural dye extracted from rose flowers (red, orange, and yellow color) were studied for dye sensitized solar cells (DSSCs) applications. The natural dye was extracted from rose flowers with various solvents. deionized water, ethanol, and methanol were used as a solvent for extraction. The optical absorption spectra and energy band gap of extracted dye solutions were investigated with a UV-Visible spectrometer. The absorption spectra of the extracted were performed in the spectral range from 210 nm to 800 nm. The effects of solvents have been investigated by analyzing the optical properties of including absorbance spectrum, energy bandgap and transmittance of the cell with the best performance were investigated. For photo energy, results show in wide energy bandgap of from 3.2 eV to 3.8 eV, were used as the deionized water, ethanol and methanol solvent.

Keywords: Absorbance, energy bandgap, roses' flowers, UV visible spectrometer

Introduction

In DSSCs, the absorbed dye behaves as a sensitizer for absorbing sunlight. The conservation of solar energy into electricity in the solar cells was based on charge separation. The use of natural dyes extracted from trees, fruits, and vegetables as sensitizers for the conservation of solar energy into electricity is very interesting because it improves the economical aspect and makes an important profit from the environment. In this paper, natural dyes were extracted from rose flowers (red, orange, and yellow color), used as DSSCs photosensitizers. Roses flowers were known as decorative plants famous for their flowers and fragrance. The parts of plants were used in the manufacturing of perfumes, essence, and flower crops. Rose flowers have attractive petals in shape, size and color. The color of flowers varies, white, yellow, blue, black, and red. Dye-sensitized solar cell were energy devices for converting light energy into electricity. Dye-sensitized solar cells offered the advantages as a new class of low cost and easy to fabricates, and can achieve high solar energy conversion efficiency. Most methods of measuring absorbance required that the compound in a liquid form or dissolved in a liquid solution. This range from 210 nm to 800 nm wavelengths. The dye sensitized solar cell appear to be highly promising and cost-effective alternatives for photovoltaic energy sectors due to its relatively cheapness to produce, environment friendly and promising effacing. In DSSCs, the dye plays an important role in harvesting solar cell energy and converting it to electrical energy with the aid of a semiconducting photo anode.

Absorption of Energy

For light, the energy of the wave was related to the frequency of particular color of light. The energy transferred through space by light obeys the Planck's relationship:

$$E = hv = hf = \frac{hc}{\lambda} \quad (1)$$

Where, h = Planck constant = 6.626×10^{-34} Js

¹ Department of Physics, Kyaukse University, Myanmar

² Department of Physics, Kyaukse University, Myanmar

³ Department of Physics, Kyaukse University, Myanmar

⁴ Department of Physics, Kyaukse University, Myanmar

$$\text{Absorption coefficient } (\alpha) = \frac{2.303A}{t} \quad (2)$$

Absorbance (A), or optical density, is a logarithmic function of T and is expressed as:

$$A = 2 - \log (\%T) \quad (3)$$

Where A = absorbance, t = thickness

$$\%T = 10^{(2 - Abs)} \quad (4)$$

Absorbance is a measure of the amount of light absorbed by a sample as a beam of light pass through it. Transmittance is the amount of light transmitted by a sample and is related to absorbance. The absorbance of light absorbing material is proportional to its concentration in solution. Transmittance was the inverse of absorbance. Absorbance is the light that the solution absorbs whereas transmittance is light passes through a solution. The value of absorption was always low and mostly less than 1 while the value of transmittance was relatively high. Transmittance depends on absorption for occurring while absorption depends on transmittance for calculation. The absorbance of a sample is directly proportional to the path length of the sample holder and the concentration of the sample. Absorbance is measured in absorbance units (Au) and are dimensionless. The natural dyes were availability abundant in nature, renewable, simple manufacturing process, and relatively low price.

Sample Preparation of Dye Solution

Natural dyes (rose flowers) were collected from local market. All sample were extracted from the deionized water, ethanol, and methanol. The raw materials were washed each flower with deionized water and left to dry at room temperature for about two weeks. After drying and crushing into a fine powder using a mixer, 2.5 g of each powder was immersed in 50 ml of deionized water, 95 % ethanol, and methanol solution at room temperature in dark for a day. The extracted were then obtained. They were filtered out to remove the remaining solids of the powders UV-Visible spectrometer was used to carry out the absorption spectra of the extracted in the range for 210 nm to 800 nm.

Result and Discussion

In DSSCs, the dye plays important roles to absorb the visible light and to inject the electrons. The absorbance spectra of the dye were measured between 210 nm to 800 nm. The UV-Vis absorption spectra for the dye solution extracted using different solvents deionized water, ethanol, and methanol solvent were shown in Figure (1), (2), and (3) below. A plot of $(\alpha(h\nu))^2$ versus photon energy ($h\nu$) showed intermediate linear region the extrapolation of the linear part can be used to calculate the energy from intersect with ($h\nu$) axis as shown in figure (4), (5), and (6). The resultant value of energy bandgap for red, orange, and yellow rose flowers were found to be about 3.2 eV to 3.8eV for extracted with various solvent. The absorption coefficient of liquid was increased with increasing photon energy, the concentrated dye was the highest absorption coefficient. The dye between the valence and conduction bands work to absorb photon with wide energies. Figure (7), (8), and (9) showed in UV-Vis optical transmittance spectra of all samples the wavelength was in the range between 210 nm to 800 nm. The relation between absorbance and transmittance is all the light passes through a solution without any absorption, then absorbance is zero, and percent transmittance is 100 %. Optical properties as absorbance and transmittance were very important properties for semiconductors tool as detectors and solar cell, and can be calculated from equations (3) and (4).

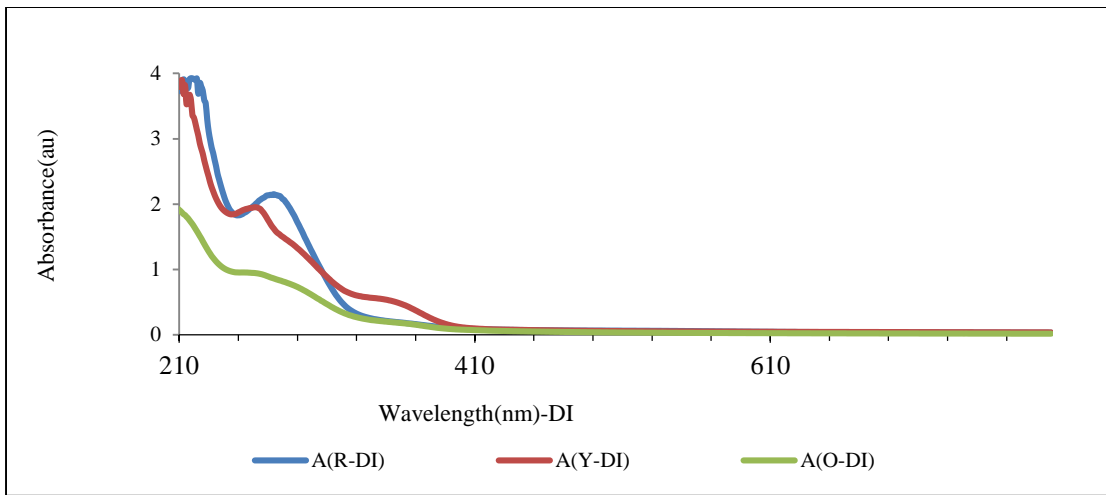


Figure 1 Comparison of UV-Vis absorption spectra for deionized water of dye from rose flowers

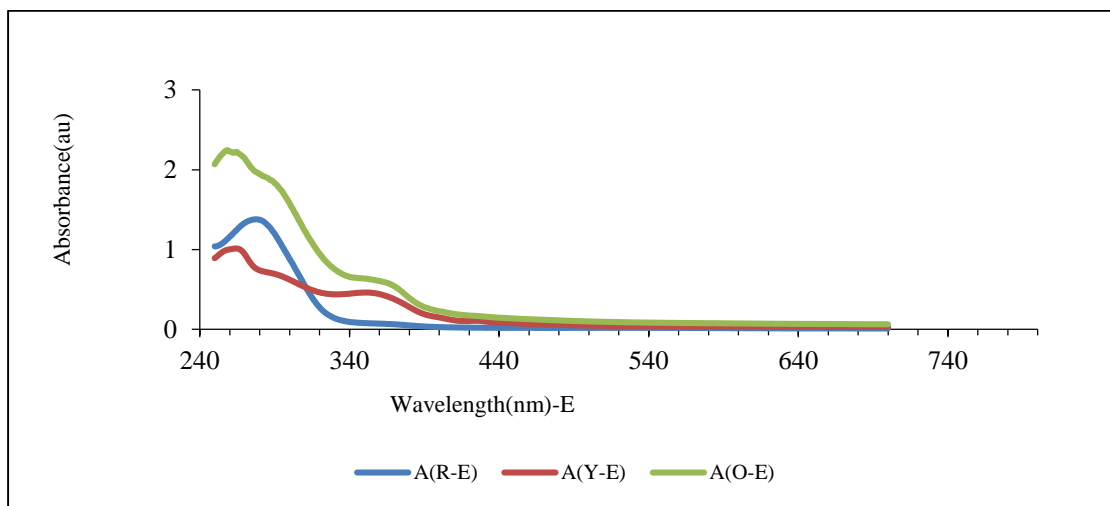


Figure 2 Comparison of UV-Vis absorption spectra for ethanol of dye from rose flowers

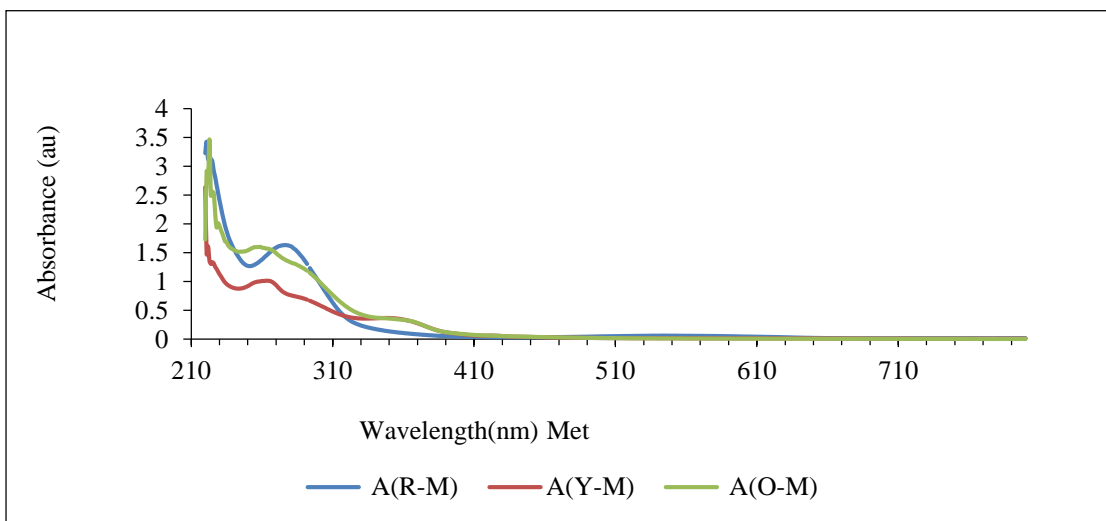


Figure 3 Comparison of UV-Vis absorption spectra for methanol of dye from rose flowers

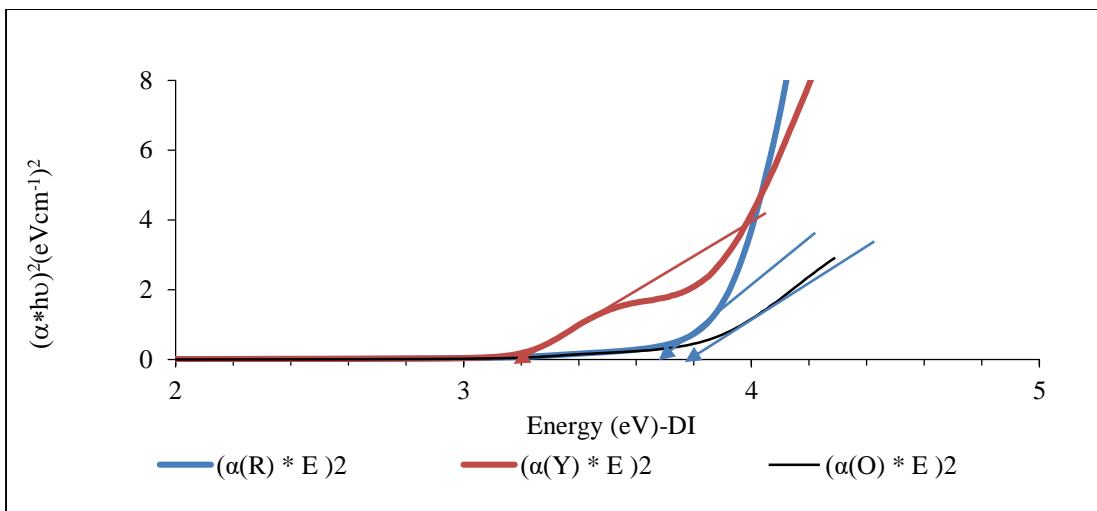


Figure 4 Comparison of $(\alpha(h\nu))^2$ versus photon energy ($h\nu$ (DI)) of rose flowers

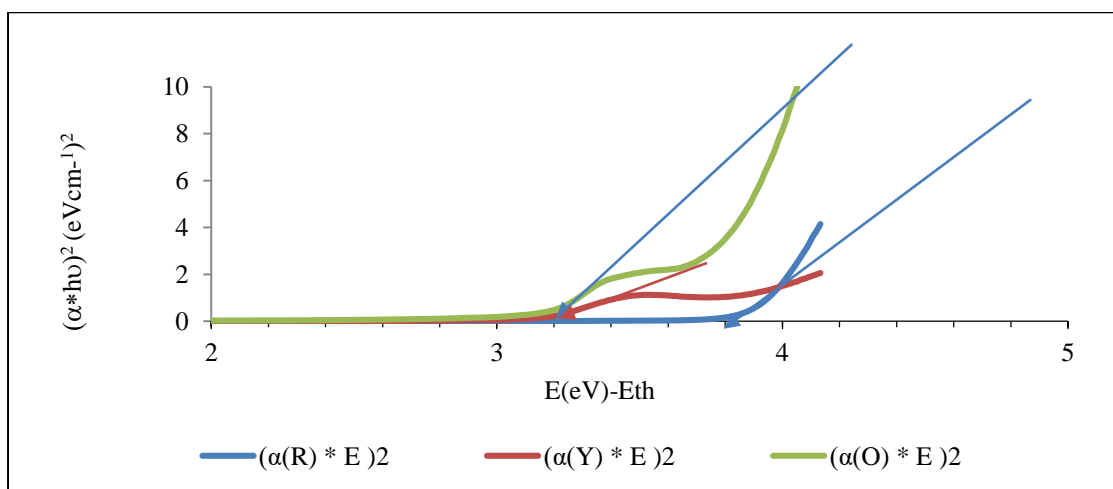


Figure 5 Comparison of $(\alpha(h\nu))^2$ versus photon energy ($h\nu$ (ethanol)) of rose flowers

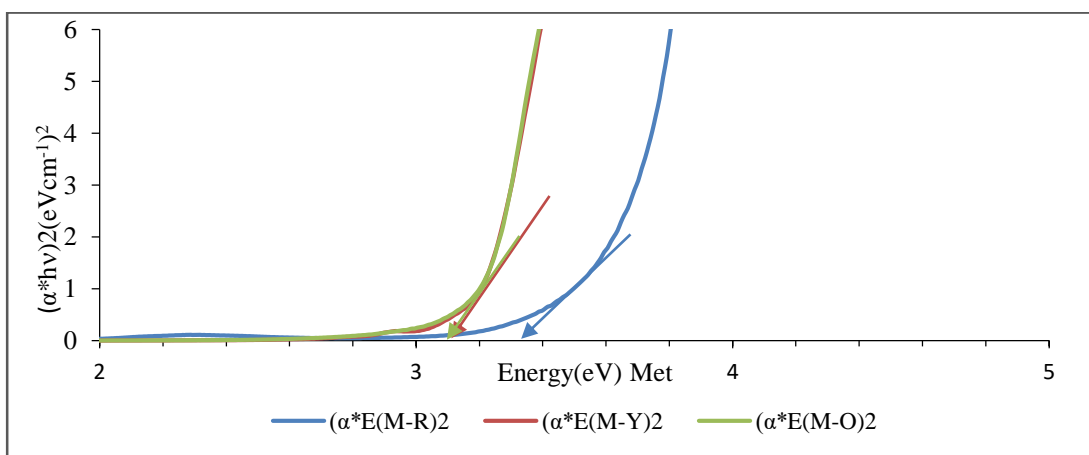


Figure 6 Comparison of $(\alpha(h\nu))^2$ versus photon energy ($h\nu$ (methanol)) of rose flowers

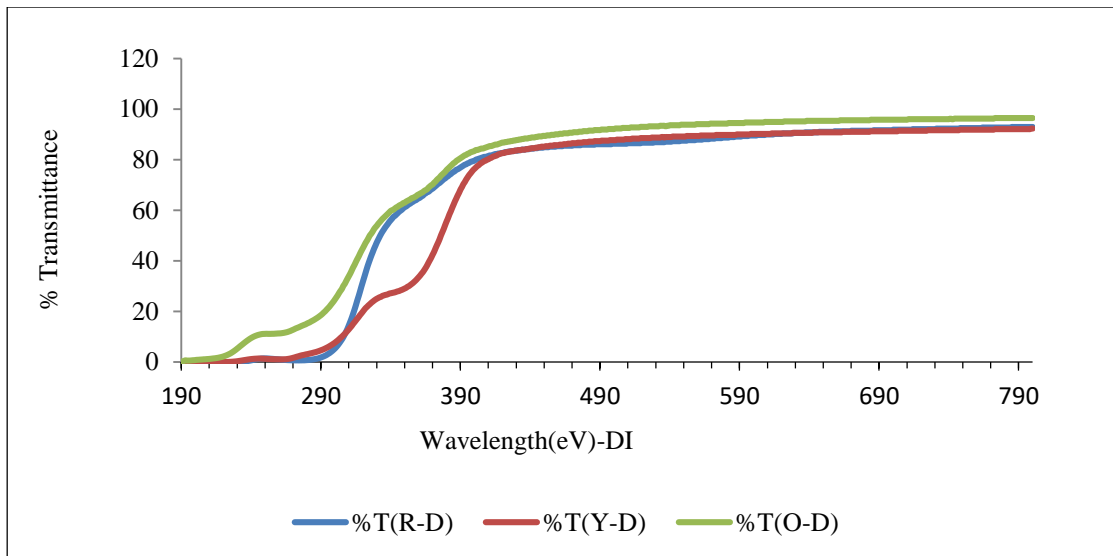


Figure 7 Comparison of transmittance of dyes for rose flowers by deionized water solvent

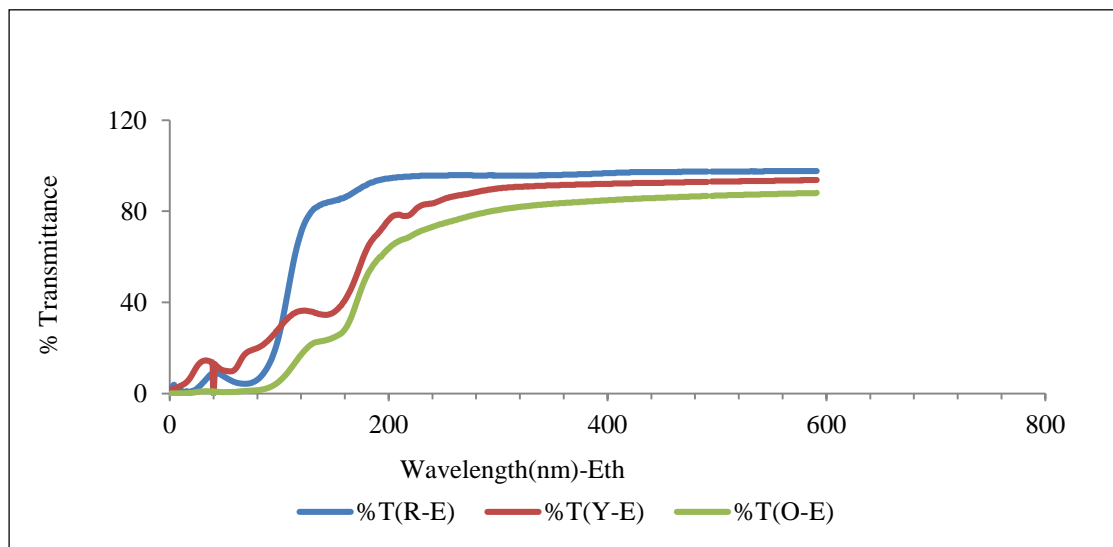


Figure 8 Comparison of transmittance of dyes for rose flowers by ethanol solvent

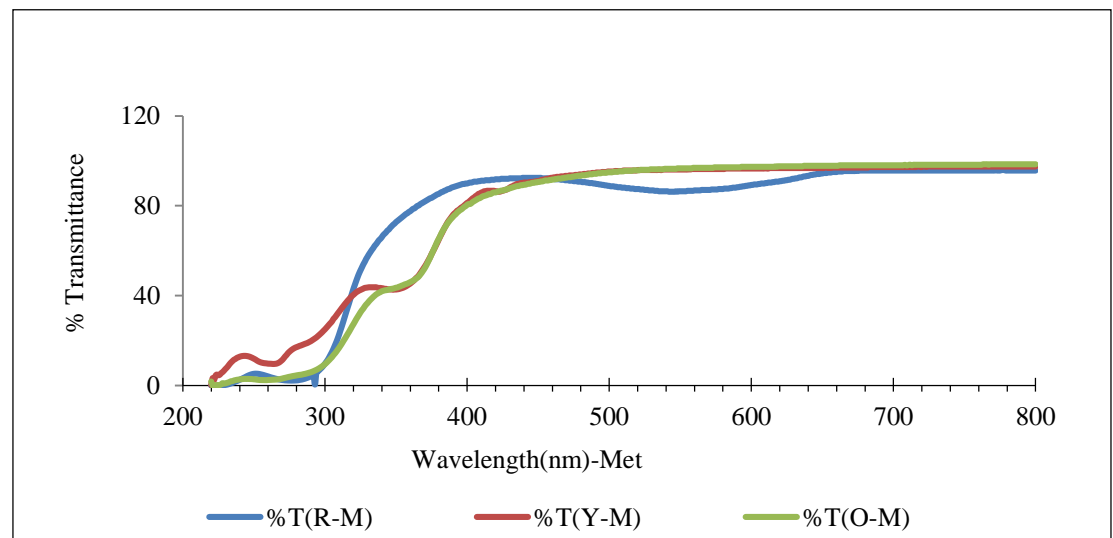


Figure 9 Comparison of transmittance of dyes for rose flowers by methanol solvent

Conclusion

The result was carried out with the aim of fabricating a dye sensitized solar cell, a low-cost solar cell using rose flowers extracted. The natural dye extracted from rose flowers of red, orange, and yellow color were used to build dye-sensitized solar cells. These natural dyes used as a light harvesting material were extracted using different solvents. The optical absorption spectra and energy bandgap of extracted dye solutions were investigated with UV-Vis spectrophotometer. The results from this work for orange, yellow, and red color of rose flowers were 3.2 eV to 3.8 eV with various solvent. It was possible to understand that the dyes extracted from orange and yellow color of rose flowers by using deionized water, ethanol and methanol solvent showed low bandgap. A low bandgap of dye helps the electron move fast from the valence band to the conduction band and only need less energy to the recombination of electrons and resulted high efficiency. Natural dyes as sensitizers, low-cost production, and simple manufacturing technique. According to UV data have low absorbance and high transmittance in the UV and visible regions. Therefore, can be used in DSSCs. The dye extracted in this research work may be applied in use for a part of dye sensitized solar cells.

Acknowledgements

We would like to thanks university of Kyaukse, Department of Physics, all my teachers, and collaborators helping us to complete this research work. And then many thanks to the Materials Science Lab members.

References

- Andualem A, Demiss S (2018) "Review on Dye-Sensitized Solar Cells" *Edelweiss Appli Sci Tech*, vol.2, pp.145-150.
- Barness Chirazo Mphande, Alexander Pogrebnoi, (2014) "Impact of Extraction Methods upon Light Absorbance of Natural Organic Dyes for Dye Sensitized Solar Cells Application" *Journal of Energy and Resources*, vol.3(3), pp. 38-45.
- Desalegn, J. & Godibo, A. (2015) "Natural Dyes foe dye sensitized solar cell: A review" *J. Braz. Chem. Soc.*, vol. 26(1), pp. 92-101.
- Hao, S., Wu, J., Huang, Y., Lin, J., "Sol. Energy" 2006, 209.
- Mark F., (2001) "Optical Properties of Solids", Oxford University press.
- M. S. Yadav, (2003). "A Text book of Spectroscopy" (New Delhi Anmol Publications PVT Ltd).
- T.J. Reinet. "Spectroscopy of a Compound: Beer's Law".
- Suyitno, D.N. Rachmad, Z. Arifin, T. J. Saputra, M. A. Omid and M. Yusuf, (2014) "Applied Mechanics and Materials" vol. 699, pp. 577-582.
- <http://www.Princetoninstruments.com>.

CHARACTERIZATION OF STRUCTURAL AND MORPHOLOGICAL PROPERTIES OF PbTiO₃ POWDER

Myat Thet Mon¹, Myat Shwe Wah², Thuzar Hnin³ and Khant Khant Lin⁴

Abstract

Lead titanate (PbTiO₃) powders were prepared by using solid state reaction method at different temperatures. The starting chemicals used in this work are lead oxide (PbO) and titanium dioxide (TiO₂). Phase identification and structural properties of PbTiO₃ powders were examined by X-ray diffraction XRD. From XRD result, PbTiO₃ powders were significantly formed with tetragonal symmetry. Surface morphology of PbTiO₃ powders was observed by Scanning Electron Microscopy (SEM). The lead titanate (PbTiO₃) powders were quite suitable for cost - effective and uncomplicated trends of ferroelectric materials such as random access memory (RAM).

Key words: lead oxide (PbO), titanium dioxide (TiO₂), lead titanate (PbTiO₃), X-ray diffraction (XRD), Scanning Electron Microscopy (SEM)

Introduction

The science and technology of nanostructured materials is advancing at a very rapid pace. Nowadays, the preparation and functionalization of one-dimensional nanostructured materials have become one of the most important roles of the nanotechnology. A perovskite is any material with the same type of crystal structure known as the perovskite structure with the oxygen in the face centers. Most of the perovskites contain oxygen as the anion. Hence, perovskite oxide can be presented by their general formula as ABO₃. Lanthanum manganite represents a class of perovskite oxide materials drew a lot of attention due to their intriguing and interesting properties like colossal magnetoresistance, ferroelectricity, superconductivity; charge ordering spin transport, thermo powder and the variation in these aforementioned properties according to change in their crystalline structure. Lanthanum manganite (LaMnO₃) and Barium Titanate (BaTiO₃) and Lead Titanate (PbTiO₃), etc. and these are based on the perovskite ABO₃ structure several ferroelectric materials have structure that are closely related to perovskite. Perovskite type oxide materials are important for electronic applications since they exhibit diverse physical properties such as super conductivity, dielectricity, ferroelectricity and magnetism.

Materials and Methods

Lead Oxide (PbO)

Lead oxide, also called lead (II) oxide or lead monoxide, is the inorganic compound with the molecular formula PbO. PbO occurs in two polymorphs: litharge having a tetragonal crystal structure and massicot having an orthorhombic crystal structure. Modern applications for PbO are mostly in lead-based industrial glass and industrial ceramics, including computer components. It is an amphoteric oxide.

Titanium Dioxide (TiO₂)

Titanium dioxide, also known as titanium (IV) oxide or titania is the naturally occurring oxide of titanium, chemical formula TiO₂. When used as a pigment, it is called titanium white,

¹ Department of Physics, West Yangon University, Myanmar

² Department of Physics, West Yangon University, Myanmar

³ Department of Physics, West Yangon University, Myanmar

⁴ Department of Physics, Yangon University of Education, Myanmar

Pigment White 6, or CI 77891. It is noteworthy for its wide range of applications from paint sunscreen to food colouring.

Titanium dioxide occurrences in nature are never pure; it is found with contaminant metals such as iron. The metal can also be mined from other minerals such as ilmenite or leucosene ores, or one of the purest forms, rutile beach sand. Figure 1 shows the starting materials used in this research work.



Lead Oxide (PbO)



Titanium Dioxide (TiO₂)

Figure 1 Starting materials

Solid State Reaction Method

The solid state reaction method is the most widely used method for the preparation of polycrystalline solids from a mixture of solid starting materials. Solids do not react together at room temperature over normal time scales and it is necessary to heat them to much higher temperatures, often to 1000 °C to 1500 °C in order for the reaction to occur at an appreciable rate. The factors on which the feasibility and rate of a solid state reaction depend include reaction conditions, structural properties of the reactants, surface area of the solids, their reactivity and the thermodynamic free energy change associated with the reaction.

Preparation of PbTiO₃ powders by Solid State Reaction Method

Lead titanate PbTiO₃ nanoparticles were successfully prepared by solid state reaction method. Lead oxide (PbO) and titanium dioxide (TiO₂) were weighed with digital balance and mixed with desired stoichiometric composition of PbTiO₃ nanoparticles. The mixture was ground by agate mortar to become a homogeneous mixture. The mixed PbTiO₃ powders were calcined at 500 °C, 600 °C and 700 °C for 1.5 h in furnace and reground with agate mortar. The reground PbTiO₃ powders passed through 100, 250 and 400 mesh sieves. Finally, homogeneous PbTiO₃ powders were obtained. In this section, the structural properties of PbTiO₃ powders were characterized by X-ray diffraction method (XRD). Figure 3 shows the block diagram of preparation of PbTiO₃ powders with different temperatures.

Mesh Sieving

Sieving is a simple technique for separating particles of different sizes. Many natural and manufactured materials consist of differently shaped and sized particles. Sieve analysis is used to divide the particulate material into size fractions and then to determine the weight of these fractions. In this way a relatively broad particle size spectrum can be analyzed quickly and reliably. Most sieving processes are carried out on dry materials. The particle size is characterized by mesh, the size of wire used in the screen. Mesh size is not a precise measurement of particle size. Screens can be made with different thicknesses of wires and the thicker the wires, the smaller the particles passing through that screen, and vice versa. The mesh size is the number of openings (little squares) in one inch of screen, so a 100 mesh screen means there are 100 openings across one linear inch of screen, a 400 mesh has 400 openings and so on. Therefore, as the mesh number increases, the particle size decreases (higher mesh number = finer powder). In this work, three-stage mesh sieves (100, 250, 400 mesh) shown in Figure 2 were used for sieving process.

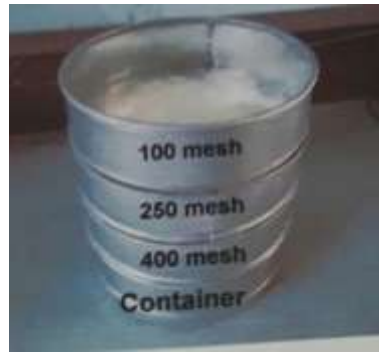


Figure 2 Photograph of Mesh Sieving

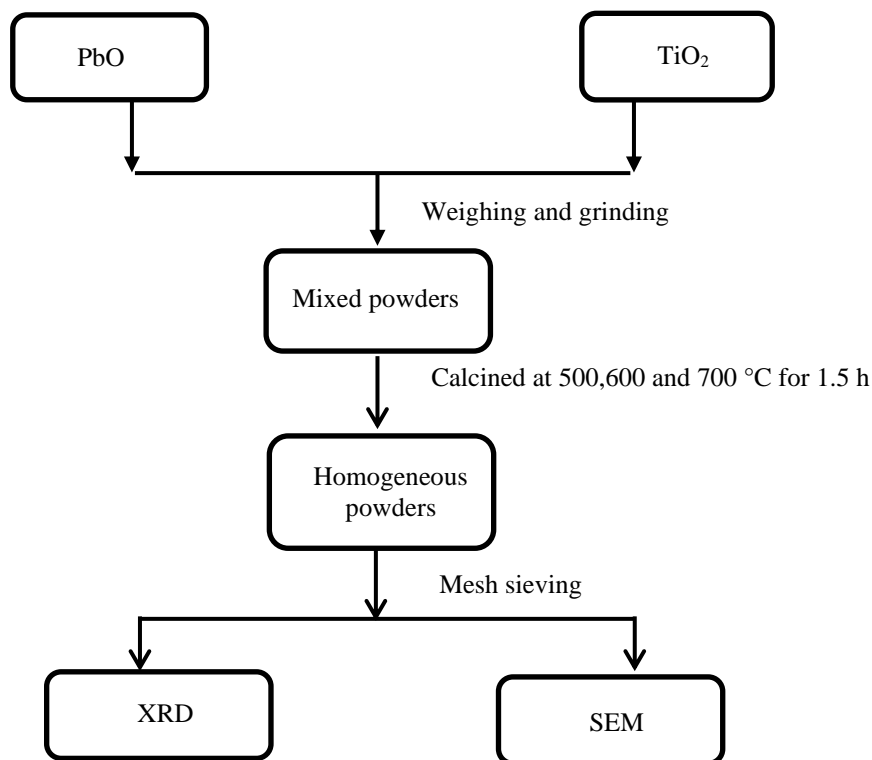


Figure 3 The block diagram of preparation of PbTiO₃ powders with different temperatures

Methods of Characterization

PbTiO₃ powders was characterized to determine their structural and morphological properties. The characterization techniques include X-ray diffraction technique (XRD) and Scanning Electron Microscopy (SEM).

Results and Discussion

XRD Analysis of PbTiO₃ Powders

The great deal of information about the crystallographic information of crystalline PbTiO₃ powder has been studied by crystallite size. The XRD patterns of PbTiO₃ specimens were perovskite type with tetragonal structure as shown in Figure 4 (a-c). There are several diffractions of the standard peaks were scanned within the diffraction angles range from 10° to 70°. PbTiO₃ powders were obtained and examined its phase formation by X-ray diffractometer using Cu-K α radiation with wavelength of 1.54056 Å. All the peak heights and peak positions were in good agreement with the JCPDS (Join Committee on Powder Diffraction Standards) in 75-1605 > PbTiO₃ library file.

The average crystallite-sizes were 23.992, 21.613, 27.245 nm for different temperatures respectively. For the powder, 2 θ , FWHM values and crystallite sizes are given in Table 2-3. The lattice parameter (a and c) and lattice distortion (lattice strain) c/a of dominant peaks are described in Table 1. The crystallite size was calculated using a well-known Debye Scherrer's formula. Thus, the PbTiO₃ powders were successfully obtained by solid state reaction method with tetragonal structure.

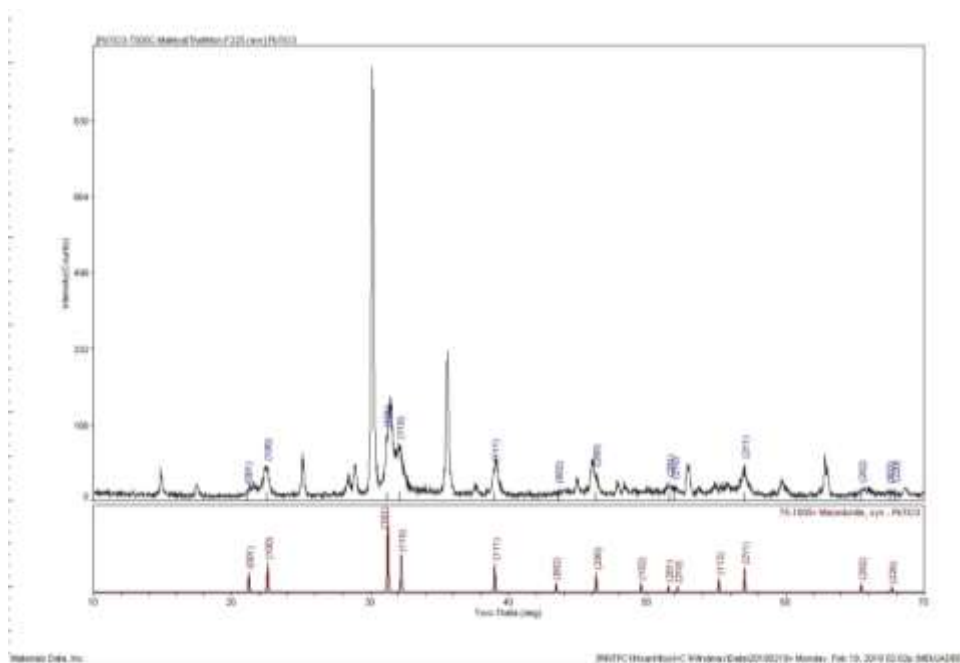


Figure 4 (a) The XRD patterns of PbTiO₃ powders at 500 °C

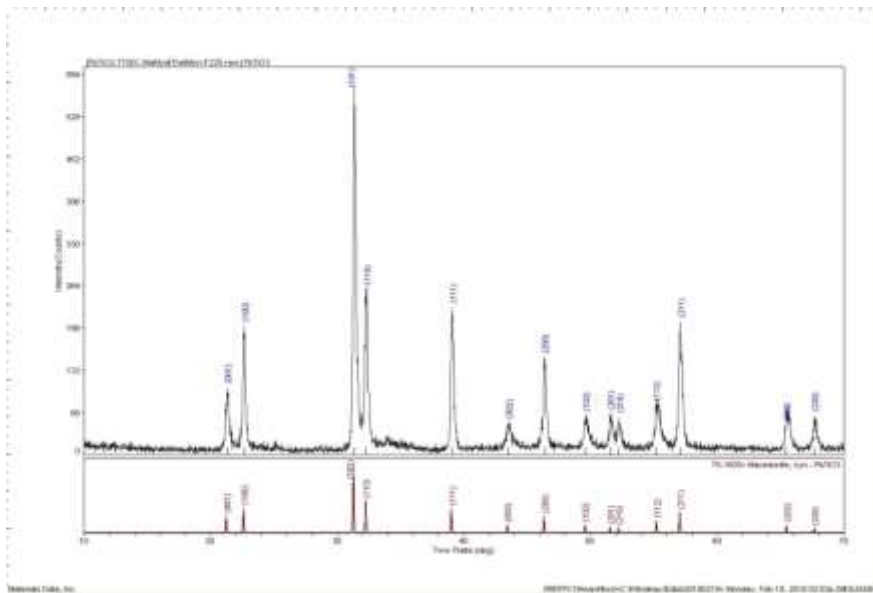


Figure 4 (b) The XRD patterns of PbTiO₃ powders at 600 °C

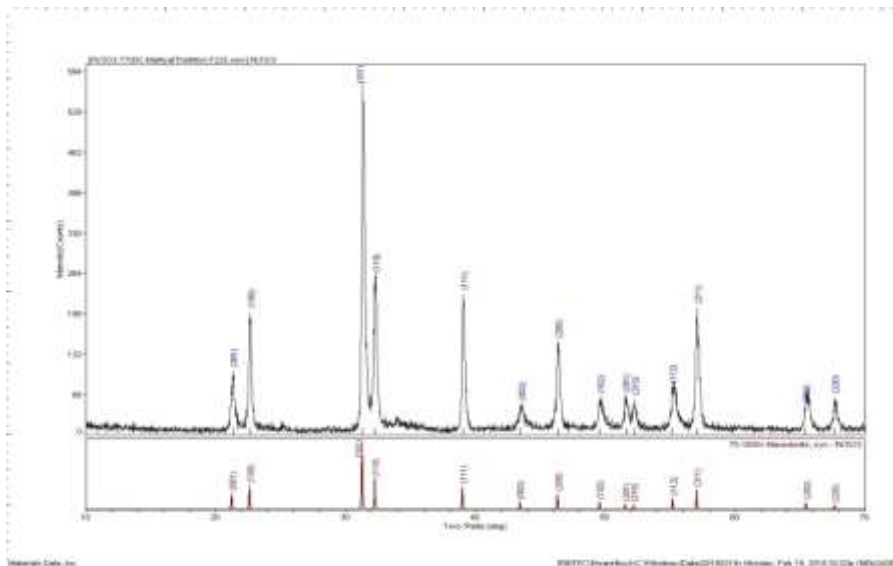


Figure 4 (c) The XRD patterns of PbTiO₃ powders at 700 °C

Table 1 Lattice Parameters and c/a ratios of different Temperatures for PbTiO₃ Powders

Temperatures	Lattice Parameter (Å)		Tetragonality c/a
	a	C	
500 °C	3.9263	4.2016	1.0701
600 °C	3.9227	4.1768	1.0648
700 °C	3.9167	4.1598	1.0621

Table 2 Structural Properties of PbTiO₃ Powders at 700 °C

Sr No.	(h k l)	2 θ (deg)	FWHM (deg)	Observed Crystallite Size (nm)
1	(001)	21.338	0.242	33.190
2	(100)	22.653	0.223	36.002
3	(101)	31.347	0.261	30.710
4	(110)	32.288	0.273	29.420
5	(111)	39.071	0.256	31.330
6	(002)	43.501	0.502	15.990
7	(200)	46.361	0.285	28.180
8	(102)	49.584	0.380	21.120
9	(201)	51.563	0.251	31.980
10	(210)	52.245	0.354	22.660
11	(112)	55.120	0.484	16.570
12	(211)	57.071	0.305	26.330
13	(202)	65.385	0.264	30.380
14	(220)	67.640	0.291	27.570
Average crystallite size				27.245

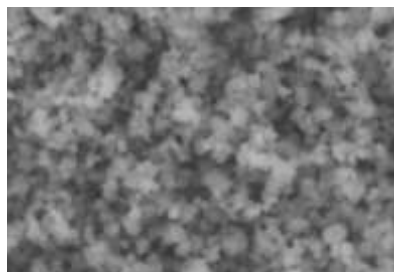
Table 3 Structural Properties of PbTiO₃ Powders at 500 °C and 600 °C

Sr No.	(h k l)	2 θ (deg)	FWHM (deg)	Observed Crystallite Size (nm)
1	(001)	21.128	0.375	21.380
2	(100)	22.536	0.474	16.930
3	(101)	31.195	0.322	24.920
4	(110)	32.114	0.718	11.180
5	(111)	38.940	0.527	15.230
6	(002)	43.571	0.100	80.260
7	(200)	46.264	0.549	14.620
8	(201)	51.577	0.521	15.400
9	(210)	51.947	0.561	14.310
10	(211)	57.028	0.410	19.560
11	(202)	65.451	0.515	15.580
12	(003)	67.491	0.256	31.330
13	(220)	67.910	0.167	48.130
Average crystallite size				23.992

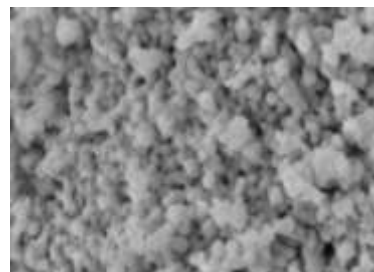
Sr No.	(h k l)	2 θ (deg)	FWHM (deg)	Observed Crystallite Size (nm)
1	(001)	21.239	0.303	26.470
2	(100)	22.552	0.267	30.050
3	(101)	31.282	0.320	25.050
4	(110)	32.235	0.277	28.990
5	(111)	39.005	0.254	31.610
6	(002)	43.388	0.483	16.610
7	(200)	46.373	0.351	23.230
8	(102)	49.463	0.721	11.130
9	(201)	51.519	0.318	25.230
10	(210)	52.132	0.587	13.660
11	(112)	55.223	0.549	14.620
12	(211)	57.036	0.354	22.660
13	(202)	65.468	0.380	21.120
14	(003)	67.566	0.604	13.290
15	(220)	67.719	0.392	20.480
Average crystallite size				21.613

SEM Analysis of PbTiO₃ Powders

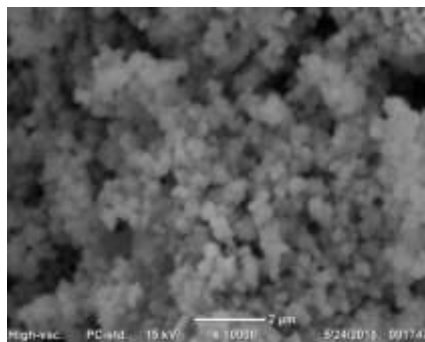
Figure 5 (a-c) shows the SEM analysis of PbTiO₃ powders annealed at 500 °C, 600 °C and 700 °C, exhibit grained microstructure and nanostructure with small grain size. The grain sizes were calculated by using well known bar code system. The average grain sizes of PbTiO₃ powder were found to be about 260 nm at 500 °C, 275 nm at 600 °C and 320 nm at 700 °C respectively. These figures indicates that most of the grain size was regular structure and a few number of large grain size were found. It looks fairly dense and smooth. From the images, they were clearly found that the little amount of pores and grain growth were examined. The orientation of grain was towards left for all images. The grain size of PbTiO₃ powders seen to be uniform but some of the grain size were slightly large.



(a) PbTiO₃ powders at 500 °C
(average grain size = 260 nm)



(b) PbTiO₃ powders at 600 °C
(average grain size = 275 nm)



(c) PbTiO₃ powders at 700 °C
(average grain size = 320 nm)

Figure 5(a- c) The SEM images of PbTiO₃ powders at 500 °C, 600 °C and 700 °C

Conclusion

PbTiO₃ powders with different temperatures were successfully prepared by solid state reaction method. In the XRD analysis produces the information on crystallite sizes of several peaks were 23.992 nm at 500 °C, 21.613 nm at 600 °C and 27.245 nm at 700 °C respectively. The crystal structure of the prepared PbTiO₃ powder was perovskite type with tetragonal symmetry. From SEM analysis, the average grain size of PbTiO₃ powders were found to be about 260 nm at 500 °C, 275 nm at 600 °C and 320 nm at 700 °C respectively. The grain size of PbTiO₃ powders seen to be uniform but some of the grain size were slightly large. As these results, the crystallite size of PbTiO₃ powders at 600 °C was smallest than other two temperatures and the average grain size at 500 °C was smallest grain size of these three temperatures. According to research data, the lead titanate (PbTiO₃) powders were quite suitable for cost effective and uncomplicated trends of ferroelectric materials such as random access memory (RAM).

Acknowledgements

We are greatly thankful to Dr. Khin Thidar, Rector, Dr. Thandar and Dr. Thet Thet Tun, Pro-rectors, West Yangon University for their encouragement, Professor Dr Maung Maung Shwe, PhD (YU), Head of Department of Physics, Professor Dr Myat Shwe Wah, PhD (YU), Professor Dr Zay Ya Aung, PhD (YU) and Dr Khin Thitsar Shin, PhD (YU), West Yangon University, for their kind permission to carry out this paper.

References

- Anthony R, West, (2006) *Solid State Chemistry and its Applications*, Wiley and Sons,
Aruta C. *et al*, *Journal of Applied Physics* 100 023910
Barrow G. M., (1962) "Introduction to Molecular Spectroscopy" (Tokyo: McGraw-Hill)
Baumgarten P.K., (1971) *Journal of Colloid and Interface Science* 36
Batista, Carlos A. *et al*, (2015), "Nonadditivity of nanoparticle interactions", *Science*. 350 (6257)
Bergshoef M.M. *et al*, 1999 *Journal of Advanced Materials* 11 (16) 1362
Cernea M., (2004) *J Opt and Mater* 6 1349-1356
Faraday, M., (1857). "Experimental relations of gold and other metals to light", *Phil. Trans.R. Soc. Lond.*147:145-181
Gerand B, *et al*, "Preparative methods in Solid State Chemistry", Academic press.
Iijima K *et al* (1986) *J Appl Phys* 60, 361
Ireme E. A., (2005) *Electronic Materials Science* (New Jersey: Wiley)
Wenk, H. Rudolf, *et al*, (2004). *Minerals: Their Constitution and Origin*. New York, NY: Cambridge University Press. ISBN 978-0-521-52958-7.

SYNTHESIS AND FABRICATION OF ZINC OXIDE ON FTO SUBSTRATES BY SPIN COATING METHOD

Nyein Nyein Htet¹, Myat Shwe Wah² and Hnin Myat Kyaw³

Abstract

ZnO plays an important role in many semiconductors technological aspects. In the present work zinc oxide particles were prepared by wet chemical method, using $(\text{Zn}(\text{NO}_3)_2 \cdot 6\text{H}_2\text{O})$ and (NaOH) with different concentrations (0.25,0.5,0.75, and,1)M and study the effect of temperature on the structures and particles sizes. ZnO nanoparticles synthesized with 1 M of NaOH at 80 °C. ZnO particles were characterized by using X-ray diffraction (XRD), Scanning Electron Microscopy (SEM) and Energy Dispersive Spectroscopy (EDS).

Key words: $\text{Zn}(\text{NO}_3)_2 \cdot 6\text{H}_2\text{O}$, NaOH, ZnO, Nanoparticles, XRD SEM and EDS

Introduction

Zinc Oxide (ZnO) is a wide band gap semiconductor with wurtzite structure. The physical and chemical properties of nanoscale particles are different when they are compared with the bulk materials. The ZnO is known as a wide band gap (3.37 eV) with a high exciton binding energy (60 meV) and exhibit the most sheeny and numerous configuration of nanostructure that one material can form. Also, ZnO as an important semiconducting material has a wide range of applications in gas sensors, chemical absorbent, nanogenerators, electrical and optical devices, electrostatic dissipative coating, and advanced ceramics. ZnO nanoparticles have been prepared by various methods such as thermal decomposition, solvothermal reaction, reactive electron beam, evaporation technique, chemical vapor deposition, hydrothermal method. Due to the simplicity, versatility and low cost of this route, the solochemical method is a process extremely viable for industrial production of zinc oxide. Among control of the particle size is one main concerned for nanostructured material synthesis because electrical and optical properties of nanomaterials depend on both size and shape of the particles. Therefore, it is desired to synthesize nanomaterial in a controllable size by a simple approach.

Materials and Methods

Starting Materials

The materials used in this study were Zinc nitrate hexahydrate, $\text{Zn}(\text{NO}_3)_2 \cdot 6\text{H}_2\text{O}$ with different concentration (0.25 ,0.5 ,0.75 .and 1) M of Sodium hydroxide, NaOH and Fluorine doped Tin Oxide (FTO) glass.

Preparation of particle

The wet chemical method was used to prepare zinc oxide (ZnO) particles. using zinc nitrate hexahydrate and sodium hydroxide as precursors. (0.25, 0.5, 0.75 and 1) M of NaOH which prepared by dissolving (40gm) of NaOH in 1liter (1000 ml) of deionized water. The solution was stirred at 70°C. 0.5M of $\text{Zn}(\text{NO}_3)_2 \cdot 6\text{H}_2\text{O}$ was prepared by dissolving (37.175 gm) $\text{Zn}(\text{NO}_3)_2 \cdot 6\text{H}_2\text{O}$ in (250 ml) of deionized water, and then added to the basic solution drop by drop, the solution was keeping stirring and heating for 3h at the temperature of 80 °C .After the completion of reaction, the solution was allowed to settle for over night and after that the supernatant solution was

¹ Department of Physics, West Yangon University, Yangon, Myanmar

² Department of Physics, West Yangon University, Yangon, Myanmar

³ Department of Physics, West Yangon University, Myanmar

discarded carefully. Thus produced particles were washed five times using deionized water. The solution was coated on the Fluorine doped Tin Oxide (FTO) glass by using spin coating machine with 500 rpm for 10 minutes. Then, the fabricated sample was dried in oven at 80°C for overnight, and calcined at 200 °C, 300 °C and 400°C for 2h in a muffle furnace. Finally, the last sample was prepared with 1 M of NaOH at temperature 80 °C. The flow diagram of preparation of zinc oxide (ZnO) was shown in Figure 1.

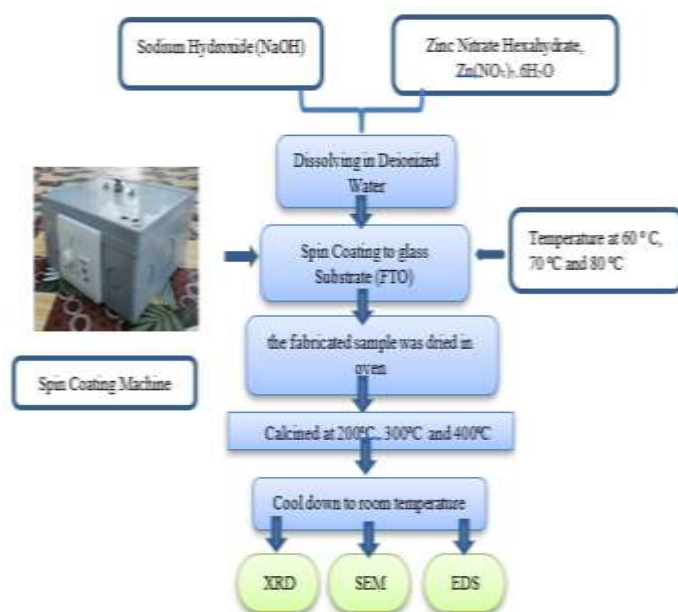


Figure 1 Block Diagram of experiment procedure

Methods of Characterization

X-ray diffraction (XRD)

The crystallinity and phases of the ZnO nanostructures were characterized by X-ray Diffractometer, XRD-6000, Shimadzu, Japan with Cu- k_{α} radiation ($\lambda = 1.5412 \text{ \AA}$), 40kV, 30mA) in the 2° range of 10° - 80° with $2^{\circ}/\text{min}$ scanning rate. The crystallite size (D) of selected samples were estimated using the Scherrer's equation,

$$G = \frac{\beta\lambda}{\text{FWHM} \cos \theta} \quad (1)$$

where β = Scherrer constant $\cong 0.899$

G = crystallite size (nm)

λ = wavelength ($\lambda = 1.5412 \text{ \AA}$)

FWHM = full width at half maximum (rad)

θ = Bragg angle (deg)

Scanning Electron Microscopy (SEM)

The morphological feature of the nanostructures was observed by a scanning electron microscope SEM-EDS. JCM-6000, JEOL. The surface morphology of Zinc Oxide samples and the size of particles can be magnified from 10 x to 600,00 x for secondary electron images and from 10 x to 300,00 x for backscattered electron images. The samples for SEM were coated with gold.

Energy-dispersive spectroscopy (EDS)

Energy-dispersive X-ray spectroscopy (EDS, also abbreviated EDX or XEDS) is an analytical technique that enables the chemical characterization/elemental analysis of materials. SEM-EDS analysis is a non-destructive analytical technique (to the sample), but unlike XRF that can be undertaken in-situ without sample removal, SEM-EDS does require sample removal. The sample material is irradiated with electrons resulting in the emission of x-rays characteristic to the elements present. The EDX detector detects the X-rays which are produced by the material when electrons interact with its surface during SEM imaging.

Results and Discussion

X-ray Diffraction (XRD) Measurement

The structural study was determined by the X-ray diffraction performed with a Multiplex's Diffractometer (model: RIGAKU-RINT 2000). XRD pattern was utilized to explore and recorded as the crystalline structures. According to Figures, the XRD patterns of the ZnO films deposited at different temperatures of 60 °C, 70 °C and 80 °C. It is observed that the nanostructures of zinc oxide (ZnO) thin films exhibit hexagonal structure with c/a ratio of about 1.63. It was observed that increasing in substrate temperature shows slightly increase in crystallite sizes and higher peak intensities, due to high crystallinity. The ZnO films exhibit highly (002) oriented nanocrystalline structure. The average crystalline size of ZnO was calculated according to Scherer's equation and the result was found to be 30.996 nm. Table 1 shows the XRD analysis result for ZnO thin films.

Table 1 XRD analysis result for ZnO thin films

Temperature (°C)	Plane (hkl)	FWHM Peak (degree)	2-Theta Value	d (Å)	Crystallite Size (nm)
200	002	0.271	34.685	2.611	30.677
300	002	0.272	34.673	2.621	30.875
400	002	0.276	34.669	2.675	31.436

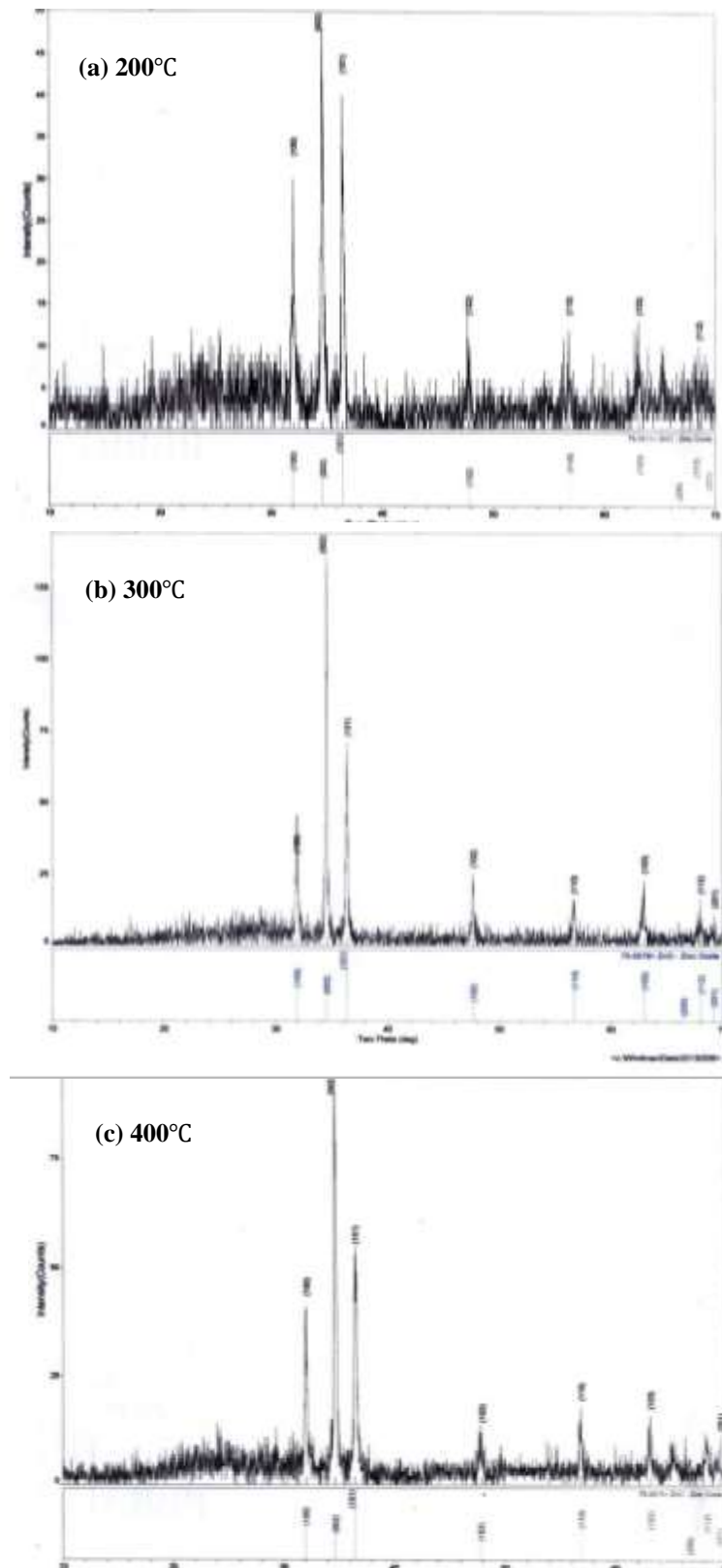
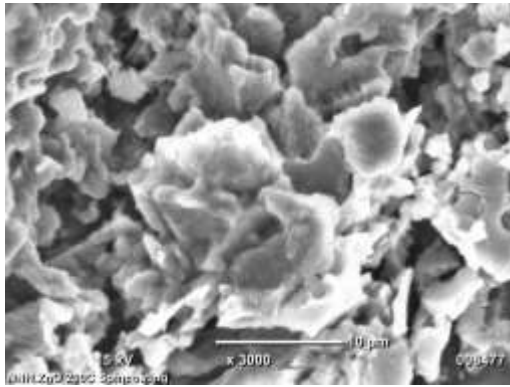


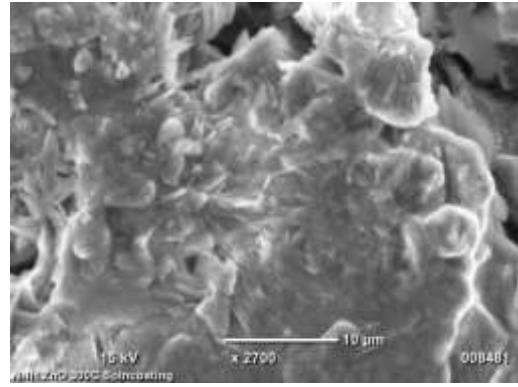
Figure 2 XRD spectra of ZnO thin films at (a) 200°C (b) 300°C (c) 400 °C

SEM Analysis of Zinc Oxide (ZnO) Nanoparticles

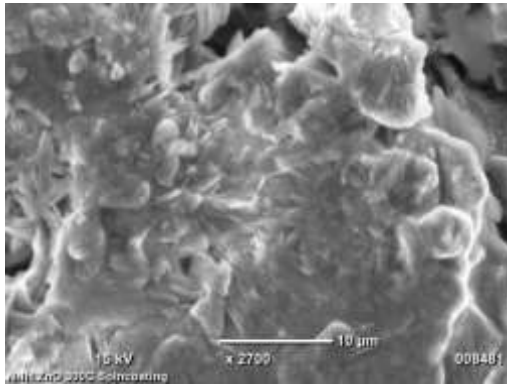
The surface morphologies by SEM observation have been characterized using JEOL Scanning Electron Microscope model JCM-6000, SEM-EDS type. In spite of such imperfection, some zinc oxide (ZnO) were well preserved and could be able to identify under SEM. According to Figures, ZnO have been successfully prepared by Spin Coating method and the shape and size are well uniformed.



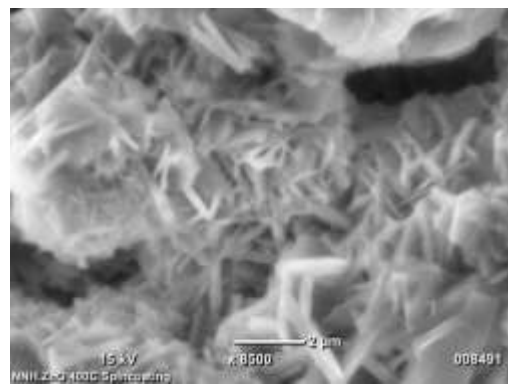
Magnified (x 3000) at 200°C



Magnified (x 2700) at 300°C



Magnified (x 2200) at 400°C



Magnified (x8500) at 400°C

Figure 3 SEM Images of ZnO at different magnification

SEM imaging to EDS Analysis

Energy Dispersive Spectroscopy (EDS) is capable of obtaining rapid qualitative chemical information, semi-quantitative composition determinations, maps showing lateral distribution of chemical elements, and compositional profiles across a surface. All stable elements can be detected with the exception of hydrogen, helium, and lithium. According to figure, the mass percentage of oxygen and zinc element in zinc oxide compound were observed by EDS analysis.

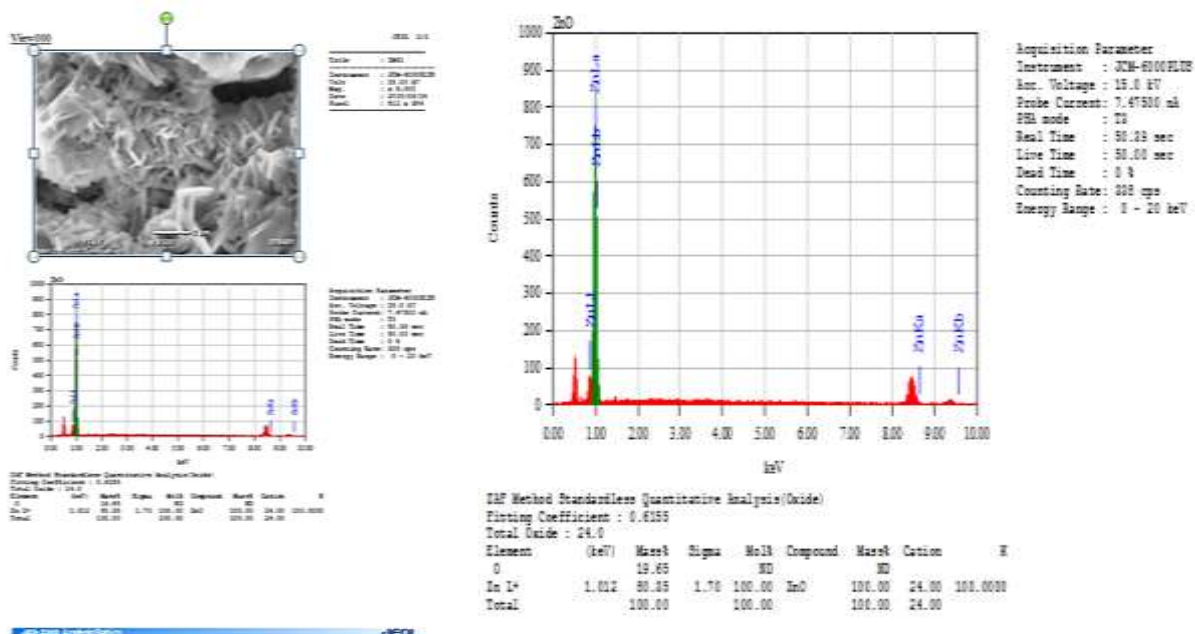


Figure 4 SEM-EDS Images of ZnO

Conclusion

Zinc oxide nanostructures were prepared by the combination of Zinc Nitrate Hexahydrate with sodium hydroxide. The XRD analysis confirmed that the ZnO nanoparticles have the hexagonal wurtzite structure. The ZnO films exhibit highly (002) oriented nanocrystalline structure. The average crystalline size of ZnO was calculated according to Scherer's equation and the result was found to be 30.996 nm. The morphology was evaluated using SEM. At 200°C, the SEM image of ZnO thin film was homogenous. The topography of the surface shows the microstructure which looks like a cluster of thread. At 80°C, the crystals are well in order and the grain sizes of the films were found to be within the range for 2 μm to 10 μm. In SEM-EDS image, the mass percentage of oxygen element was found in 9.65% and zinc element in 80.35%. Zinc Oxide compound was found in 100%. The crystallized sizes of ZnO nanoparticles presented in this study leads to the possibility of several applications in nanotechnology, such as advanced ceramics, solar cells and antimicrobial agent.

Acknowledgements

I would like to thank Professor Dr Maung Maung Shwe, PhD (YU), Head of Department of Physics, Professor Dr Myat Shwe Wah, PhD (YU) and Professor Dr Zay Ya Aung, PhD (YU), West Yangon University, for their kind permission to carry out this paper.

References

- Cao, G.Z., (2004)'' Growth of zinc oxide nanorod arrays through sol electrophoretic deposition''*The Journal of Physical Chemistry*, vol. 108, pp.19921-19931
- Chase, D.W. , Kim. B.C., (2005) Characterization on Polystyrene/ Zinc Oxide nanocomposites prepared from solution mixing. *Polymers for Advanced Technologies*, vol.16, pp.846-850
- El-Kemary, M., El-Shamy, H., El-Mehasseb. I., ''Photocatalytic degradation of ciprofloxacin drug in water using ZnO nanoparticles'' *Journal of Luminescence*, vol. 130, pp.2327-2331
- Hu, S-H., Chen, Y-C., Hwang, C-C., Peng, C-H., Gong. D-C.,(2010)''Development of a wet chemical method for the synthesis of arrayed ZnO nanorods'' *Journal of Alloys and Compounds*, vol.500, pp.117-121
- Liu, X., Yamilov, A., Wu, X.,Zheng, J-G., Cao, H., Chang, R.P.H. (2004) ''Effect of ZnO nanostructures on 2-dimensional random lasing properties'' *Chemistry of Materials*, vol.16, pp.5414-5419
- Moezzi, A., McDonagh, A-M., Cortie. M.B., (2012) ''Zinc oxide particles: synthesis, properties and applications'' *Chemical Engineering Journal*, vol.185-186, pp.1-22
- Raoufi. D., (2013) ''Synthesis and photoluminescence characterization of ZnO nanoparticles'' *Journal of Luminescence*, vol.134, pp. 213-219
- Xiong, M., Gu, G., You, B., Wu. L., (2003) ''Preparation and Characterization of poly(styrene butylacrylate) latex/nano-ZnO nanocomposites'' *Journal of Applied Polymer Science*, vol.90, pp.1923-1931
- Zhou, W.D., Wu, X., Zhang, Y.C., (2007) Solvothermal synthesis of hexagonal ZnO nanorods and their photoluminescence properties. *Materials Letters*, vol.61, pp. 2054-2057,

AN INNOVATIVE HOME AUTOMATION SYSTEM USING ARDUINO AND BLUETOOTH MODULE

Soe Moe May Me¹

Abstract

Home Automation System plays an important role in our daily life. Nowadays people are looking forward to control the home appliances through remote control. The main objective of this research paper is to create and design a home automation system (HAS) using Android with Bluetooth module. In general, Home Automation System provides a simple as well as reliable technology with Android application. On the other hand, it can be controlled the appliances using a smartphone from a remote location. A simple Home Automation System can be designed and constructed using simple components such as an Arduino Uno, Bluetooth module, 8 channel relay module and smartphone. Bluetooth module and Arduino Uno application are remotely and mutually applied for controlling the system. Home appliances like fan, bulb, AC, automatic door lock is controlled by home automation system using Arduino Uno with Bluetooth module. The program for this system is written in C language and upload into the memory of the microcontroller on Arduino board by Arduino Uno window software. The operations of the whole circuit are controlled by the program. The circuit presented in this research is designed and created to control the three electrical devices to turn on or turn off appliances remotely i.e using a smartphone.

Keywords: Home Automation Systems; Arduino; Bluetooth; Smartphone; Relay module

Introduction

At the present time, people who are using a smartphone with Arduino Uno and need to control everything from smart phone based on home automation system (Figure 1). Likewise, everyone understands how to control mobile phone thus it is easy to comprehend and use. Currently, the designing of home automation is going to develop simpler and more popular because most of people use smart phone. There has been a significant development in the area of an individual's routine tasks and those can be automated. In the present times, we can find most of the people clinging to their mobile phones and smart devices throughout the day.



Figure 1 Home Automation System

In this device we are using Arduino which is most commonly applied device for automation. Accordingly, Arduino is a hardware which is used to connect computer and the project model thus we can control it by using Arduino code. Arduino Uno is an open-source electronics

¹ Department of Physics, West Yangon University

platform based on easy-to-use hardware and software. It is used for artists, designers, hobbyists, and anyone interested in creating interactive objects or environments. Generally, Arduino is a tiny computer system that can be programmed with the instructions to interact with various forms of input and output. Arduino is connected with the Bluetooth module which receives the information from user. Arduino also connected relay, which receives information from Arduino and perform the operation as switch. Bluetooth technology is Wireless radio transmissions in a short distance providing a necessary technology to create intelligence and controllability (Bharanialankar and Manikanda Babu., 2014). This generates personal area network in home environment, where all these appliances can be interconnected and monitored applying a microcontroller with Arduino using smart phone.

The main process of this system is intended to study the method of application of the wireless communication between Arduino as well as Bluetooth module HC-06 and Android mobile phone (Figure 2). Arduino Uno is used in this system to control Bluetooth module and relay module. Home Automation System contains a degree of computerized or automatic control to certain electrical and electronic systems in a building. In this regard, home automation provides a better solution. The device incorporated not only consumes less power but also saves energy in home automation system. Therefore, home automation technology is so far environmentally suitable. The comfort and security of houses and offices have been developed in home automation system.

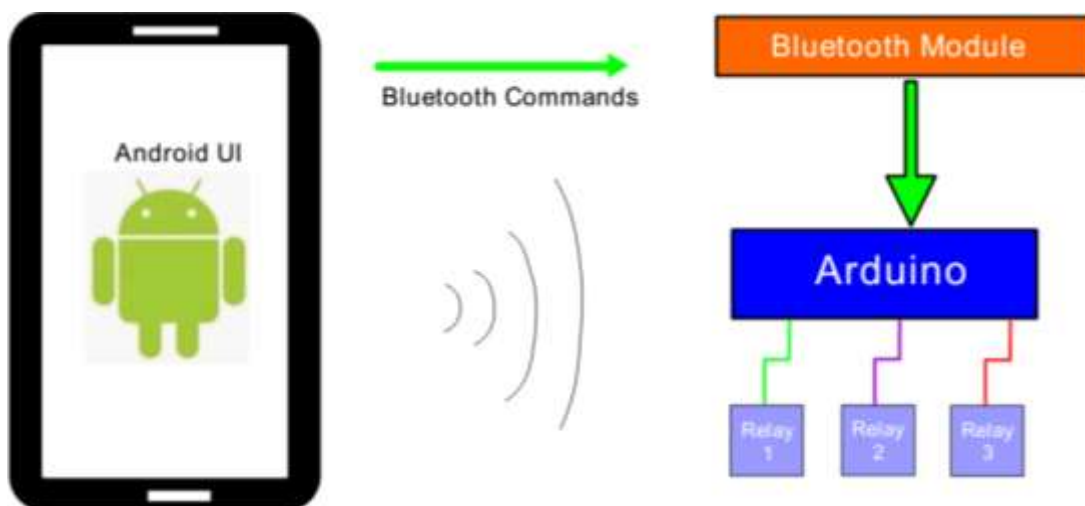


Figure 2 Home Automation System using android mobile phone

Objectives of Research

The principal objectives of the current research are:

- To create and design a Home Automation System (HAS) using Android with Bluetooth Module
- To control different home appliances using a smartphone
- To design and implement a low cost, reliable and scalable home automation system that can be used to remotely switch on or off any commercial/household appliance
- To update and consideration in latest technology and make cost effective, power efficient, safely operating system

Methodology

Home automation represents a system of networked, controllable device that work all together to make your home more comfortable, customized, efficient and secure. In this device, there are four principal parts including Arduino Uno, Bluetooth module, Relay drivers, and android smart phone application respectively. The aim of this system is to control different home appliances using a smartphone. This system needs to download and install the Bluetooth serial controller application into Android Phone from the Play Store and then pair it with Bluetooth Module. The android application software for this system can be downloaded from the Google. After the application is installed on android mobile phone, it is ready to use Bluetooth control system. TX and RX pins of the Bluetooth module can be connected to RX and TX pins of the Arduino (Figure 3). When connecting RX of Bluetooth to TX of Arduino (or any microcontroller as a matter of fact), it needs to be careful as the pin can tolerate only 3.3V. The voltage from TX or Arduino will be 5V. When the power is turned on, the connection LED on the Bluetooth module starts blinking. If the pairing is successful, the LED becomes stable. Now, in the application, the different keys are set for different loads and their corresponding value that must be transmitted when that key is pressed. Using this type of connection, it can control i.e. turn on or off different home electrical appliances using the smartphones. It can be used to control home electrical appliance remotely by Bluetooth communication. An electrical home automation system has been developed demonstrating the use of Arduino Uno board and wireless Bluetooth communication (ElShafee and Hamed., 2012).

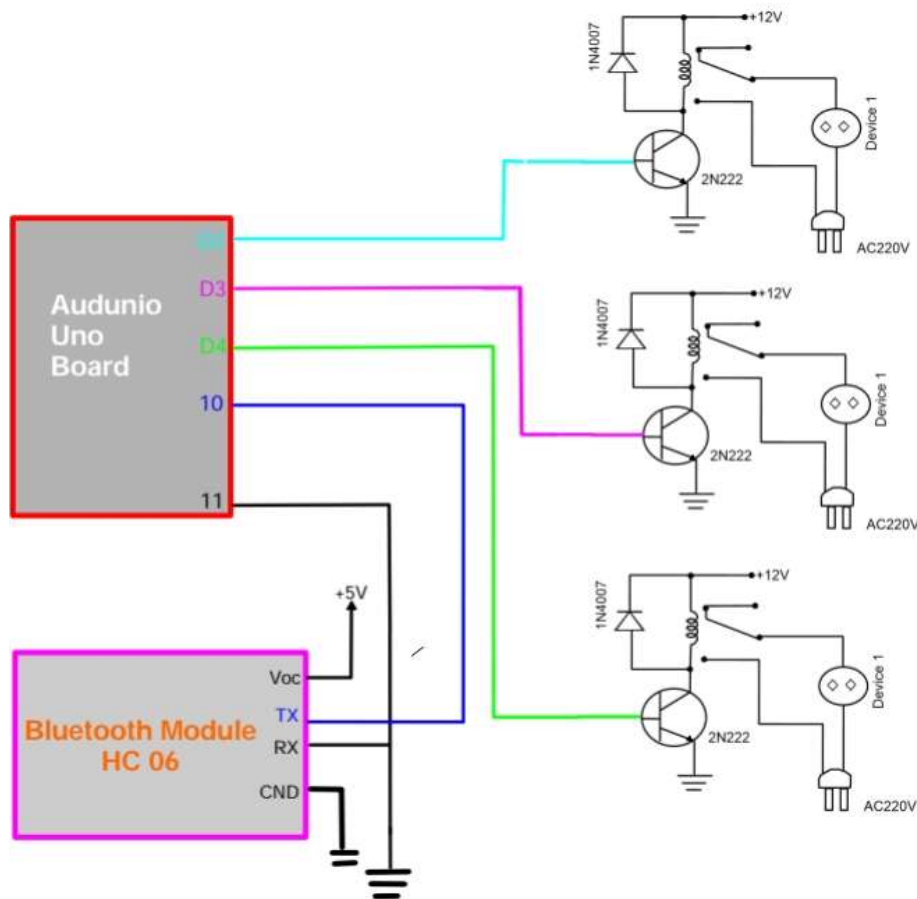


Figure 3 Complete circuit diagram of the whole system

Tools and Technology

Arduino Uno Microcontroller

Arduino Uno is a microcontroller board based on the Atmega328(datasheet). It possesses 14 digital input/output pins in which 6 analog inputs, a 16 MHz quartz crystal, a USB connection, an ICSP (In- Circuit Serial Programmer) header, a power jack and a reset button respectively (Figure 4a). In general, it is required to assist and support the microcontroller that connect to a computer with a USB cable or power it with an AC-to-DC adapter or battery to obtain started (Bharanialankar and Manikanda Babu., 2014). The Arduino Uno can also be powered as well as the USB connection or with an external power supply is also displayed in (Figure 4b). It can be operated on an external supply of 6 to 20 volts. If it is supplied with less than 7V or 5V, it will be unstable. If it is used more than 12V, the voltage regulator will overheat and damage the board. The recommended range is 7 to 12 volts. On the other hand, the chip near the power connector is the heart of the board. It is a tiny computer that contains a processor to execute instructions which includes various types of memory to control data and instructions from our sketches. The ATmega328 has 32 KB as well as 2 kB of RAM and 1 kB of EEPROM (Figure 4c).

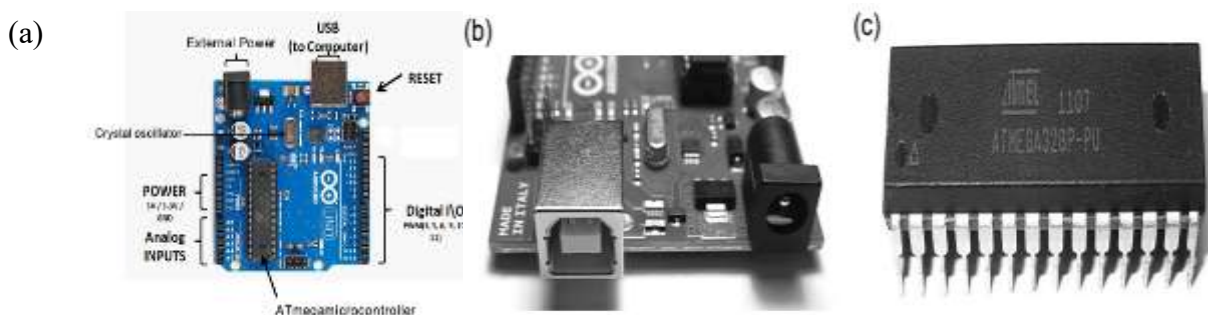


Figure 4 (a) Components of Arduino, (b) USB and power connectors, (c) ATMEGA328P-PU microcontroller

Features of the Arduino Uno

- Microcontroller: ATmega328
- Operating Voltage: 5V
- Input Voltage (recommended): 7-12V
- Input Voltage (limits): 6-20V
- Digital I/O Pins: 14 (of which 6 provide PWM output)
- Analog Input Pins: 6
- DC Current per I/O Pin: 40 mA
- DC Current for 3.3V Pin: 50 mA
- Flash Memory: 32 KB of which 0.5 kB used by bootloader
- SRAM: 2 kB (ATmega328)
- EEPROM: 1 kB (ATmega328)
- Clock Speed: 16 MHz

Bluetooth Module HC 06

Bluetooth receives the information from user and lead to the microcontroller (Arduino Uno). It is a wireless technology standard that is applied for exchange data over short distances using short-wavelength radio transmission. It was designed primarily as a cable replacement

technology for consumer electronic devices and data communication that applies short-range radio links (Ericsson, 2000). The module works on Bluetooth 2.0 communication protocol and it can only act as a slave device. This is the cheapest method for wireless data transmission and more flexible compared to other methods and it even can transmit files at speed up to 2.1Mb/s. HC-06 uses frequency hopping spread spectrum technique (FHSS) to avoid interference with other devices and to have full duplex transmission (Rajeev Piyare and Tazil M., 2011). The device works on the frequency range from 2.402 GHz to 2.480GHz. In this module have six (or four) leads but it will genuinely care about only four of them. Where, the two are V_{CC} and GND. V_{CC}= Power Supply (in other words 5V or 3.3V) GND= Ground (in other words 0 volt) (Figure 5). And the next two leads are for RX (Receiving End) and TX (Transmitting End). On the basic of idea, the RX of the module will go to the TX of the Arduino Uno. In the same way, the TX of the module can be connected with the RX of the Arduino Uno.

Features

HC-06 is good option when short distance wireless communication is needed. The module is used for wireless communications of less than 100 meters. The module is very easy to interface and to communicate. The module is one of the cheapest solutions for wireless communication of all types present in the market. The module consumes very less power to function and can be used on battery operated mobile systems. The module can be interfaced with almost all controllers or processors as it uses UART interface.

Specifications

- Bluetooth protocol: Bluetooth V2.0 protocol standard
- Power Level: Class2(+6dBm)
- Band: 2.40GHz—2.48GHz, ISM Band
- Receiver sensitivity: -85dBm
- USB protocol: USB v1.1/2.0
- Modulation mode: Gauss frequency Shift Keying
- Safety feature: Authentication and encryption
- Operating voltage range:+3.3V to +6V
- Operating temperature range: -20°C to +55°C
- Operating Current: 40mA

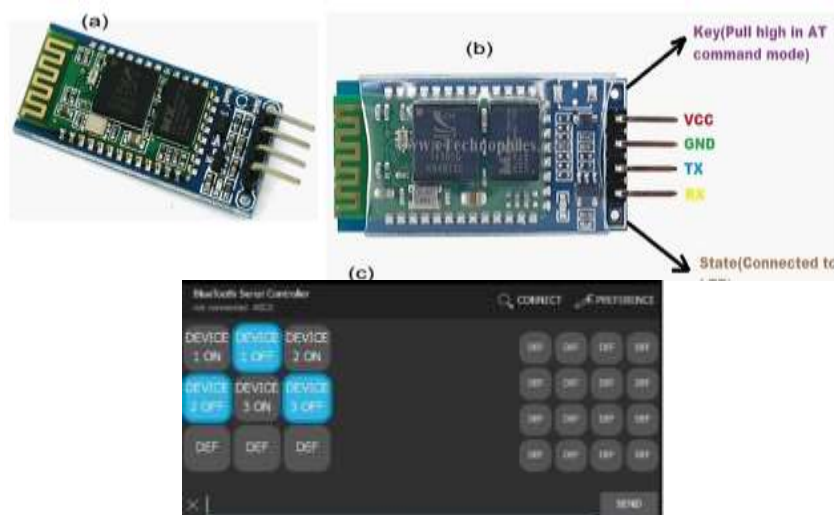


Figure 5 Bluetooth module HC 06

Eight (8) Channel Relay Module

In this research paper, 8 Channel Relay Module is applied for controlling the load like on/off operation (Chandra et al., 2016). The 8 Channel Relay Module is a convenient board and contains eight 5V relays. It can be used to control high voltage, high current load such as motor, solenoid valves, lamps and AC load (Figure 6). The module is associated with switching and isolating components, which makes interfacing with a microcontroller or sensor easy with minimum components and connections. This is useful in creating a central hub from where multiple remote loads can be powered, which is useful for tasks like home automation where the module can be placed in the main switchboard and can be connected to loads in other parts of the house and can be controlled from a central location using a microcontroller (Pooja et al., 2016). The 8 Channel Relay Module can be used to switch multiple loads at the same time since there are eight relays on the same module (Figure 6). Each relay on the board has the same circuit and the input ground is common to all eight channels.

The eight relays on the module are rated for 5V, which means the relay is activated when there is approximately 5V across the coil. The contacts on each relay are specified for 250 VAC and 30 VDC and 10A in each case, as marked on the body of the relays. The switching transistors act as a buffer between the relay coils that require high currents, and the inputs which do not draw much current. They amplify the input signal so that they can drive the coils to activate the relays. The freewheeling diodes prevent voltage spikes across the transistors when the relay is turned off since the coils are an inductive load. The indicator LEDs glow when the coil of the respective relay is energized, indicating that the relay is active. Eight separate loads (represented by light bulbs) have been connected to the NO terminals of the relay. The live wire has been connected to the common terminal of each relay. When the relays are activated, the load is connected to the live wire and is powered. This setup can be reversed by connecting the load to the NC terminal, which will keep it powered on till the relay is activated.

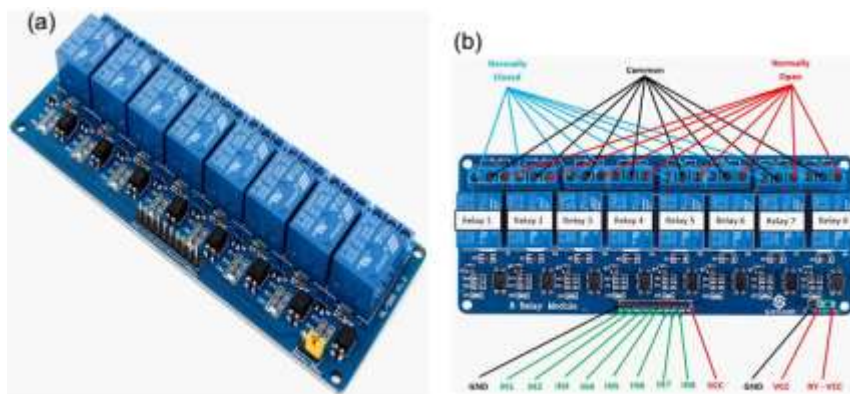


Figure 6 (a) Eight channel Relay Module, (b) Eight (8) Channel Relay Module Pinout

Eight (8) Channel Relay Module Specifications

- Supply voltage – 3.75V to 6V
- Trigger current – 5mA
- Current when relay is active - ~70mA (single), ~600mA (all eight)
- Relay maximum contact voltage – 250VAC, 30VDC
- Relay maximum current – 10A

Results and Discussion

Home Automation System Circuit Board (HASCB) consists mainly of an Arduino-Uno board, a Bluetooth module, an Android phone, eight (8) channel relay module, home appliances and an android Application. It is user friendly and it is cost effective. Through this research project, home automation system circuit board has been created to be easily controlled home appliances like as fan, tube light, air conditioner, bulb, etc. Bluetooth and Android application are recognized to develop and create a smart home in this article. In general, modern houses are expected to have centralized control system, instead of conventional switches which are fitted on walls. Managed to be successfully this research using mobile technology for controlling various electrical home appliances ON and OFF. On the other hand, we have provided information about Arduino Uno, Bluetooth controller and relay module. Final outcome of the research project is given below in Figure 7.

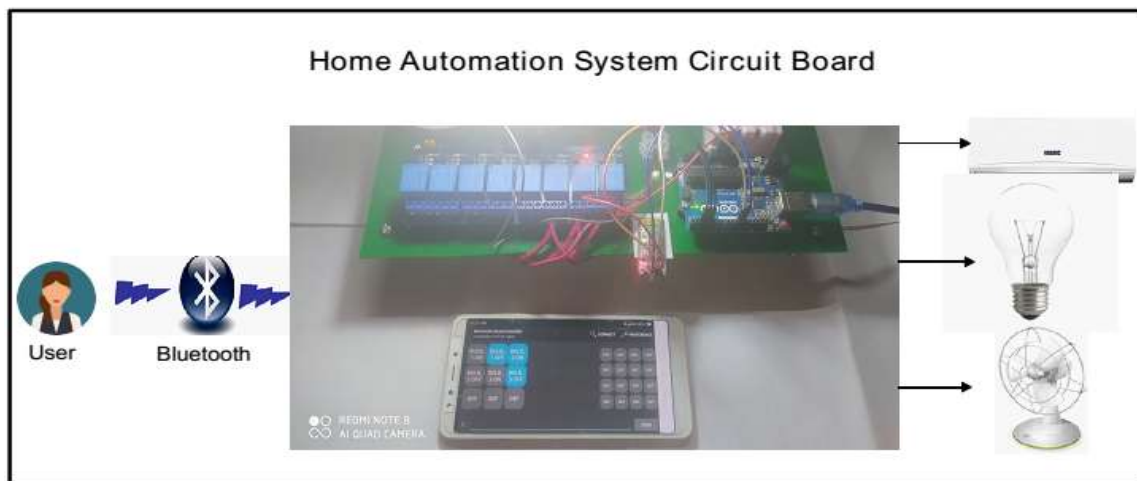


Figure 7 Home Automation System Circuit Board

Advantages of Research

Home Automation System is greatly sensitive system. This system works with any mobile phone from anywhere. This system is of low cost and having reliable arrangement. Home Automation System is durable and efficient. It works on arduino based system so we can easily understand how it works. It saves our time. Every home appliance can control by using android application based on the home automation system. Home automation system is widely used for the control of home appliances, hotel lights or fans, shops and showrooms appliances and industrial appliances.

Conclusion

The proposed work has developed a Home Automation System using Bluetooth, Android and Arduino. This is a cost-effective, low maintenance and user-friendly automation system to assist and support for the elderly and differently skilled people. Main motive of this paper is to have a centralized control system to operate the appliances through an Android phone. It also saves the time for operating appliances to the consumers. The appliances in the home can be controlled and its status (ON or OFF condition) can be monitored from a remote location. The idea proposed in this research paper can also be extended for the automation of industries, malls and hospitals. Moreover, the requirement of this research paper is to create a device which saves the electricity and improve human life style.

Acknowledgements

The author would like to acknowledge Rector Dr Khin Thidar, Rector of West Yangon University for giving me the opportunity to submit this manuscript to the Arts and Science Research Journal (MAAS) 2022 Conference. I am also indebted to my supervisor, Dr Win Win Thein (Retired), Professor and Head of Physics Department, Hinthada University, for her valuable guidance, suggestions, and insight from the initial to reach the final goal of this research. Finally, I would like to express sincere thanks to Dr Maung Maung Shwe, Professor and Head of Physics Department, West Yangon University for his permission to carry out this research and to submit this manuscript to the conference.

References

- Bharanialankar, S.R., and Manikanda Babu, C.S., (2014), Intelligent HomeAppliance Status Intimation Control and System Using GSM”, 2014, International Journal of Advanced Research in Computer Science and Software Engineering, Vol. 4(4), pp.554 - 556.
- Chandra Shakher Tyagi., Mega Agarwal., and Renu Gola., (2016), Home Automation Using Voice Recognition and Arduino, IJRTER, Vo.1 2, Issue 7, ISSN: 2455.1457.
- ElShafee., and Hamed, K.A., (2012), Design and Implementation of a Wi-Fi Based Home Automation System, World Academy of Science, Engineering and Technology, vol. 68, pp. 2177-2180.
- Ericsson., (2000), Mobile Communications AB, User Manual-Bluetooth PC Reference Stack, 1543 VNX 2/901 184 Uen Version R1a.
- Pooja N., Pamar, Shruthi Ramachandran., Nisha P., Singh., Varsa V., and Wagh (2016), A Home Automation System using Internet of Things, IJRCCE, Vol.4, Issue 4, pp. 6555-6563.
- Rajeev Piyare., and Tazil M., (2011), Bluetooth Based Home Automation System using Cell Phone, *IEEE International Symposium on Consumer Electronics*, pp.192-195.

SYNTHESIS AND CHARACTERIZATION OF Ca DOPANT EFFECT ON PbCaTiO₃ POWDERS

Thuzar Hnin¹, Myat Shwe Wah², Myat Thet Mon³ and Zin Min Tun⁴

Abstract

The purpose of this work was to synthesize Pb_{1-x}Ca_xTiO₃ (x = 0, 0.1, 0.2, 0.3 wt%) in the form of powder phase by solid state mixed oxide technique and to study the structural properties of this laboratory-made PbCaTiO₃ specimen by a systematic analysis of XRD and SEM for the potential applications in the ferroelectric devices. From XRD results, PbCaTiO₃ powders were significantly formed with tetragonal symmetry. According to SEM results, these PbCaTiO₃ powders were composed of regular and sphere grains with sizes ranging from (278.5 nm-433.75 nm) for various x contents. The PbCaTiO₃ powders were quite suitable for cost effective and uncomplicated trends of ferroelectric materials such as random access memory (RAM).

Keywords: PbCaTiO₃, solid state mixed oxide technique, X-ray diffraction (XRD) and Scanning Electron Microscope (SEM)

Introduction

The science and technology of nanostructured materials is advancing at a very rapid pace. Nowadays, the preparation and functionalization of one-dimensional nanostructured materials has become one of the most important roles of the nanotechnology. Nanotechnology is employed in many different electronics communications, and computing applications, providing smaller, faster, and more portable systems. In general, the size of a nanoparticle spans the range between 1 and 100 nm. Metallic nanoparticles have different physical and chemical properties from bulk metals, properties that might prove attractive in various industrial application are the simplest form of structures with sizes in the nm range. In principle, any collection of atoms bonded together with a structural radius of < 100 nm can be considered a nanoparticle.

Nanoparticles can be in the form of nanocrystals, nanopowders, or nanoclusters, and the particles act as a bridge between bulk materials and atomic or molecular structures. Nanoparticles have a very high surface area to volume ratio, which provides a great driving force for diffusion, particularly at high temperature.

A perovskite is any material with the same type of crystal structure known as the perovskite structures with the oxygen in the face centers. Perovskite-type materials can be represented by their general formula as ABO₃ where, A and B are any two different sized cations and B is the anion bonding them. Most of the perovskites contain oxygen as the anion. Hence, perovskite oxides can be presented by their general formula as ABO₃. Perovskite type oxide materials are important for electronic applications since they exhibit diverse physical properties such as super conductivity, dielectricity, ferroelectricity and magnetism.

¹ Department of Physics, West Yangon University, Myanmar

² Department of Physics, West Yangon University, Myanmar

³ Department of Physics, West Yangon University, Myanmar

⁴ Department of Physics, Sagaing University, Myanmar

Experimental Procedure

Starting Materials

The materials used in this study were Lead Oxide (PbO), Calcium Oxide (CaO) and Titanium Dioxide (TiO₂) with different molar ratio of calcium. Figure 1 shows the Starting materials.



Figure 1 Starting materials

Preparation of Pb_{1-x}Ca_xTiO₃ powders

Calcium ($x = 0$ g, 0.1 g, 0.2 g, 0.3 g) doped lead titanate PbTiO₃ was successfully prepared by solid state reaction method. Lead oxide (PbO), calcium oxide (CaO) and titanium dioxide (TiO₂) were weighed with digital balance and mixed with desired stoichiometric composition of PbCaTiO₃ powders. The mixture was ground by agate mortar to become a homogeneous mixture. The mixed PbCaTiO₃ powders were calcined at 800 °C for 1.5 h in furnace and reground with agate mortar. The reground PbCaTiO₃ powders passed through 100, 250 and 400 mesh sieves. Finally, homogeneous PbCaTiO₃ powders were obtained. In this section, the structural properties of PbCaTiO₃ powders were characterized by X-ray diffraction method (XRD). Figure 2 showed the block diagram of preparation of PbCaTiO₃ powders with different x contents.

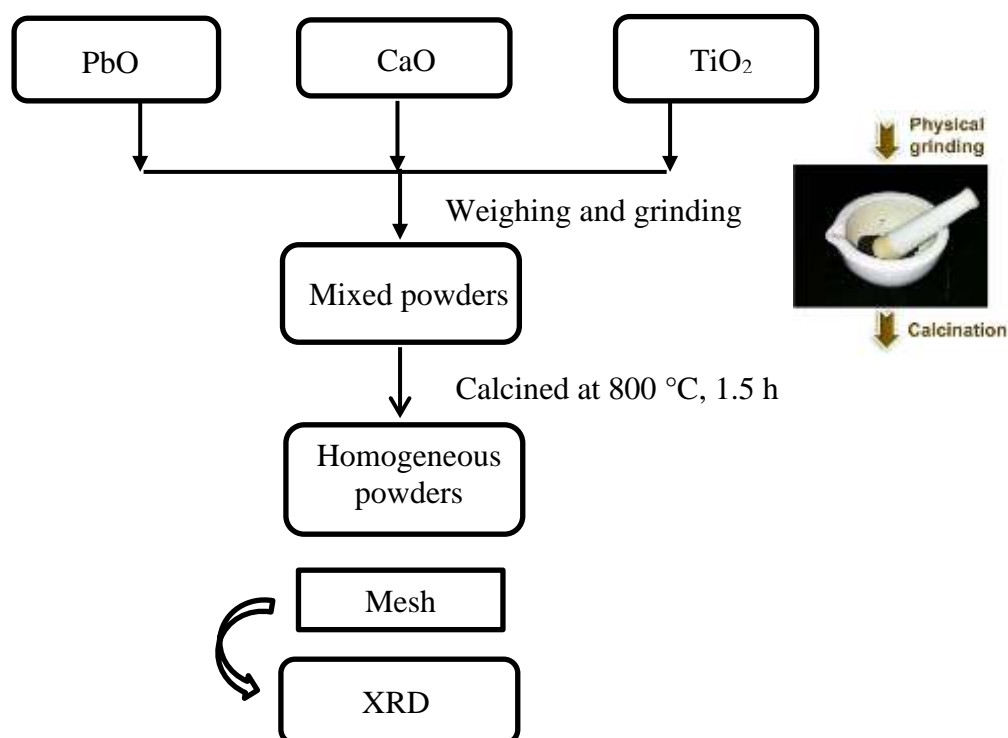


Figure 2 The block diagram of preparation of PCT nanoparticles with different x contents

Results and Discussion

XRD analysis of PbCaTiO₃ powders

X-ray diffraction technique (XRD) is a powerful technique for determination of crystal structure. It provides simple nondestructive information on the nature of intermetallic and crystal phase usually in a very short time. The great deal of the crystallographic information of crystalline PbCaTiO₃ powder has been studied by crystallite size. The XRD patterns of PbCaTiO₃ specimens were perovskite type with tetragonal structure as shown in figure 3 (a-d). There are several diffractions of the standard peaks which were scanned within the diffraction angles range from 10° to 70°. Some extra peaks were formed on all XRD profile and they could not be identified. PCT powders were obtained and examined its phase formation by X-ray diffractometer using Cu-K_α radiation with wavelength of 1.54056 Å. All the peak heights and peak positions were in good agreement with the JCPDS (Join Committee on Powder Diffraction Standards) in 49-0863 > PbCaTiO₃ library file. The average crystallite-sizes were 29.872, 25.253, 24.827, 28.019 nm for various x contents respectively. For the powder, 2θ, FWHM values and crystallite sizes were given in Table 1-2. The lattice parameter (a, b and c) and lattice distortion (lattice strain) c/a of dominant peaks were described in Table 3. Thus, the PCT powders were successfully obtained by solid state reaction method with tetragonal structure.

The crystallite size was calculated using a well-known Debye Scherrer's formula in equation:

$$G = \frac{0.899 \times \lambda}{FWHM \times \cos \theta} \tag{1}$$

where,

- G = crystallite size
- λ = 1.54056 Å for Cu K_α
- FWHM = full width at half maximum at dominant peak
- θ = Bragg angle.

Table 1 Structural Properties of Pb_{1-x}Ca_xTiO₃ Powders for (x = 0 , 0.1wt %)

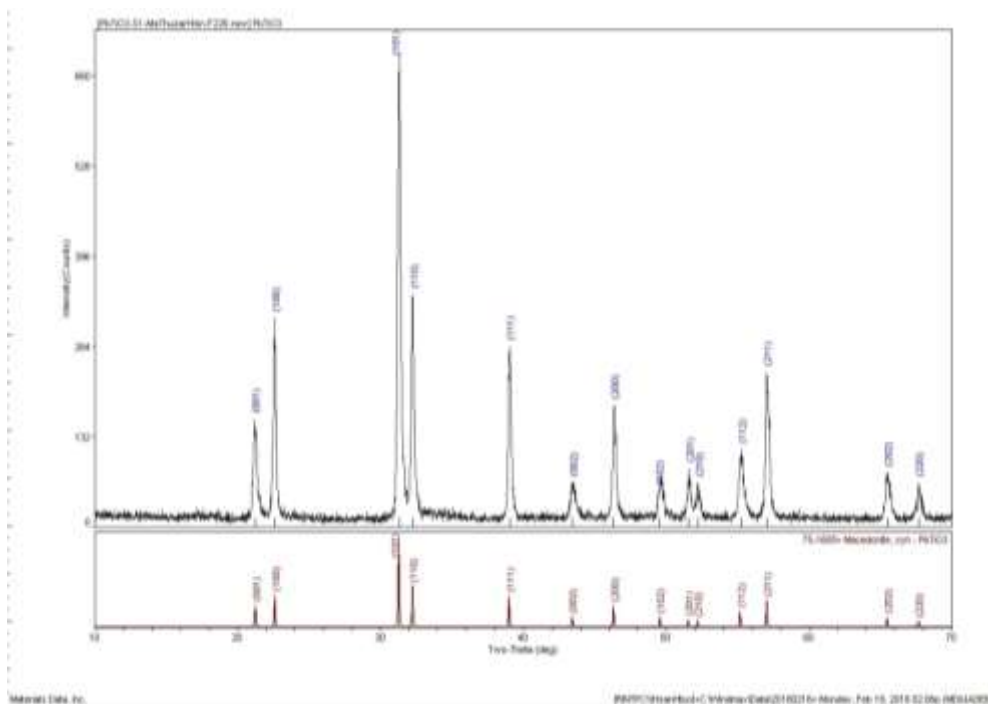
Sr No.	(h kl)	2 θ (deg)	FWHM M (deg)	Observed Crystallite Size (nm)	Sr No.	(h kl)	2 θ (deg)	FWHM (deg)	Observed Crystallite Size (nm)
1	(001)	21.205	0.262	33.700	1	(001)	21.252	0.327	27.030
2	(100)	22.581	0.200	44.100	2	(100)	22.571	0.238	37.120
3	(101)	31.300	0.249	35.500	3	(101)	31.309	0.270	32.710
4	(110)	32.269	0.232	38.000	4	(110)	32.311	0.300	29.430
5	(111)	39.039	0.246	35.900	5	(111)	39.056	0.250	35.300
6	(002)	43.447	0.378	23.400	6	(002)	44.037	0.575	15.360
7	(200)	46.347	0.262	33.700	7	(200)	46.343	0.301	29.340
8	(102)	49.490	0.585	15.100	8	(102)	49.926	0.532	16.590
9	(201)	51.594	0.288	30.600	9	(201)	51.587	0.440	20.050
10	(210)	52.223	0.367	24.100	10	(210)	52.219	0.407	21.690
11	(112)	55.239	0.386	22.800	11	(112)	55.415	0.440	20.050
12	(211)	57.053	0.297	29.700	12	(211)	57.100	0.342	25.840
13	(202)	65.487	0.376	23.500	13	(202)	65.653	0.416	21.220
14	(220)	67.675	0.314	28.110	14	(220)	67.669	0.360	24.530
Average crystallite size				29.872	15	(003)	68.250	0.396	22.290
					Average crystallite size				25.235

Table 2 Structural Properties of $Pb_{1-x}Ca_xTiO_3$ Powders for ($x = 0.2, 0.3$ wt%)

Sr No.	(h kl)	2 θ (deg)	FWHM (deg)	Observed Crystallite Size (nm)	Sr No.	(h kl)	2 θ (deg)	FWHM (deg)	Observed Crystallite Size (nm)
1	(001)	21.252	0.329	26.840	1	(001)	21.408	0.703	12.560
2	(100)	22.558	0.244	36.200	2	(100)	22.561	0.231	38.220
3	(101)	31.97	0.281	31.440	3	(101)	31.272	0.276	31.980
4	(110)	32.227	0.255	34.620	4	(110)	32.210	0.289	30.560
5	(111)	39.026	0.283	31.180	5	(111)	39.080	0.228	38.800
6	(002)	43.944	0.626	14.100	6	(002)	43.880	0.640	13.790
7	(200)	46.325	0.300	29.400	7	(200)	46.293	0.249	35.500
8	(102)	49.915	0.584	15.120	8	(102)	50.039	0.252	35.100
9	(201)	51.548	0.383	23.100	9	(201)	51.534	0.311	28.370
10	(210)	52.203	0.319	27.710	10	(210)	52.125	0.284	31.120
11	(112)	55.441	0.495	17.830	11	(211)	57.013	0.310	28.470
12	(211)	57.054	0.331	26.690	12	(202)	65.760	0.417	21.190
13	(202)	65.443	0.511	17.270	13	(220)	67.552	0.473	18.650
14	(003)	67.149	0.549	16.080	Average crystallite size			28.019	
Average crystallite size				24.827					

Table 3 Lattice parameters and c/a ratios of various x contents for $Pb_{1-x}Ca_xTiO_3$ Powders

x contents (wt%)	Lattice Parameter (Å)		Tetragonality c/a
	a	c	
x = 0	3.9162	4.1804	1.0674
x = 0.1	3.9170	4.1602	1.0621
x = 0.2	3.9218	4.1624	1.0613
x = 0.3	3.9313	4.1412	1.0534

**Figure 3 (a)** The XRD patterns of $PbCaTiO_3$ powders ($x = 0$ wt%)

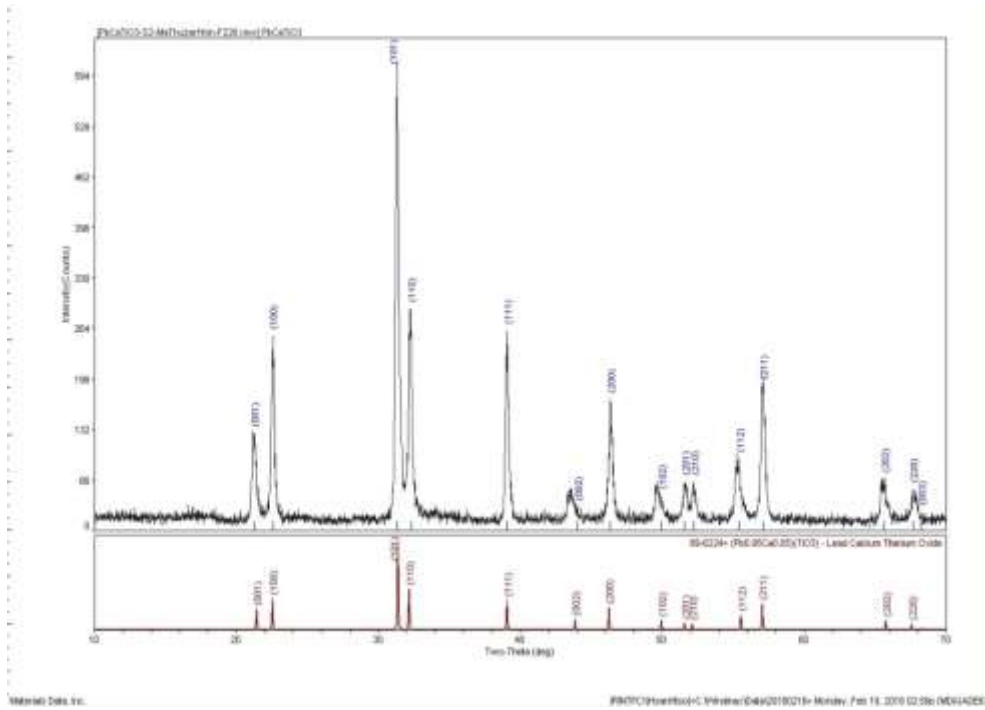


Figure 3 (b) The XRD patterns of PbCaTiO₃ powders (x = 0.1 wt%)

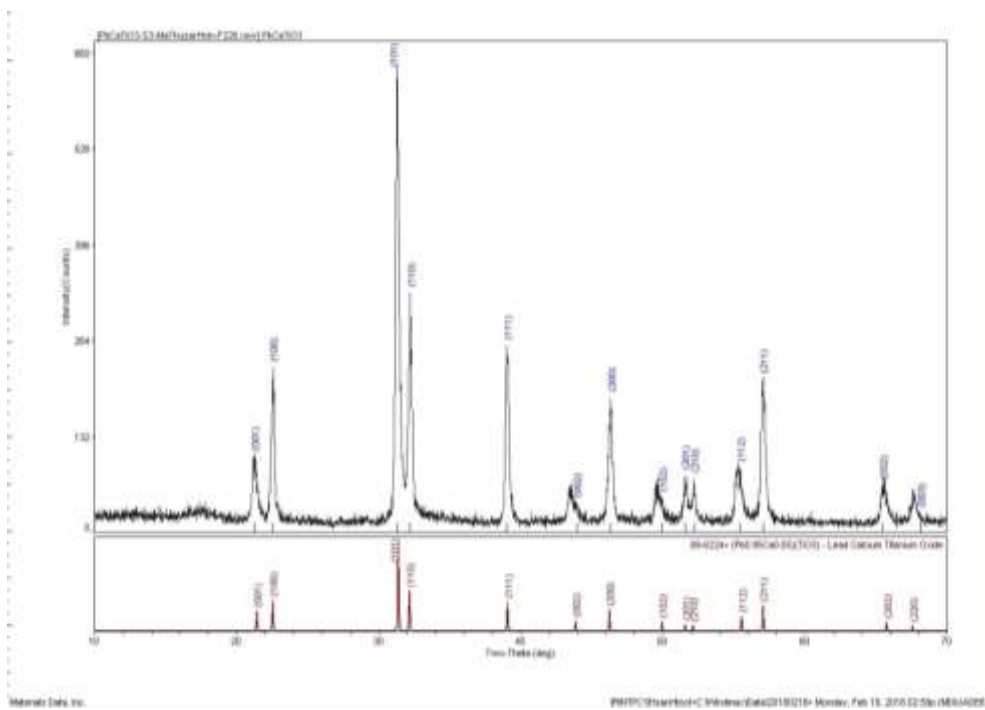
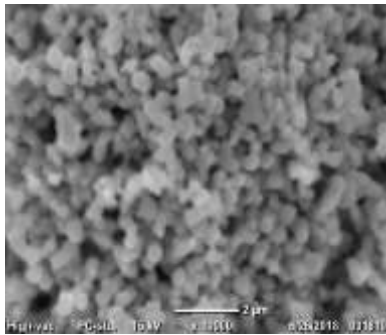
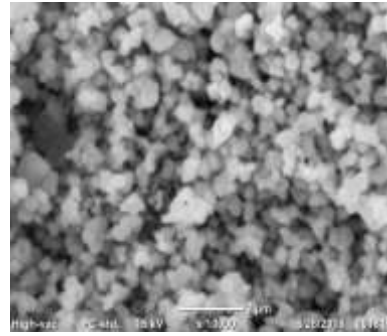


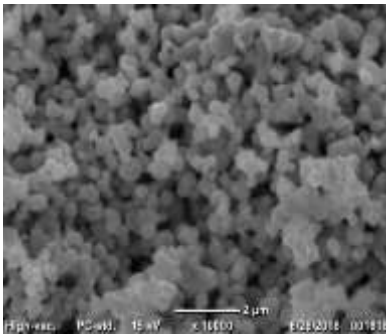
Figure 3 (c) The XRD patterns of PbCaTiO₃ powders (x = 0.2 wt%)



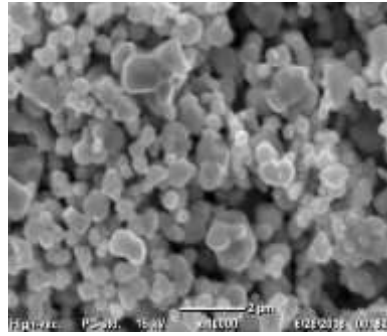
(a) ($x = 0$ wt%, Average grain size = 278.5 nm)



(b) ($x = 0.1$ wt%, Average grain size = 324.25 nm)



(c) ($x = 0.2$ wt%, Average grain size = 333 nm)



(d) ($x = 0.3$ wt%, Average grain size = 433.75 nm)

Figure 4 (a-d) SEM photographs of PbCaTiO_3 crystalline powder ($x = 0, 0.1, 0.2$ and 0.3 wt%) at calcined temperatures 800°C

Conclusion

$\text{Pb}_{1-x}\text{Ca}_x\text{TiO}_3$ powders with different x contents were successfully prepared by solid state reaction method. In the XRD analysis, crystallite sizes of several peaks were 29.872 nm, 25.253 nm, 24.827 nm, 28.019 nm for various x contents respectively. From XRD results, the crystal structure of the prepared PbCaTiO_3 powders was perovskite type with tetragonal symmetry. According to SEM analysis results, PbCaTiO_3 powders were smooth, sphere, and uniform grain with sizes ranging from (278.5 nm-433.75 nm) for various x contents. As these research data, the PbCaTiO_3 powders were quite suitable for cost effective and uncomplicated trends of ferroelectric materials such as random access memory (RAM).

Acknowledgements

We are greatly thankful to Dr. Khin Thidar, Rector, Dr. Thandar and Dr. Thet Thet Tun, Pro-rectors, West Yangon University for their encouragement, Professor Dr Maung Maung Shwe, PhD (YU), Head of Department of Physics, Professor Dr Myat Shwe Wah, PhD (YU), Professor Dr Zay Ya Aung, PhD (YU) and Dr Khin Thitsar Shin, PhD (YU), West Yangon University, for their kind permission to carry out this paper.

References

- Anthony R., West (2005), "Solid State Chemistry and its Applications", Wiley and Sons.
- Aruta C., *et al* (2006) *Journal of Applied Physics* 100 023910
- Batista, Carlos A. *et al*, (2015), *Nonadditivity of nanoparticle interactions*, *Science*. 350 (6257)
- Baumgarten P.K., (1971) *Journal of Colloid and Interface Science* 36
- Bergshoef M.M. *et al*, (1999) *Journal of Advanced Materials* 11 (16) 1362
- Barrow G. M. (1962) "Introduction to Molecular Spectroscopy" (Tokyo: McGraw-Hill)
- Cernea M., (2004) *J Opt and Mater* 6 1349-1356
- Faraday, M., (1857). "Experimental relations of gold and other metals to light", *Phil. Trans.R. Soc. Lond.* 147:145-181
- Gerand B., *et al*, *Preparative methods in Solid State Chemistry*, Academic press.
- Iijima K. *et al* (1986) *J Appl Phys* 60, 361
- Ireme E. A. (2005) *Electronic Materials Science* (New Jersey: Wiley)
- Wenk, H. Rudolf, *et al*, (2004). *Minerals: Their Constitution and Origin*. New York, NY: Cambridge University Press. ISBN 978-0-521-52958-7.

STRUCTURAL CHARACTERIZATION AND ELECTRICAL PROPERTIES OF ZnFe₂O₄ SPINEL FERRITE

May Thwe Soe¹ and Myat Shwe Wah²

Abstract

Zinc ferrite, ZnFe₂O₄, has been prepared by solid state reaction method at 1150 °C for 5 h in vacuum chamber (160 mmHg). Analar (AR) grade zinc oxide, ZnO, and ferric oxide, Fe₂O₃, were used to prepare and characterize for the sample. The as-prepared ZnFe₂O₄ sample was characterized by XRD methods. XRD pattern reveals that the sample belongs to spinel type cubic structure and the lattice parameters of the sample are obtained as a = b = c = 8.86 Å respectively. Crystallite size of the sample is also obtained as 46.06 nm. Variation of the electrical conductivity and dielectric constant with temperature were studied by electrical resistance and capacitance measurements. The electrical conductivity results show that the sample is a superionic conductor or fast ion conductor at high temperature (T ≥ 523 K).

Keywords: Zinc Ferrite (ZnFe₂O₄) Spinel, Zinc Oxide (ZnO), and Ferric Oxide (Fe₂O₃), electrical conductivity and dielectric constant

Introduction

There are various types of microwave absorbers such as dielectric absorbers, magnetic absorbers, resonant absorbers and hybrid absorbers. Ferrites are preferred as microwave absorbers for portable wireless devices operating in the microwave band because they are compact, light weight, less costly and can be easily developed. In view of its several potential applications, a zinc spinel ferrite, ZnFe₂O₄ microwave absorber has been developed and characterized for use in the 2.4 GHz ISM band. Zinc ferrite (ZnFe₂O₄) having a cubic spinel structure is a soft magnetic material and is widely studied as microwave absorbing material. In the present work, the compound of zinc spinel ferrite, ZnFe₂O₄, was prepared by conventional solid state reaction method and characterized by XRD, electrical conductivity and dielectric measurements to study the structural, microstructural, vibrational, thermal and electrical properties of the sample.

Materials and Method

In this chapter, the main constituents of the present experimental work include the sample preparation of the zinc ferrite, ZnFe₂O₄ spinel, structural analysis by powder X-ray diffraction measurement, electrical conductivity and dielectric constant measurements of the ZnFe₂O₄ spinel.

Preparation of Zinc Ferrite, ZnFe₂O₄

The raw materials used for the preparation of samples are conventional oxides. The candidate material of zinc ferrite, ZnFe₂O₄, was prepared by solid state reaction method. The preparation of sample includes the following steps:

- (i) weighing the starting materials,
- (ii) mixing, grinding,
- (iii) pumping, and annealing
- (iv) characterizing.

¹ Department of Physics, West Yangon University, Myanmar

² Department of Physics, West Yangon University, Myanmar

The starting materials of Analar (AR) grade zinc oxide, ZnO, and ferric oxide, Fe₂O₃, were weighed with stoichiometric composition to prepare, ZnFe₂O₄. The mixture powder was ground by an agate motor for 1 h to be homogeneous and to obtain fine grain samples. The powder was annealed at 1150 °C for 5 h in vacuum chamber (160 mmHg) by using DELTA A SERIES temperature controller. The K-type thermocouple was used as the temperature senso. Finally, the candidate material of ZnFe₂O₄ spinel was obtained. The procedure for the preparation of zinc ferrite is described by the flow chart in Figure 2.

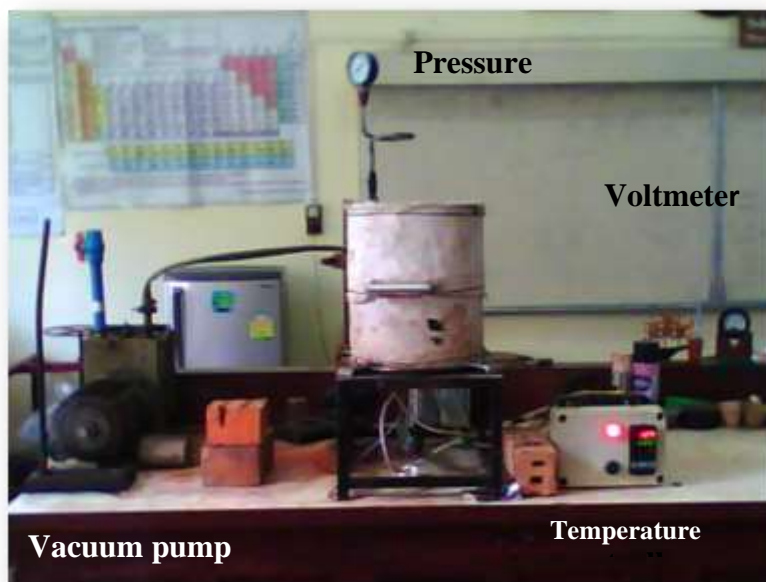


Figure 1 Photograph of the experimental setup of sample preparation system

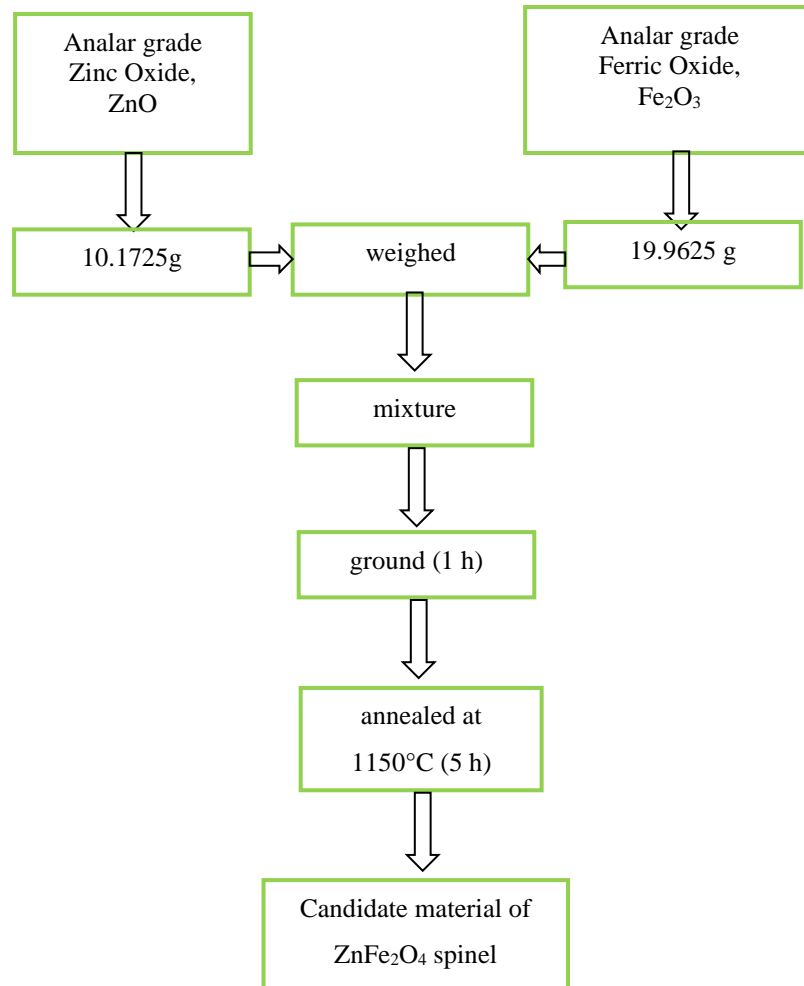


Figure 2 Procedure for the preparation of zinc ferrite

Electrical Conductivity and Dielectric Constant Measurement

The electrical conductivity and dielectric constant of the pelletized ZnFe_2O_4 sample were investigated in the temperature range 300 K (27 °C) - 923 K (650 °C) by using CAHO SR-T903 Temperature Controller. The diameter and thickness of the sample were used as 1.20 cm and 0.17 cm respectively. The dimensions of the sample were measured by using Digital Vernier Caliper (Taiwan). Firstly, the sample was fixed on glass plate and silver contacts were made over the sample to ensure good electrical contacts to measure the electrical properties such as resistances that change with temperatures. Of course, the surfaces of the palletized sample (sample surfaces) and electrodes (copper plates) are not optically homogeneous, But, in practice, the surfaces of the sample and electrodes must be homogeneously contacted with each other when the light or temperature dependence measurements of electrical parameters, such as resistance, capacitance and voltage of the samples. Thus, silver paste (electrical and thermal conducting paste) was used to interface or homogeneously contacted between surfaces of crystal and electrodes. Electrical conductivity measurements were made on the sample in a stainless-steel conductivity cell in which the sample is maintained by a spring-loaded support between copper leads using two polished Cu disc as electrodes.

The temperature sensor of K-type thermocouple (up to 1073 K) was placed near the sample to record real temperatures throughout the measurement. The copper block holder (heater chamber) was heated by using the four of 300W heater coils. The electrical resistances and capacitances of

the sample were measured by using FLUKE 45 Dual Display digital multimeter and FUKE DM6013A Digital CAPACITANCE METER with heat conduction technique. The electrical conductivity of ionic crystals have been calculated by using the formula

$$\sigma = \frac{t}{R A}$$

where,

- t = the thickness of the sample or the distance between the two electrodes
- A = the cross-sectional area of the electrodes or sample
- R = the resistance of the sample

Photograph of the experimental setup of electrical conductivity measurement is shown in Figure 3. The dielectric constants have been calculated by using the formula

$$\varepsilon_r = \frac{C t}{\varepsilon_0 A}$$

where,

- C = the capacitance
- t = the thickness
- ε_0 = the permittivity of free space (8.8541×10^{-12} F)



Figure 3 Photograph of the experimental setup of electrical resistance and capacitance measurement

Characterization of ZnFe_2O_4

This research work describes the experimental results and discussion of structural and electrical characteristics of zinc ferrite, ZnFe_2O_4 from the measurements of XRD and electrical conductivity measurements.

Results and Discussion

Structural Analysis by XRD

X-ray diffraction data were collected from powder samples of the zinc ferrite, ZnFe_2O_4 using a PC-controlled RIGAKU MULTIFLEX automated X-ray diffractometer with monochromatic $\text{CuK}\alpha$ ($\lambda=1.54056 \text{ \AA}$) using Ni-filter (scan speed $4^\circ/\text{min}$). The NaI(Tl) scintillation counter was used to detect the diffracted X-ray from the sample. The measurement was taken from 10° to 70° with 2θ diffraction angle. Lattice parameters were determined from the indexed data using experimental results of low angle reflections.

Powder X-ray diffraction pattern of ZnFe_2O_4 spinel is shown in Figure 4. The collected XRD data were compared to those of JCPDS data library to identify the collected XRD pattern of sample. Most of the collected diffraction lines were assigned by JCPDS. Some of the diffraction lines (e.g, 2θ is 24.18°) were not assigned with JCPDS files due to small crystallite effects, crystal defects or chemical heterogeneity of the samples. In this XRD pattern, the diffraction line at 33.30° or (311) plane is found to be the strongest among all lines and it indicated the (311) peak is dominated in the as-grown polycrystalline ZnFe_2O_4 spinel. Some of the XRD data of diffraction angle (2θ), atomic spacing (d), miller indices (hkl), full width at half maximum (FWHM) and peak height of the sample are tabulated in Table 1.

According to XRD pattern, zinc ferrite, ZnFe_2O_4 belongs to spinel type cubic structure at room temperature. The lattice parameters were evaluated by using crystal utility of the equation of

$$\frac{\sin^2 \theta}{(h^2 + k^2 + l^2)} = \frac{\lambda^2}{4a^2}$$

Lattice parameters of the sample are $a = b = c = 8.86 \text{ \AA}$. From the observed XRD data, the crystalline size of the ZnFe_2O_4 was estimated by using the Scherrer formula,

$$t = \frac{0.9 \lambda}{B \cos \theta}$$

where,

t = the crystallite size (nm)

λ = the wavelength of incident X-ray (nm)

θ = the diffraction angle of the peak under consideration at FWHM ($^\circ$)

B = the observed FWHM (radians)

In this work, we used the diffraction line 2θ is 33.30° . Miller index (hkl) is (311) and FWHM is 0.18° to calculate the crystallite size of the sample because this line is the strongest in intensity among the observed XRD pattern. The crystallite size of the sample was obtained as 46.06 nm.

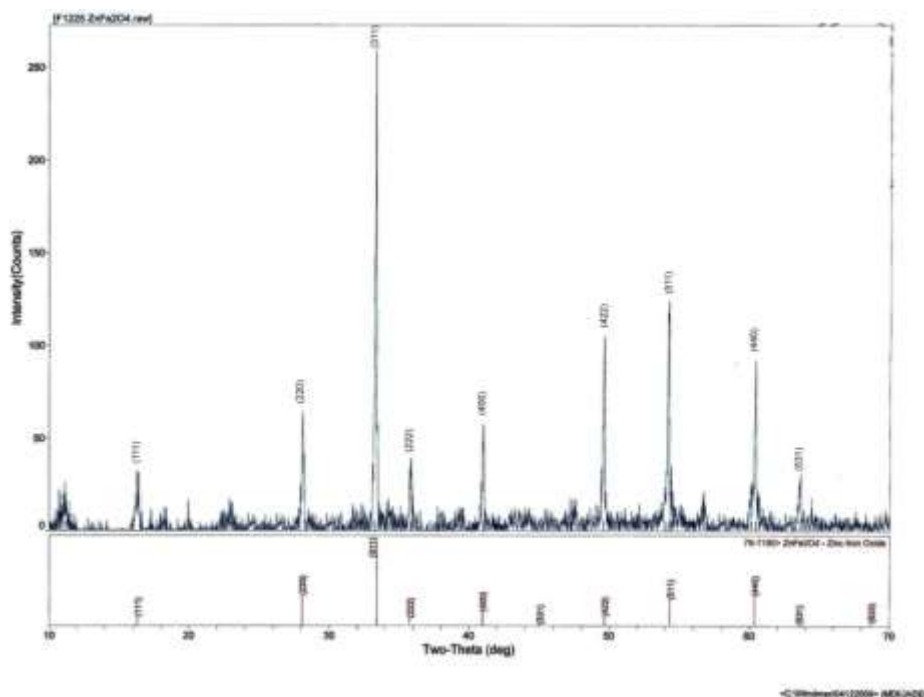


Figure 4 XRD pattern of zinc ferrite, $ZnFe_2O_4$

Table 1 Powder XRD data of zinc ferrite, $ZnFe_2O_4$

Line No.	2θ ($^\circ$)	(hkl)	d (\AA)	FWHM ($^\circ$)	Intensity (%)
1	16.18	(111)	7.95	0.23	9.50
2	28.04	(220)	3.15	0.15	24.00
3	33.30	(311)	2.69	0.18	100.00
4	35.79	(222)	2.51	0.14	14.70
5	41.02	(400)	2.20	0.12	21.40
6	49.60	(422)	1.84	0.15	40.50
7	54.41	(511)	1.69	0.09	43.90
8	62.27	(440)	1.49	0.16	25.10
9	63.71	(531)	1.45	0.13	7.20

The electrical conductivities of the sample at 300 K (starting temperature) and 773 K (temperature of superionic conductivity state) are obtained as $5.3653 \times 10^{-9} \text{ S cm}^{-1}$ and $1.4414 \times 10^{-5} \text{ S cm}^{-1}$ respectively. The experimental data are tabulated in Table 2. As presented in Table 1, the electrical conductivity of the sample at $T \geq 773\text{K}$ is found to be $\sim 10^{-5} \text{ S cm}^{-1}$ that shows the superionic conductivity of the sample. Thus, the sample is a superionic conductivity of the sample. Thus, the sample is a superionic conductor or fast ion conductor at high temperature ($T \geq 773 \text{ K}$).

If a material contains polar molecules, they will generally be in random orientations when no electric field is applied. An applied electric field will polarize the material by orienting the dipole moments of polar molecules. This decreases the effective electric field between the plates and will increase the capacitance of the parallel plate structure. The dielectric constant is the relative permittivity of a dielectric material. It is an important parameter in characterizing capacitors. The capacitance of a set of charged parallel plates is increased by the insertion of a dielectric material.

In the present work, variation of the dielectric constants with temperatures of $ZnFe_2O_4$ sample in the temperature range 300 K – 923 K is shown in Figure 5. The dielectric constants of

the sample are found to linearly increase with increasing temperatures. As shown in (ϵ_r -T) relationship, the slope of the curve is found to linear type and that indicates any phase changes characters are not occurred in the sample due to thermal agitation. It can be said that the sample is a thermally stable or thermally inert material.

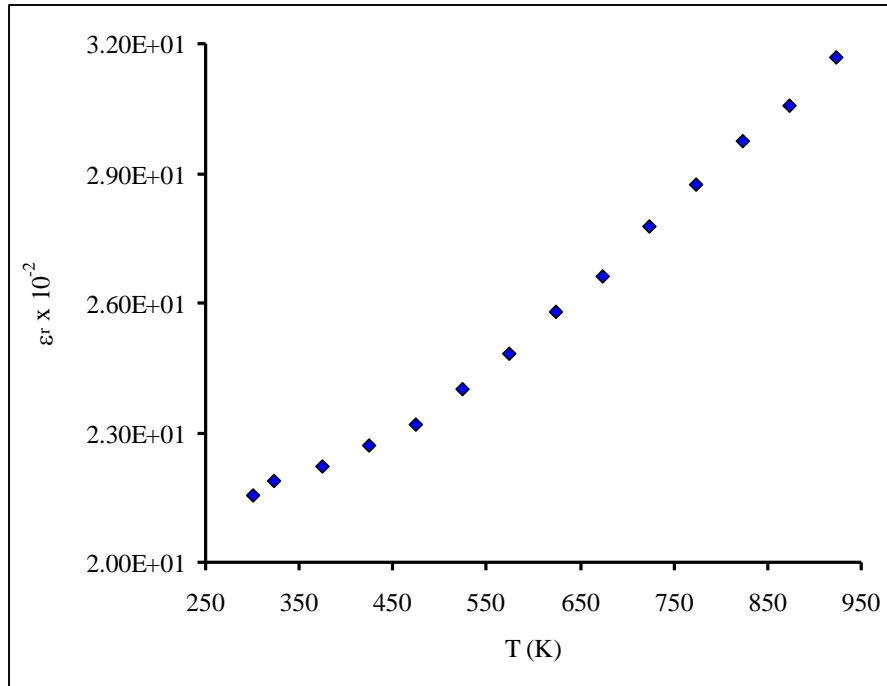


Figure 5 Plot of the variation of dielectric constants with temperatures of ZnFe₂O₄

Table 2 Experimental data of electrical conductivity and dielectric constant measurements of ZnFe₂O₄

T (K)	1000/T (K ⁻¹)	R (kΩ)	σ (S cm ⁻¹)	ln σ	ε _r	ε _r × 10 ⁻²
300	3.3333	27000.00	5.3653E-09	-19.0433	2.16E+03	2.16E+01
323	3.0960	18150.00	7.9815E-09	-18.6461	2.19E+03	2.19E+01
373	2.6810	8560.00	1.6923E-08	-17.8946	2.22E+03	2.22E+01
423	2.3641	2630.00	5.5081E-08	-16.7145	2.27E+03	2.27E+01
473	2.1142	920.00	1.5746E-07	-15.6641	2.32E+03	2.32E+01
523	1.9120	560.00	2.5869E-07	-15.1677	2.40E+03	2.40E+01
573	1.7452	408.00	3.5506E-07	-14.8510	2.48E+03	2.48E+01
623	1.6051	120.00	1.2072E-06	-13.6272	2.58E+03	2.58E+01
673	1.4859	76.50	1.8936E-06	-13.1770	2.66E+03	2.66E+01
723	1.3831	37.50	3.8630E-06	-12.4641	2.78E+03	2.78E+01
773	1.2937	10.05	1.4414E-05	-11.1473	2.88E+03	2.88E+01
823	1.2151	5.25	2.7593E-05	-10.4979	2.98E+03	2.98E+01
873	1.1455	4.40	3.2924E-05	-10.3213	3.06E+03	3.06E+01
923	1.0834	4.25	3.4086E-05	-10.2866	3.17E+03	3.17E+01

Conclusion

Zinc ferrite, ZnFe_2O_4 was prepared by solid state reaction method. Structural, microstructural, vibrational and thermal characteristics of the sample were studied by XRD methods. The electrical conductivities and dielectric constants of the sample were investigated in the temperature range 300 K - 923 K. Powder XRD pattern indicates that the ZnFe_2O_4 spinel belongs to cubic structure and the lattice parameters of the sample are obtained as $a = b = c = 8.86 \text{ \AA}$ respectively. The crystallite size of the sample is also obtained 46.06 nm. The electrical conductivities of the sample at 300 K and 773 K are obtained as $5.3653 \times 10^{-9} \text{ S cm}^{-1}$ and $1.4414 \times 10^{-5} \text{ S cm}^{-1}$ respectively. The activation energy is obtained as 0.3530 eV. The sample is a superionic conduction or fast ion conductors at the temperature $T \geq 773 \text{ K}$. From the (ϵ_r-T) relationship, the dielectric constants of the sample are increased with increasing temperatures. The slope of the (ϵ_r-T) graph is found to linear and it indicates any phase changes are not occurred. According to experimental result, ZnFe_2O_4 spinel can be considered as the solid electrolyte materials or first ion conductors at high temperatures.

Acknowledgements

I would like to thank Professor Dr Maung Maug Shwe, PhD (YU), Head of Department of Physics, Professor Dr Myat Shwe Wah, PhD (YU) and Professor Dr Zay Ya Aung, PhD (YU), West Yangon University, for their kind permission to carry out this paper.

References

- Banwell C.N. & Mc Cash E.M., (1994) *Fundamentals of Molecular Spectroscopy*
- Bolton W., (1991) *Instrumentation & Measurement* (Oxford: Newnes)
- Callister W.D. (2001) *Fundamentals of Materials Science and Engineering* (New York: Wiley)
- Candeia R.A., et al (2004) *Materials Letters* 58 569
- Cullity B.D. (1978) *Elements of X-Ray Diffraction* (Reading: Wesley)
- Goldstein et al, (1981) *Scanning Electron Microscopy and X-Ray Microanalysis Manuals*
- Hollas J.M., (2004) *Modern Spectroscopy* (New York: Wiley)
- Iqbal M.J. (2009) *Lecture on Synthesis and Characterization of Nanostructured Spinel Ferrites* (Islamabad: Quaid – i-Azam University)
- Kakirda A., et al (2008) *Bulletins Materials Science* 31 (5) 767
- Kanagadurai R. et al (2009) *E Journal of Chemistry* 6(3) 871
- Li D. S., Harikawa T., Liu J. R., Itoh M., and Machida K., (2006) *J Alloys Compd* 408 1429
- Li Z. W., Yang Z. H. and Kong L. B. (2010) *Journal of Applied Physics* 108 063927
- Liu J. R., Itoh M., and Machida K., (2006) *Appl Phys Lett* 88 062503/1.
- Masala O., Haffman D., Sundaram N., Page K., Proffen T., Lawes G., and Seshadri R., (2006) *Solid State Sci* 8 1015.
- Moulson A.J. & Herbert J.M. (1997) *Electroceramic Materials, Properties & Applications* (London: Chapman & Hall)
- Nell J. & Wood B.J. (1989) *American Mineralogist* 74 1000
- Peng C.H., Hwang C.C, Wan J., Tsai J.S., and Chen S.Y., (2005) *Mater Sci Eng B* 117
- Pillai S.O., (2006) *Solid State physics* (New Delhi: New Age)
- Qiu J.X., Wang C.Y., and Gu M.Y., *Master Sci Eng B* 112 (2004) 1.
- Ross S.D. (1972) *Inorganic Infrared and Raman Spectra* (London: Me Graw-Hill)

BEHAVIOR AND FERROELECTRIC PROPERTIES OF LEAD TITANATE FILMS AS A GATE MATERIAL

Pwint Yi Thein¹, Ye Myint Win², Aye Thandar Twin³, Nyo Nyo Myint⁴ and Yin Yin Swe⁵

Abstract

PbTiO₃: Sr thin film devices are prepared by colloidal solution route at different Sr contents. Structural features of prepared samples are examined with the help of x - rays diffraction technique. From the x - rays spectra, lattice dimensions, such as lattice constants, lattice distortion, unit cell volume, crystallite size and lattice micro strain of prepared samples at different Sr contents are evaluated. It is obvious that, there are single phase, tetragonal, polycrystalline and perovskite - type PbTiO₃ structure in prepared samples. FET behavior, known as drain and transfer characteristics of prepared samples are also studied. From the drain characteristic, operation of prepared samples is either enhancement mode or depletion mode is determined. It is obtained that; operations of prepared samples are enhancement mode and normally off nature. Maximum drain current threshold voltage and transconductance values are estimated from the transfer variations. Ferroelectric properties of prepared samples are characterized by using Sawyer - Tower circuit and ferroelectric parameters are investigated. It is known that, ferroelectric parameters (P_s , P_r and E_c) increase as Sr content increases in prepared samples. It might be due to strengthening of second order hybridization, caused by isovalent Sr²⁺ ions in prepared samples. It may be conclude that, our prepared samples are suitable for one transistor (1T) of FeRAM application.

Keywords: PbTiO₃, isovalent Sr ions, XRD, FET, ferroelectricity

Introduction

Ferroelectric materials exhibit a spontaneous polarization in the absence of external electric field. This polarization can be reoriented by ion displacement in the crystal and polarization can be triggered by an external electric field, such that ferroelectric materials can have two electrically - controllable non - volatile states [Miller L. S. and McWhorter P. J., 1992; Sakai S., 2006]. As a result, ferroelectric random access memory (FeRAM) has long been studied as a non - volatile technology [Ishikawa H., 2001]. In a ferroelectric field effect transistor (FeFET), a ferroelectric insulator is employed as a gate insulator in a metal - oxide - semiconductor field effect transistor (MOSFET). It is known to be ferroelectric behavior is added to CMOS performance, while maintaining the back - bone of CMOS logic [Ishikawa H., 2012]. The channel conductance is used to detect the polarizarion state in the ferroelectric gate insulator, so data reading operation in FeFET is non - destructive. FeFET is a promising memory technology due to the fast switching speed in ferroelectric materials (nanosecond or less), its non - destructive readout, its non - volatile state and its simple structure for high density integration [Mikolajick T., *et al.*, 2018; Kim J. Y., *et al.*, 2021]. Lead titanate (PbTiO₃: PT), known as fundamental ferroelectric perovskite, has been constant interest because of its piezoelectric and pyroelectric properties, and high spontaneous polarization, and relatively small permittuy [Wang D. G., *et al.*, 2008; Bhatti H. S., *et al.*, 2016]. PT can accept considerable substitution in one or both cations site, while maintaining its original crystal structure. Partial replacement of cation site(s) with foreign metal ions, can modify the its already reported that, substitutions of isovalent ions, Ca²⁺, Ba²⁺, Sr²⁺ and Cd²⁺ into Pb site exhibit the strong ferroelectric behavior, while maintaining its perovskite crystal structure in PT [Pratiksha Devi *et al.*, 2012]. In this study, isovalent Sr²⁺ ions are chosen as a substituent for doping owing to the fact that, ionic radius of Sr²⁺ ions (113 pm) is slightly smaller than Pb²⁺ ions (119 pm). It is also expected that isovalent Sr²⁺ ions can be easily incorporated into Pb site in host PbTiO₃ crystal [Jian M. and Katiyar R. S. 2002; Mesquita W. D., *et al.*, 2022; Pontes F. M., 2003]. Effect of isovalent Sr²⁺ ions doping

¹ Department of Physics, Nationality Youth Resources Development Degree College Yangon, Myanmar

² Department of Physics, Defence Services Academy, Pyin Oo Lwin, Myanmar

³ Department of Physics, Technological University, Yangon, Myanmar

⁴ Department of Physics, Yanchaund University, Myanmar

on structural features, FET behavior and ferroelectric properties of PbTiO_3 gate material, prepared by colloidal precursor solution method is examined in this research work.

Experimental Procedure

2.1 Sample Preparation

To prepare isoalent Sr^{2+} ions doped PbTiO_3 colloidal precursor solution, commercial grade PbO , TiO_2 and SrO were used as starting precursors. Firstly, these precursors were weighted and mixed, according to following stoichiometric compositions: $\text{Pb}_{(1-x)}\text{Sr}_{(x)}\text{TiO}_3$, where $x = 0.05, 0.10, 0.15, 0.20$ and 0.25 respectively. The mixed precursors were grinded by ball - milling process for each 3 hrs. And then, the mixed precursors were conventionally sintered at 700 C° for each 3 hrs. Solid state sintering meant the bonding and densification of particles by the application of heat below the melting point of a material. During the sintering, the free surface area of the compact decreased, and it was normally accompanied with an increase of the density. After first sintering, the mixed precursors were grinded again for each 3 hrs. Then, the mixed precursors were sintered for each 3 hrs. After second sintering, the mixed precursors were dissolved in 2 - methoxyetanol ($\text{CH}_3\text{COCH}_2\text{CH}_2\text{OH}$) solvent. The mixed solutions were heated and stirred with water batch, known as indirect heat treatment, for each 2 hrs. The p - Si (111) wafers with dimension ($1.5\text{ cm} \times 1\text{ cm} \times 125\text{ }\mu\text{m}$) were used as substrates. Before deposition process, Si substrates were cleaned by using standard semiconductor cleaning procedure. An insulating layer, silicon dioxide SiO_2 , were thermally deposited on Si substrates. An insulating layer SiO_2 between ferroelectric PbTiO_3 : Sr and Si, could reduce the intermixing problem. It could also minimize the effect of charge injection and weaken the electric field across the ferroelectrics. The middle zone of SiO_2/Si structures were covered with apezone wax, and the remaining two - end zones were etched with HF: DI with the ratio of 1: 3, to remove the insulating layers. To create the source (S) and drain (D) regions, n - type phosphorus was deposited on these two - end regions, and sintered at 600 C° for 2 hr. The source (S) and drain (D) regions were formed at two - end regions by diffusion mechanism. Further, isoalent Sr^{2+} doped lead titanate (PbTiO_3 : Sr) colloidal precursor solutions were deposited onto middle zone of SiO_2/Si structure with the help of spin coating technique with 45 rpm in the clean chamber. Wet films were thermally dried at ambient temperature and sintered at 600 C° for each 2 hrs. Silver pastes with diameter 3 mm were formed onto these three regions source (S), drain (D) and gate (G). Three copper wires were attached to these regions as electrodes.

2.2 XRD Measurements

XRD studies were used to determine the phase formation, structural features and lattice dimensions of prepared samples by meant of Rigaku Multiflux x - rays diffractometer with Cu K_α ($\lambda = 1.5418\text{ \AA}$) monochromatic radiation. The prepared samples, known as PbTiO_3 : Sr films were scanned in the 2θ range from 10° to 70° with a scanned speed of $0.01^\circ/\text{sec}$. Applied voltage and current of x - rays generator were set to be 50 kV and 40 mA. From the x - rays spectra, variations of Sr content with lattice dimensions, such as lattice constants " a " and " c ", lattice distortion (c/a), unit cell volume, crystallite size and lattice micro strain were examined in PbTiO_3 : Sr films.

2.3 FET Characteristic Measurements

For drain and transfer characteristic measurements, two power supplies (model abc) and two digital multimeters (model xyz) were used. Measurements were carried out in the DC voltage range from 0 V to 10 V, both for drain to source voltage (V_{ds}) and gate to source voltage (V_{gs}).

Further, to eliminate the transient responses, step voltage and delay time were set to be 0.1 V and 1 min. I (V) data were recorded manually. From the I (V) data, drain and transfer variations were studied.

2.4 Ferroelectric Characteristic Measurements

Ferroelectric behavior of the prepared samples was examined with the help of Sawyer - Tower circuit.

Results and Discussion

3.1 XRD Studies

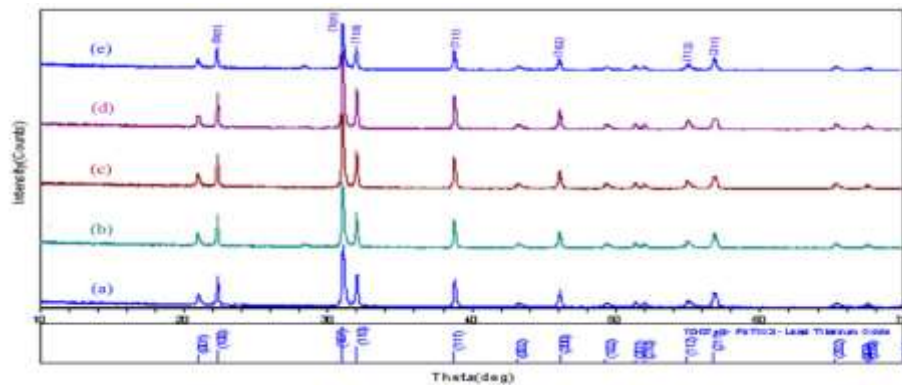


Figure1 XRD Spectra of PbTiO₃ : Sr Films (a) Sr = 5 mol %, (b) Sr = 10 mol %, (c) Sr = 15 mol % (d) Sr = 20 mol % and (e) Sr = 25 mol %

Figure (1) depicted the x - rays diffraction spectra of PbTiO₃: Sr films. Peak search algorithm (Jade Software) was used to identify the all unknown peaks in this research work. Only diffraction peaks from tetragonal, single phase, polycrystalline, perovskite - type PbTiO₃ structure with reference (70 - 0746 > JCPDS file no.) were observed. In addition, the most intense peak was (101) peak and a little shift of (101) peak (in term of 2θ value) was obtained in all x - rays spectra. It was also noticed that, there were no considerable change of tetragonal - phase PbTiO₃ structure after Sr doping. It was reported that, tetragonal to cubic phase transition, known as structural phase evolution was x = 0.50 by XRD technique in Sr doped PbTiO₃ films. However, FT Raman scattering revealed that tetragonal to cubic structural phase transition was x = 0.58. This contradiction could be explained by the fact that, Raman scattering probed short - range structural order, while XRD probed long - range structural order [Pontes F. M., 2003]. These results indicated that additional isovalent Sr²⁺ ions were easily incorporated into Pb - site in host PbTiO₃ lattice. From the x - rays spectra, lattice constants " a " and " c " of PbTiO₃ : Sr films were evaluated by substituting interplanar spacing " d " values of (101) and (110) peaks in the following equation (1).

$$\frac{1}{d^2} = \frac{h^2+k^2}{a^2} + \frac{l^2}{c^2} \quad (1)$$

d = interplanar spacing

h, k, l = miller indices

a, c = lattice parameters

Interplanar spacing of 'd' values (101) and (110) peaks were substituted in equation (1) and lattice parameters 'a, c' were estimated. Unit cell volume of PbTiO₃: Sr films were determined by using following equation (2) :

$$\text{tetragonal cell volume} = a \times a \times c \quad (2)$$

where a, c = lattice parameters,

Unit cell volumes of the PbTiO₃: Sr films were examined by using the following equation (2). Lattice constants " a " and " c ", lattice distortion (c/a) and unit cell volume of PbTiO₃: Sr films were collected and listed in table (1)

Table 1 List of lattice constants, lattice distortion and unit cell volume of PbTiO₃: Sr films.

Sr Content (%)	Lattice Parameter "a (Å)"	Lattice Parameter "c (Å)"	Lattice Distortion (c/a)	Cell Volume (×10 ⁻³⁰ m ³)
5	3.871	4.092	1.057	61.317
10	3.879	4.077	1.051	61.345
15	3.886	4.065	1.046	61.386
20	3.893	4.053	1.041	61.425
25	3.898	4.045	1.038	61.461

Crystallite size and lattice micro strain of PbTiO₃ : Sr films were calculated by using the following Debye - Scherrer equations (3) and (4).

$$D = \frac{0.9 \lambda}{\beta \cos \theta} \quad (3)$$

$$\varepsilon = \frac{\beta}{4 \tan \theta} \quad (4)$$

In the above two equations, β is the full width at half maximum (FWHM) of the most intense peak (101), λ is the wavelength of the using x - rays, θ is the peak position of the (101) peak, known as Bragg's peak. Crystallite size, lattice micro strain and FWHM of the most intense peak (101) were collected and listed in table (2).

Table 2 List of crystallite size, lattice micro strain and FWHM of (101) peak, of PbTiO₃: Sr films.

Sr Content (%)	Crystallize Size (nm)	Micro Strain (× 10 ⁻³)	FWHM of (101) Plane (Rad) (×10 ⁻³)
5	29.54	4.259	4.884
10	29.18	4.311	4.949
15	29.73	4.379	5.022
20	28.36	4.436	5.087
25	28.07	4.482	5.140

It was studied that, lattice constant " a ", unit cell volume, FWHM of (101) peak, and lattice micro strain increased as Sr content increased in PbTiO₃: Sr films. However, lattice constant " c ", lattice distortion (c/a) and crystallite size were lowered, as listed in tables (1 & 2). In PbTiO₃: Sr films, lattice distortion c/a was ~ 1.06, that caused the micro strain during the doping mechanism.

Further, there might be large lattice mismatch between PbTiO_3 : Sr film and SiO_2/Si structure. Therefore, SiO_2/Si structure induced the lattice micro strain in PbTiO_3 : Sr films. In addition, dislocation density was inversely proportional to the square of crystallite size. These results could be interpreted as the small variation of lattice dimensions in PbTiO_3 : Sr films after Sr doping.

3.2 FET Studies

3.2.1 Drain Characteristic

Drain characteristic, known as $I_{ds} - V_{ds}$ variations at different gate to source voltage (V_{gs}), were displayed in figure 2 (a ~ e).

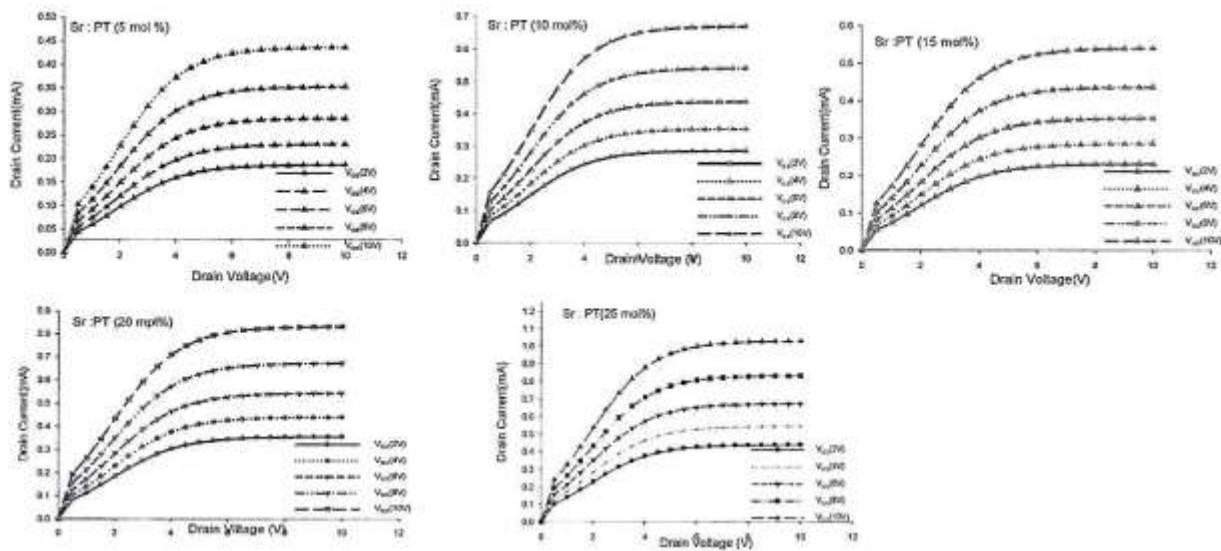


Figure. 2 Drain Characteristic of FET with PbTiO_3 : Sr Gate Materials (a) Sr = 5 mol %, (b) Sr = 10 mol %, (c) Sr = 15 mol %, (d) Sr = 20 mol % and (e) Sr = 25 mol %.

From these variations, two regions, linear and saturation were observed. At low drain to source voltage, between 0 V to 4 V, the drain current (I_{ds}) linearly increased when the drain to source voltage (V_{ds}) was raised. In this region, FET with PbTiO_3 :Sr gate materials, exhibited the resistive characteristic, and as a function of gate to source voltage (V_{gs}). Further, drain to source current (I_{ds}) saturated at pin - off point and $I_{ds} - V_{ds}$ variations saturated. Moreover, drain current (I_{ds}) was enhanced when the gate to source voltage (V_{gs}) was raised. It might be due to FET with PbTiO_3 : Sr gate materials exhibited enhancement mode operation. In addition, the drain to source current (I_{ds}) was zero, when zero - bias gate - source voltage (V_{gs}) was applied. It was very similar to normally off nature of FET.

3.2.2 Transfer Characteristic

Transfer characteristic, known as $I_{ds} - V_{gs}$ variations were studied at saturation mode and illustrated in figure 3 (a ~ e).

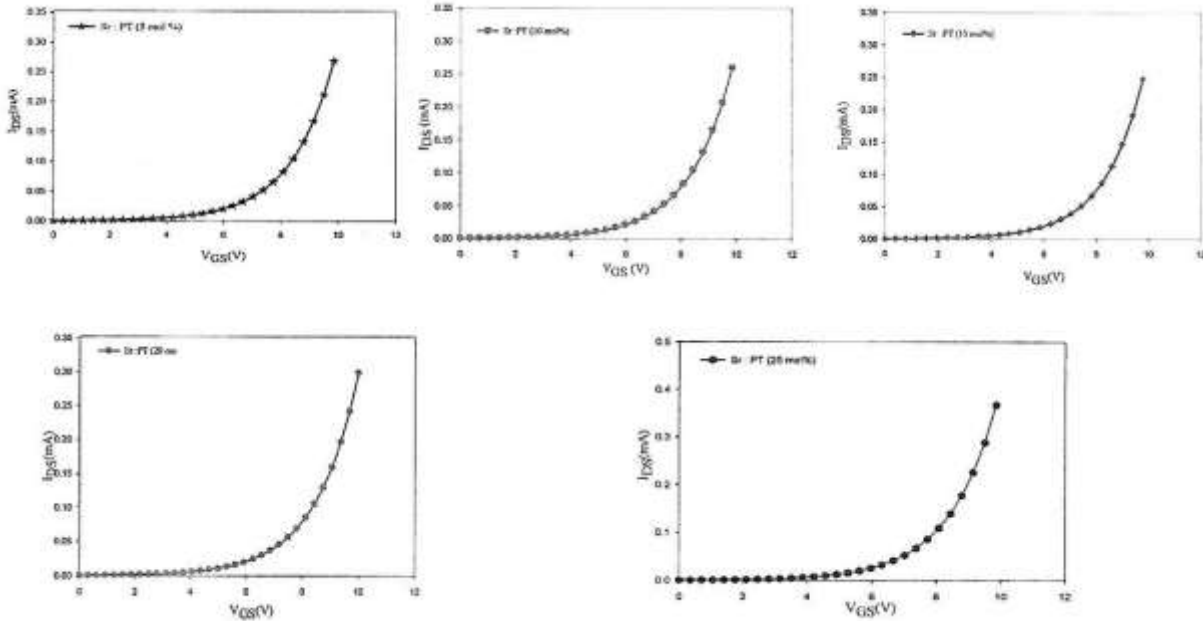


Figure 3 Transfer Characteristic of FET with PbTiO₃ : Sr Gate Materials (a) Sr = 5 mol %, (b) Sr = 10 mol %, (c) Sr = 15 mol %, (d) Sr = 20 mol % and (e) Sr = 25 mol %.

From these variations, it was obvious that, drain to source current (I_{ds}) increased exponentially with increasing gate to source voltage (V_{gs}). Further, threshold voltage (V_{th}) and maximum drain current (I_{dmax}) varied with Sr content in all transfer variations. To examine the parabolic nature of transfer variation, known as I_{ds} vs. $(V_{gs} - V_{th})$ variation, m^{th} power of $(V_{gs} - V_{th})$ was studied by substituting the experimental data, such as V_{gs} , V_{th} and I_{ds} in equation (5), and m^{th} power values for different Sr content in FET with PbTiO₃ : Sr gate materials could be obtained.

$$I_{ds} = K. (V_{gs} - V_{th})^m \tag{5}$$

where I_{ds} = drain to source current

K = constant

V_{gs} = gate to source voltage, and

V_{th} = threshold voltage

To examine the transconductance value of fabricated FET, $I_{ds}^{(1/m)}$ vs. V_{gs} variations were plotted and shown in figure 5 (a ~ e). From these variations, it was noticed that, $I_{ds}^{(1/m)}$ was linearly enhanced with increasing gate to source voltage (V_{gs}). The transconductance value (g_m) value was examined by the equation.

$$g_m = \frac{\delta I_d}{\delta V_{gs}} \tag{6}$$

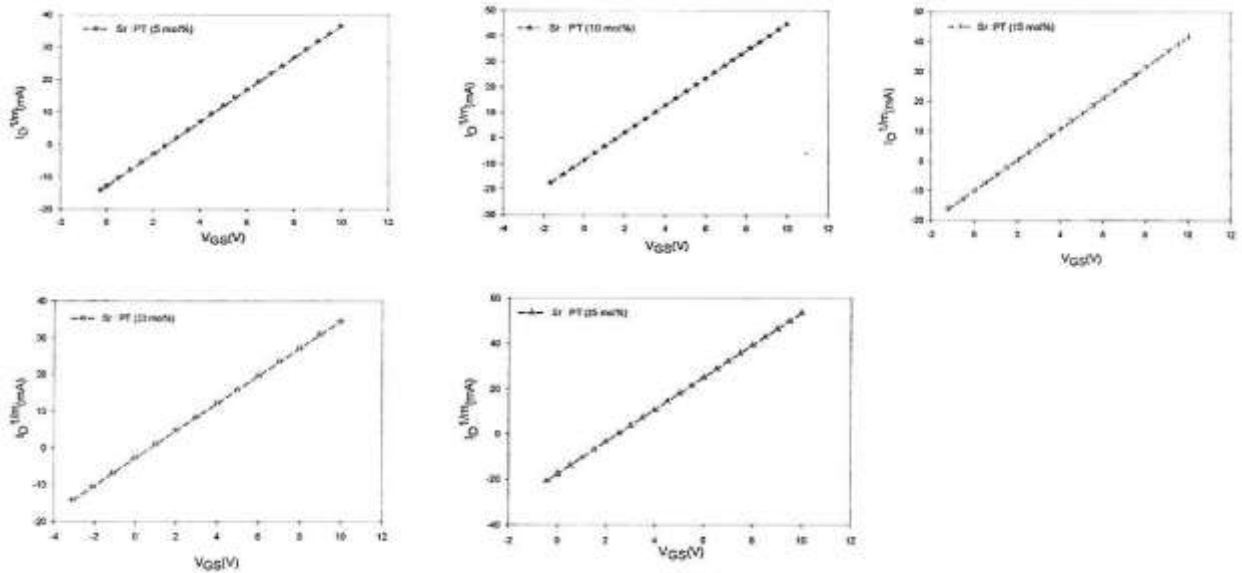


Figure 4 Transconductance Variations of FET with PbTiO₃ : Sr Gate Materials (a) Sr = 5 mol %, (b) Sr = 10 mol %, (c) Sr =15 mol %, (d) Sr = 20 mol % and (e) Sr = 25 mol %.

Threshold voltage (V_{th}), maximum drain current (I_{dmax}), m^{th} power and transconductance value (g_m) at different Sr content in fabricated FET with PbTiO₃: Sr gate materials were collected and listed in table (3).

Table 3 List of Threshold Voltage, Maximum Drain Current, m^{th} Power and Transconductance Value at Different Sr Content in Fabricated FET.

Sr Content mol (%)	V_{th} (V)	I_{dmax} (mA)	g_m (mS)	m^{th} power
5	3.46	192.65	4.87	2.05
10	2.84	191.18	6.61	1.94
15	2.82	190.48	10.36	2.07
20	2.74	190.13	5.28	2.09
25	2.72	190.00	3.81	1.98

3.3 Ferroelectric Studies

Ferroelectricity or non - volatility of prepared FET with PbTiO₃: Sr gate materials, was characterized by using Sawyer - Tower circuit, by means of its electric polarization vs. electric field characteristic, as depicted in figure 5 (a ~ b).

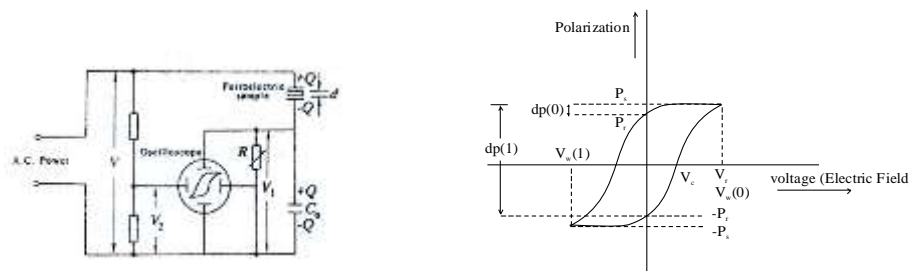


Figure. 5 (a) Sawyer - Tower Circuit (b) Estimation of Ferroelectric Parameters P_s , P_r and E_c .

Ferroelectric hysteresis loops were displayed in figure 6 (a ~ e). From these variations, it was noticed that, $I_{ds}^{(1/m)}$ was linearly enhanced with increasing gate to source voltage (V_{gs}). The transconductance value (g_m) value was examined by the equation.

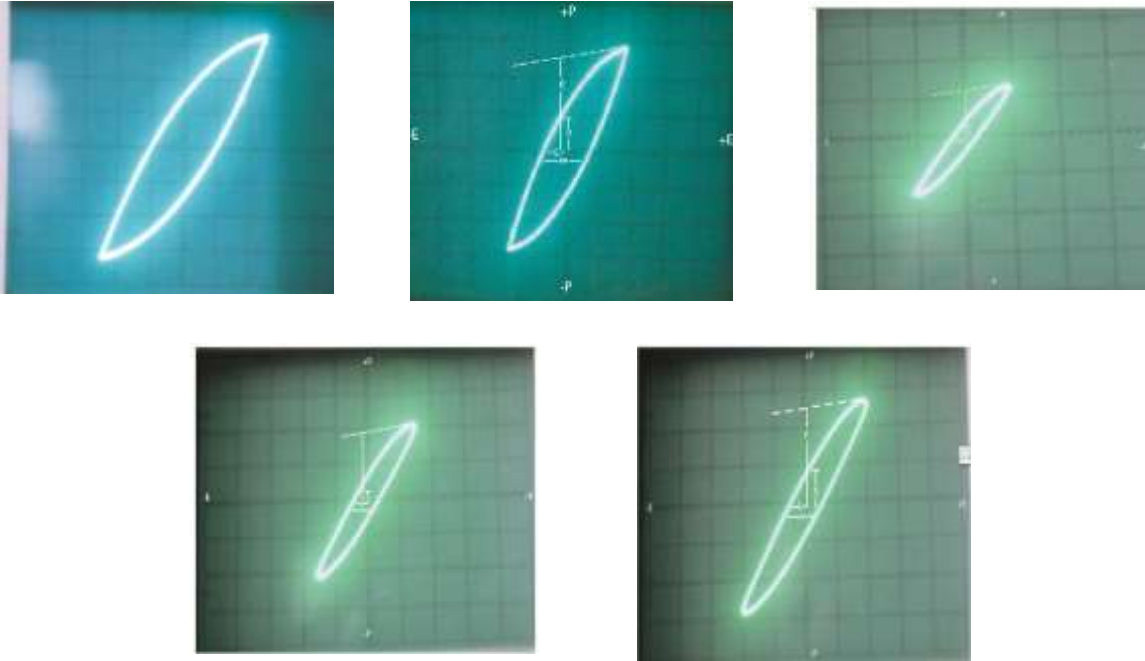


Figure 6 Ferroelectric Hysteresis Loops of $PbTiO_3 : Sr$ Gate Materials (a) $Sr = 5$ mol %, (b) $Sr = 10$ mol %, (c) $Sr = 15$ mol %, (d) $Sr = 20$ mol % and (e) $Sr = 25$ mol %.

Ferroelectric Parameters were listed in table (4).

Table (4) Ferroelectric properties P_s , P_r and E_c of prepared FET with $PbTiO_3 : Sr$ gate materials.

Ba Content (%)	Spontaneous polarization $P_s(\mu C-cm^{-2})$	Remanent polarization $P_r(\mu C-cm^{-2})$	Coercive field $E_c (kV cm^{-1})$
5	11.4	2.4	3.6
10	11.6	2.6	3.9
15	11.9	2.8	4.1
20	12.2	3.1	4.3
25	12.6	3.4	4.6

It was obvious that, ferroelectric properties, such as P_s , P_r and E_c increased when the Sr dopant concentration was raised in prepared FET with $PbTiO_3 : Sr$ gate materials. It might be due to strengthening of second - order hybridization, caused by isovalent Sr^{2+} ions in $PbTiO_3$ lattice [Cohen R. E. and Krakauer H., 1992 : Turik A. V. and Khasabov A. G., 2000]. According to the experimental data, it is expected that our fabricated FET with $PbTiO_3 : Sr$ gate materials are suitable for ferroelectric field effect transistor (1 T) application.

Conclusion

Colloidal precursor solution derived FETs with ferroelectric PbTiO₃: Sr gate materials with different Sr content, are studied by means of its structural features, FET behavior and ferroelectric properties. XRD results reveal that, there are small variations of lattice dimensions with Sr contents, due to doping mechanism and large lattice mismatch between SiO₂/Si structures and PbTiO₃: Sr films. However, there are no considerable change of tetragonal phase, perovskite - type PbTiO₃ structure after Sr dopings. FET results can be interpreted as our fabricated FETs exhibit enhancement mode operation and normally off nature, known as n - channel enhancement - mode MOSFET behavior. Ferroelectric properties of our fabricated FET indicate that, ferroelectric parameters, such as P_s, P_r and E_c increase as Sr dopant increases in our fabricated FET. It may be due to strengthening of second - order hybridization, caused by isovalent Sr²⁺ ions in PbTiO₃ : Sr gate materials. It can be concluded that, our fabricate FETs with ferroelectric PbTiO₃ : Sr gate materials are suitable for one transistor (1 T) in ferroelectric random access memory (FeRAM) applications.

Acknowledgements

This research project is fully supported by Department of Education and Planning, Ministry of Border Affairs, Union of Myanmar. The authors thank to Universities ' Research Center (URC), University of Yangon for XRD examinations. Special thanks are due to U Htein Lin, Principal, Nationalities Youth Resource Development Degree College (NRDC - Yangon), for his enthusiastic support in this study. Thanks are also due to all faculty members in Department of Physics, Nationalities Youth Resource Development Degree College (Yangon), for various assistances.

References

- Bhatti H. S., et al., (2016): "Synthesis and Induced Multi - Ferroelectricity of Perovskite PbTiO₃: A Review", Applied Surface Science, Vol 357, pp 291 - 306.
- Cohen R. E. and Krakauer H., (1992): " Electronic Structure Studies of the Differences in Ferroelectric Behavior of BaTiO₃ and PbTiO₃ ", Ferroelectrics, Vol 138 (1), pp 737 - 738.
- Gene H. H., (1999): " Ferroelectric Ceramics: History and Tehgnology ", Journal of American Ceramic Society, Vol 82 (4), pp 797 - 818.
- Ishikawa H., (2001): "Current Status and Prospect of FET Type Ferroelectric Memory", Journal of Semiconductor Science and Technology, Vol 1, pp 1 - 14.
- Ishikawa H., (2012): "FeFET and Ferroelectric Random Access Memory", Journal of Nanoscience and Nanotechnology, Vol 12, pp 7619 - 7627.
- Jian M. and Katiyar R. S. (2002): " Synthesis and Characterization of Lead Strontium Titanate Thin Films Prepared by Sol - Gel Technique ", Materials Letters, Vol 56, pp 692 - 697.
- Kim J. Y., et al., (2021): " Ferroelectric Field Effect Transistors: Progress and Perspective ", Applied Physics Letters Materials, Vol 9, 022102.
- Mesquita W. D. et al., (2022): " Theoretical Studies of the Structural Properties of the Lead Titanate Doped with Storntium", Orbital Electronic Journal of Chemistry Vol 11, pp 91 - 96.
- Mikolajick T., et al., (2018): "Ferroelectric Hafnium Oxide for Ferroelectric Random Access Memories and Ferroelectric Field Effect Transistors", Materials Research Society Bulletin, Vol 43, pp 340 - 346.
- Miller L. S. and McWhorter P. J., (1992): " Physics of Ferroelectric Field Effect Transisto ", Journal of Applied Physics, Vol 72, pp 5999 - 6010.
- Pontes F. M., et al., (2003): " Structural Phase Evolution of Strontium Doped Lead Titanate Thin Films Prepared by Soft Chemical Technique ", Journal of Materials Research, Vol 18 (3), pp 659 - 663.
- Prartikhda Devi et al., (2012): " Effect of Sr on Structural and Dielectric Properties of Lead Lathanum Zirconate Titanate Perovskite Ceramics ", International Journal of Education Planning and Administration ", Vol 2 (2), pp 97 - 108.
- Sakai S., (2006): "Gate Materials and Fabrication Process of Metal - Ferroelectrics - Insulator Memory with Long Data Retention", Advances in Science and Technology, Vol 45, pp 2382 - 2391.
- Turik A.V. and Khasabov A. G., (2000): " Origin of Ferroelectricity in PbTiO₃ ", Ferroelectrics, Vol 237 (1), pp 65 - 71.
- Wang D.G., et al., (2008): "Lead Based Titanate Thin Films Fabricated by Sol - Gel Technique", Applied Surface Science, Vol 255, pp 1637 - 1645.

INVESTIGATION ON ENERGY LEVELS OF BOTTOMONIUM

Yin Min Thant¹, Aye Thandar Htay²

Abstract

Energy levels of the bottomonium are determined by solving Schrödinger equation with Numerov method. In this paper, we solved the non-relativistic Schrödinger equation theoretically with screened potential that includes spin dependent terms in the potential. It was used to predict the bottomonium η_b 's (singlet S and D states), Υ 's (triplet S and D states), h_b 's (singlet P and F states) and χ 's (triplet P and F states).

Keywords: bottomonium states, Numerov's method, screened potential

Introduction

Bottomonium is the bound state of a bottom quark (b) and its anti bottom quark (\bar{b}). The bottom quark was first described theoretically in 1973 by physicists Kobayashi and Maskawa and name "bottom" was introduced in 1975 by Harari [M. Kobayashi and T. Maskawa, Prog. Theor. Phys. **49** (1973) 652, H. Harari, Phys. Lett. **B 57** (1975) 265]. The mass of bottom quark is about $4.2 \text{ GeV}/c^2$. It is four times the mass of a proton and many orders of magnitude larger than common "light" quarks such as up, down and strange. If one attempts to separate a quark-antiquark pair, the energy of the gluon field becomes larger and larger until a new quark-antiquark pair can be created. As a result, one does not end up with two isolated quarks but with new quark-antiquark pairs instead. This absolute imprisonment of quarks is called quark confinement. So, it is impossible to observe a free quark in nature. An illustrative picture depicting the quark confinement is shown in Fig. 1.

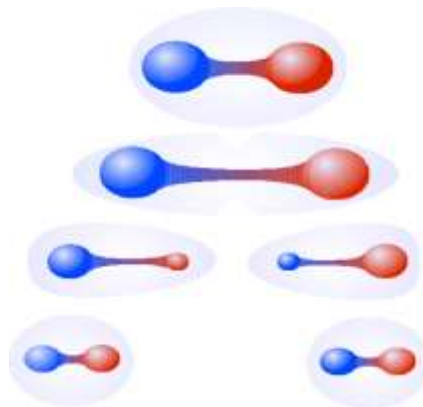


Figure 1 Quark confinement

Bottomonium States

The total spin of quark-antiquark bound state system have either spin singlet ' $S = 0$ ' or spin triplet ' $S = 1$ '. The parity and charge-conjugation eigenvalues can be written as $P = (-1)^{L+1}$ and $C = (-1)^{L+S}$ respectively. In this equation, ' L ' represents the orbital angular momentum. The notation S, P, D and F for states corresponds to $L = 0, 1, 2$ and 3 . The states of the quark-antiquark bound state system can be represented by $n^{2S+1}L_J$; J and n stand for total angular momentum of quark-antiquark bound state system and the principle quantum number $n = 1, 2, 3$ and so on. As an example, the full notation for $\Upsilon(1S)$ is 1^3S_1 .

¹ Department of Physics, University of Mandalay, Mandalay, Myanmar

² Department of Physics, Mandalay University, Mandalay, Myanmar

There are experimental observations of bottomonium states with different orbital angular momenta which are ‘upsilon (Υ)’ for triplet S-states; $\Upsilon(1S)$, $\Upsilon(2S)$, $\Upsilon(3S)$, $\Upsilon(4S)$, $\Upsilon(5S)$ and $\Upsilon(6S)$, ‘eta (η_b)’ for singlet S-states; $\eta_b(1S)$, $\eta_b(2S)$, $\eta_b(3S)$, $\eta_b(4S)$, $\eta_b(5S)$ and $\eta_b(6S)$, ‘chi (χ)’ for triplet P-states; $\chi_b(1P)$, $\chi_b(2P)$, and $\chi_b(3P)$, h_b for singlet P-states; $h_b(1P)$, $h_b(2P)$ and $h_b(3P)$, upsilon $\Upsilon(1D)$ for triplet D-state and η_{b2} for singlet D-states respectively. In other words, ‘upsilon and eta’ are defined as the principal quantum numbers (odd) for triplet and singlet states and then ‘chi and h_b ’ are assigned for even quantum numbers.

Potential Models for Interaction between Bottom and Antibottom

There are various non relativistic potential models to describe the bottomonium spectrum. Also potential models have been successful in describing the spectra below the open-flavor thresholds for both charmonia and bottomonia. However, it is well known that these potential models, which incorporates a Coulomb term at short distances and a linear confining potential at large distance. It is useful to improve the potential model itself to incorporate the screening effect and compare the model predictions with the experimental data as a phenomenological way to investigate the screening effects on heavy quarkonium spectrum [E. Eichen *et al.*, Phys. Rev. **D17** (1978) 3090, E. Eichen *et al.*, Phys. Rev. **D21** (1980) 203 and S. Godfrey *et al.*, Phys. Rev. **D** 32 (1985) 189]. In calculation of bottomonium states, a non-relativistic potential model will use with the screening effect. The potential is described as

$$V(r) = V_v(r) + V_s(r) \quad (1)$$

where,

$$V_v(r) = -\frac{4}{3} \frac{\alpha_c}{r}, \quad (2)$$

$$V_s(r) = \frac{b(1 - e^{-\mu r})}{\mu}. \quad (3)$$

Here, $V_v(r)$ represents the vector-like one-gluon exchange potential, α_c is the coefficient of the Coulomb potential and μ is the screening factor which makes the long-range scalar potential of $V_s(r)$ behave like “ br ” when $r \ll \frac{1}{\mu}$, and become a constant b/μ when $r \gg \frac{1}{\mu}$. The main effect of the screened potential on the spectrum is that the masses of the higher excited states are lowered. Vector potential $V_v(r)$, scalar potential $V_s(r)$, and vector potential $V_v(r)$ plus scalar potential $V_s(r)$ are shown in Fig. 2, 3 and 4 respectively. The screening effect is very important to describe the higher excited states. In calculation, spin-dependent potentials include as follows:

(i) the spin-spin contact hyperfine potential

$$H_{SS} = \frac{32\pi\alpha_c}{9m_b^2} \left(\frac{\sigma}{\sqrt{\pi}}\right)^3 e^{-\sigma^2 r^2} \vec{S}_b \cdot \vec{S}_{\bar{b}} \quad (4)$$

where \vec{S}_b and $\vec{S}_{\bar{b}}$ are spin matrices acting on the spins of the quark and antiquark.

In the $|^{2S+1}L_J\rangle$ basis, the matrix element for the spin-spin operator $\vec{S}_b \cdot \vec{S}_{\bar{b}}$ is

$$\langle \vec{S}_b \cdot \vec{S}_{\bar{b}} \rangle = \frac{1}{2} S(S+1) - \frac{3}{4}. \quad (5)$$

(ii) the spin-orbit term,

$$H_{SL} = \frac{1}{2m_b^2 r} \left(3 \frac{dV_v}{dr} - \frac{dV_s}{dr} \right) \vec{L} \cdot \vec{S} \tag{6}$$

$$= \frac{1}{2m_b^2 r} \left(4 \frac{\alpha_c}{r^2} - b e^{-\mu r} \right) \vec{L} \cdot \vec{S} \tag{7}$$

The matrix element of the spin-orbit operator is

$$\langle \vec{L} \cdot \vec{S} \rangle = \frac{1}{2} [J(J + 1) - L(L + 1) - S(S + 1)], \tag{8}$$

where, L is the orbital angular momentum quantum number, S is the spin quantum number and $J = L \pm S$ is the total angular momentum quantum number. [W. Deng, *etal.*, Phys. Rev. **D95** (2017) 074002]

(iii) the tensor term,

$$H_T = \frac{1}{12m_b^2} \left(\frac{1}{r} \frac{dV_v}{dr} - \frac{d^2V_v}{dr^2} \right) \vec{S}_T. \tag{9}$$

The element of the tensor operator S_T is

$$S_T = 4 \langle \vec{S}^2 \vec{L}^2 - \frac{3}{2} \vec{L} \cdot \vec{S} - 3(\vec{L} \cdot \vec{S})^2 \rangle. \tag{10}$$

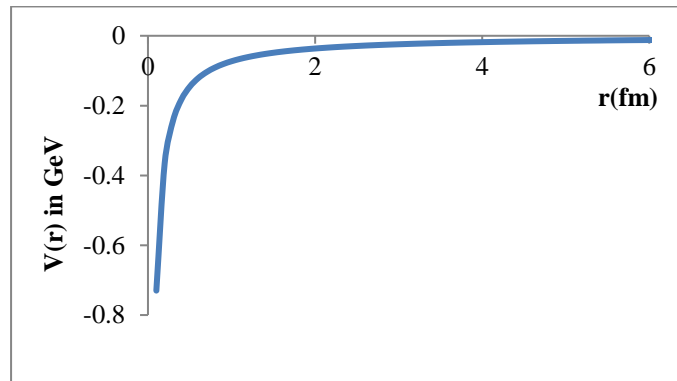


Figure 2 Vector potential $V_v(r)$ in GeV with the distance r in fm

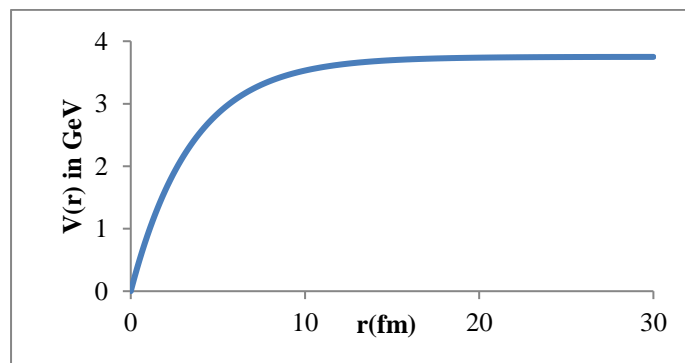


Figure 3 Scalar potential $V_s(r)$ in GeV with the distance r in fm

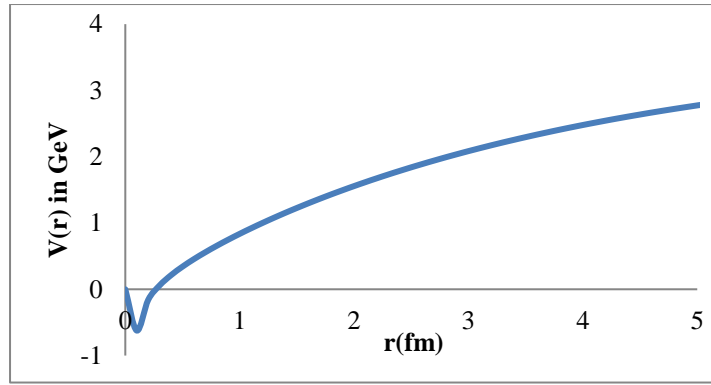


Figure 4 Vector potential $V_V(r)$ plus scalar potential $V_S(r)$

Energy Levels of Bottomonium

Energy levels of the bottomonium are determined by solving Schrödinger equation with Numerov method. To obtain energy (masses) and wave functions of the bottomonium states, this radial equation need to solve.

$$\frac{d^2u(r)}{dr^2} + \frac{2\mu}{\hbar^2} \left[E - V_{b\bar{b}}(r) - \frac{\hbar^2 \ell(\ell+1)}{2\mu r^2} \right] u(r) = 0 \quad (11)$$

where,

$$\mu = \frac{m_b m_{\bar{b}}}{m_b + m_{\bar{b}}} \quad (12)$$

μ is the reduced mass of the system and E is the binding energy of the system. Then, the mass of a $b\bar{b}$ state is obtained by $M_{b\bar{b}} = 2m_b + E$. In this calculation, screened potential model with spin-spin term, spin-orbit term and tensor term described as the following equation,

$$V_{b\bar{b}}(r) = V(r) + H_{SS} + H_{SL} + H_T. \quad (13)$$

Therefore, our potential form is

$$V_{b\bar{b}}(r) = -\frac{4\alpha_c}{3r} + \frac{b(1 - e^{-\mu r})}{\mu} + \frac{32\pi\alpha_c}{9m_b^2} \left(\frac{\sigma}{\sqrt{\pi}} \right)^3 e^{-\sigma^2 r^2} \vec{S}_b \cdot \vec{S}_{\bar{b}} \\ + \frac{1}{2m_b^2 r} \left(4\frac{\alpha_c}{r^2} - b e^{-\mu r} \right) \vec{L} \cdot \vec{S} + \frac{1}{12m_b^2} \left(\frac{1}{r} \frac{dV_V}{dr} - \frac{d^2V_V}{dr^2} \right) \vec{S}_T. \quad (14)$$

We calculated energy eigenvalues and the corresponding eigenfunctions by using numerical Numerov method in FORTRAN programming.

Results and Discussion

Energy Search for Bottomonium States

The Schrödinger equation has been solved with screen potential model including spin-orbit term and tensor term to obtain the energy levels of all bottomonium states. The angular momentum states S, P, D and F ($L = 0, 1, 2$ and 3) have been calculated.

Orbital Angular Momentum S (L = 0) States

Orbital angular momentum $L = 0$ states with spin singlet and triplet states are calculated by solving the Schrödinger equation with Numerov (Difference) numerical method. Our calculated masses of S-states are in good agreement with those found in literatures. The corresponding reduced radial wavefunction of bottomonium singlet and triplet states (5S, 6S) are expressed in Fig. 5 and 6. The comparison between the experimental data and our calculated masses of bottomonium for S states is shown in Table (1).

Higher Orbital Angular Momentum States (L =1, 2 and 3)

In this section, we explain the calculation of higher angular momentum states P, D and F which are $L = 1, 2$ and 3 by using the same procedure as that of S state calculation. We calculated the energy eigenvalues and eigenfunctions of higher orbital angular momentum states for principle quantum numbers $n = 1, 2$ and 3 .

For these states the spin-orbit term is to be included and the term $1/r^3$ appears in the potential. Accordingly, when $r \rightarrow 0$ the wavefunction near the origin does not obey the relation $u(r \rightarrow 0) \propto r^{L+1}$. In order to overcome this problem, it is assumed that in a small range $r \in (0, r_c)$, the $V_{b\bar{b}}(r) \propto 1 / (r_c)^3$, which is a finite constant where r_c is a cut off distance. For the model parameters, we take $\alpha_c = 0.37$, $b = 0.210 \text{ GeV}^2$, $\mu = 0.060 \text{ GeV}$, $m_b = 4.760 \text{ GeV}$ and $\sigma = 3.10 \text{ GeV}$. In our calculation, the cutoff distance $r_c = 0.06 \text{ fm}$ is adopted. With this cutoff distance r_c , the energy levels of the higher orbital states ($L = 1, 2, 3$) are in good agreement with the experimental data and the predicted masses of bottomonium [W. Deng, *et al.*, Phys. Rev. **D95** (2017) 074002]. The comparison results are listed in Table (2) and (3). The reduced radial wavefunction of some bottomonium states are shown in Fig. 7-11. The experimental data and our calculated masses of bottomonium are shown in Fig. 13.

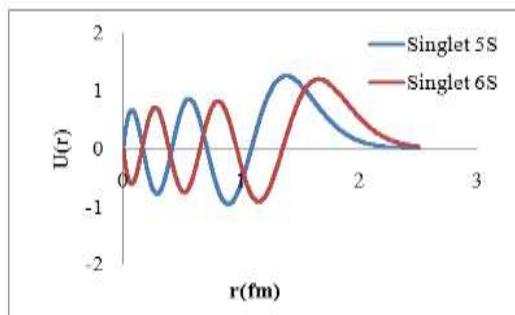


Figure 5 Reduced radial wavefunction of bottomonium for singlet 5S and 6S state

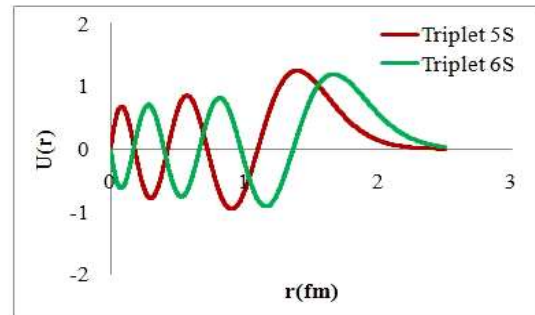


Figure 6 Reduced radial wavefunction of bottomonium for triplet 5S and 6S state

Table 1 Comparison between the experimental data [PDG], predicted values [W. Deng, *etal.*,] and our calculated masses of bottomonium for S states

$n^{2S+1}L_J$	State	J^{PC}	Bottomonium masses (MeV)		
			[PDG]	Predicted Values	Our Calculated Results
1^3S_1	$\Upsilon(1S)$	1^{--}	9460	9460	9465.52
1^1S_0	$\eta_b(1S)$	0^{++}	9398	9390	9393.59
2^3S_1	$\Upsilon(2S)$	1^{--}	10023	10015	10025.28
2^1S_0	$\eta_b(2S)$	0^{++}	9999	9990	9999.46
3^3S_1	$\Upsilon(3S)$	1^{--}	10355	10343	10354.65
3^1S_0	$\eta_b(3S)$	0^{++}		10326	10337.21
4^3S_1	$\Upsilon(4S)$	1^{--}	10579	10577	10609.26
4^1S_0	$\eta_b(4S)$	0^{++}		10584	10595.65
5^3S_1	$\Upsilon(5S)$	1^{--}	10865	10811	10822.46
5^1S_0	$\eta_b(5S)$	0^{++}		10800	10811.18
6^3S_1	$\Upsilon(6S)$	1^{--}	11020	10997	11007.88
6^1S_0	$\eta_b(6S)$	0^{++}		10988	10998.20

Table 2 Comparison between the experimental data [PDG], predicted values [W. Deng, *etal.*,] and our calculated masses of bottomonium for P states

$n^{2S+1}L_J$	State	J^{PC}	Bottomonium masses (MeV)		
			[PDG]	Predicted Values	Our Calculated Results
1^3P_2	$\chi_{b2}(1P)$	2^{++}	9912	9921	9934.50
1^3P_1	$\chi_{b1}(1P)$	1^{++}	9893	9903	9903.95
1^3P_0	$\chi_{b0}(1P)$	0^{++}	9859	9864	9883.80
1^1P_1	$h_b(1P)$	1^{+-}	9899	9909	9918.64
2^3P_2	$\chi_{b2}(2P)$	2^{++}	10269	10264	10277.84
2^3P_1	$\chi_{b1}(2P)$	1^{++}	10255	10249	10254.65
2^3P_0	$\chi_{b0}(2P)$	0^{++}	10233	10220	10239.54
2^1P_1	$h_b(2P)$	1^{+-}	10260	10254	10265.23
3^3P_2	$\chi_{b2}(3P)$	2^{++}		10528	10541.79
3^3P_1	$\chi_{b1}(3P)$	1^{++}	10516	10515	10522.23
3^3P_0	$\chi_{b0}(3P)$	0^{++}		10490	10509.60
3^1P_1	$h_b(3P)$	1^{+-}		10519	10530.86

Table 3 Comparison between the experimental data [PDG], predicted values [W. Deng, *et al.*,] and calculated masses of bottomonium for D and F states

$n^{2S+1}L_J$	State	J^{PC}	Bottomonium masses (MeV)		
			[PDG]	Predicted Values	Our Calculated Results
1^3D_3	$\Upsilon_3(1D)$	3^-		10157	10172.25
1^3D_2	$\Upsilon_2(1D)$	2^-	10164	10153	10161.68
1^3D_1	$\Upsilon_1(1D)$	1^-		10146	10153.99
1^1D_2	$\eta_{b2}(1D)$	2^{++}		10153	10165.27
2^3D_3	$\Upsilon_3(2D)$	3^-		10436	10450.98
2^3D_2	$\Upsilon_2(2D)$	2^-		10432	10441.71
2^3D_1	$\Upsilon_1(2D)$	1^-		10425	10434.87
2^1D_2	$\eta_{b2}(2D)$	2^{++}		10432	10444.84
1^1F_3	$h_{b3}(1F)$	3^{++}		10339	10352.07
1^3F_4	$\chi_{b4}(1F)$	4^{++}		10340	10356.45
1^3F_3	$\chi_{b3}(1F)$	3^{++}		10340	10350.58
1^3F_2	$\chi_{b2}(1F)$	2^{++}		10338	10346.00

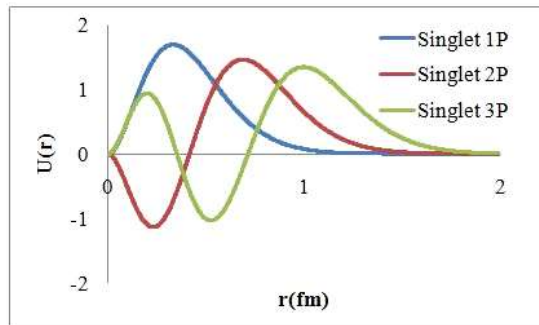


Figure 7 Reduced radial wavefunction of bottomonium for singlet 1P, 2P and 3P states

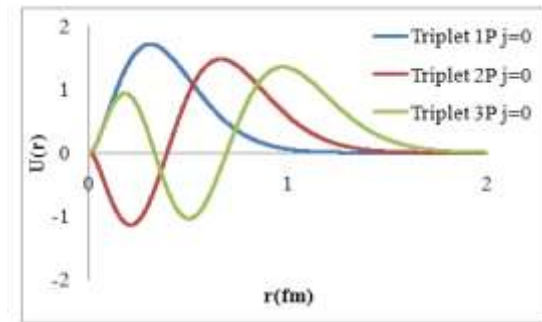


Figure 8 Reduced radial wavefunction of bottomonium for triplet 1P, 2P and 3P(j = 0) states

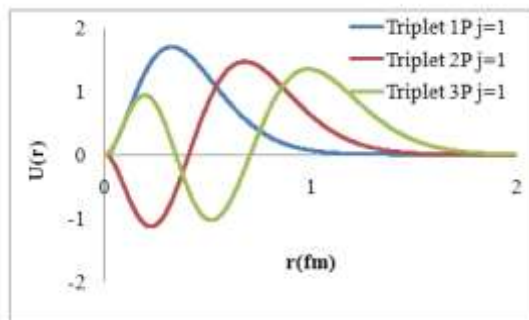


Figure 9 Reduced radial wavefunction of bottomonium for singlet 1P, 2P and 3P (j = 1) states

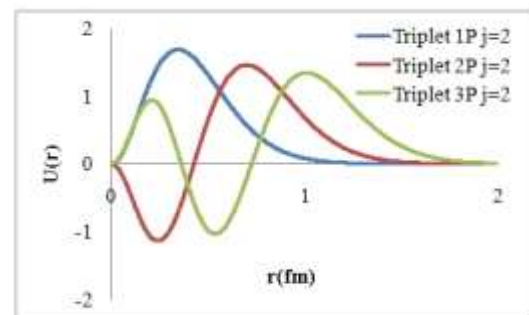


Figure 10 Reduced radial wavefunction of bottomonium for triplet 1P, 2P and 3P(j = 2) states

Conclusion

The masses of bottomonium states have been calculated in the non-relativistic screened potential model. Although the mass differences between the experimental data and our calculated values are 1 - 5 MeV for 1S, 2S and 3S states, 10 - 25 MeV for 1P state and 1 - 8 MeV for 2P, 3P and 1D states, our results for the bottomonium spectrum are in good agreement with the experimental data and the predicted values [K. A. Olive *et al.*, Particle Data Group Collaboration, Review of Particle Physics, Chin. Phys. **C 38**, (2014) and W. Deng, *et al.*, Phys. Rev. **D95** (2017) 074002]. Therefore, our calculated results would be reasonable for determining the energy levels of bottomonium.

Acknowledgements

We would like to express our deep gratitude to Dr Khin Swe Myint, Rector (Retired), University of Mandalay for her supervision and valuable suggestions to complete the whole work. We would like to thank Professor Dr Nyein Wint Lwin, Professor and Head, Department of Physics, University of Mandalay for her kind permission to carry out this research paper.

References

- E. Eichen *et al.*, Phys. Rev. **D17** (1978) 3090.
- E. Eichen *et al.*, Phys. Rev. **D21** (1980) 203.
- H. Harari, Phys. Lett. **B 57** (1975) 265.
- K. A. Olive *et al.*, [Particle Data Group Collaboration], Review of Particle Physics, Chin. Phys. **C 38**, (2014).
- M. Kobayashi and T. Maskawa, Prog. Theor. Phys. **49** (1973) 652.
- S. Godfrey *et al.*, Phys. Rev. **D 32** (1985) 189.
- W. Deng, *et al.*, Phys. Rev. **D95** (2017) 074002.

INVESTIGATION ON ELECTROCHEMICAL PROPERTIES OF ELECTROCHROMIC TUNGSTEN TRIOXIDE THIN FILMS

Mono Zaw¹, Kyaw Kyaw², Nyein Wint Lwin³, Than Zaw Oo⁴

Abstract

Electrochemical properties of electrochromic (EC) tungsten trioxide (WO₃) thin films on the fluorine doped tin oxide (FTO) coated glass substrates have been studied. Different molar concentrations of WO₃ precursor solution were sprayed on FTO glass substrates to synthesize amorphous and crystalline phase tungsten trioxide thin films by conducting different annealing temperature. From the different WO₃ precursor concentrations, 0.05 M enabled to increase current densities of WO₃ film. The present study indicated that the optimum processing condition of annealing temperature 400 °C and WO₃ precursor concentration 0.05 M would produce the WO₃ film with higher electrochemical current densities which is attributed to a higher crystallinity and lower band gap energy. In examining the electrochromic performance of WO₃ film, its color is blue upon coloring and colorless upon bleaching and the coloration efficiency is 1.89 cm²C⁻¹ in KI and 2.01 cm²C⁻¹ in KCl electrolytes. The color change would be associated with the intercalation (deintercalation) of K⁺ ions. The diffusion of ions in the insertion/ extraction process thus play a role. The diffusion coefficient of WO₃ film is observed to be quite high and is in the range of 1.1 – 1.4 × 10⁻¹² cm²s⁻¹ in both KI and KCl electrolytes. The higher electrochemical activity renders it as promising material for smart windows and energy saving applications.

Keywords: Tungsten trioxide film, Electrochromic behaviors, Smart Window

Introduction

Tungsten trioxide (WO₃) is the most studied among the electrochromic materials and exhibits an n-type semiconducting behavior with a band gap energy of 2.5-3.3 eV. [Jayachandran M. *et al.*]. Specifically, it is a cathodic electrochromic material used as a working electrode in electrochromic devices. It is a transition metal oxide with excellent chemical and thermal stability. It has promising electrochromic properties such as high coloration efficiency and fast switching response. It is used as a functional layer in the applications of gas sensors, solar cells and electrochromic devices such as smart windows can meet the market demand of energy-saving devices. There are various choices for preparing WO₃ films with the development of thin film technology. These include sputtering, chemical vapor deposition, spray pyrolysis, evaporation, sol-gel and laser ablation deposition. Among these, spray pyrolysis method is the most cost-effective for producing large-area films, and enables a better control over the film growth and hence more homogenous and more transparent films are yielded [M.F. Daniel *et al.*, (1987)].

Materials and Methods

Preparation of Tungsten trioxide (WO₃) thin films

Tungsten trioxide (WO₃) film was prepared using spray pyrolysis method to be used as electrochromic layer in the electrochromic device. Electrochromic devices (ECDs) are normally composed of five layers as shown in Figure 1. Tungsten trioxide (WO₃) powder (0.03 M, 0.05 M and 0.07 M) was dissolved in 50 ml of ammonia at 80 °C under continuous stirring for 30 min to form tungsten trioxide (WO₃) precursor solution. The obtained WO₃ solution was diluted with 10 ml of deionized water and then cooled down to room temperature and filtered. After that, the

¹ Department of Physics, University of Mandalay, Mandalay, Myanmar

² Department of Physics, University of Mandalay, Mandalay, Myanmar

³ Department of Physics, University of Mandalay, Mandalay, Myanmar

⁴ Department of Higher Education, Ministry of Education, Myanmar

final WO_3 solution was sprayed on the FTO substrate (substrate temperature is $300\text{ }^\circ\text{C}$) by using spray pyrolysis method to obtain WO_3 films. The resulting WO_3 films with the varying concentration of (0.03 M, 0.05 M and 0.07 M) were annealed at $400\text{ }^\circ\text{C}$ for 1 h.

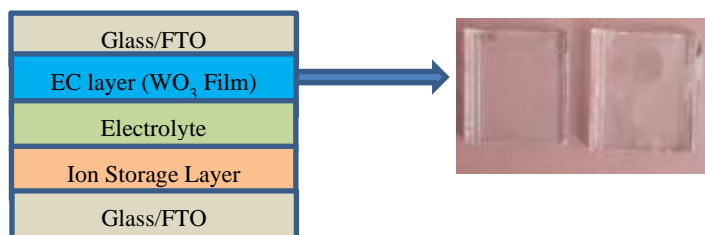


Figure 1 Basic design of electrochromic device

Characterization of WO_3 Films

The structural properties of WO_3 films were investigated X-ray diffractometer (RIGAKU Multiflex (Japan)). The optical properties of WO_3 films were performed using UV-vis spectrophotometry (Genesys 10S). The electrochemical properties of WO_3 films were characterized by cyclic voltammetry. (Electrochemical Workstation- CorrTest CS350). Taking the optimum WO_3 films (annealing temperature $400\text{ }^\circ\text{C}$, 0.05 M) the coloration efficiency of WO_3 films with different electrolyte (KI & KCl) were measured. Cyclic voltammetry was used to obtain the electrochemical properties of the WO_3 films under oxidation state. During coloration the WO_3 film becomes blue color and turns into colorless during the bleaching. The transmission of the samples at colored state and bleached state was measured by UV-vis spectrophotometry.

Results and Discussion

Crystalline Structure of WO_3 Films

XRD profiles of WO_3 films annealed at different temperatures are depicted in Figure 2. From the XRD measurement, WO_3 films annealed at $300\text{ }^\circ\text{C}$ shows amorphous nature. At the elevated temperatures $400\text{ }^\circ\text{C}$ and $500\text{ }^\circ\text{C}$, WO_3 films reveal the orthorhombic structure. The main diffraction peak positions of WO_3 films for $400\text{ }^\circ\text{C}$ and $500\text{ }^\circ\text{C}$ are observed at 2θ angle of 22° , 23° , 24° and 34° with the corresponding plane of (020), (002), (200) and (220). The main diffraction peak intensity of WO_3 films annealed at $400\text{ }^\circ\text{C}$ shows the stronger peak intensity. It may be due to the formation of better crystallinity. At the annealing temperature $500\text{ }^\circ\text{C}$, the main diffraction peak positions WO_3 films are still the same but the width of the diffraction peak position and intensity are slightly broad and declined.

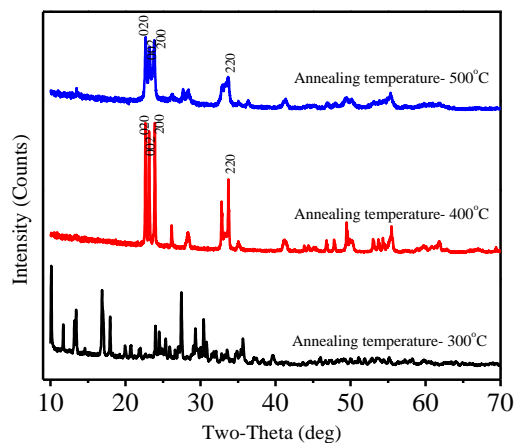


Figure 2 XRD profiles of WO_3 films with varying annealing temperatures

Optical Transmission and Band Gap Energy of WO₃ Films

Figure 3 (a) shows the optical transmission spectra of WO₃ films for all WO₃ precursor concentrations. As can be seen in Figure 3 (a), the values of the optical transmission of WO₃ films decreased from 80% to 65% upon increasing WO₃ precursor concentrations. It may be due to the higher content of WO₃ precursor and thicker film formation. Figure 3 (b) shows the plot of $(\alpha hv)^{1/2}$ versus hv graph. The optical band gap energy of WO₃ films was determined from Tauc's plot equation, $(\alpha hv)^n = A (hv - E_g)$, where α is absorption coefficient, hv is incident light energy, and E_g is the band gap of the material. The exponent 'n' indicates the transition type of the material. The value of n is 1/2 for indirect transition and 2 for direct transition. The value of the optical band gap energy of WO₃ films was obtained by extrapolating the linear portion of the curve to photon energy axis. The optical band gap energy of WO₃ films decreased from 3.3 eV to 2.8 eV when the WO₃ precursor increased from 0.03 M to 0.07 M. The decreasing trend of optical transmission and band gap energy was observed upon increasing WO₃ precursor concentrations. The band gap energy depends on the materials preparation conditions.

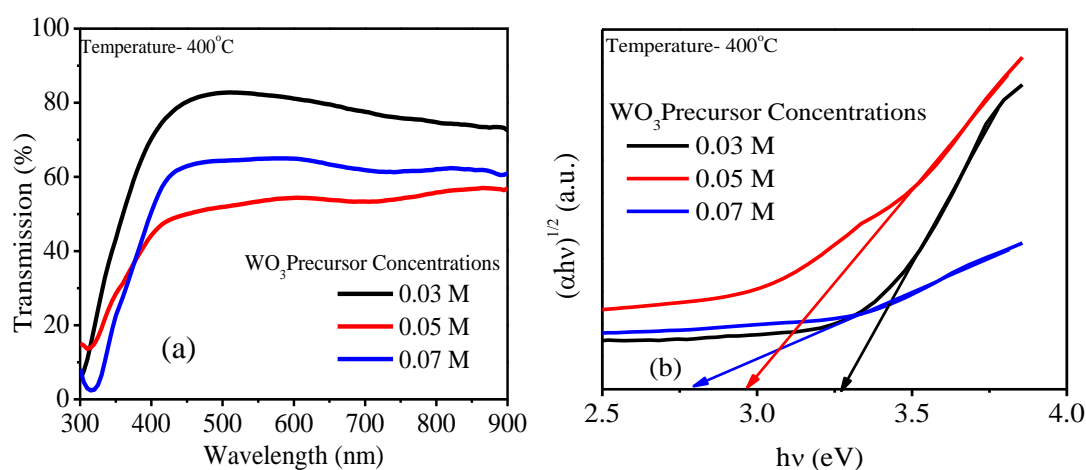


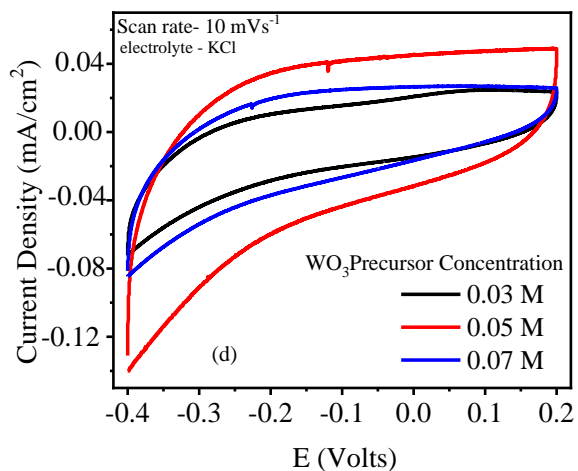
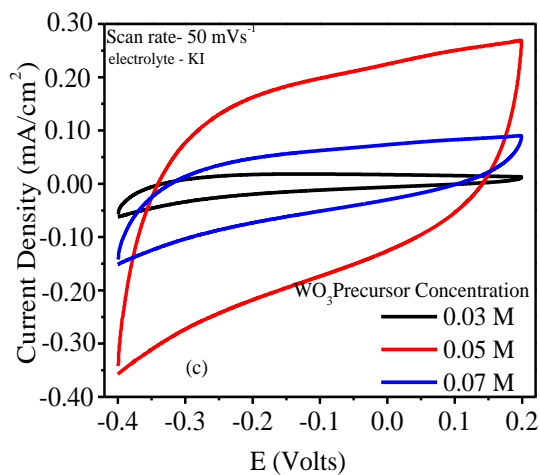
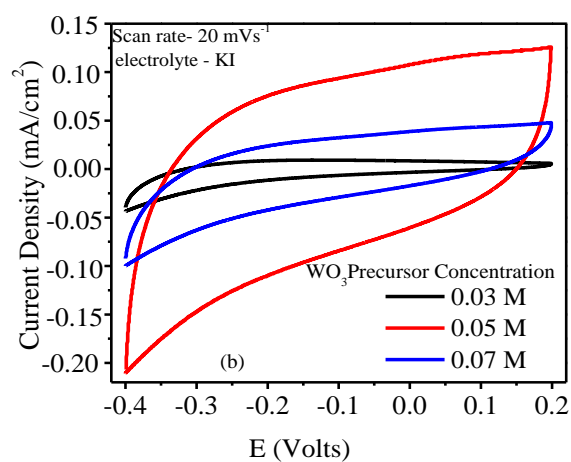
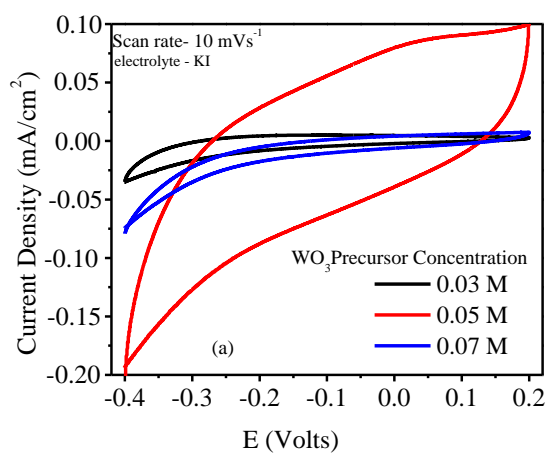
Figure 3 (a) Optical transmission spectra and (b) Plot of $(\alpha hv)^{1/2}$ versus hv of WO₃ films prepared from different WO₃ precursor concentrations

Electrochemical Properties of WO₃ Films

The electrochromic behavior of WO₃ films was tested by cyclic voltammetry (CV) for different WO₃ precursor concentrations. Figure 4 (a-f) shows the CV graph of WO₃ films prepared from various WO₃ precursor concentrations in KI and KCl electrolyte for each scan rate. The cyclic voltammograms of WO₃ films were recorded in the potential range from -0.4 V to +0.2 V for each scan rate. From the CV measurement, the values of the anodic peak current densities of WO₃ films are extracted. The obtained values of the anodic peak current density of WO₃ films are listed in Table 1. The highest anodic peak current density of WO₃ films was observed at 0.05 M for each scan rate. The highest anodic peak current density of WO₃ films was observed at WO₃ precursor concentration of 0.05 M. The values of the anodic peak current density of WO₃ films with different WO₃ precursor concentrations are varied upon changing electrolyte. It would be related to the surface roughness of the WO₃ films. Since, the ion insertion/extraction reaction depends on the number of reaction sites on the surface.

Table 1 The value of anodic peak current densities of WO₃ films with varying WO₃ precursor concentrations in KI & KCl electrolyte

Scan Rate (mV/s)	WO ₃ precursor concentrations	Potential (V)	Anodic Peak Current Density (mA/cm ²) KI electrolyte	Anodic Peak Current Density (mA/cm ²) KCl electrolyte
10	0.03 M	0.08	0.01	0.02
	0.05M	0.08	0.09	0.05
	0.07 M	0.08	0.01	0.03
20	0.03 M	0.08	0.01	0.03
	0.05M	0.08	0.12	0.10
	0.07 M	0.08	0.03	0.05
50	0.03 M	0.08	0.01	0.07
	0.05M	0.08	0.24	0.21
	0.07 M	0.08	0.09	0.12



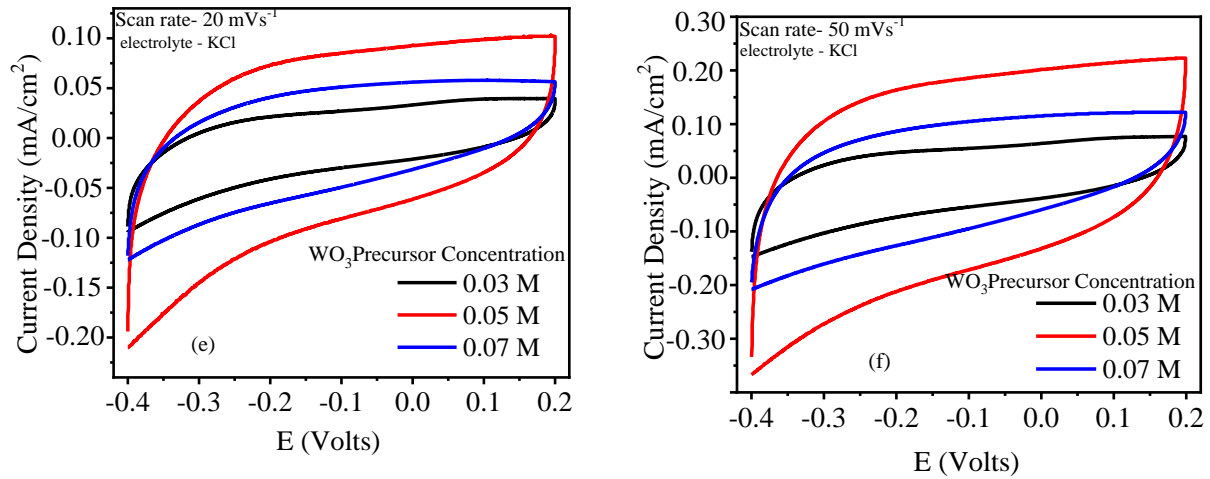


Figure 4 (a–f) Cyclic voltammogram of WO₃ films varying WO₃ precursor concentrations (0.03 M, 0.05 M and 0.07 M) in KI & KCl electrolytes

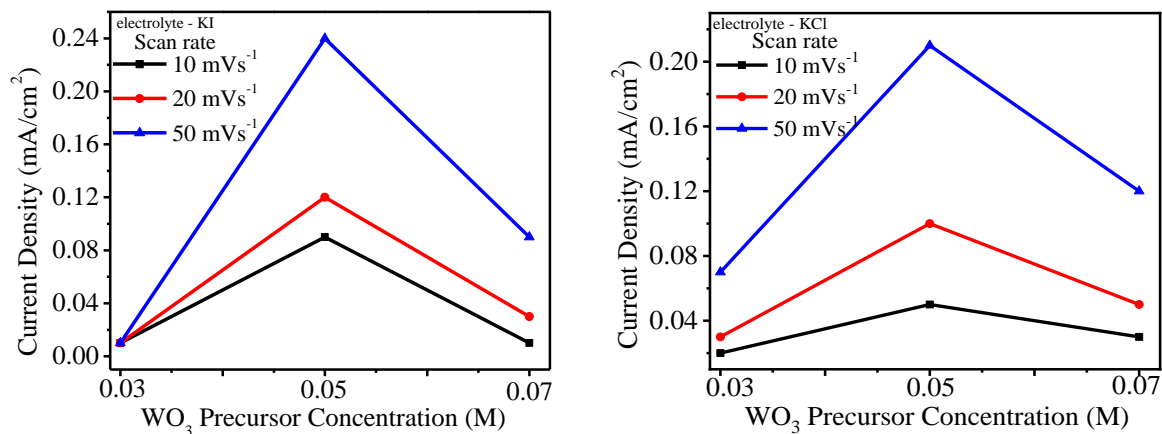


Figure 5 Plot of current density (mA/cm²) vs WO₃ precursor concentration (M) in KI and KCl electrolyte

Coloration efficiency and Diffusion coefficient of WO₃ Films

The electrochromic behaviors specially coloration efficiency of WO₃ films in KI and KCl electrolyte were studied. Cyclic voltammetry was used to obtain the electrochemical properties of the WO₃ films under oxidation state. The value of peak current density gave a rough estimation of electrochromical activity of the working electrode. The main parameter that will be determined from the cyclic voltammetry was the current peak *I_p*, which depends strongly on the diffusion coefficient. Anodic peak refers here to the current peak caused by insertion of K⁺ ions into the WO₃ films, while the cathodic peak refers to exertion of K⁺ ions. The WO₃ films have electrochromic properties, which is associated with the electrochemical intercalation and de-intercalation of K⁺ ions and electrons into the WO₃ film. The experiments were recorded for different scan rates like 10 mVs⁻¹, 20 mVs⁻¹ and 50 mVs⁻¹ in the KI and KCl electrolyte. During coloration the WO₃ film becomes blue color and turns into colorless during the bleaching. The diffusion coefficients of K⁺ ions during intercalation and de-intercalation can be calculated by employing the Randles-Servick equation [P.R.Patil *et al.*, (2004) “Preparation and Characterization of Spray Deposited n-type WO₃ thin Films for Electrochromic Devices” Materials Research Bulletin, United States, vol.39, pp.1479-1489].

$$i_p = 2.72 \times 10^5 n^{3/2} D^{1/2} C v^{1/2} \tag{1}$$

where D is the diffusion coefficient of K⁺ ions; v, scan rate; C, concentration of electrolyte solution; n, number of electrons and it is assumed to be 1 and *i_p* is the peak current density. Figure 4 (a-f)

show the CV curves recorded for WO₃ films (0.05 M, 400°C) with different scan rate in potassium iodide (KI) and potassium chloride (KCl) electrolytes. Table 2 shows the various electrochemical parameters: the scan rate and diffusion coefficient extracted from Figure 6 (a-c). In the present work, the calculated diffusion coefficient is $(1.08 - 1.35) \times 10^{-12} \text{ cm}^2\text{s}^{-1}$ in KI electrolyte and $(1.09 - 1.38) \times 10^{-12} \text{ cm}^2\text{s}^{-1}$ in KCl electrolyte. Diffusion coefficient values for the K⁺ ion process using different concentrations of KI, KCl electrolyte were of the order of $(1.35 - 3.10) \times 10^{-12} \text{ cm}^2\text{s}^{-1}$ for spray pyrolyzed. From the electrochemical analysis it is observed that the films have changed their colors in accordance with the applied potential. Also the films have the capability to withstand in the electrolyte throughout the entire scan rates; it confirms the better reversibility of the films in the electrochromic process. The electrolyte content and the porosity play a great role in the diffusion coefficient by increasing the diffusion coefficient value with the K⁺ ions. From this, WO₃ films prepared in the present work would be suitable for development of low cost electrochromic cells.

Figure 7 shows the UV-Vis spectra of the WO₃ films at colored and bleached state upon being subjected to -0.4 and 0.2 V in KI and KCl solution for 240 s. As shown in Figure 7, both films show a high transmittance which is as high as 80% at positive voltage. When applied to a negative voltage, a significant absorbance in the wavelength ranging from 550 nm to near IR region caused by the K⁺ intercalation is observed. Both films turned from blue at colored state to colorless at bleached states as the voltage switched from negative to positive. The coloration efficiency, η , was calculated at constant $\lambda = 550 \text{ nm}$ by applying a constant current on it ($I = 1 \text{ mA}$) in the 0.1 M KI and KCl electrolyte solutions for 240 seconds. The charge, Q , inserted in the sample of (area $A = 2 \text{ cm}^2$) is:

$$Q = I \times t \quad (2)$$

$$= 0.001 \times 240 = 0.24 \text{ C},$$

$$Q/A = 0.24/4 = 0.06 \text{ Ccm}^{-2}. \quad (3)$$

By using the equation (3), η can be calculated as follows:

$$\eta = \frac{\Delta OD}{\Delta Q} = \frac{\log\left(\frac{T_b}{T_c}\right)}{\left(\frac{Q}{A}\right)}, \quad (4)$$

where ΔOD is the optical density difference, T_b and T_c are transmittance at bleached state and colored state respectively as shown in Figure 6. The calculated coloration efficiency is $1.89 \text{ cm}^2\text{C}^{-1}$ in KI and $2.01 \text{ cm}^2\text{C}^{-1}$ in KCl electrolyte. The color change is believed to be associated with the intercalation (deintercalation) of the K⁺ ions into (or out from) the WO₃ films. The the diffusion coefficient of WO₃ films in KI and KCl electrolyte solutions are not significantly varied. Consequently, the coloration efficiencies (color change) are not significantly varied in KI and KCl electrolytes.

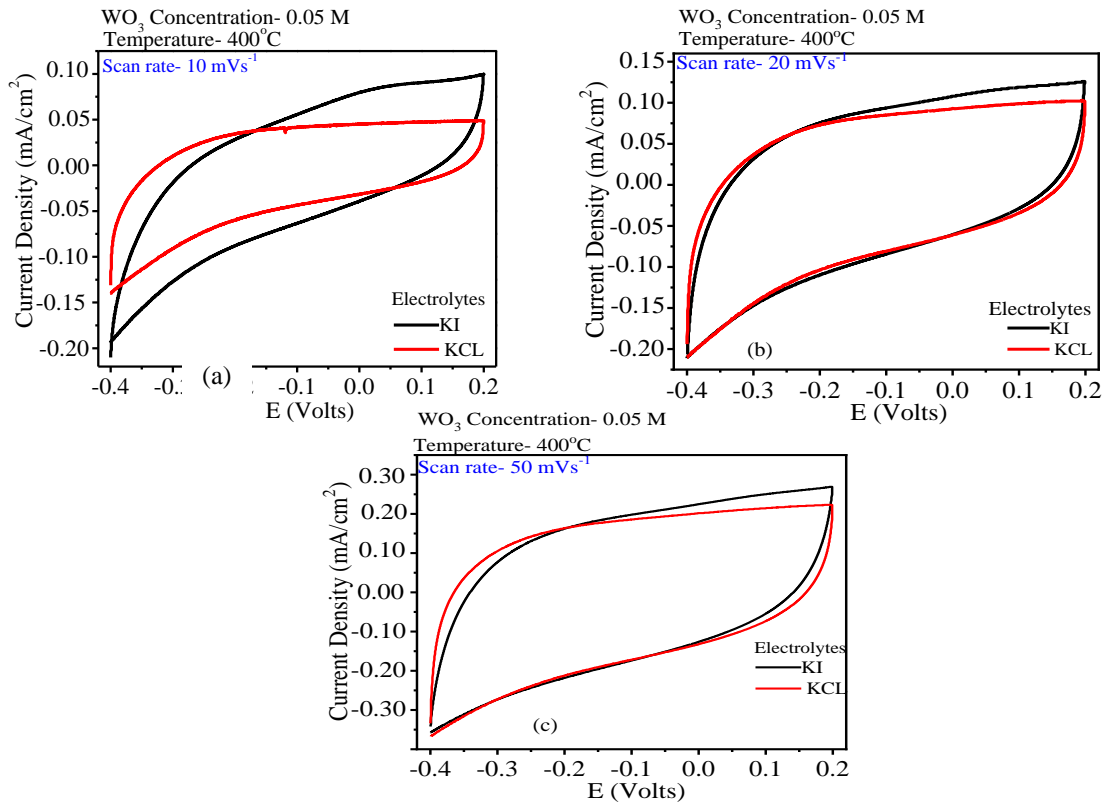


Figure 6 (a–c) Cyclic voltammograms of WO_3 films (400°C and 0.05M) in KI and KCl electrolyte

Table 2 Diffusion coefficients of potassium ions (K^+) calculated using Randles-Sevcik equation for WO_3 films in KI and KCl solution

Scan Rate (mV/s)	Diffusion Coefficient (anodic peak) ($\times 10^{-12} \text{cm}^2 \text{s}^{-1}$)	
	Electrolyte (KI)	Electrolyte (KCl)
10	1.35	1.38
20	1.14	1.14
50	1.08	1.09

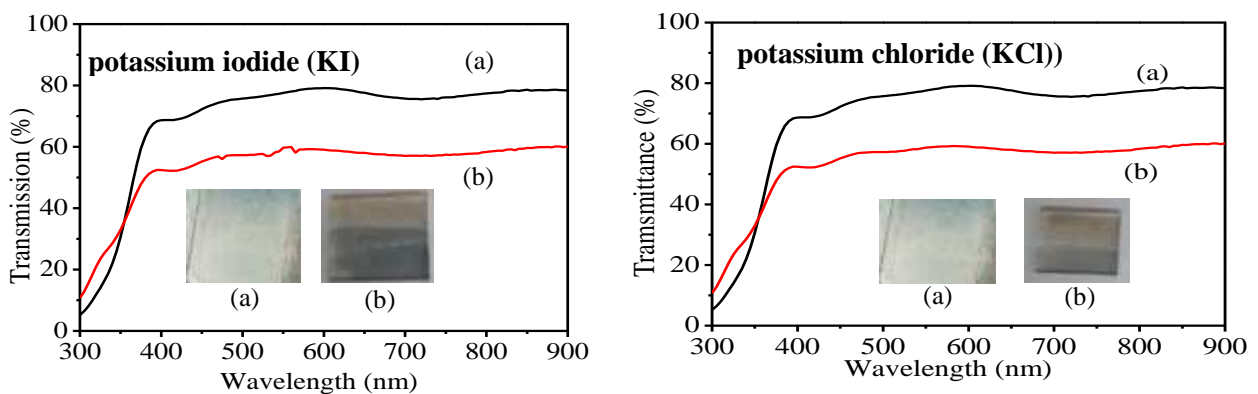


Figure 7 Transmittance spectra of WO_3 films with potassium iodide (KI) and potassium chloride (KCl) at (a) bleached state and (b) colored state

Summary and Conclusion

Tungsten trioxide (WO₃) films were fabricated by spray pyrolysis method varying WO₃ precursor concentrations. The XRD measurement indicated that WO₃ film annealed at 300 °C shows the amorphous phase. When the annealing temperatures increased to 400 °C and 500 °C, WO₃ films reveal the orthorhombic structure. The main diffraction peak positions of WO₃ films annealed at 400 °C and 500 °C remain unchanged but the peak intensities declined. The stronger peak intensity of WO₃ films was observed at annealing temperature 400 °C. The optical transmission and band gap energy of WO₃ films decreased upon increasing WO₃ precursor concentrations. It may be due to the higher content of WO₃ precursor and thicker film formation. In the case of change in WO₃ precursor, the highest anodic peak current density was observed in WO₃ films (0.05 M) at each scan rate. Annealing temperature (400°C) and WO₃ precursor concentration (0.05 M) were selected for determining the performance of electrochromic device. The calculated diffusion coefficient is $1.08 - 1.35 \times 10^{-12} \text{ cm}^2\text{s}^{-1}$ in KI electrolyte and $1.09 - 1.38 \times 10^{-12} \text{ cm}^2\text{s}^{-1}$ in KCl electrolyte. From the electrochemical analysis it is observed that the films have changed their colors in accordance with the applied potential. Also the films have the capability to withstand in the electrolyte throughout the entire scan rates; indicating the better reversibility of the films in the electrochromic process. The higher diffusion coefficient indicates a larger contact area and greater porosity resulting in faster ion insertion/extraction. The coloration efficiency, η calculated at constant $\lambda = 550 \text{ nm}$ is found to be $1.89 \text{ cm}^2\text{C}^{-1}$ in KI and $2.01 \text{ cm}^2\text{C}^{-1}$ in KCl electrolyte.

Acknowledgement

The authors special thanks to ISP (International Science Program), Sweden, for their support in measurement of cyclic voltammetry (Electrochemical Workstation- CorrTest CS350) and also grateful thank to all the Materials Science Laboratory members (University of Mandalay) for their helpful discussion.

References

- Jayachandran M. *et al.*, (2005) "Materials Properties, Preparation Techniques and Electrochromic Devices" Transactions of the SAEST, India, vol. 40, pp.42-60.
- M.F. Daniel *et al.*, (1987) "Infrared and Raman Study of Tungsten Trioxides and Tungsten Trioxide Hydrates" Journal of Solid State Chemistry, United States, vol. 67, pp.235-247.
- P.R.Patil *et al.*, (2004) "Preparation and Characterization of Spray Deposited n-type WO₃ thin Films for Electrochromic Devices" Materials Research Bulletin, United States, vol.39, pp.1479-1489.

EVALUATION OF BAND GAPS AND URBACH ENERGIES FOR ZnO THIN FILMS BY THERMAL EFFECT

Nay Min Hla¹, Aye Khaing Soe², Moe Sandar Than³,

Mono Zaw⁴, Soe Ko Ko Aung⁵, San Yu Swe⁶

Abstract

Zinc Oxide (ZnO) nanoparticles were synthesized by the sol-gel technique. As prepared ZnO thin films were deposited by spin coating method on different annealing temperatures at 200 °C and 300 °C. Optical properties of ZnO thin films were investigated by Ultraviolet–visible spectroscopy (UV–VIS). Energy gaps were decreased from 3.27 eV at 200 °C to 3.18 eV at 300 °C with increasing temperature. On the contrary, Urbach energy was decreased from 180 meV (300 °C) to 92 meV (200 °C) due to effect of annealing temperature. This mainly comes from decreasing of interatomic spacing and the average potential energy by defects and imperfection of semiconductor materials. Hence, Lower Urbach energy and higher transmittance of ZnO nanoparticles thin film is suitable electron transport layer in low temperature processed for flexible perovskite solar cells.

Keywords: Energy Gap, Urbach energy, Zinc oxide, thin film, Annealing temperature

Introduction

Perovskite solar cells (PSCs) initially investigated from methylammonium lead halide which are promising light harvesters in the field of next-generation solar cells. In 2009, Miyasaka (Kojima et al., 2009) applied an organic-inorganic lead halide perovskite compounds as visible-light utilized in ETLs structure and received an initial power conversion efficiency (PCE) of 4%. Later on, power conversion efficiency has drastically improved up to 22.7% due to adorable optical and electrical properties such as long diffusion length up to 175 μm, high carrier mobility, direct optical band gap, extensive absorption range (Ansori, 1972; Brivio et al., 2013; D’Innocenzo et al., 2014; Etgar et al., 2012; Jeong et al., 2021; Saliba et al., 2016; Stranks et al., 2013; Tao et al., 2015).

In order to improved perovskite solar cell efficiency, different types of electron transport layers (ETLs) have been studied in recent year. The ETLs normally used in perovskite-based solar cells as titanium dioxide TiO₂ (Gao et al., 2015; Hadouchi et al., 2016). TiO₂ films need high temperature 500 C° which is not suitable for flexible perovskite solar cells (Kim et al., 2012; Liu et al., 2013). This problem is one of the boundaries for commercialization of perovskite solar cells. As an alternative, Zinc oxide (ZnO) can be substituted instead of TiO₂ as an ETLs in PSCs (Luo et al., 2018). In addition, ZnO is a wide band gap semiconductor and electron mobility higher than that of TiO₂, which is favorable for electron transport layers (Zhang et al., 2009) and it need low temperatures process, which have great advantages in tandem and flexible devices (Seo et al., 2019). Furthermore, ZnO has a high exciton binding energy of 60 meV that contributes to its excellent optical properties (Gu et al., 2013) and It has a favorable conduction level of 4.4 eV (Wright and Uddin, 2012) which facilitates electron extraction from LUMO level (3.9 eV) (Choi et al., 2015) of methylammonium iodide perovskite. Thus, ZnO can simultaneously play a role of n-type conducting layer in a perovskite solar cell and deposited by spin coating for flexible substrates at low temperature to achieve smooth and high- quality films (Hadouchi et al., 2016).

¹ Department of Physics, Materials Research Laboratory, University of Mandalay, 05061, Mandalay, Myanmar

² Department of Physics, Materials Research Laboratory, University of Panglong, 06114, Shan State, Myanmar

³ Department of Physics, Materials Research Laboratory, University of Kalay, 02093, Sagaing, Myanmar

⁴ Department of Physics, Materials Research Laboratory, University of Mandalay, 05032, Mandalay, Myanmar

⁵ Department of Physics, Materials Research Laboratory, University of Mandalay, 05032, Mandalay, Myanmar

⁶ Department of Physics, Materials Research Laboratory, University of Mandalay, 05032, Mandalay, Myanmar

However, it is not clear that what is scientific reason for low temperature process is used for ZnO thin film compared than that of high temperature sintering.

In our work, ZnO colloidal nanoparticle solution was synthesized by sol gel method. Resulted ZnO thin films were deposited by spin coated method under different temperature of 200 °C and 300 °C. The effect of thermal annealing on their optical properties were studied.

Materials and Method

Materials

Zinc acetate dihydrate ($\text{Zn}(\text{CH}_3\text{COO})_2 \cdot 2\text{H}_2\text{O}$, 99%), Potassium hydroxide (KOH, 99%), and methanol (CH_3OH , 96%) are purchased from Sigma-Aldrich and Merck sources.

Synthesis of ZnO nanoparticles

ZnO_x nanoparticle was synthesized following by the sol gel method (Dehghan and Behjat, 2019). 0.11 M of Zinc acetate dihydrate $\text{Zn}(\text{CH}_3\text{COO})_2 \cdot (\text{H}_2\text{O})_2$ was dissolved in methanol (CH_3OH) under magnetic stirrer at 60 °C for 30 min to obtain a clearly solution. Potassium hydroxide (KOH) (0.45M) was dissolved in methanol with another vial and stirred for 30 min at 60 °C. Finally, KOH clearly solution was slowly added to the zinc acetate solution at 60°C while vigorous stirring. The white solution was formed within 5 min then transformed into clearly solution within 30 min. Colloidal solution was precipitated after 2 h stirring at 60°C. ZnO nanoparticle solution was obtained and ready to use by spin coating method.

Sample preparation

Glass substrates ($2.5 \times 2.5 \text{ cm}^2$) were ultrasonically cleaned with distilled water, acetone, ethanol and isopropanol for each 15 minutes. The cleaned glass substrates were further treated with UV/ozone for 15 minutes before film deposition.

Films deposition

The ZnO colloidal solution was deposited onto the glass substrate by spin coating method using spinning speed at 2000 rpms for 30 s and annealed at 200 °C and 300 °C for 30 minutes each.

Characterization of ZnO thin films

The absorption and transmission spectra of ZnO films were recorded from the spectral range of 300 nm to 900 nm using UV-Vis spectrophotometer (Genesys 10S). The baseline scan was taken using a bare glass substrate (for thin films) prior to the measurement.

Results and Discussion

Figure 1 shows the prepared ZnO colloidal solution is deposited on the glass substrate by spin coated method and then annealed for 200 °C and 300 °C for 30 min each.

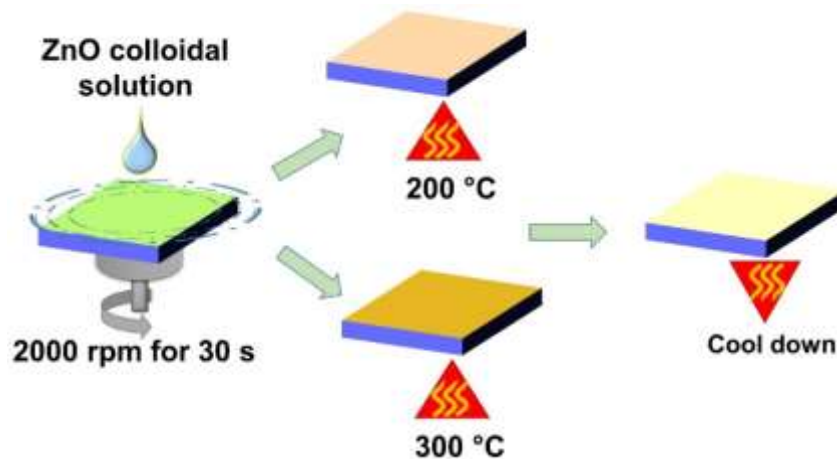


Figure 1. Schematic illustration of deposited ZnO thin films

The optical properties of deposited films were characterized by UV- vis spectrophotometry. Figure 2 shows the measured transmittance, absorption spectra of ZnO films and corresponding Tauc's plot. These results exhibit the optical transmission and absorption of ZnO film with varying temperatures at 200 °C and 300 °C. The higher optical transmission of ZnO film is observed when temperature is set at 200 °C (see Figure 2a). On the contrary, transmittance is decreased with increasing temperature at 300 °C. The low temperature deposited film can be attributed to lower energy loss due to highest transmittance for suitable electron transport layer in perovskite solar cells. Higher absorption of ZnO films (300 °C) can be observed in the wavelength of 300–350 nm range as shown in Figure 2b. Lower absorption spectrum of annealing film (200 °C) exhibits a UV shift character corresponding to the higher energy bandgap. Furthermore, energy gaps of ZnO annealing films is also estimated from Tauc's plot equation (Makuła et al., 2018): $(\alpha h\nu)^n = A (h\nu - E_g)$, where α is absorption coefficient, $h\nu$ is incident light energy, and E_g is the band gap of the material. The exponent 'n' is the transition type of the material. The n value is 2 for direct transition for ZnO (Dehghan and Behjat, 2019). The optical band gap of ZnO annealed films are decreased with increasing annealing temperatures in Figure 2c. The band energies of resulted films are obtained by extrapolating the linear portion of the curve to photon energy axis. The calculated energy gap for low temperature (200 °C) annealed film is 3.29 eV (C. Nehru et al., 2012; Srikant and Clarke, 1998). The band gap energy is decreased to 3.21 eV when temperature is increased to 300 °C. It may increase grain sizes of ZnO film due to decrease energy gap with increasing temperature.

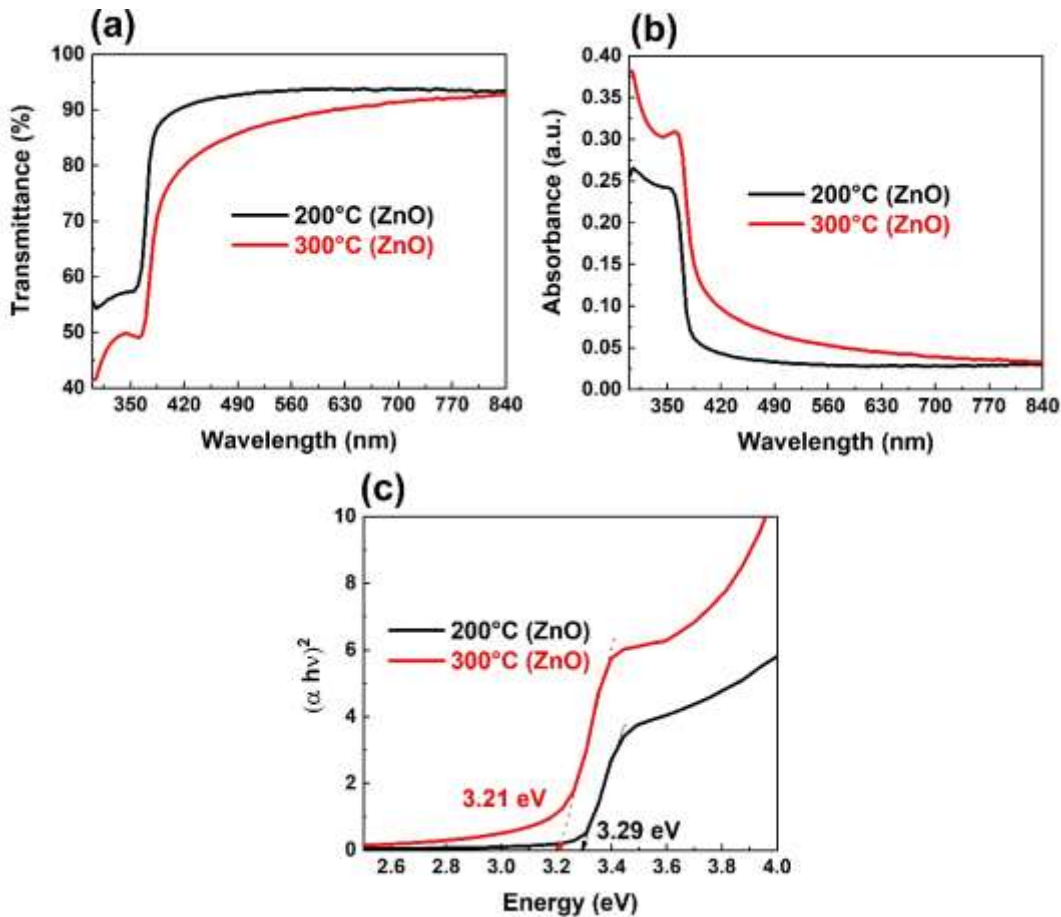


Figure 2. UV-Vis spectra of different annealing temperature (a) optical transmittance (b) absorption spectra (c) plot of $(\alpha h\nu)^2$ versus $h\nu$ of ZnO films

This results can be further analyzed upon different temperature by a combination of the thermal effect and the Urbach effect (Skettrup, 1978; Urbach, 1953). The origin of the Urbach energy mainly comes from the impurities, defects and imperfection of growth thin films by annealing temperature (Rai et al., 2012). Figure 3 exhibits the Urbach tails from the Sgreen region for 200 °C and yellow region for 300 °C. It can be clearly seen the broadened behavior by thermal effect at increased temperatures (300 °C). The Urbach energy can be determined from Urbach tails which refers charge excitation transition between the valence band tail to the conduction band edge in the semiconductor following equation: $\alpha = \alpha_0 \exp [(h\nu)/E_U]$ (Skettrup, 1978). From the slope of simplified equation: $\ln(\alpha) = \ln(\alpha_0) + [1/(E_U)] \times h\nu$, E_U can be determined. Urbach energy is increased from 91 meV (200 °C) to 182 meV (300 °C). Lower Urbach energy indicates in the range of 80–100 meV, suggesting that low defect and disorder in the semiconductor materials (Rai et al., 2012). Interestingly, low temperature prepared ZnO thin film has lower Urbach energy and higher transmittance which are appropriate for electron transport layer utilized in the flexible perovskite solar cells.

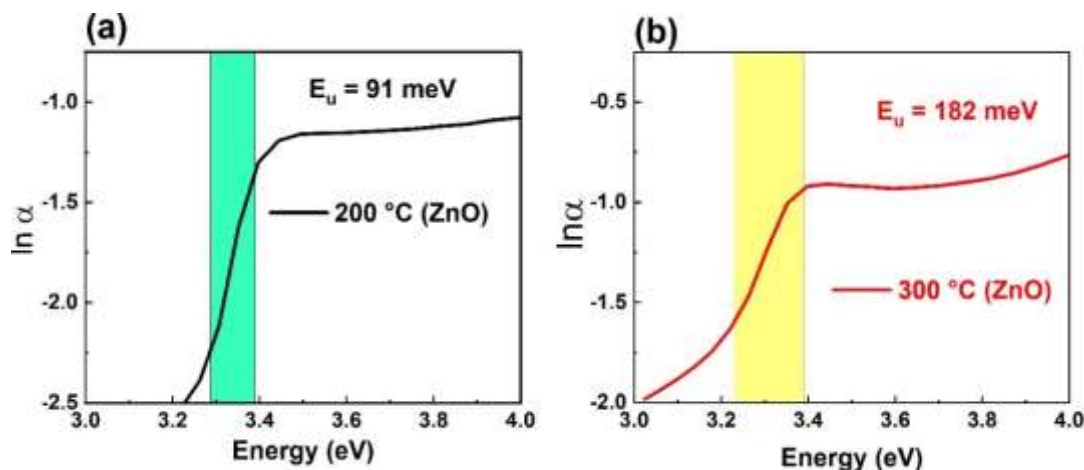


Figure 3. Estimated Urbach energies from $\ln \alpha$ vs photon energy's plot, where E_u is Urbach energy

Conclusion

In this work, ZnO nanoparticles colloidal solution has been synthesized by sol gel method. And ZnO thin films were prepared by spin coated method under different annealing temperature at 200 °C and 300 °C. The resulted ZnO film annealed at 200 °C was higher transmittance and lower Urbach energy. However, the transmittance of ZnO film decreased and its Urbach energy increased when it was annealed at 300 °C. This result shows that higher defect and disorder form in high temperature annealed film. Hence, ZnO thin film annealed at low temperature (200 °C) is a suitable electron transport layer for flexible perovskite solar cells.

Acknowledgements

The authors acknowledge the financial support from the International Science Programme (Uppsala University), grand no. MYA:01 and materials research laboratory, department of physics, University of Mandalay. The author thank to Prof. Dr Nyein Wink Lwin for strongly support.

References

- Ansori, 1972. Toward a Unified Theory of Urbach's Rule and Exponential Absorption Edges. Towar. A UNIFIED THEORY URBACH'S RULE 5, 2.
- Brivio, F., Walker, A.B., Walsh, A., 2013. Structural and electronic properties of hybrid perovskites for high-efficiency thin-film photovoltaics from first-principles. APL Mater. 1.
- C. Nehru, L., Umadevi, M., Sanjeeviraja, C., 2012. Studies on Structural, Optical and Electrical Properties of ZnO Thin Films Prepared by the Spray Pyrolysis Method. Int. J. Mater. Eng. 2, 12–17.
- Choi, H., Mai, C.K., Kim, H.B., Jeong, J., Song, S., Bazan, G.C., Kim, J.Y., Heeger, A.J., 2015. Conjugated polyelectrolyte hole transport layer for inverted-type perovskite solar cells. Nat. Commun. 6, 7348.
- D'Innocenzo, V., Grancini, G., Alcocer, M.J.P., Kandada, A.R.S., Stranks, S.D., Lee, M.M., Lanzani, G., Snaith, H.J., Petrozza, A., 2014. Excitons versus free charges in organo-lead tri-halide perovskites. Nat. Commun. 5, 5386.
- Dehghan, M., Behjat, A., 2019. Deposition of zinc oxide as an electron transport layer in planar perovskite solar cells by spray and SILAR methods comparable with spin coating. RSC Adv. 9, 20917–20924.
- Etgar, L., Gao, P., Xue, Z., Peng, Q., Chandiran, A.K., Liu, B., Nazeeruddin, M.K., Grätzel, M., 2012. Mesoscopic CH₃NH₃PbI₃/TiO₂ heterojunction solar cells. J. Am. Chem. Soc. 134, 17396–17399.

- Gao, Q., Yang, S., Lei, L., Zhang, S., Cao, Q., Xie, J., Li, J., Liu, Y., 2015. An effective TiO₂ blocking layer for perovskite solar cells with enhanced performance. *Chem. Lett.* 44, 624–626.
- Gu, Y.Z., Lu, H.L., Geng, Y., Ye, Z.Y., Zhang, Y., Sun, Q.Q., Ding, S.J., Zhang, D.W., 2013. Optical and microstructural properties of ZnO/ TiO₂ nanolaminates prepared by atomic layer deposition. *Nanoscale Res. Lett.* 8, 107.
- Hadouchi, W., Rousset, J., Tondelier, D., Geffroy, B., Bonnassieux, Y., 2016. Zinc oxide as a hole blocking layer for perovskite solar cells deposited in atmospheric conditions. *RSC Adv.* 6, 67715–67723.
- Jeong, J., Kim, Minjin, Seo, J., Lu, H., Ahlawat, P., Mishra, A., Yang, Y., Hope, M.A., Eickemeyer, F.T., Kim, Maengsuk, Yoon, Y.J., Choi, I.W., Darwich, B.P., Choi, S.J., Jo, Y., Lee, J.H., Walker, B., Zakeeruddin, S.M., Emsley, L., Rothlisberger, U., Hagfeldt, A., Kim, D.S., Grätzel, M., Kim, J.Y., 2021. Pseudo-halide anion engineering for α -FAPbI₃ perovskite solar cells. *Nature* 592, 381–385.
- Kim, H.S., Lee, C.R., Im, J.H., Lee, K.B., Moehl, T., Marchioro, A., Moon, S.J., Humphry-Baker, R., Yum, J.H., Moser, J.E., Grätzel, M., Park, N.G., 2012. Lead iodide perovskite sensitized all-solid-state submicron thin film mesoscopic solar cell with efficiency exceeding 9%. *Sci. Rep.* 2, 1–7.
- Kojima, A., Teshima, K., Shirai, Y., Miyasaka, T., 2009. Organometal halide perovskites as visible-light sensitizers for photovoltaic cells. *J. Am. Chem. Soc.* 131, 6050–6051.
- Liu, M., Johnston, M.B., Snaith, H.J., 2013. Efficient planar heterojunction perovskite solar cells by vapour deposition. *Nature* 501, 395–398.
- Luo, J., Wang, Y., Zhang, Q., 2018. Progress in perovskite solar cells based on ZnO nanostructures. *Sol. Energy* 163, 289–306.
- Makula, P., Pacia, M., Macyk, W., 2018. How To Correctly Determine the Band Gap Energy of Modified Semiconductor Photocatalysts Based on UV-Vis Spectra. *J. Phys. Chem. Lett.* 9, 6814–6817.
- Rai, R.C., Guminiak, M., Wilser, S., Cai, B., Nakarmi, M.L., 2012. Elevated temperature dependence of energy band gap of ZnO thin films grown by e-beam deposition. *J. Appl. Phys.* 111, 073511.
- Saliba, M., Matsui, T., Seo, J.Y., Domanski, K., Correa-Baena, J.P., Nazeeruddin, M.K., Zakeeruddin, S.M., Tress, W., Abate, A., Hagfeldt, A., Grätzel, M., 2016. Cesium-containing triple cation perovskite solar cells: Improved stability, reproducibility and high efficiency. *Energy Environ. Sci.* 9, 1989–1997.
- Seo, J., Moon, Y., Lee, S., Lee, C., Kim, D., Kim, H., Kim, Y., 2019. High efficiency tandem polymer solar cells with MoO₃/Ni/ZnO:PEOz hybrid interconnection layers. *Nanoscale Horizons* 4, 1221–1226.
- Skettrup, T., 1978. Urbach's rule derived from thermal fluctuations in the band-gap energy. *Phys. Rev. B* 18, 2622–2631.
- Srikant, V., Clarke, D.R., 1998. On the optical band gap of zinc oxide. *J. Appl. Phys.* 83, 5447–5451.
- Stranks, S.D., Eperon, G.E., Grancini, G., Menelaou, C., Alcocer, M.J.P., Leijtens, T., Herz, L.M., Petrozza, A., Snaith, H.J., 2013. Electron-hole diffusion lengths exceeding 1 micrometer in an organometal trihalide perovskite absorber. *Science* (80-). 342, 341–344.
- Tao, C., Neutzner, S., Colella, L., Marras, S., Srimath Kandada, A.R., Gandini, M., Bastiani, M. De, Pace, G., Manna, L., Caironi, M., Bertarelli, C., Petrozza, A., 2015. 17.6% Stabilized Efficiency in Low-Temperature Processed Planar Perovskite Solar Cells. *Energy Environ. Sci.* 8, 2365–2370.
- Urbach, F., 1953. The long-wavelength edge of photographic sensitivity and of the electronic Absorption of Solids [8]. *Phys. Rev.* 92, 1324.
- Wright, M., Uddin, A., 2012. Organic-inorganic hybrid solar cells: A comparative review. *Sol. Energy Mater. Sol. Cells* 107, 87–111.
- Zhang, Q., Dandeneau, C.S., Zhou, X., Cao, C., 2009. ZnO nanostructures for dye-sensitized solar cells. *Adv. Mater.* 21, 4087–4108.

ASSESSMENT OF HEAVY METALS CONCENTRATION IN WATER SAMPLES FROM MANDALAY CITY

May Zin Oo¹, Kalyar Thwe²

Abstract

The objective of this paper is to investigate heavy metal concentration and water quality parameters of different water stations in Mandalay city. Water samples were collected from six different townships in Mandalay City. The selected water samples are currently used for human consumption at the Mandalay region of Myanmar. The study provides an assessment of the present status of the concentration of heavy metals (Cu, Fe, Mn, Pb and Zn) of the Mandalay urban area. The concentration of Cu, Fe, Mn, Pb and Zn were determined using Inductively Coupled Plasma Optical Emission Spectroscopy (ICP-OES) techniques for heavy metal evaluation index (HEI). Concentration of heavy metals in the water samples from the study area were Fe>Mn>Zn>Pb>Cu. In order to risk levels of Heavy Metal Evaluation Index (HEI) was evaluated. According to the pollution index, 67% of water samples were good as reported by heavy metal evaluation index (HEI).

Keywords: heavy metal, heavy meal evaluation index, drinking water

Introduction

Water is the most important, abundant and useful resources on the earth because no life is possible without water. It is the most essential basic component to all living being as most of the biochemical reactions that takes place through the metabolism and growth of living organisms involve water. Contamination of the environment with toxic heavy metals has become one of the major causes of concern for human kind. Heavy metals in surface water bodies, groundwater and soils can be either form natural or anthropogenic sources. The two basis categories of pollution are organic and inorganic. Inorganic pollution is basically from heavy metals. Chemical substances such as heavy metals are one of the factors which contribute to environmental pollution and it was believed that it can disrupt living ecosystem. Currently, anthropogenic inputs of metals exceed natural inputs due to increased urbanization and industrialization. Healthy drinking water is the basic need of the human health. Contaminated drinking water is a significant risk to human health. The high concentration of heavy metal intensively effects on health, no. of disease increase day by day like cancers that are associated with heavy metal. The heavy metals can enter into the environment through anthropogenic activates and natural process.

The purpose of this research is to increase the awareness about heavy metal and its high concentration effect on living things.

Materials and Methods

Mandalay is the second largest city in Myanmar and the economic centre of Upper Myanmar. In this research, the samples were collected from 6 BPS which based on the municipal water supply system at different townships in Mandalay urban area. In this research, the samples were collected from 6 BPS which based on the municipal water supply system at different townships in Mandalay urban area. The samples were collected 6 polyethylene bottles in ice boxes and the bottles were rinsed with the target water before sampling. And then, the concentrations of heavy metals (Cu, Fe, Mn, Pb and Zn) were analyzed using Inductively Coupled Plasma Optical Emission Spectroscopy (ICP-OES), Perkin Elmer Optima 3000 at the Environmental Science Research Center, Chiang Mai University, Thailand. After analyzing, the risk level of heavy metal concentrations in the samples were investigated the quantitative methods: Heavy Metal Evaluation Index (HEI).

¹ Department of Physics, University of Mandalay

² Department of Physics, University of Mandalay

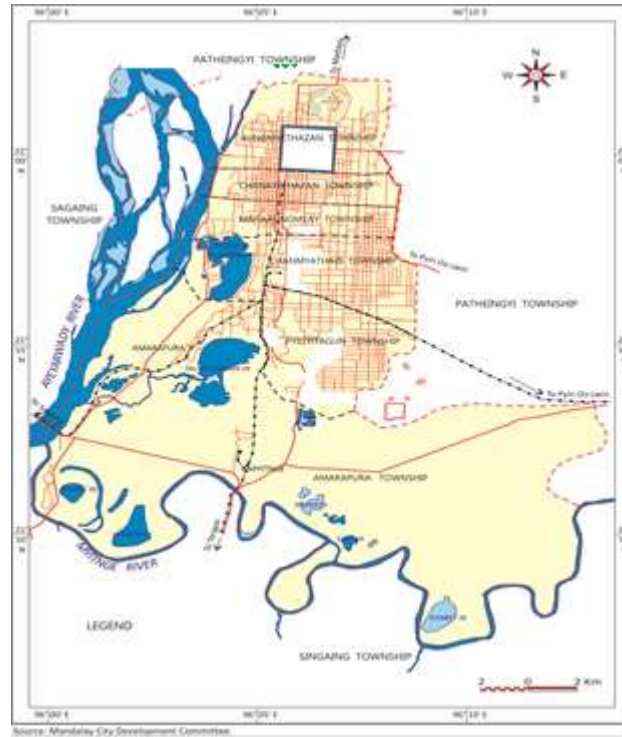


Figure 1. Geographical Map of Mandalay showing the study area

Table 1 Samples Descriptions of Study Area

Samples Code	Study Area	Water Characteristics	Townships
W-1	BPS-1	Groundwater	Chanayethazan
W-2	BPS-2	Groundwater	Chanmyathazi
W-3	BPS-3	Groundwater	Aungmyaethazan
W-4	BPS-5	Groundwater	Mahaaungmyae
W-5	BPS-10	Groundwater	Amarapura
W-6	BPS-15	Groundwater	Pyigyidagun

Heavy Metal Evaluation Index (HEI)

Heavy metal evaluation index provided an overall quality of water for heavy metals and can be calculated as follows:

$$HEI = \sum_{i=1}^n \frac{H_c}{H_{MAC}}$$

Where, H_c is the monitored value and H_{MAC} is the maximum admissible concentration (MAC) of the i^{th} parameter.

Table 2 Classification for Heavy Metal Evaluation Index (HEI) [Mohan *et al.*, 1996]

HEI Value	Pollution Level
<10	Low
10-20	Medium
>20	High

Results and Discussion

Heavy metals concentration in water samples were measured by using Inductively Coupled Plasma Optical Emission Spectrometry (ICP-OES). The mean concentration of Cu, Fe, Mn, Pb and Zn in water samples were LOD, 3.362, 0.296, 0.022 and 0.128 mg/L. Heavy metal concentration of analyzed water samples and compare the guidelines value as specified by the World Health Organization (WHO) for drinking water quality are in Table (3). The variations of heavy metal concentration in water samples are demonstrated in Figure (2) to Figure (5).

Table 3 Heavy Metal Concentration in Water Samples

Study Area	Heavy Metal (mg/L)				
	Cu	Fe	Mn	Pb	Zn
W-1	LOD	4.707	0.445	LOD	0.161
W-2	LOD	4.704	0.443	LOD	0.162
W-3	LOD	0.681	LOD	0.066	0.056
W-4	LOD	0.672	LOD	0.068	0.055
W-5	LOD	4.703	0.446	LOD	0.174
W-6	LOD	4.706	0.444	LOD	0.161
Average	-	3.362	0.296	0.022	0.128
WHO	2	0.3	0.4	0.01	3

LOW: Lower Limited of Detection
 WHO:World Health Organization

Copper

Copper is an essential element and is contained in many foods. In this research, the concentration of Cu in all samples were estimated as zero by the detection instrument that means either there was no Cu present in water or the levels of Cu were lower than the detection limit of the instrument.

Iron

Iron (Fe) is an essential element for human health that performs various function in our body, the most well-known of them is production of protein hemoglobin, which carry oxygen from our lungs to transfer it throughout the body. In this study, the concentration of iron in water samples ranged from 0.672 to 4.707 mg/L with an average value 3.362 mg/L. All of the water samples are higher than the range of WHO Standard.

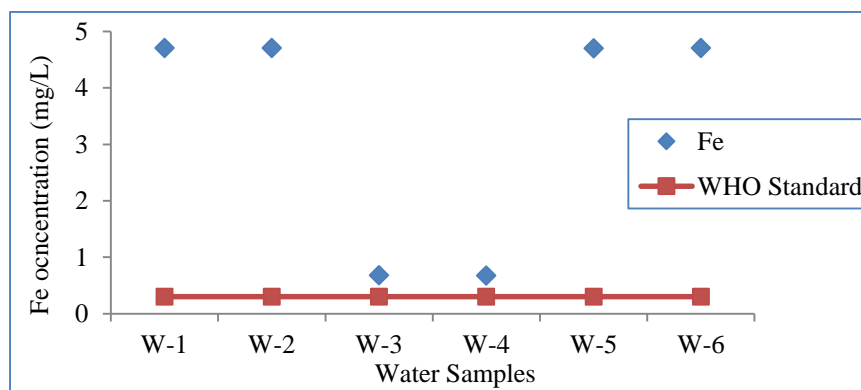


Figure 2 Fe concentration in water samples

Manganese

Manganese is an important trace mineral that is needed by our body in little amounts for the production of digestive enzymes, absorption of nutrients, wound healing, bone development and immune-system defenses. In the present investigation, the value of manganese ranged from 0 to 0.446 mg/L with an average value 0.296 mg/L. The concentrations of manganese are slightly larger than the WHO standard at W-1, W-2, W-5, W-6.

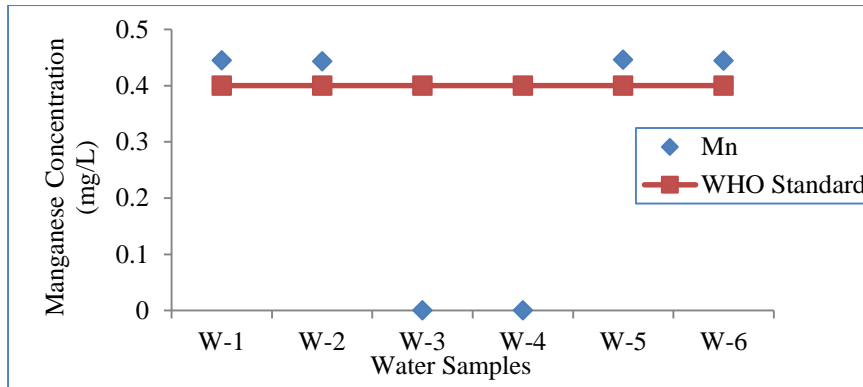


Figure 3 Mn concentration in water samples

Lead

Lead is toxic heavy metal and it is found in the earth crust. The excess amount of lead creates harmful effect on health and it can directly destroy the major organs and system of body. In the present study, the concentrations of lead were found below the permissible limit of WHO standard except water samples of W-3 and W-4.

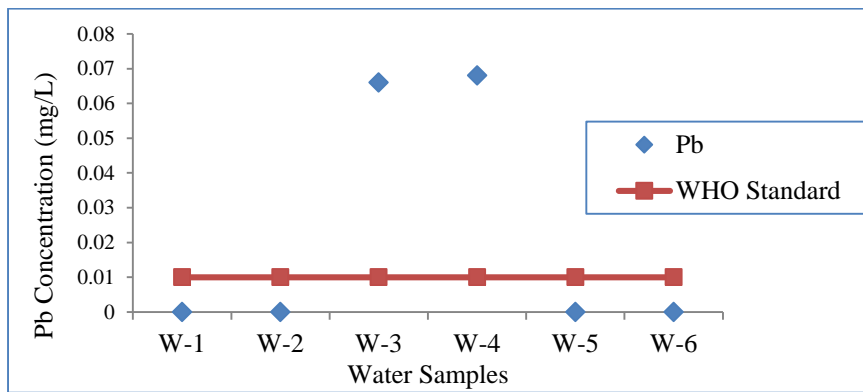


Figure 4 Pb concentration in water samples

Zinc

Zinc is an essential trace element, which is required in small quantity to maintain human health. Zinc helps in production of hormones, growths, improvement of immune and digestive system. In the present investigation, all of the water samples were found below the permissible limit of WHO standard.

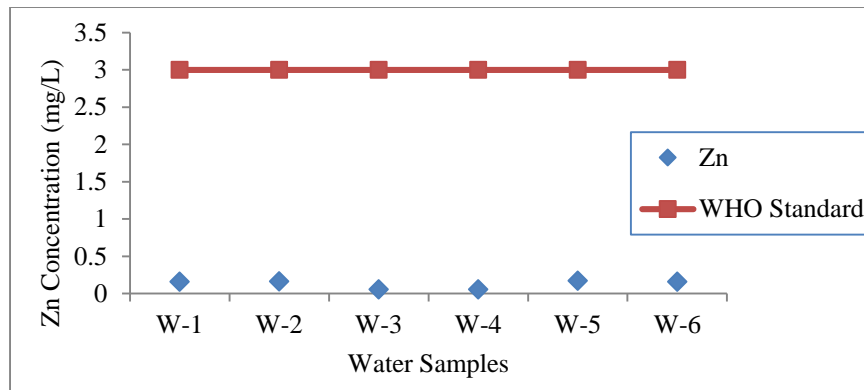


Figure 5 Zn concentration in water samples

Pearson Correlation Analysis of Water Samples

Pearson correlation analysis coefficient was applied to determine the relationship between heavy metals (Cu, Fe, Mn, Pb and Zn). Pearson correlation analysis of heavy metals in water samples from Mandalay urban area is shown in Table (4). According to the obtained data, Fe showed a significant positive correlation with Mn and Zn. Mn has positively correlated with Zn. The correlations between the concentrations of different heavy metals in the study area have been illustrated using a scatter plot in Figure (6).

Table 4 Pearson Correlation Analysis of Heavy Metals in Mandalay Urban Area

	<i>Fe</i>	<i>Mn</i>	<i>Pb</i>	<i>Zn</i>
<i>Fe</i>	1			
<i>Mn</i>	0.999989	1		
<i>Pb</i>	-0.99985	-0.99982	1	
<i>Zn</i>	0.995885	0.996203	-0.99586	1

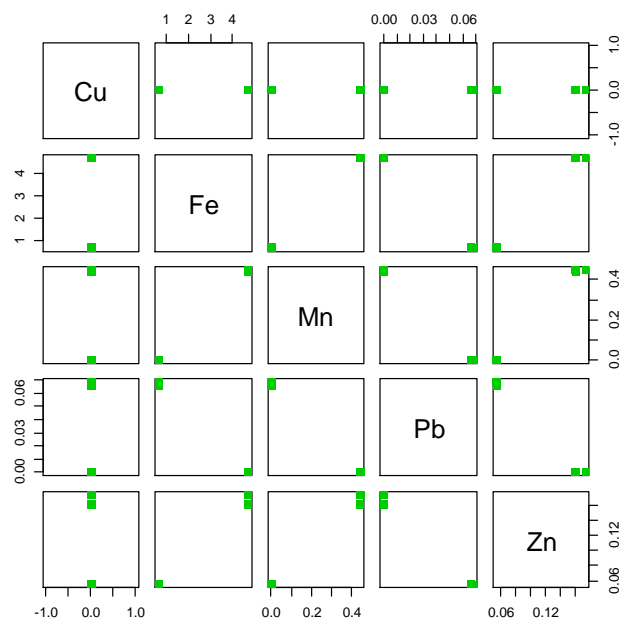


Figure 6 Scatter plot of heavy metal concentration in water samples

Assessment of Metal Contamination

Metals contaminations of heavy metals (Cu, Fe, Mn, Pb and Zn) were calculated for the study area. In the present investigation, Heavy Metal Evaluation Index (HEI) values were found in the range of 8.89 to 16.85 respectively. The observed HEI values of all the water samples are found within the medium pollution level and this indicates that the water is not critically polluted with respect to studied heavy metals. The observed data of HEI are presented in Figure (8).

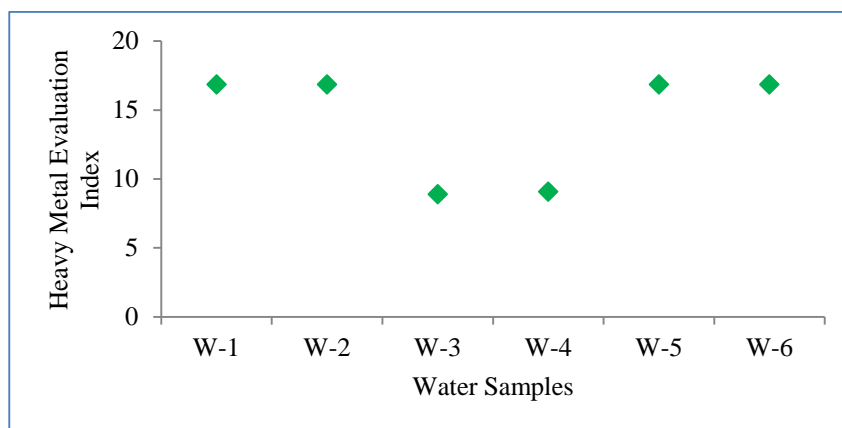


Figure 8 Variations of Heavy Metal Evaluation Index of Water Samples

Conclusion

Health water is a basic need for life. The excess amount of heavy metal present as pollutant in unhealthy water. In some area of present study, the concentrations of heavy metals are higher than the permissible limit of WHO standard. Fe, Mn and Zn are essential for health but in limited concentration, high concentration creates harmful effect on health. According to the obtained results, water used for human consumption in all sites had the correlation of Iron followed by Mn, Zn and Pb. We are able to control these serious diseases by removing excess amount of heavy metal in drinking water. If the people of Mandalay are going to use this water as drinking water, they should use it after treatment. Conducting this research helps to prevent the pollution of the water used by the people of Mandalay.

Acknowledgements

Firstly, I would like to thank my Rector, Dr Tin Tun, Rector, University of Mandalay for his permission. I would like to express thank Dr Nyein Wint Lwin, Professor and Head, Department of Physics, University of Mandalay for her invaluable advice. I would like to express my supervisor deep an sincere gratitude thanks to Dr Kalyar Thwe, Professor and Head (Retd.), Department of Physics, University of Mandalay for her support and for patiently guiding me how to carry out the best research. And then, I greatly acknowledge to International Science Program (ISP), Uppsala University, Sweden which financially supported my research work visit at Chiang Mai University, Thailand. Finally, I am very thankful to the collaborators from Experimental Nuclear Physics Laboratory, Department of Physics, University of Mandalay.

References

- Aweng.E.R, Karimah.M, Suhaimi.O, (2011) “ Heavy Metals Concentration of Irrigation Water, Soils and Fruits Vegetables in Kota Bharu Area, Kelantan, Malaysia” *Journal of Applied Sciences in Environmental Sanitation*, Malaysia, vol.6, pp.463-470.
- D.Chapman, (1996) “*Water Quality Assessments – A Guide to Use of Biota, Sediments and Water in Environmental Monitoring*”, Second Edition.
- Mansour.G, Bhram.k, (2018) “Heavy Metals Analysis and Quality Assessment in Drinking Water“ *Journal of Nutritional Health Research Center*, Iran, vol.16, pp.685-692.
- May Zin Oo (2021) *Study on Pollution Monitoring Parameters of the Water Quality from Mandalay Area*, Mandalay University (Ph.D).
- Mirza.A.T, Moutushi.P, Nikhil.B (2020) “Heavy Metal Pollution Assessment in the Groundwater of the Megha Ghat Industrial Area, Bangladesh by Using Water Pollution Indices” *Journal of Applied Water Science*, Bangladesh, vol.10, pp.1-15.
- Muhammad.J, Arshad.A.K, Kashif.A, (2018) “Heavy Metal In Drinking Water Its Effect On Human Health And Its Treatment Techniques” *International Journal of Biosciences*, Pakistan, vol.12, pp.223-240.
- P.Kumar, P.Verma, A. Kumar Tiwari, (2014-2015) “Review of Various Contamination Index Approaches to Evaluate Groundwater Quality With Geographic Information System (GIS)” *International Journal of ChemTech Reserarch*, India, vol.7, pp.1920-1929.
- World Health Organization (WHO), (2003), (2008), (2011).

INVESTIGATION OF NUCLEON SINGLE-PARTICLE ENERGY LEVELS IN ^{90}Zr USING NUMEROV METHOD

Pyae Wa Maung¹, May Saw Ohn²

Abstract

In this research work, nucleons single-particle energy levels of ^{90}Zr have been investigated by solving non-relativistic Schrödinger equation within the framework of Numerov method. In this calculation, phenomenological Wood-Saxon potential has been applied and Coulomb interaction is taken into account for proton state investigation. Due to the effect of Coulomb repulsion the single-particle energy levels of proton is higher than neutron. Moreover, ^{90}Zr permits the application of Hartree-Fock Random Phase Approximation RPA based Skyrme effective nucleon-nucleon interaction KDE0v1, BsK1, SIII, SVII and SGOI. So, the calculated results were compared with two set parameters of Skyrme interaction: BsK1, SVII and available experimental data. The results were agreed with these two parameters and experimental data.

Keywords: single-particle energy levels, Numerov method, ^{90}Zr

Introduction

The understanding of nuclear structure and energy levels of nuclei is important because it make an effort to study strong nuclear interaction between the nucleons that form a nucleus. The single-particle energies of a nucleon in the potential of the core, provide severe tests of nuclear model. The nuclear models are restored to find a wide range of nuclear properties and many nuclear models such as Fermi gas model, liquid drop model, single-particle shell model and cluster model have been introduced. Among them the single-particle shell model is one of the most essential models in order to make predictions and extrapolations for the properties of nuclei even further from stability (A. Signoracci and B. Alex Brown, 2007).

^{90}Zr is one of the medium mass nuclei with doubly closed shells where the number of neutrons is unequal to the number of protons. The nucleon single-particle energy levels of this nucleus can be investigated by using a self-consistent spherical Hartree-Fock HF method and Random Phase Approximation RPA with five different Skyrme type effective nucleon-nucleon interaction: KDE0v1, BsK1, SIII, SVII and SGOI. In the present work, we investigate single-particle energy levels of ^{90}Zr within the shell model approach using numerov method and compared with two sets parameters of Skyrme type effective nucleon-nucleon interaction BsK1, SVII and the available experimental data.

Numerov Method

Numerov method is a numerical method to solve second order differential equations. In this research work, the nucleon single-particle energies of Zr have been investigated within the framework of shell model approach and one body Schrödinger radial equation will be applied.

The Schrödinger radial equation can be represented by

$$\frac{d^2}{dr^2}u(r) + \frac{2m}{\hbar^2} \left[E - V(r) - \frac{\hbar^2}{2m} \frac{l(l+1)}{r^2} \right] u(r) = 0 \quad (1)$$

¹ Department of Physics, Mandalay University of Distance Education

² Department of Physics, Yadanabon University

where $u(r) \equiv rR_n$ is reduced radial wave function. A regular solution near the origin is $u(r \rightarrow 0) \rightarrow r^{l+1}$ and asymptotic solution is $u(r \rightarrow \infty) \rightarrow u(r) = e^{-\alpha r^2}$ where α is a constant. Now the Schrödinger equation becomes

$$\frac{d^2 u(r)}{dr^2} + k(r) u(r) = 0 \quad (2)$$

where $k(r) \equiv \frac{2\mu}{\hbar^2} \left[E - V(r) - \frac{\hbar^2}{2\mu} \frac{l(l+1)}{r^2} \right]$ is the kernel of the equation, μ is mass of nucleon single particle and $V(r)$ is single nucleon potential. Eq (2) can be solved by means of Numerov Algorithm. In this method, the range (r) is split into N points according to the formula $r_n = r_{n+1} + h$ where h is the step. Then the wave function and kernel of the equation become $u_n \equiv u(r_n) = u(r_{n-1} + h)$ and $k_n \equiv k(r_n) = k(r_{n-1} + h)$. By using Taylor series, the reduced radial wave function $u(r)$ can be expand as

$$u_{n+1} \equiv u(r_n + h) = u(r_n) + hu'(r_n) + \frac{h^2}{2} u''(r_n) + \frac{h^3}{6} u'''(r_n) + \frac{h^4}{24} u^{(iv)}(r_n) + O(h^5) \quad (3)$$

$$u_{n-1} \equiv u(r_n - h) = u(r_n) - hu'(r_n) + \frac{h^2}{2} u''(r_n) - \frac{h^3}{6} u'''(r_n) + \frac{h^4}{24} u^{(iv)}(r_n) + O(h^5) \quad (4)$$

By adding Eq. (3) and (4), we get

$$u(r_n + h) = 2u(r_n) - u(r_n - h) - h^2 k(r_n) u(r_n) + \frac{h^4}{12} u^{(iv)}(r_n) \quad (5)$$

Similarly for the wave function with second-order derivative,

$$u''_{n+1} \equiv u''(r_n + h) = u''(r_n) + hu'''(r_n) + \frac{h^2}{2} u^{(iv)}(r_n) + \frac{h^3}{6} u^{(v)}(r_n) + O(h^6) \quad (6)$$

$$u''_{n-1} \equiv u''(r_n - h) = u''(r_n) - hu'''(r_n) + \frac{h^2}{2} u^{(iv)}(r_n) - \frac{h^3}{6} u^{(v)}(r_n) + O(h^6) \quad (7)$$

According to the same operation of Eq. (3) and (4), we get

$$h^2 u^{(iv)}(r_n) = -k(r_{n+1}) u(r_{n+1}) - k(r_{n-1}) u(r_{n-1}) + 2k(r_n) u(r_n) \quad (8)$$

Substituting Eq. (8) into (5), we get the following forward recursive relation u_n and backward recursive relation u_{n-1} to find the wave function.

$$u_n = \frac{2 \left[1 - \frac{5h^2}{12} k_{n-1} \right] u_{n-1} - \left[1 + \frac{h^2}{12} k_{n-2} \right] u_{n-2}}{\left[1 + \frac{h^2}{12} k_n \right]} \quad (9)$$

$$u_{n-1} = \frac{2 \left[1 - \frac{5h^2}{12} k_n \right] u_n - \left[1 + \frac{h^2}{12} k_{n+1} \right] u_{n+1}}{\left[1 + \frac{h^2}{12} k_{n-1} \right]} \tag{10}$$

To find the wave function by using these forward-backward technique, it is necessary to give two initial values for each direction and the first derivative wave function is

$$u'_n = \frac{1}{2h} \left[\left(1 + \frac{h^2}{6} k_{n+1} \right) u_{n+1} - \left(1 + \frac{h^2}{6} k_{n-1} \right) u_{n-1} \right] \tag{11}$$

Since both outward and inward wave functions $u_{out}(r)$ and $u_{in}(r)$ satisfy homogeneous equation, their normalization can always be chosen so that they are set to be equal at the match point r_c . At that point the eigen functions must satisfy the following continuity conditions

$$(u_{out})_{r_c} = (u_{in})_{r_c}, (u'_{out})_{r_c} = (u'_{in})_{r_c} \tag{12}$$

A function $G(E)$ can be defined at r_c point whose zeros correspond to the energy eigenvalues as

$$G(E) = \left[\frac{u'_{out}}{u_{out}} \right]_{r_c} - \left[\frac{u'_{in}}{u_{in}} \right]_{r_c} \tag{13}$$

Now we proceed numerically in the following way: firstly, we set a trial energy as an input at $r = 0$ and this energy is increased by the formula $E_n = E + \Delta E$ where ΔE is energy step within the N points. Then the eigen functions of u_{out} and u_{in} for each E_n can be calculated at r_c point and build the $G(E)$ function. In this function, we carefully looked for and checked a change of sign and then perform a fine tuning closing the energy range until the required tolerance. If the value of this function is zero or close to zero, the correct energy eigen value and corresponding eigen function can be obtained simultaneously.

Normalized Wave Function

In order to investigate the properties of nucleon single-particle states, the two wave functions must be taken in normalization condition. The eigen functions of $u_{out}(r)$ and $u_{in}(r)$ obtained from the recursive formulas can be written as

$$u_{out}(r) = A \Phi(r), \quad u_{in}(r) = B I(r) \tag{14}$$

where A and B are constants and their derivatives also become

$$u'_{out}(r) = A \Phi'(r), \quad u'_{in}(r) = B I'(r) \tag{15}$$

By substituting Eq. (14) and (15) in Eq. (12), we get

$$(A\Phi)_{r_c} = (BI)_{r_c} \text{ and } (A\Phi')_{r_c} = (BI')_{r_c} \tag{16}$$

and taking the difference of above equations, we obtain $A = \left[\frac{I - I'}{\Phi - \Phi'} \right]_{r_c} B \equiv f_c B$, where f_c is a scaling factor and this equation relates between constant A and B. We have already got outwards wave function (Φ) and inward wave function (I) from the recursive formulas. After taking their derivative, we can find the constant value A. After obtaining the value of constant A, the value of constant B can be acquired. So Eq. (15) can be represented as

$$u_{out}(r) = f_c B \Phi(r), \quad u_{in}(r) = B I(r) \tag{17}$$

where B is a global factor and it must be taken into account in the normalization process. Then the normalized constant B can be obtained by using the following normalization conditions

$$\int_0^{r_{max}} |u_l(r)|^2 dr = \int_{r_0}^{r_c} |u_{out}(r)|^2 dr + \int_{r_c}^{r_{max}} |u_{in}(r)|^2 dr = 1 \tag{18}$$

The global factor $B = \frac{1}{\sqrt{N}}$ and where $N = \left[f_c^2 \int_0^{r_c} |\Phi(r)|^2 dr + \int_{r_c}^{r_{max}} |I(r)|^2 dr \right]$

Then the normalized outwards and inwards eigen functions becomes

$u_{out}(r) = \frac{1}{\sqrt{N}} f_c \Phi(r)$ from $r = 0$ fm to r_c point and $u_{in}(r) = \frac{1}{\sqrt{N}} I(r)$ from $r = r_c$ fm to r_N point.

Interaction

I. Woods-Saxon potential

The Woods-Saxon potential is the sum of a spin-independent central potential, a spin-orbit potential and the Coulomb potential:

$$V(r) = V_o(r) + V_{so}(r) \mathbf{l} \cdot \mathbf{s} + V_c(r) \tag{19}$$

$$V_o(r) = \frac{V_0}{1 + \exp\left(\frac{r-R}{a}\right)}, \quad R = r_0 A^{1/3} \tag{20}$$

where $V_o(r)$ = spin independent central potential, R = nuclear radius,

$$V_{so}(r) = V_{so} \frac{1}{r} \frac{d}{dr} \frac{1}{1 + \exp\left(\frac{r-R}{a}\right)} = -V_{so} \frac{1}{ra} \frac{\exp\left(\frac{r-R}{a}\right)}{\left(1 + \exp\left(\frac{r-R}{a}\right)\right)^2} \tag{21}$$

$V_{so}(r)$ = spin-orbit potential

$$V_c(r) = \frac{Ze^2}{r} \quad \text{for } r \geq R \tag{22}$$

$$V_c(r) = \frac{Ze^2}{r} \left[\frac{3}{2} - \frac{r^2}{2R^2} \right] \quad \text{for } r \leq R \quad (23)$$

Parameters

$$V_0 = 53 + \frac{N-Z}{A} V_1 \quad \text{for protons}$$

$$V_0 = 53 - \frac{N-Z}{A} V_1 \quad \text{for neutrons}$$

$$V_1 = -30 \text{ MeV}, \quad V_{so} = 22 \text{ MeV}, \quad r_0 = 1.25 \text{ fm}, \quad a = 0.65 \text{ fm}$$

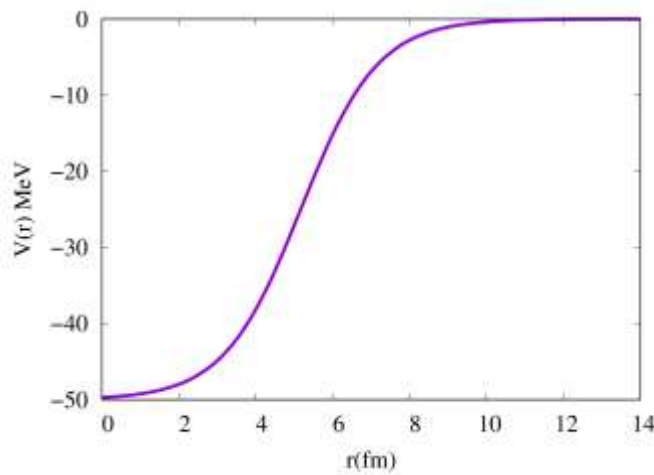


Figure (1) Woods-Saxon potential with spin-orbit for ⁹⁰Zr

II. Derivation of Spin-orbit Interaction

Woods-Saxon central potential does not have any energy level splitting and so spin-orbit interaction is used to get energy level splitting. Woods-Saxon potential with spin-orbit coupling term is represented as follows.

$$V_{l.s}(r) = V_{so} \left[\frac{\hbar}{m_\pi c} \right]^2 \left[\vec{l} \cdot \vec{s} \right] \frac{1}{r} \frac{d\rho(r)}{dr} \quad (24)$$

$$\rho(r) = \text{nuclear density}, \quad \rho(r) = \frac{1}{1 + e^{\frac{r-R}{a}}} \quad (25)$$

$$\frac{d\rho(r)}{dr} = \frac{d}{dr} \left[\frac{1}{1 + e^{\frac{r-R}{a}}} \right] = \frac{d}{dr} \left[1 + e^{\frac{r-R}{a}} \right]^{-1}$$

$$\frac{d\rho(r)}{dr} = - \frac{e^{\frac{r-R}{a}}}{\left[1 + e^{\frac{r-R}{a}} \right]^2} \frac{1}{a} \quad (26)$$

The spin-orbit term with the scalar product of the orbital angular momentum operator L and the intrinsic operator S , can be represented by using the total angular momentum.

$$\vec{J} = \vec{L} + \vec{S} \quad (27)$$

$$J^2 = (\vec{L} + \vec{S}) \cdot (\vec{L} + \vec{S}) \quad (28)$$

$$J^2 = L^2 + 2\vec{L} \cdot \vec{S} + S^2 \quad (29)$$

The magnitude of the total angular momentum, the orbital angular momentum and the spin angular momentum are

$$J^2 = j(j+1)\hbar^2, \quad L^2 = l(l+1)\hbar^2, \quad S^2 = s(s+1)\hbar^2$$

$$J^2 - L^2 - S^2 = 2\vec{L} \cdot \vec{S}$$

$$\vec{L} \cdot \vec{S} = \frac{1}{2} [J^2 - L^2 - S^2] = \frac{1}{2} [j(j+1) - l(l+1) - s(s+1)] \hbar^2$$

$$\vec{L} \cdot \vec{S} = \frac{1}{2} \left[j(j+1) - l(l+1) - \frac{1}{2} \left(\frac{1}{2} + 1 \right) \right] \hbar^2$$

$$\vec{L} \cdot \vec{S} = \frac{1}{2} \left[j(j+1) - l(l+1) - \frac{3}{4} \right] \hbar^2 \quad (30)$$

If $j = l + \frac{1}{2}$, Eq. (30) becomes $\vec{L} \cdot \vec{S} = \frac{1}{2} \left[\left(l + \frac{1}{2} \right) \left(l + \frac{1}{2} + 1 \right) - l(l+1) - \frac{3}{4} \right] \hbar^2$

$$\vec{L} \cdot \vec{S} = \frac{1}{2} \hbar^2 \quad (31)$$

If $j = l - \frac{1}{2}$, Eq. (30) becomes $\vec{L} \cdot \vec{S} = \frac{1}{2} \left[\left(l - \frac{1}{2} \right) \left(l - \frac{1}{2} + 1 \right) - l(l+1) - \frac{3}{4} \right] \hbar^2$

$$\vec{L} \cdot \vec{S} = -\frac{1}{2} (l+1) \hbar^2 \quad (32)$$

There are two possible conditions such as $j = l + \frac{1}{2}$ and $j = l - \frac{1}{2}$.

If $j = l + \frac{1}{2}$, Eq. (24) becomes

$$V_{l,s}(r) = V_{so} \left[\frac{\hbar}{m_{\pi} c} \right]^2 \left(\frac{1}{2} \right) \frac{1}{r} \frac{d\rho(r)}{dr} \quad (33)$$

If $j = l - \frac{1}{2}$, Eq. (24) becomes

$$V_{l,s}(r) = V_{so} \left[\frac{\hbar}{m_{\pi} c} \right]^2 \left(-\frac{1}{2}(1+1) \right) \frac{1}{r} \frac{d\rho(r)}{dr} \tag{34}$$

The spin orbit interaction term of Eq. (33) and (34) are substituted in Eq. (19) then we get

$$V(r) = V_0(r) + V_{so} \left[\frac{\hbar}{m_{\pi} c} \right]^2 \left(\frac{1}{2} 1 \right) \frac{1}{r} \frac{d\rho}{dr} + V_c(r)$$

$$V(r) = V_0(r) + V_{so} \left[\frac{\hbar}{m_{\pi} c} \right]^2 \left(-\frac{1}{2}(1+1) \right) \frac{1}{r} \frac{d\rho}{dr} + V_c(r)$$

Results and Discussions

Firstly, the proton single-particle energies of ^{90}Zr for various states such as s, p, d and f states of $1 + \frac{1}{2}$ case and $1 - \frac{1}{2}$ case were calculated by using phenomenological Woods-Saxon potential and the calculated results are shown in Fig. (2) and (3).

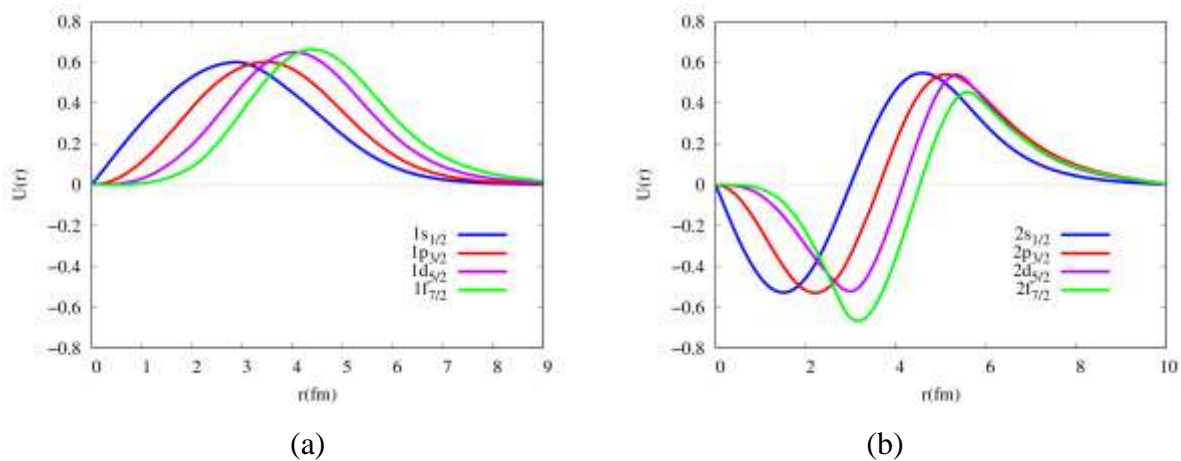


Figure (2) (a) Proton wave functions $\left(1 + \frac{1}{2}\right)$ case for $1s_{1/2}, 1p_{3/2}, 1d_{5/2}, 1f_{7/2}$ states

(b) Proton wave functions $\left(1 + \frac{1}{2}\right)$ case for $2s_{1/2}, 2p_{3/2}, 2d_{5/2}, 2f_{7/2}$ states

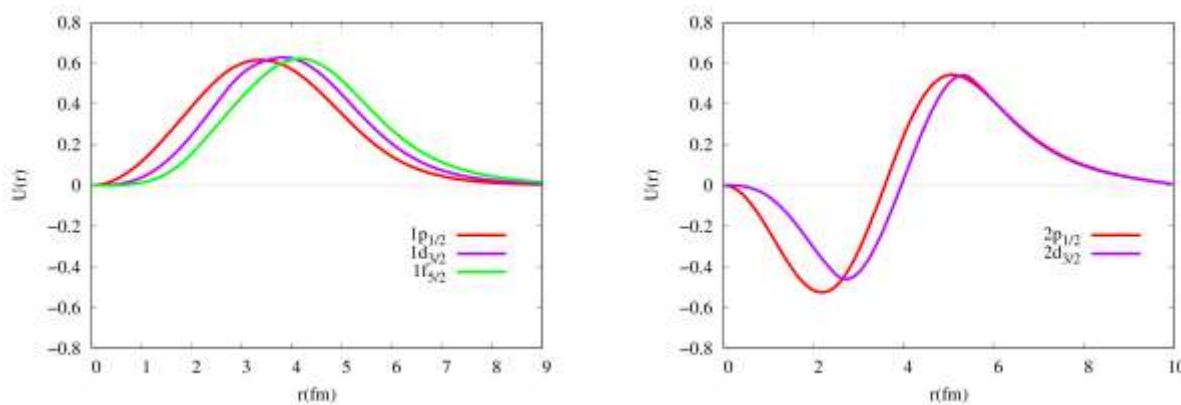


Figure (3) (a) Proton wave functions $\left(1 - \frac{1}{2}\right)$ case for $1p_{1/2}, 1d_{3/2}, 1f_{5/2}$ states

(b) Proton wave functions $\left(1 - \frac{1}{2}\right)$ case for $2p_{1/2}, 2d_{3/2}$ states

Fig. (2) and (3) show the calculated results of various s states, p states and d states proton wave functions with phenomenological Woods-Saxon potential for ^{90}Zr . The wave functions are shifted to outer region for higher orbital angular momentum and it is seen that all wave functions are finite. There is no node in 1s, 1p, 1d and 1f states and one node in 2s, 2p, 2d and 2f states of both $(1 + \frac{1}{2})$ and $(1 - \frac{1}{2})$ cases. Similarly, the neutron single-particle energies of ^{90}Zr in various states were obtained in the same way. But neutron is a chargeless particle so Coulomb potential are not taken into account in this calculation. Then the calculated results are shown in Figure (4) and (5).

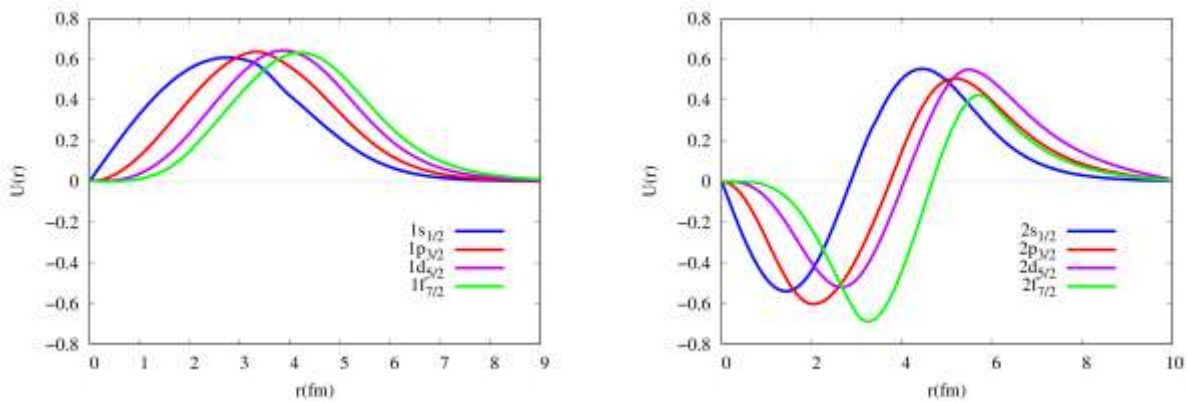


Figure (4) (a) Neutron wave functions $(1 + \frac{1}{2})$ case for $1s_{1/2}, 1p_{3/2}, 1d_{5/2}, 1f_{7/2}$ states
 (b) Neutron wave functions $(1 + \frac{1}{2})$ case for $2s_{1/2}, 2p_{3/2}, 2d_{5/2}, 2f_{7/2}$ states

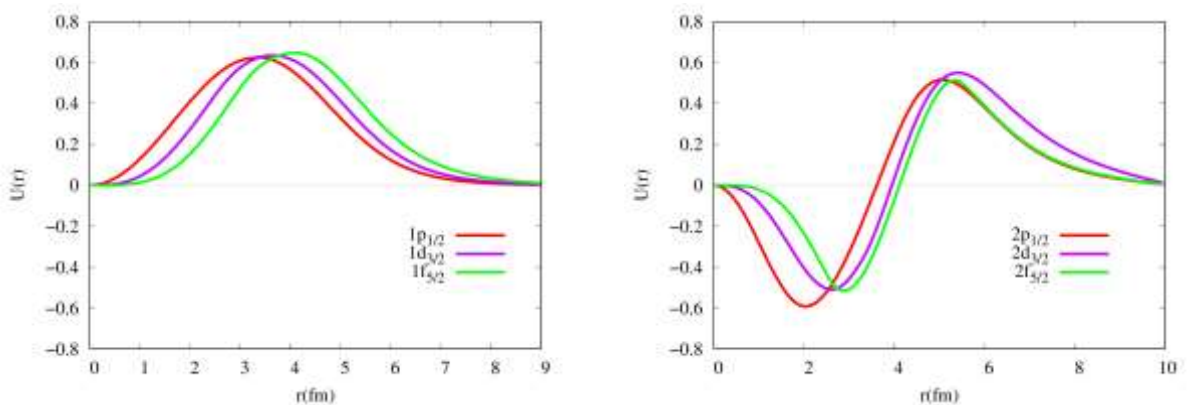


Figure (5) (a) Neutron wave functions $(1 - \frac{1}{2})$ case for $1p_{1/2}, 1d_{3/2}, 1f_{5/2}$ states
 (b) Neutron wave functions $(1 - \frac{1}{2})$ case for $2p_{1/2}, 2d_{3/2}, 2f_{5/2}$ states

Figure (6) (a) and (b) shows energy levels for proton and neutron state for $(1 + \frac{1}{2})$ and $(1 - \frac{1}{2})$ cases. According to this figure, 1s state has the largest binding energy among the other states. If the nucleon is in the innermost shell of the nucleus, it will have largest binding energy and gradually decreases with shell level ordering.

Finally, the calculated results were compared with two sets parameters of Skyrme type effective nucleon-nucleon interaction BsK1, SVIII and the available experimental data in Table (1) and (2). The results were agreed with these two theoretical and experimental results.

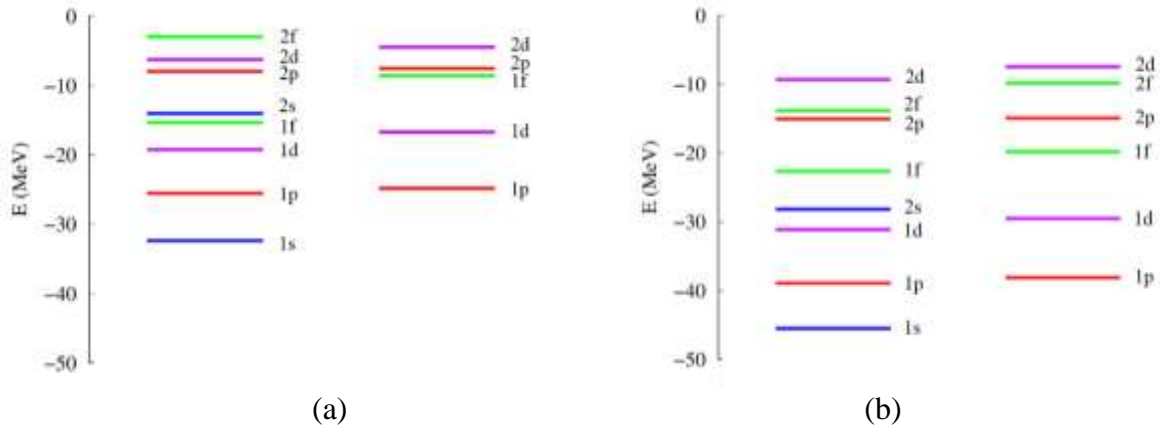


Figure (6) (a) Proton single-particle energy levels for $(1 + \frac{1}{2})$ case and $(1 - \frac{1}{2})$ case
 (b) Neutron single-particle energy levels for $(1 + \frac{1}{2})$ case and $(1 - \frac{1}{2})$ case

Table 1 Comparison of experimental results, Skyrme type interaction based two set parameters and our calculated results for proton single-particle energies in ^{90}Zr

Subshell	Exp	Skyrme type effective nucleon-nucleon interaction		Our calculated results
		BsK1	SVIII	
$1s_{1/2}$	43 ± 8	33.02	32.44	32.36
$2s_{1/2}$	-	16.78	16.58	15.84
$1p_{3/2}$	35 ± 8	27.17	27.72	25.51
$2p_{3/2}$	-	8.79	8.02	7.92
$1d_{5/2}$	27 ± 8	21.27	21.72	19.21
$2d_{5/2}$	-	-	-	7.22
$1f_{7/2}$	-	14.47	14.70	15.32
$2f_{7/2}$	-	-	-	2.93
$1p_{1/2}$	33 ± 8	24.45	26.29	24.80
$2p_{1/2}$	-	7.21	6.58	8.30
$1d_{3/2}$	26 ± 8	17.63	18.66	16.69
$2d_{3/2}$	-	-	-	4.43
$1f_{5/2}$	-	8.65	9.65	8.53

Table 2 Comparison of experimental results, Skyrme type interaction based two set parameters and our calculated results for neutron single-particle energies in ^{90}Zr

Subshell	Exp	Skyrme type effective nucleon-nucleon interaction		Our calculated results
		BsK1	SVIII	
$1s_{1/2}$	-	45.31	43.78	45.51
$2s_{1/2}$	-	27.85	27.54	28.14
$1p_{3/2}$	-	39.19	37.94	38.90
$2p_{3/2}$	15.10	15.78	15.17	15.01
$1d_{5/2}$	-	30.37	30.27	31.17
$2d_{5/2}$	-	8.71	8.74	9.30
$1f_{7/2}$	-	22.00	21.95	22.62
$2f_{7/2}$	-	-	-	13.81
$1p_{1/2}$	-	38.27	37.81	38.13
$2p_{1/2}$	13.60	14.87	14.52	14.91
$1d_{3/2}$	-	28.98	28.48	29.5
$2d_{3/2}$	-	7.11	7.40	7.42
$1f_{5/2}$	18.50	19.19	18.98	19.81
$2f_{5/2}$	-	-	-	9.83

Conclusion

In this paper, the nucleon wave functions and their single-particle energy levels in ^{90}Zr were investigated by solving one-body Schrödinger equation within the frame work of numerov method. The results of all of wave functions were found to be convergent. In this investigation, phenomenological Woods-Saxon central potential including spin-orbit interaction was used. The numerical calculation was solved by using FORTRAN-90 code. Then the calculated results were compared with two set parameters of Skyrme type based nucleon-nucleon interaction and available experimental results. As a result, the calculated shell structures of nucleon single-particle energies were agreed with both theoretical and experimental results. Therefore, numerov method is reliable for investigation of single-particle energy of nuclei and our program code is also reliable to use one body potential form.

Acknowledgements

My great thank goes to Dr May Saw Ohn, Associate Professor, Department of Physics, Yadanabon University, for her warm support, valuable ideas and advices throughout my research.

References

- Signoracci, A. and B. Alex Brown (2007) "Proton Single-particle Energies in ^{23}F ", Phys. Rev. C 75 024303.
- Taqi, Ali H. and Zainab Q. Mosa (2020) "Nuclear Structure of Zirconium Isotopes $^{90,96,106}\text{Zr}$ Using Skyrme HF-RPA" *Egyptian Journal of Physics*, Egypt, vol.48, pp.1-9.

LAMBDA SINGLE-PARTICLE ENERGY LEVELS IN ${}^{139}_{\Lambda}La$ BY USING NUMEROV METHOD

May Saw Ohn*

Abstract

In this research paper, the Λ single particle energies and radial wave functions of ${}^{139}_{\Lambda}La$ have been investigated, by solving numerically Schrödinger equation with Numerov Method. The phenomenological Woods-Saxon central potential and Woods-Saxon potential including spin orbit term are used in this calculation. The root-mean square distances between Λ and core nucleus ${}^{139}_{\Lambda}La$ were calculated with normalized wave function. In this calculation, Λ single particle energy levels of ${}^{139}_{\Lambda}La$ are $1s_{1/2}$, $1p_{1/2}$, $1p_{3/2}$, $1d_{3/2}$, $1d_{5/2}$, $1f_{5/2}$, $1f_{7/2}$, $1g_{9/2}$, $2s_{1/2}$, $2p_{1/2}$, $2p_{3/2}$. This calculated results are agree with H.Bando calculated results and slightly different from experimental results.

Keywords: Numerov method, Behaviour of wave functions and energy levels, Lambda hyper nuclei.

Introduction

Hyperon and Hypernucleus

Hyperons are special class of baryons and consisting of one or more strange quarks. All hyperons are fermions and they have half-integer spin. Hyperons are unstable particles and heavier than nucleons. They have the life time of the order of 10^{-10} s and they decay weakly into nucleons and light particles such as π -mesons, electrons and neutrinos. Their formation time is 10^{-23} s which is typical for strong interaction.

Various types of hyperons are lambda (Λ^0), sigma ($\Sigma^-, \Sigma^0, \Sigma^+$), xi (Ξ^-, Ξ^0) and omega (Ω). All hyperons have a spin of (1/2), but omega has a spin of (3/2). The Λ hyperon is an isospin singlet of strangeness -1. The Σ hyperon occurs as an isospin triplet of baryons $\Sigma^-, \Sigma^0, \Sigma^+$ and they have strangeness -1. The cascade particles xi (Ξ^-, Ξ^0) have strangeness -2. The omega-minus (Ω) is strangeness -3 because it is composed of three strange quarks.

The lambda hyperon Λ^0 was firstly discovered in October 1950, by V.D.Hopper and S. Biswas of the University of Melbourne, as a neutral V particle with a proton as decay product, thus correctly distinguishing it as a baryon. Λ hyperon is the lightest particle and it can stay in contact with nucleons inside the nucleus and form lambda-hypernucleus. It has zero charge, zero isospin, the strangeness number -1 and the value of mass 1115.684 ± 0.006 MeV/c². Λ hyperon is composed of three quarks; (uds).

In today's nuclear physics, new nuclei or nuclear matter have been searched for along new axes such as isospin, spin and new flavor, namely strangeness. In the strangeness nuclear physics, new nuclei which has strangeness quantum number has been produced to study its structure and hence to gain information about nuclear force with strangeness. A hypernucleus consists of one or more hyperons bound to a nuclear core in addition to nucleon. The first hypernucleus was discovered in Warsaw in September 1952 by Marian Danysz and Jerzy Pniewski. The first hypernucleus was discovered in nuclear emulsion experiments as a fragment from the nuclear reaction by cosmic ray. A Λ -hypernucleus ${}^{\Lambda}_X$ is a bound state of Z protons, (A-Z-1) neutrons and a Λ -hyperon.

* Department of Physics, Yadanabon University.

Interactions

In research paper, we use the phenomenological Λ -nucleus potential which has the Woods-Saxon form as in equation (1).

$$V_{\Lambda}(r) = \frac{V_s}{1 + \exp\left(\frac{r-R}{a}\right)} \quad (1)$$

where, V_0 =depth of the potential well

A =mass number of the core nucleus

V_s =strength of Woods-Saxon potential

R =radius of the core nucleus

a =the diffuseness parameter

Phenomenological Woods-Saxon Potential For Λ -Core Nucleus

In this calculation, we considered that a Λ moves freely in an average potential well generated by the other nucleus. To study the Λ single-particle energy level of ${}^{139}_{\Lambda}La$, the phenomenological Woods-Saxon potential energies is used which is described by the following equation (2),

$$V_{w.s} = -V_0 \rho(\mathbf{r}) \quad (2)$$

where, V_0 is the strength of Woods-Saxon potential and the nuclear density $\rho(\mathbf{r}) = \frac{1}{1 + e^{r-R/a}}$.

Woods-Saxon potential together with spin-orbit interaction which is described as follows:

$$V_{\ell.s} = V_{so} \left(\frac{\hbar}{m_{\pi} c} \right)^2 (\ell \cdot s) \frac{1}{r} \frac{d\rho(\mathbf{r})}{dr} \quad (3)$$

Woods-Saxon potential including spin-orbit interaction is

$$V(\mathbf{r}) = V_{w.s}(\mathbf{r}) + V_{\ell.s}(\mathbf{r})$$

Thus, the potential becomes;

$$V(\mathbf{r}) = -V_0 \rho(\mathbf{r}) + V_{so} \left(\frac{\hbar}{m_{\pi} c} \right)^2 (\ell \cdot s) \frac{1}{r} \frac{d\rho(\mathbf{r})}{dr} \quad (4)$$

where, R =nuclear radius= $r_0 A^{1/3} = 1.1 A^{1/3}$ fm

r = radial distance from the centre

a = diffuseness parameter=0.6fm

V_0 = strength of Woods-Saxon potential

V_{so} = spin-orbit constant and

$\frac{\hbar}{m_{\pi} c}$ = Compton wavelength

The chosen parameters for the potential strength V_{so} and V_0 are 4MeV and 30 MeV.

The scalar product of LS coupling is

$$\ell \cdot \mathbf{s} = \frac{1}{2} \left(\mathbf{j}(\mathbf{j} + \mathbf{1}) - \ell(\ell + \mathbf{1}) - \frac{\mathbf{3}}{\mathbf{4}} \right) \tag{5}$$

If the potential is the phenomenological Woods-Saxon

For $j = \ell + \frac{1}{2}$ state, $\ell \cdot s = \frac{1}{2} \ell$ and the potential can be expressed as the following equation,

$$\mathbf{V}(\mathbf{r}) = \frac{-\mathbf{V}_0}{\mathbf{1} + \mathbf{e}^{(\mathbf{r}-\mathbf{R})/\mathbf{a}}} - \mathbf{V}_{so} \left(\frac{\hbar}{\mathbf{m}_\pi \mathbf{c}} \right)^2 \left(\frac{\mathbf{1}}{\mathbf{2}} \ell \right) \left(\frac{\mathbf{1}}{\mathbf{r}} \frac{\mathbf{e}^{(\mathbf{r}-\mathbf{R})/\mathbf{a}}}{(\mathbf{1} + \mathbf{e}^{(\mathbf{r}-\mathbf{R})/\mathbf{a}})^2} \frac{\mathbf{1}}{\mathbf{a}} \right) \tag{6}$$

For $j = \ell + \frac{1}{2}$ state, $\ell \cdot s = -\frac{1}{2}(\ell + 1)$ and we can express the potential as

$$\mathbf{V}(\mathbf{r}) = \frac{-\mathbf{V}_0}{\mathbf{1} + \mathbf{e}^{(\mathbf{r}-\mathbf{R})/\mathbf{a}}} + \mathbf{V}_{so} \left(\frac{\hbar}{\mathbf{m}_\pi \mathbf{c}} \right)^2 \frac{\mathbf{1}}{\mathbf{2}} (\ell + \mathbf{1}) \left(\frac{\mathbf{1}}{\mathbf{r}} \frac{\mathbf{e}^{(\mathbf{r}-\mathbf{R})/\mathbf{a}}}{(\mathbf{1} + \mathbf{e}^{(\mathbf{r}-\mathbf{R})/\mathbf{a}})^2} \frac{\mathbf{1}}{\mathbf{a}} \right) \tag{7}$$

Calculations

Numerov Method

The Schrodinger Radial Equation (SRE) is

$$\frac{\mathbf{d}^2 \mathbf{u}(\mathbf{r})}{\mathbf{d}\mathbf{r}^2} + \frac{2\mu}{\hbar^2} \left[\mathbf{E} - \mathbf{V}(\mathbf{r}) - \frac{\hbar^2}{2\mu} \frac{\ell(\ell + \mathbf{1})}{\mathbf{r}^2} \right] \mathbf{u}(\mathbf{r}) = \mathbf{0} \tag{8}$$

where E is total energy of the system, V is the potential energy of the system due to the forces acting between the two nucleons, μ is reduced mass and $u(r) = r R_{nl}$ is the reduced radial wave function.

At the origin: $u(r) : u(r \rightarrow 0) \rightarrow r^{\ell+1}$

The asymptotic solution at $r \rightarrow \infty : u(r \rightarrow \infty) \rightarrow u(r) = e^{-\alpha r^2}$, $\alpha = \text{constant}$

The SRE can be written as $\frac{\mathbf{d}^2 \mathbf{u}(\mathbf{r})}{\mathbf{d}\mathbf{r}^2} + \mathbf{k}(\mathbf{r}) \mathbf{u}(\mathbf{r}) = \mathbf{0}$ (9)

$$\mathbf{k}(\mathbf{r}) = \frac{2\mu}{\hbar^2} \left[\mathbf{E} - \mathbf{V}(\mathbf{r}) - \frac{\hbar^2}{2\mu} \frac{\ell(\ell + \mathbf{1})}{\mathbf{r}^2} \right] \text{ is kernel equation of the equation:}$$

Here (setting $\ell = 0$), Schrodinger's Equation becomes $\frac{\mathbf{d}^2 \mathbf{u}(\mathbf{r})}{\mathbf{d}\mathbf{r}^2} = \mathbf{u}''(\mathbf{r}) = -\mathbf{k}(\mathbf{r}) \mathbf{u}(\mathbf{r})$

can be solved by Numerov Algorithm as follows:

Firstly, we split the r range into N points according to $r_n = r_{n-1} + h$ (where h is the step); then we write the wave function $u_n \equiv u(r_n) = u(r_{n-1} + h)$, and $k_n \equiv k(r_n) = k(r_{n-1} + h)$.

By using Taylor's series, we calculate the Forward Recursive Relation and Backward Recursive Relation,

Forward Recursive Relation,

$$\mathbf{u}_n = \frac{2 \left[1 - \frac{5h^2}{6} \mathbf{k}_{n-1} \right] \mathbf{u}_{n-1} - \left[1 + \frac{h^2}{12} \mathbf{k}_{n-2} \right] \mathbf{u}_{n-2}}{\left[1 + \frac{h^2}{12} \mathbf{k}_n \right]} \quad (10)$$

Backward Recursive Relation,

$$\mathbf{u}_{n-1} = \frac{2 \left[1 - \frac{5h^2}{6} \mathbf{k}_n \right] \mathbf{u}_n - \left[1 + \frac{h^2}{12} \mathbf{k}_{n+1} \right] \mathbf{u}_{n+1}}{\left[1 + \frac{h^2}{12} \mathbf{k}_{n-1} \right]} \quad (11)$$

Therefore, when we calculate our wave function using the backward-forward recursive technique, we should note that the recursive formulas imply having knowledge of two initial values for each direction. Since both $u_{\text{out}}(r)$ and $u_{\text{in}}(r)$ satisfy a homogeneous equation, their normalization can always be chosen so that they are set to be equal at the r_c point. An energy eigen value is then signaled by the equality of derivatives at this point.

At the matching point the eigen functions $u_{\text{out}}(r)$ and $u_{\text{in}}(r)$ and first derivatives $u'_{\text{out}}(r)$ and $u'_{\text{in}}(r)$ must all satisfy the continuity conditions:

$$\left. \begin{aligned} (u_{\text{out}})_{r_c} &= (u_{\text{in}})_{r_c} \\ (u'_{\text{out}})_{r_c} &= (u'_{\text{in}})_{r_c} \end{aligned} \right\}$$

thus, we can write the corresponding condition for the logarithmic derivative at r_c as

$$\left[\frac{u'_{\text{out}}}{u_{\text{out}}} \right]_{r_c} = \left[\frac{u'_{\text{in}}}{u_{\text{in}}} \right]_{r_c} \quad (12)$$

and then we define a $G(E)$ function at whose value zeros correspond to the energy eigenvalues as

$$\mathbf{G}(E) = \left[\frac{u'_{\text{out}}}{u_{\text{out}}} \right]_{r_c} - \left[\frac{u'_{\text{in}}}{u_{\text{in}}} \right]_{r_c} \quad (13)$$

Therefore, we proceed numerically in the following way: we set a trial energy range splitting this E range into N points, corresponding to where is the energy step. For each we calculate their eigenfunctions and at the point; and we build the $G(E)$ function here, looking for a change of sign in it (which implies a zero cross). Once we find it, we perform a fine turning closing the energy range until the required tolerance.

Root-mean square distance

Root-mean-square distance means the maximum probability distance between Lanthanum core nucleus and lambda particle. The root-mean square distance is evaluated by the following equation with the numerical calculated results of wave functions.

$$\left\langle \sqrt{\bar{r}_{\text{rms}}} \right\rangle^2 = \int \Psi^* r^2 \Psi dr \quad (14)$$

Results and Discussion

The Λ single-particle energies of $^{139}_{\Lambda}La$ and corresponding wave functions have been investigated by solving Numerically Schrodinger radial equation with Numerov Method. Numerov Method can be evaluated both energy eigen values and wave functions simultaneously. This method can be calculated both bound state problems and scattering problems. Bound state energies give negative values and Scattering gives positive values. In this paper, about the bound state energies have been calculated. And also calculated the radial wave functions and corresponding root mean square distances. Lambda single particle energy levels are summarized in Table (1).The calculated results of Binding energy with W-S potential without L-S term are shown in Table (2). The single-particle energy levels of $^{139}_{\Lambda}La$ is are $1s_{1/2}$, $1p_{1/2}$, $1p_{3/2}$, $1d_{3/2}$, $1d_{5/2}$, $1f_{5/2}$, $1f_{7/2}$, $1g_{9/2}$, $2s_{1/2}$, $2p_{1/2}$, $2p_{3/2}$. The energy level diagrams for these Λ hypernuclei are in Figure (5). The calculated results by using Woods-Saxon potential including spin-orbit interaction are in good agreement with H.BANDO results and quite different from experimental results. To agree with experimental data, the calculations need to consider the additional potential such as spin-spin interaction, paring effect etc.

Table (1) BANDO calculated results, calculated results and experimental results with W-S potential including L-S term.

States	H. BANDO Calculated Results	Calculated Results (MeV)	Experimenal results (MeV)	Calculated RMS (fm)
$1s_{1/2}$	-24.7	-24.66	-24.5 ± 0.6	1.6064
$1p_{1/2}$		-19.45	-20.4 ± 0.6	1.911
$1p_{3/2}$	-19.7	-19.73		1.9277
$1d_{3/2}$		-13.39	-14.3 ± 0.6	2.1484
$1d_{5/2}$	-14.1	-14.02		2.1745
$1f_{5/2}$		-6.635	-8.0 ± 0.6	2.3703
$1f_{7/2}$	-7.8	-7.75		2.3936
$1g_{9/2}$	-1.2	-1.087		2.6239
$2s_{1/2}$		-12.06		2.0649
$2p_{1/2}$		-4.95		2.4016
$2p_{3/2}$	-5.4	-5.34		2.3955

Table (2) The calculated results of Binding energy with W-S potential without L-S term.

States	1s	1p	2p	1d	1f
Calculated Results (MeV)	-24.658	-19.638	-5.209	-13.77	-7.265
RMS (fm)	1.6066	1.9219	2.3975	2.1634	2.3844

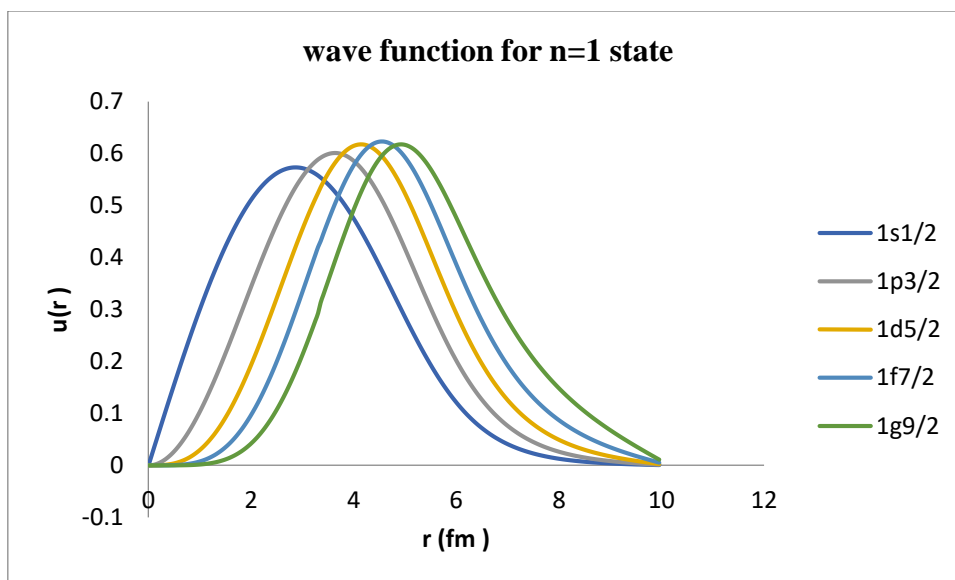


Figure 1 Behaviour of wave function of Lambda in Woods-Saxon potential well for $n = 1$ state ($^{139}_{\Lambda}La$)

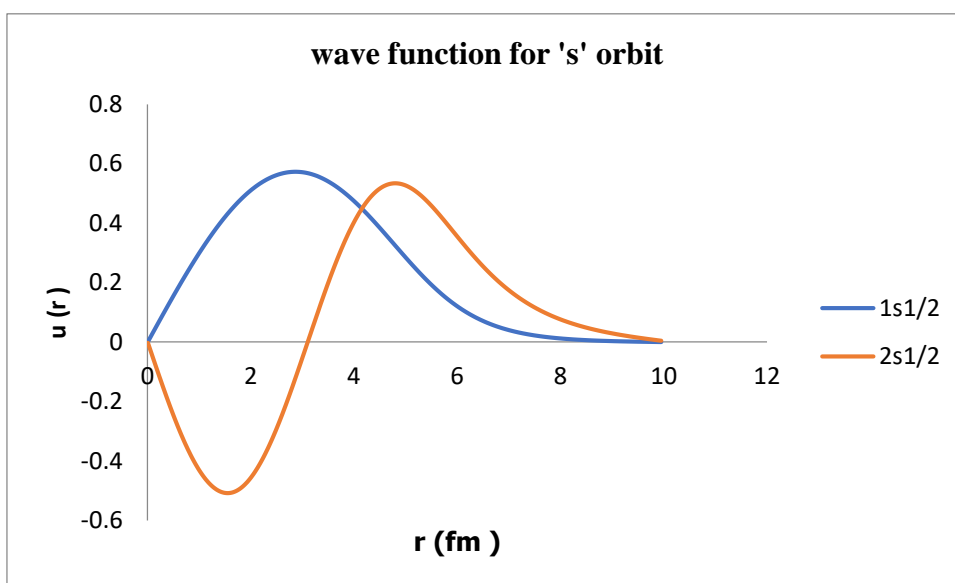


Figure 2 Behaviour of wave function of Lambda in Woods-Saxon potential well for $1s_{1/2}$ state and $2s_{1/2}$ state ($^{139}_{\Lambda}La$)

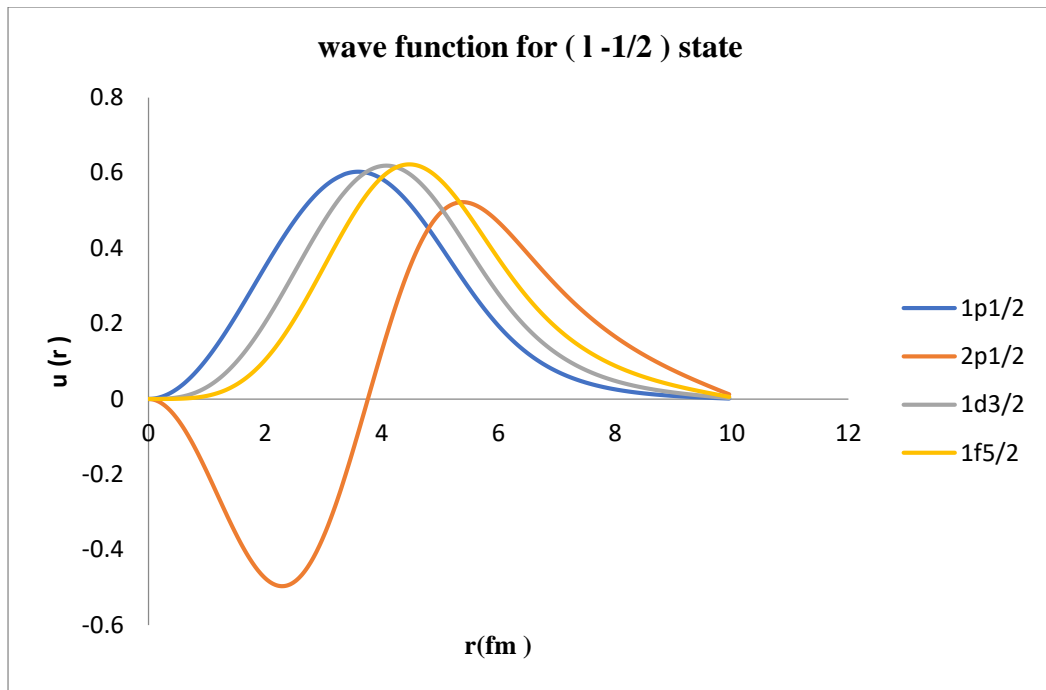


Figure 3 Behaviour of wave function of Lambda in Woods-Saxon potential well for $\left(\ell - \frac{1}{2}\right)$ state in $({}^{139}_{\Lambda}La)$

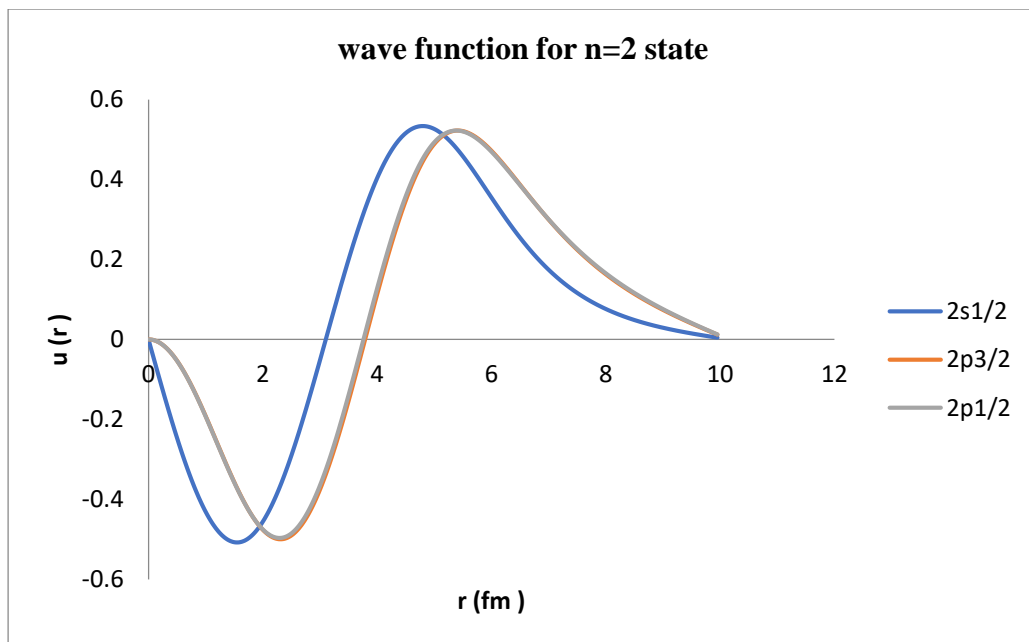


Figure 4 Behaviour of wave function of Lambda in Woods-Saxon potential well for $2s_{1/2}$ state, $2p_{3/2}$ state and $2p_{1/2}$ state $({}^{139}_{\Lambda}La)$

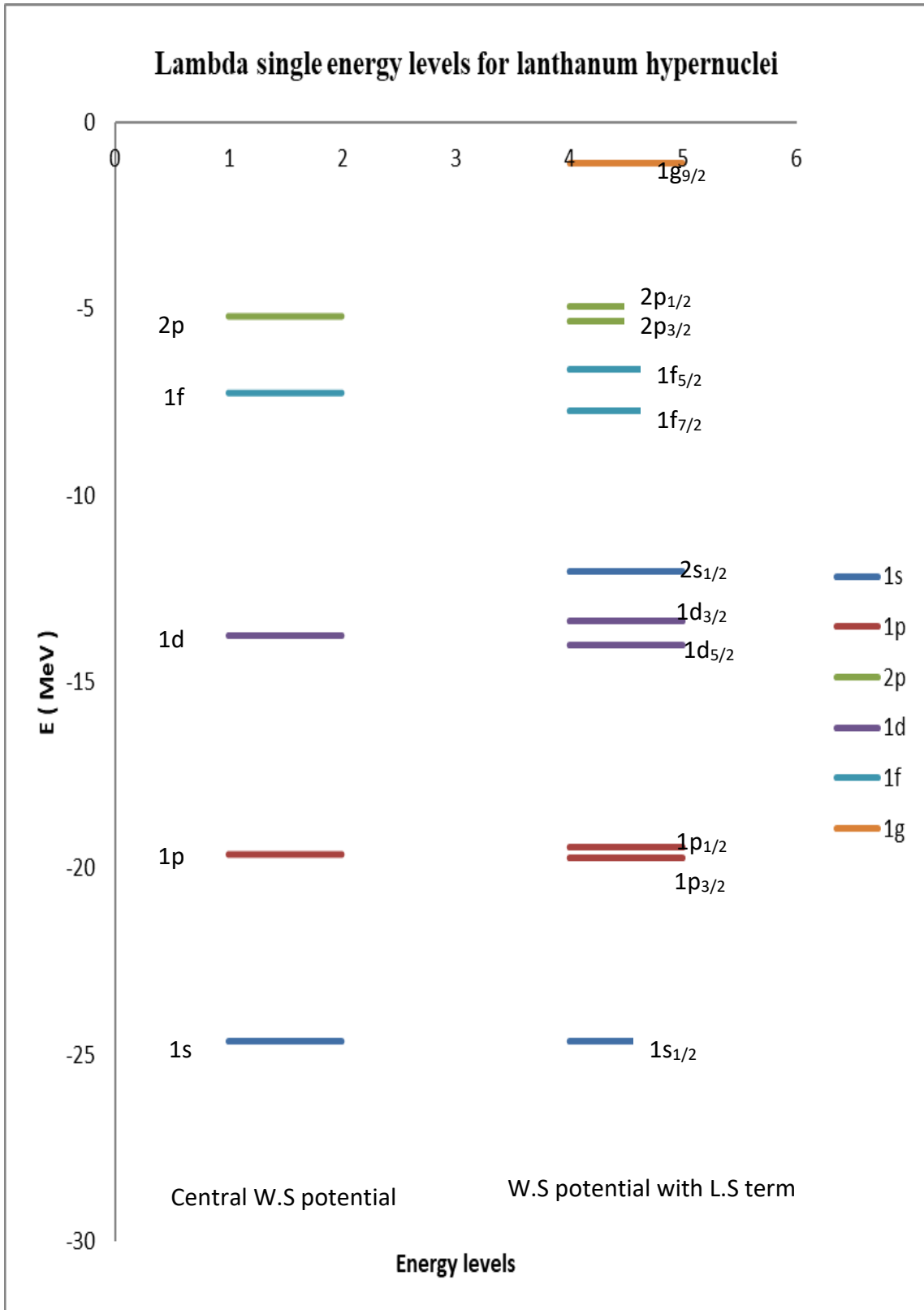


Figure 5 Energy level diagram of $^{139}_{\Lambda}La$ for Woods-Saxon potential with central term and Woods-Saxon potential including spin orbit term.

Conclusion

The Λ hyperon does not suffer from Pauli blocking by the other nucleons, it can penetrate into the nuclear interior and form deeply bound hypernuclear states. There are no nodes for principal quantum number $n = 1$, one node for $n = 2$. The wave function is shifted to outer region for higher orbital angular momentum. The higher the orbital angular momentum, the higher the spacing between $(\ell + \frac{1}{2})$ and $(\ell - \frac{1}{2})$. According to calculated results, there is no nuclear bound state above $1g_{9/2}$ state for ${}^{139}_{\Lambda}\text{La}$ system. After the research, the analytical and numerical calculation about the Numerov method have been known. And also, the behavior of wave functions, energy levels and the corresponding root mean square distances have been known.

Acknowledgement

I would like to thank Rector Dr Tint Moe Thu Zar. Yadanabon University, for her kind permission to conduct this paper. I am also thankful to Professor Dr Khin Thidar, Head of Physics Department and Professor Dr Sandar Min, Physics Department, Yadanabon University, for their permission to do this research.

I am very thankful to my PhD supervisor, professor Dr Khin Swe Myint, Rector (Rtd), University of Mandalay, for her valuable advice and encouragement.

References

- H. Tamura, (2012) , Prog. Theo. Expt. Phys.**1**, 02B012.
- H. Bando, T. Motoba and J. Zofka, (1990), Intl. J. Mod.Phys.A **5**, 4079 and references are therein.
- H. Tamura and O. Hashimoto, (2005), Prog. Part. Nucl. Phys. **57**, 564.
- M. Danysz and J. Pniewski, (1953), Philos. Mag. **44**, 348.
- M.Ikramet *et al.*, (2014), Intl. J. Mod. Phys. **E**.
- O. Hashimoto and H. Tamura, (2006), Prog. Part. Nucl. Phys. **57**, 564.
- V.D. Hopper and S. Biswas, (1950), 'Evidence concerning the existence of the new unstable elementary neutral particle', Phys. Rev. **80**, 1099.

INVESTIGATION OF RADIOACTIVE ELEMENTS IN SEDIMENTS FROM THE AYEYARWADY RIVER BANK AT MAGWAY TOWNSHIP

Hnin Thidar Soe¹, Nanda Phone Lin Wai², Ei Thiri Khaing³

Abstract

The radioactive elements contain in sediment of Ayeyarwady River Bank at Magway Township were determined by Gamma Ray Spectroscopy of HPGe Detector. The aim of this study is to determine the natural (²³⁸U, ²³²Th, ⁴⁰K) radioactive levels in sediments collected from four different places in Ayeyarwady River Bank and also Ra_{eq} , D_R and H_{ex} will be calculated and compared with the recommended levels from UNSCEAR (2000) reports. The concentration of the natural radionuclide activity of ²²⁶Ra, ²³²Th, and ⁴⁰K are 0.0456 Bqkg⁻¹, 14.1361 Bqkg⁻¹ and 1.1639 Bqkg⁻¹ were observed. These values are lower than the worldwide average value. The radiation hazard parameters of radium equivalent activity, absorbed dose rate and external hazard index for all samples are 20.3754 Bqkg⁻¹, 8.6079nGh⁻¹ and 0.0549 mSvy⁻¹. These are not exceeded the maximum admissible limit. So, it can be assumed that the sediments are not hazard to the surrounding.

Keywords: Radium Equivalent Activity (Ra_{eq}), Absorbed Dose Rate (D_R), External Hazard Index (H_{ex}), HPGe Detector and radionuclide

Introduction

Naturally Occurring Radiation

Naturally occurring radiation or so-called “background radiation” can be found all around us. Natural radioactivity widely exists in the air, water, plants and the soil of earth’s environment. Radiation come from soil have a significant portion of background radiation exposure of the population. Because it occurs in our natural environment, we encounter it every day through the food we eat, the water we drink, and the air we breathe. It is also in building materials and items we commonly use.

Natural environmental radioactivity and the associated external exposure due to gamma radiation depend primarily on the geological and geographical conditions and appear at different levels in the soils of each region in the world. Gamma radiation emitted from terrestrial materials is known as the major external source that affects the human body. The interaction of radiation with human body leads to various biological effects which may later show up many diseases. Information of radioactive level of an environment leads to control and preventing of diseases. Therefore, monitoring natural radioactivity in the environment is an important parameter for public health studies and assessing possible changes in the environment radioactivity. The aim of this study is to determine the natural (²³⁸U, ²³²Th, ⁴⁰K) radioactive levels in sediments collected from different four places in Ayeyarwady River Bank and also Ra_{eq} , D_R and H_{ex} will be calculated and compared with the recommended levels from UNSCEAR (2000) reports.

Radioactivity Measurements

Activity Calculations

The specific activity of ²³⁸U, it is found from gamma-ray lines of ²²⁶Ra at 186.04 keV, ²¹⁴Pb at 295.34 keV, ²¹⁴Pb at 351.69 keV and ²¹⁴Bi at 609.61 keV while the specific activity of ²³²Th was evaluated from gamma-ray lines of ²⁰⁸Tl at 75.43 keV, ²¹²Pb at 238.61 keV and ²⁰⁸Tl at 583.71

¹ Department of Physics, Yadanabon University

² Department of Physics, Yadanabon University

³ Department of Physics, Yadanabon University

keV. The specific activity of ^{40}K was determined directly from its 1460.8 keV gamma-ray line. The calculation of the activity concentrations is given by equation;

$$A = \frac{N_A}{m \varepsilon P_\gamma T} \quad (1)$$

where,
 N_A = net count rate for sample,
 m = mass of the sample,
 ε = efficiency of the interest gamma energy,
 P_γ = emission probability of gamma ray intensity and
 T = counting time

Radium Equivalent Activity (R_{eq})

Radium equivalent activity (R_{eq}) is used to assess the hazards associated with materials that contain ^{226}Ra , ^{232}Th and ^{40}K in Bq kg^{-1} , which is determined by assuming that 370 Bq kg^{-1} of ^{226}Ra or 259 Bq kg^{-1} of ^{232}Th or 4810 Bq kg^{-1} of ^{40}K produce the same γ dose rate. The R_{eq} of a sample in (Bq kg^{-1}) can be achieved using the following relation;

$$R_{\text{eq}} = A_{\text{Ra}} + 1.43A_{\text{Th}} + 0.077A_{\text{K}} \quad (2)$$

where, A_{K} , A_{Ra} and A_{Th} are the specific activities of ^{226}Ra , ^{232}Th and ^{40}K in Bqkg^{-1} .

Absorbed Dose Rate (D_{R})

Absorbed dose rate (D_{R}), due to γ -rays emitted from radionuclides maintained in those samples can be calculated from the following equation;

$$D_{\text{R}} (\text{nGy h}^{-1}) = 0.462 A_{\text{Ra}} + 0.604 A_{\text{Th}} + 0.042 A_{\text{K}} \quad (3)$$

where, A_{Ra} , A_{Th} and A_{K} are the specific activities of ^{226}Ra , ^{232}Th and ^{40}K in Bqkg^{-1} .

External Hazard Index (H_{ex})

The external hazard index is an evaluation of the hazard of the natural gamma radiation. The objective of this index is to limit the radiation dose to the admissible dose equivalent limit around 1mSvy^{-1} . In order to evaluate this index, one can use the following relation;

$$H_{\text{ex}} = \frac{A_{\text{Ra}}}{370} + \frac{A_{\text{Th}}}{259} + \frac{A_{\text{K}}}{4810} \leq 1 \quad (4)$$

Materials and Methods

Sample Collection and Preparation

Four soil samples (S1, S2, S3 and S4) were collected from different places of Ayeyarwady River Bank at Magway Township, Magway region. Sample 1 (S1) was collected from near the Mya Thalon Pagoda, Sample 2 (S2) was collected from near the Magway Bridge, Sample 3 (S3) was collected from around the view point of We Love Magway and Sample 4 (S4) was collected from in front of the Nan Htike Thu Hotel. The location map of collected samples and geographic coordinates of the samples are shown in Figure 1 and Table 1. Each sample was air dried in about two weeks and removing unwanted materials by sieved with 0.5

cm meshes and ground to get homogeneous powder. Then the samples were weighed 500 g by using digital balance. And then they were analyzed by HPGe detector.

Table 1. Geographic Coordinates (latitudes and longitudes) of the Sampling Locations

No.	Sampe	Latitude	Longitude
1	S1	20° 9' 56.92" N	94° 54' 59.76" E
2	S2	20° 8' 58.59" N	94° 54' 57.62" E
3	S3	20° 8' 32.43" N	94° 55' 02.64" E
4	S4	20° 7' 59.30" N	94° 55' 28.07" E



Figure 1 Location Map for Collected Samples

Experimental Procedure

In this experiment, HPGe detector was used to detect the gamma radiation after passing through the absorbing material and this passed information (electron pulses) were amplified by preamplifier and the fast spectroscopy amplifier and collected by using MCA based on personal computer. The HPGe detector used in operating voltage is -1500V. This value is fixed for all measurements and measuring time in 7200 seconds. The experimental set-up used in this investigation is shown in Figure (2) and the detector efficiency is presented in Figure (3).



Figure 2 The Experimental Set-up

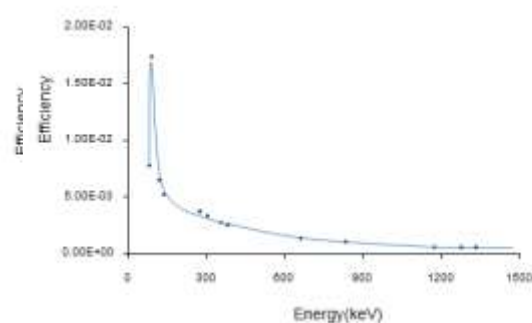


Figure 3 The Detector Efficiency

Results and Discussions

In the present work, the natural radionuclides contained in sediments samples were determined by gamma spectroscopy system. The naturally occurring gamma radionuclides: ^{212}Pb (238.22 keV), ^{228}Ac (338.12 keV), ^{214}Pb (351.76 keV), ^{208}Tl (510.68keV), ^{228}Ac (583.31 keV), ^{214}Bi (609.03 keV), ^{228}Ac (911.55 keV), ^{228}Ac (969.01keV) and ^{40}K (1460.2 keV) were identified in sediment samples.

The comparative values of background and sediment samples are shown in Figure (4) and (5). The net counts values of different sediment samples are shown in Table 2. It was found that the net area counts of ^{212}Pb (238.63 keV) is highest and ^{228}Ac (968.97 keV) is lowest. Similarly, activities with different energies are presented in Table 3 and their comparisons are described in Figure (6). The activities of ^{208}Tl (510.68 keV) and ^{228}Ac (583.41 keV) are the highest values in these elements.

Moreover, the activities of A_{Ra} , A_{Th} and A_{K} in sediment samples with worldwide average are shown in Table 4 and Figure (7). The average value of A_{Ra} is 0.0456 Bqkg^{-1} , A_{Th} is $14.1361 \text{ Bqkg}^{-1}$ and A_{K} is 1.1639 Bqkg^{-1} . These values are lower than the worldwide average value.

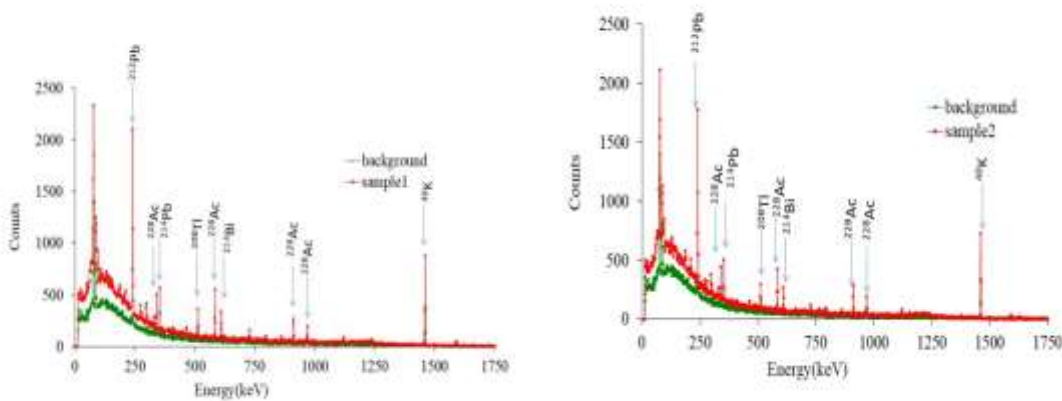


Figure 4 Comparison of background and sediment samples (S1) and (S2)

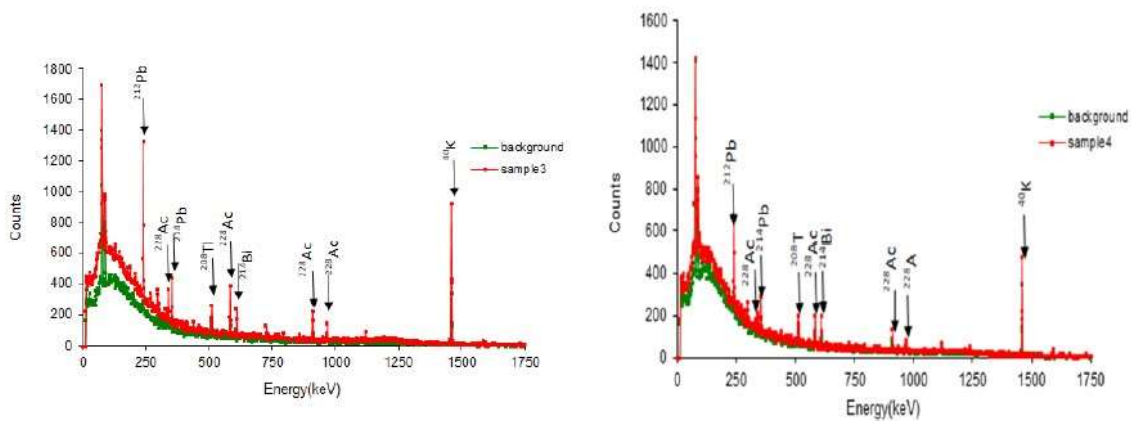


Figure 5 Comparison of background and sediment samples (S3) and (S4)

Table 2. Comparison of Net Area (counts) for Sediment Samples

No.	Series	Element	Energy (keV)	Net area (counts) for sediment samples			
				sample 1	sample 2	sample 3	sample 4
1	²³² Th	²¹² Pb	238.63	3878±448	3310±447	3268±454	3193±447
2	²³² Th	²²⁸ Ac	338.32	793±272	687±259	741±268	640±276
3	²³⁸ U	²¹⁴ Pb	351.93	933±280	807±272	766±270	832±272
4	²³² Th	²⁰⁸ Tl	510.68	439±221	365±134	406±198	414±196
5	²³² Th	²²⁸ Ac	583.41	897±275	702±289	717±250	677±287
6	²³⁸ U	²¹⁴ Bi	609.31	548±267	417±201	516±221	426±204
7	²³² Th	²²⁸ Ac	911.20	113±90	80±20	76±20	55±07
8	²³² Th	²²⁸ Ac	968.97	22±10	19±02	17±09	179±20
9	⁴⁰ K	⁴⁰ K	1460.83	1000±287	852±282	1253±292	1169±292

Table 3 Activities of Various Radionuclides in Sediment Samples

No	Series	Element	Energy (keV)	Activity Bq/kg (S1)	Activity Bq/kg (S2)	Activity Bq/kg (S3)	Activity Bq/kg (S4)
1	²³² Th	²¹² Pb	238.63	0.4878	0.4164	0.4111	0.4016
2	²³² Th	²²⁸ Ac	338.32	0.4072	0.3528	0.3805	0.3286
3	²³⁸ U	²¹⁴ Pb	351.93	0.0162	0.0140	0.0133	0.0145
4	²³² Th	²⁰⁸ Tl	510.68	37.4983	31.1774	34.6795	35.3629
5	²³² Th	²²⁸ Ac	583.41	59.0722	46.2304	47.2183	44.5841
6	²³⁸ U	²¹⁴ Bi	609.31	0.0881	0.0670	0.0829	0.0685
7	²³² Th	²²⁸ Ac	911.20	0.0406	0.0287	0.0273	0.0197
8	²³² Th	²²⁸ Ac	968.97	0.0131	0.0113	0.0101	0.1067
9	⁴⁰ K	⁴⁰ K	1460.83	1.0893	0.9281	1.3649	1.2734

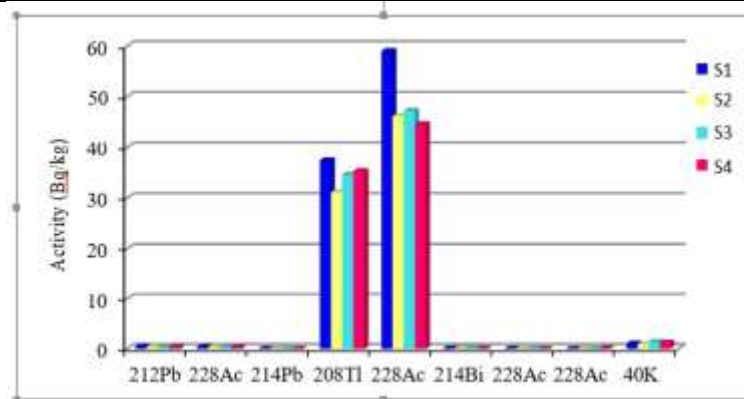


Figure 6 Comparison of Activity for Various Radionuclides in Sediment Samples

Table 4 Activities of A_{Ra} , A_{Th} and A_K in Sediment Samples with Worldwide Average

No.	Sample	A_{Ra} (Bqkg ⁻¹)	A_{Th} (Bqkg ⁻¹)	A_K (Bqkg ⁻¹)
1	S1	0.0521	16.2532	1.0893
2	S2	0.0405	13.0362	0.9281
3	S3	0.0481	13.7878	1.3649
4	S4	0.0415	13.4673	1.2734
5	Range	0.0405-0.0521	13.0362-16.2532	1.0893-1.3649
6	Average	0.0456	14.1361	1.1639
7	Worldwide Average UNSCEAR (2000)	35	30	400

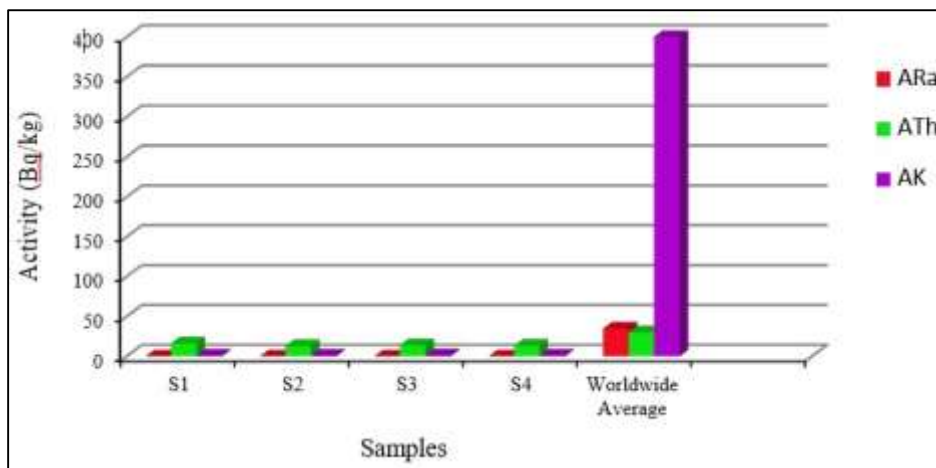


Figure 7 Values of A_{Ra} , A_{Th} and A_K in Sediment Samples Compare with Worldwide Average

The results of the radium equivalent activity, absorbed dose and external hazard index for all samples are presented in Table (5) and Figure (8). This shows that the R_{aeq} values of sediment samples varied from 18.7537 to 23.4755 Bqkg⁻¹ with an average of 20.3754 Bqkg⁻¹. It can be seen that the value of all samples does not exceed the maximum admissible value (worldwide average) of 370 Bqkg⁻¹.

For the absorbed dose values which is ranged from 7.9315 to 9.8868 nGh⁻¹ with a mean value of 8.6079 nGh⁻¹. The estimated mean value of D_R in the samples is lower than the worldwide average absorbed dose rate value of 60 nGh⁻¹.

Moreover, the calculated value of external radiation hazard index (H_{ex}) of sediment samples varied from 0.0506 to 0.0631 mSvy⁻¹ and with an average of 0.0549 mSvy⁻¹ which is also lower than the recommended value ≤ 1 . So, it can be assumed that this area is not hazard to the surrounding.

Table 5. Values of the Radium Equivalent Activity, Absorbed Dose and External Hazard Index in Sediment Samples with Worldwide Average

No.	Sample	Ra _{eq} (Bq kg ⁻¹)	D _R (nGyh ⁻¹)	H _{ex} (mSvy ⁻¹)
1	S 1	23.4755	9.8868	0.0631
2	S 2	18.7591	7.9315	0.0506
3	S 3	19.8698	8.4073	0.0536
4	S 4	19.3978	8.2063	0.0524
5	Range	18.7537	7.9315	0.0506
		-	-	-
6	Average	23.4755	9.8868	0.0631
		20.3754	8.6079	0.0549
7	Worldwide Average UNSCEAR (2000)	370	60	≤ 1

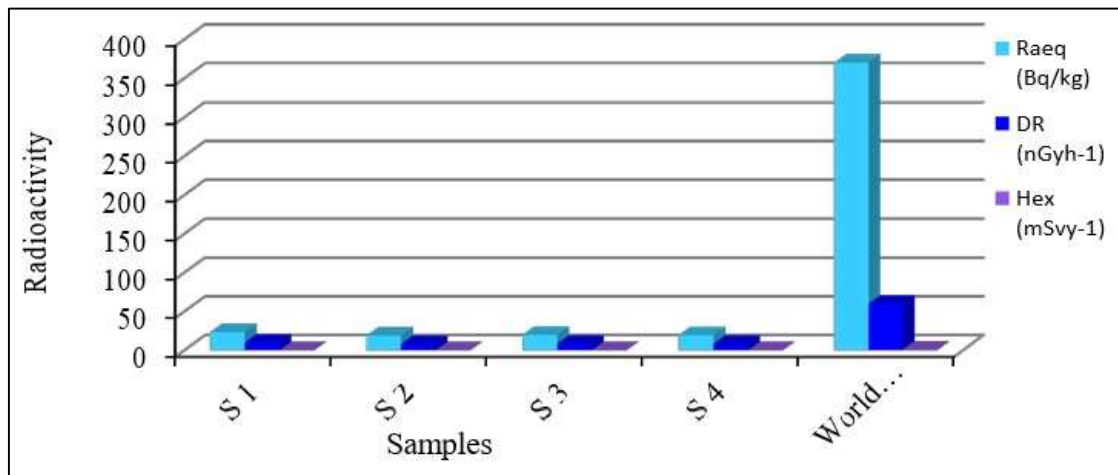


Figure 8 Values of Ra_{eq}, D_R and H_{ex} in Sediment Samples Compare with Worldwide Average

Conclusion

The activity of radionuclides of ²²⁶Ra, ²³²Th, and ⁴⁰K were measured by a gamma-ray spectrometry system in sediment samples collected from the Ayeyarwady River Bank. The activity concentrations of ²²⁶Ra, ²³²Th and ⁴⁰K in all sediments were found to be normal. The radiological assessment of Ra_{eq}, D_R and H_{ex} are good agreement in the worldwide average value. So, the river bank at Magway Township may not pose radiology risk to harmful effects of ionization from the natural radionuclide in the sediment.

Acknowledgement

The author is grateful to Dr Tint Moe Thu Zar, Rector, Yadanabon University, for her valuable suggestion and advices in preparation this work. Special thanks should go to Dr Khin Thida, Professor and Head of Department of Physics and Professor Dr Sandar Min for their continuous encouragement and systematic guidance without which this research project would not be possible. I also indebted to Dr Kalyar Thwe, Professor and Head, Department of Physics, URC at University of Mandalay, for allowing and using the research facilities for this work.

References

- Caspah Kamunda, et.al (2016), "An Assessment of Radiological Hazards from Gold Mine Tailings in the Province of Gauteng in South Africa" *International journal of Environmental Research and Public Health* 13,138.
- H. M. Zakaly, M. Y. A. Mostafa1, et.al, "Natural radioactivity in sediments along the middle region of red sea coast, Egypt", *Ural Federal University, Yekaterigburg, Russia*, 89-93.
- M.Tzortzis and H.Tsertos (2002), "Gamma Ray Measurement of Naturally Occurring Radioactive Samples From Cyprus Characteristic Geological Rocks", *University of Cyprus, Nicosia, Cyprus*.
- S.Sivakumar, A. Chandrasekarn et.al (2014), "Measurement of Natural Radioactivity and Evaluation of radiation Hazards in Coastal Sediments of East Coast of Tamilnadu using Statistical Approach", *Engineering Collage, Tamilnadu, India*.
- UNSCEAR (2000), "Sources and effects of ionizing radiation", *Report to the General Assembly of the United Nations with Scientific Annexes, United Nations sales publication E.00.IX.3, New York*.

DESIGN AND CONSTRUCTION OF FOUR CHANNELS AUTOMATIC BLUETOOTH CONTROL SYSTEM

Aung Zaw Myint¹, Kyaw Soe Moe², Su Myat Aung³, Nyunt Khat Khat Wai⁴

Abstract

In this work, four channels automatic Bluetooth control system is designed and developed. The system consists of the regulated power supply, Bluetooth module, relay drivers and Arduino microcontroller uno board. An Arduino which is an open-source microcontroller board can be controlled or programmed by the computer. The Arduino programming language is used to program Arduino board through serial communication. The firmware program on the Arduino board is controlled by the android application program on the smart phone. Totally, four channels' appliances are controlled separately from the smart phone.

Keywords: Bluetooth control system, Arduino microcontroller, smart phone serial communication.

Introduction

Now a day, home and office appliance controlling are common things. For controlling appliances, machineries in companies and industries uses different types of automation systems. Automatic Bluetooth control system means that allow users to control electrical appliances of varying kind such as lighting control [Simon.M, (2010)]. An Arduino Uno is a single-board microcontroller board based on the ATmega328. "Uno" means one in Italian [John.B, (2013)]. The Arduino output has 3.3 V and 5 V supply. If supplied less than five volts, the board may be unstable. If using more than 12 V, the voltage regulator may overheat and damage the board. The recommended range is 7 V to 12 V. The pins labeled "GND" on the Arduino, these are ground pins. The labeled A0-A5 is the analog input pins. These pins are used to make analog measurements of sensors or other components [Floyd.T.L, (2006)] . Analog inputs are especially good for measuring things with a range of possible values [Charles Roth.H, J., & L.K.Larry, (2015)]. The component of Arduino board is shown in figure 1. It can be programmed from the Arduino development software [Harold.T, (2011)]. In this research work, Bluetooth module XM-15B SPP is connected with a microcontroller board to study the method of application of the wireless communication between Arduino via Bluetooth module and android smart phone. Bluetooth module is shown in figure 2.

Methodology of the System

Hardware Development of the System

Hardware of the constructed system mainly consists of three main sections. They are Arduino via Bluetooth module control section, relay driver circuit section and android smart phone control section. Block diagram of four channels automatic Bluetooth control system is shown in figure 3. Firstly, the Bluetooth module of TX pin and RX pin are connected to the Arduino uno board of digital I/O pin 10 and pin 11. The digital I/O pins 4, 5, 6 and 7 are output signals which are connected relay driver circuit to control AC main line. The circuit is controlled by android smart phone wirelessly through Bluetooth module. After the application is installed

¹ Department of Physics, Shwebo University

² Department of Physics, Magway University

³ Department of Physics, Shwebo University

⁴ Department of Physics, Shwebo University

on android smart phone, it can be sent message as a single digit (or single alphabet) from a phone to the constructed circuit.

Software written using Arduino is called sketches. These sketches are written in the text editor. Sketches are saved with the file extension (.ino). Figure 4 is flowchart of application software for the system. Sketches are shown in figure 5. It has features for cutting/pasting and for searching & replacing text. The message area gives feedback while saving and exporting and also displays errors. The console displays text output by the Arduino environment including complete error messages and other information. The bottom right-hand corner of the window displays the current board and serial port. The toolbar buttons allow verifying and uploading programs, creating, opening, and saving sketches, and open the serial monitor.

Bluetooth Module

Bluetooth is a wireless technology standard that is used to exchange data over short distances using short-wavelength radio transmission. It was created by the telecom company Ericsson in 1994. Bluetooth operates at a range of 2400 - 2483.5 MHz as a packet-based protocol using master-slave structure and provides a secure way to connect and exchange information between devices. In this research, Bluetooth module is used XM-15B SPP (Serial Port Profile). It can be connected directly to a microcontroller board via two wires (TX and RX).

Operation of the System

The Bluetooth name is 'New Name' and default pairing code is 1234. The blue status LED on Bluetooth module switches from a blinking to steady on when it is connected. When the system components are constructed and requirements software are already installed, the four channels Bluetooth control system is implemented successfully. If the digital output signal from Arduino board is HIGH, the relay will convert from normally open to close condition of AC main line. If the digital output signal from Arduino board is LOW, the relay is steady open condition. The communication distance is under open conditions 30 m and the normal use of the environment around 15 m.



Figure 1: The components of Arduino uno board **Figure 2:** The component of Bluetooth module

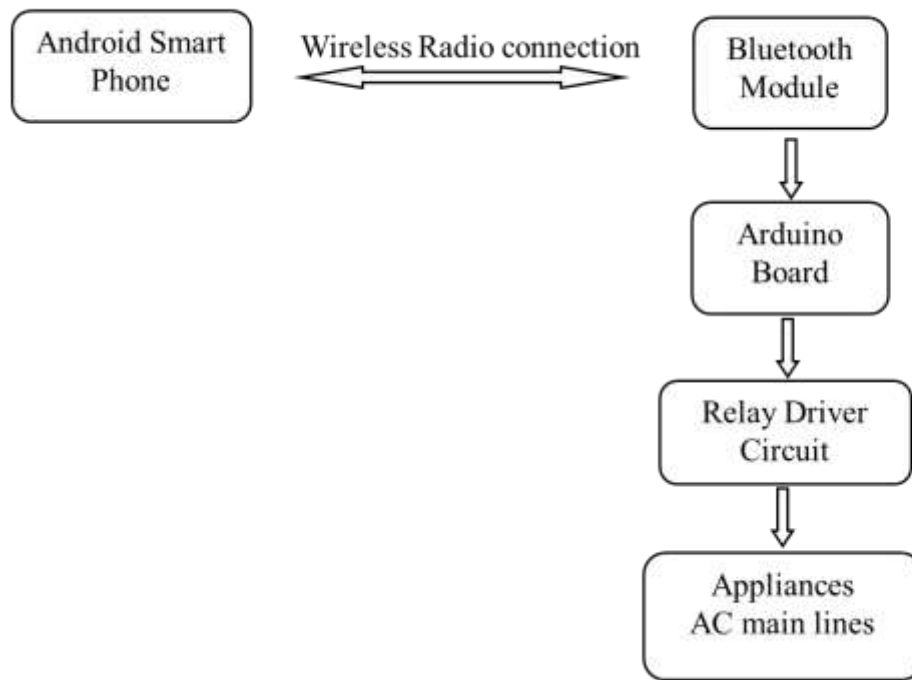


Figure 3: Block diagram of four channels automatic Bluetooth control system

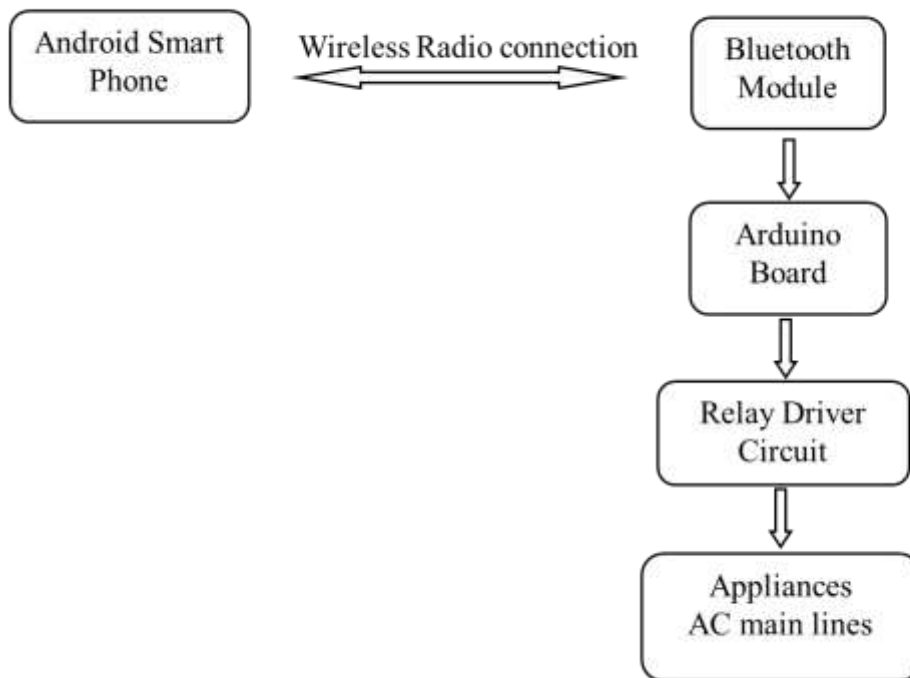


Figure 4: Flowchart of application software

```
FourChannels | Arduino 1.8.9
File Edit Sketch Tools Help
FourChannels
// Four Channels Automatic Bluetooth Control System -Dr. Amyr Zam
#include <SoftwareSerial.h>
SoftwareSerial bluetooth(10,11); // RX, TX
int lightONE = 4;
int lightTWO = 5;
int lightTHREE = 6;
int lightFOUR = 7;
int BluetoothData;
void setup()
{
  bluetooth.begin(9600);
  pinMode(lightONE,OUTPUT);
  pinMode(lightTWO,OUTPUT);
  pinMode(lightTHREE,OUTPUT);
  pinMode(lightFOUR,OUTPUT);
}
void loop()
{
  if (bluetooth.available())
  {
    BluetoothData=bluetooth.read();
    if (BluetoothData=="1")
    {
      digitalWrite(lightONE,1);
      bluetooth.println("ONE OFF");
    }
    if (BluetoothData=="2")

```

Figure 5: Programming Arduino language of Sketches software

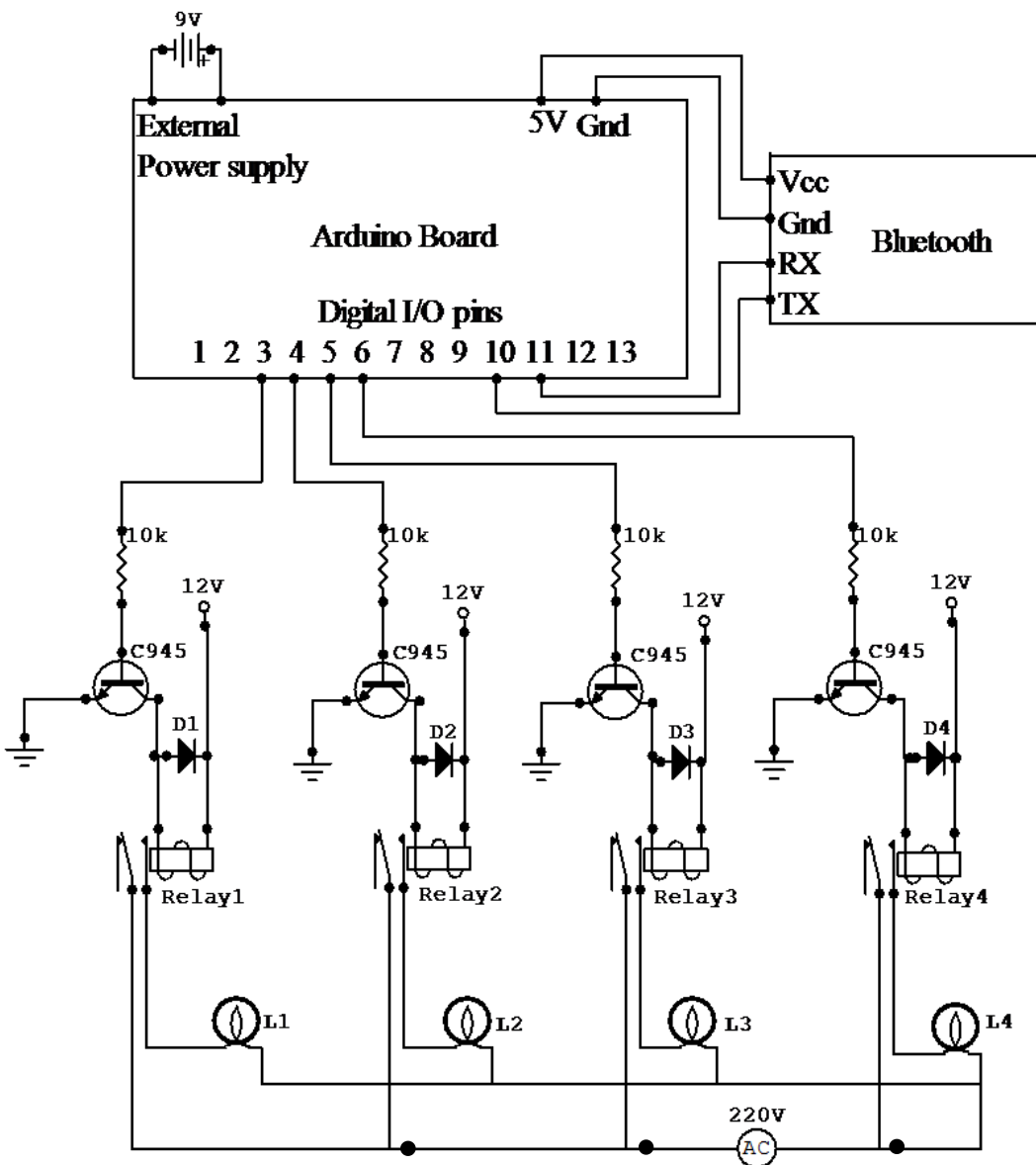


Figure 6: Circuit diagram of four channels Bluetooth control system



Figure 7: The photograph of four channel Bluetooth control system

Results And Discussion

In this paper, four channels automatic Bluetooth control system has been constructed successfully. Circuit diagram of four channels Bluetooth control system is shown in figure 6. The photograph of four channel Bluetooth control system is shown in figure 7.

If typing “1” in the Bluetooth console screen box on Android phone, Arduino output pin 3 is high. The first relay driver circuit is connected to the output pin 3, so the first bulb works in the close condition that turns it on. The Android phone then received the message “ONE ON” on the Bluetooth console screen. If not, typing “a” in the Bluetooth console screen field on the Android phone, the first bulb will turn off and the android phone will receive the message “ONE OFF”. Similarly, if typing “2” in the Bluetooth console screen field on Android phone, the android phone receives the message “TWO ON” and the second bulb is turned on. If typing the letter “b”, the Android phone will receive the message “TWO OFF” and the second light will turn off. If the android phone send message “3”, the third light bulb is turned on. If typing of alphabet “c”, android phone receives the message “THREE OFF” and the third light bulb is turned off. If the android phone send message “4”, the fourth light bulb is turned on. If typing of alphabet “d”, android phone receives the message “FOUR OFF” and the fourth light bulb is turned off. If the android phone sends messages “0”, all light bulbs are turned off and the message “ALL OFF” is received. If the android phone send message “5”, all light bulbs are turned on and the message “ALL ON” is received.

Conclusion

The constructed system can be used to control household electrical appliance remotely by Bluetooth communication technology. Bluetooth technology is a short distance communication technology used by almost all phones including smart phones and all laptops. The relay driver circuit could be directly controlled by Arduino through digital IOs. The all of AC light bulbs can be replaced applicable electrical devices for automation system. The Arduino uno board provides 14 digital I/O pins. Therefore, two pins are used for receiving and transmitting Bluetooth data command. The other 12 pins can be used for output control system. In this paper, 4 pins are used as output control system only for experiment and demonstration of 4 light bulbs ON/OFF conditions. The system can be used for electrical appliances such as TV, air conditioning, pumping water, security and lighting, etc. Four channels automatic Bluetooth control system takes care of a lot of different activities in the house or factory.

Acknowledgements

The authors would like to express our gratitude to Dr Thida Win, Professor and Head, Shwebo University for her kind permission to conduct this research paper, valuable suggestion and comments for this work.

References

- Charles Roth.H, J., & L.K.Larry, (2015) Fundamentals of Logic Design. Seventh Edition.
- Floyd.T.L, (2006) Digital Fundamentals. 9th Edition, Pearson Education Inc, New Jersey, USA.
- Harold.T, (2011) Practical Arduino Engineering. Electronic, ISBN-13978-1-4302-3886-7.
- John.B, (2013) Arduino Workshop. William Pollock: ISBN-13: 978-1-59327-448-1.
- Simon.M, (2010) Arduino 30-Projects for the Evil Genius. McGraw-Hill: ISBN: 978-0-07-174134-7

CALCULATION OF CHARGE DENSITY DISTRIBUTION PARAMETERS OF SILICON ISOTOPE $^{30}_{14}\text{Si}$ FOR 3PG-MODEL

Zin Mar Naing¹, Aung Zaw Myint², Nu Nu Yi³, Nyunt Khat Khat Wai⁴

Abstract

In this research, three parameters Fermi model of $^{30}_{14}\text{Si}$ are change to three parameters Gaussian model of $^{30}_{14}\text{Si}$ in which the parameters of charge density distribution are calculated. The differential scattering cross section of two-body nuclear system is studied in this work. The charged form factors are fitted for 3pG charge distribution model based on the 3pF model which is used as references for this study. The charge form factor which connects scattering cross section and the size of nucleus was discussed. From our calculations, it is found that our fitted charge density distribution and form factor are in good agreement with that of 3pF model. In particular, the purpose of the research shows that the charge form factor is an observable manifestation of an internal structure and shape of the nuclei.

Keywords: Differential scattering cross section, charge form factor, charge density distribution.

Introduction

Nuclear charge density distribution parameters are obtained from elastic electron scattering. They can be expressed in various form factors depending upon nuclear models. Nuclear models are two parameters Fermi model, three parameter Fermi model, three parameter gaussian model, harmonic oscillator model and uniform gaussian model. In this research, the charge form factor for silicon isotope nucleus $^{30}_{14}\text{Si}$ will be studied for 3PG model with the help of reference 3pF charge distribution model [Schneuwly.R., H.Vuilleumier & J.L Walter, et.al, (1974)]. Silicon is used for electronic devices as a semiconductor. At still higher energies, quark degrees of freedom and nucleon resonances may play an important role [Williams.W.S.C, (1991)]. In this research, the charge form factor for silicon isotope nucleus $^{30}_{14}\text{Si}$ will be studied for 3PG model with the help of reference 3pF charge distribution model. The form factor of a nucleus is of fundamental importance for our understanding of its internal structure. Form factor give information about charge distributions and size of nucleus [Angeli. L. & K.P Marinova, (2013)].

Rutherford Differential Scattering Cross Section

In this section, we can obtain the differential cross section from an asymptotic form of the solution of the Schrödinger equation. Let us first focus on the determination $f(\theta, \phi)$; it can also be obtained from the solution of the equation, which is in the form of

$$-\frac{\hbar^2}{2\mu}\vec{\nabla}^2 \psi(\vec{r}) + \hat{V}(\vec{r})\psi(\vec{r}) = E\psi(\vec{r})$$
$$\vec{\nabla}^2 \psi(\vec{r}) + \frac{2\mu}{\hbar^2}[E - \hat{V}(\vec{r})]\psi(\vec{r}) = 0 \quad (1)$$

This equation (1) in turn can be rewritten as follow;

$$(\vec{\nabla}^2 + k^2)\psi(\vec{r}) = \frac{2\mu}{\hbar^2}V(\vec{r})\psi(\vec{r}) \quad (2)$$

¹ Department of Physics, Shwebo University

² Department of Physics, Shwebo University

³ Department of Physics, Shwebo University

⁴ Department of Physics, Shwebo University

The general solution to this above equation consists of a sum of two components; homogeneous (incident plane wave) and particular solution to equation (2). We can express it in terms of The Green’s function. Thus, the general solution of equation (2) is given by

$$\Psi(\vec{r}) = \psi_{\text{inc}}(\vec{r}) + \frac{2\mu}{\hbar^2} \int G(\vec{r} - \vec{r}') V(\vec{r}') \psi(\vec{r}') d^3 r' \tag{3}$$

Where $G(\vec{r} - \vec{r}')$ is a green’s function corresponding to the operator on left hand side on equation (2). The function $G(\vec{r} - \vec{r}')$ is obtained by solving the point source equation;

$$(\nabla^2 + k^2) G(\vec{r} - \vec{r}') = \delta(\vec{r} - \vec{r}') \tag{4}$$

Where $\delta(\vec{r} - \vec{r}')$ is Dirac delta function. $G(\vec{r} - \vec{r}')$ and $\delta(\vec{r} - \vec{r}')$ are given by the Fourier transform as follow;

$$G(\vec{r} - \vec{r}') = \frac{1}{(2\pi)^3} \int e^{i\vec{q}\cdot(\vec{r}-\vec{r}')} G(\vec{q}) d^3 \vec{q} \tag{5}$$

$$\delta(\vec{r} - \vec{r}') = \frac{1}{(2\pi)^3} \int e^{i\vec{q}\cdot(\vec{r}-\vec{r}')} d^3 \vec{q} \tag{6}$$

We can write using equation, the scattering amplitude and differential scattering cross section in the first-Born approximation as follow;

$$f(\theta, \phi) = -\frac{\mu}{2\pi\hbar^2} \int_{\text{inc}} e^{-i\vec{k}\cdot\vec{r}'} e^{i\vec{q}\cdot\vec{r}'} d^3 r'$$

$$f(\theta, \phi) = \frac{2\mu}{\hbar^2} \frac{Ze^2}{\alpha^2 + [2k \sin(\frac{\theta}{2})]^2}$$

For the pure Coulomb’s potential, the range $\alpha = 0$ and then, we can write as follow;

$$f(\theta, \phi) = \frac{2\mu}{\hbar^2} \frac{Ze^2}{4k^2 \sin^2(\frac{\theta}{2})}$$

Since $\frac{d\sigma}{d\Omega} = |f(\theta, \phi)|^2$, we made by squaring of both sides to the above equation. Then we get, the differential scattering cross section is

$$\frac{d\sigma}{d\Omega} = |f(\theta, \phi)|^2 = \frac{4\mu^2 Z^2 e^4}{\hbar^4 (2^4 k^4 \sin^4(\frac{\theta}{2}))}$$

$$\left(\frac{d\sigma}{d\Omega}\right)_{\text{Rutherford}} = \frac{4\mu^2 Z^2 e^4}{\hbar^4 q^4} \tag{7}$$

The above equation (7) is the Rutherford differential scattering cross section.

Form Factor F(q)

In an electron elastic scattering process with a target nucleus, we have presented about the non-relativistic differential cross section (Rutherford). For a target nucleus having an extended finite size, the differential cross section differs from that of the Rutherford by a factor called form factor F(q) such as

$$\left(\frac{d\sigma}{d\Omega}\right)_{\text{extended charged distribution}} = \left(\frac{d\sigma}{d\Omega}\right)_{\text{Rutherford}} |F(q)|^2 \tag{8}$$

Thus, the form factor indicates the effect of nuclear size upon the differential cross section, where q is the momentum transfer of the scattering process and $\vec{q} = \vec{k}_0 - \vec{k}$. When $|\vec{k}_0| = |\vec{k}| = k$, which can be express as $q = 2k \sin(\frac{\theta}{2})$. The form factor is known as the Fourier transform of the charge density distribution and it can be expressed as follow;

$$F(q) = \frac{1}{Z} \int \rho_{ch}(r) e^{i\vec{q}\cdot\vec{r}} d^3\vec{r} \tag{9}$$

The verification of the above equation (9) will be given later in the next section. The form factor plays an important role because it is the most important link between experimental observation and theoretical analysis. In an experiment, the form factor is the direct result of a cross section measurement. From the theoretical side, charge density distribution $\rho_{ch}(r)$ is a solution of the Schrodinger equation, which can be considered as the following relation.

$$\frac{d\sigma}{d\Omega_{Exp}} \rightarrow |F(q)| \Leftrightarrow |F(q)| \leftarrow \frac{d\sigma}{d\Omega_{Theory}} \leftarrow \rho_{ch}(r) \leftarrow \Psi(r) \leftarrow \text{Schrodinger Equation}$$

Relation between Charge Form Factor and Density Distribution

Now we will give the derivation of equation (9). Let us compute the scattering of an electron by a spherically symmetric nucleus having a finite size. The screened Coulomb potential between an electron and a point charge nucleus is

$$V(x) = -\frac{Ze^2}{x} e^{-x/a}. \tag{10}$$

However, we now consider the interaction between the electron and nucleus having a charge distribution. Thus, the screened Coulomb potential $V(x)$ at the position of the electron “ x ” consists of contributions from the entire nucleus. An infinitesimal volume element $d\vec{r}$ contains a charge $dq = Ze\rho_{ch}(r)d\vec{r}$ which gives a contribution of

$$V(x) = -\frac{Ze^2}{y} e^{-y/a} \rho_{ch}(r) d\vec{r}, \quad \text{where } \vec{y} = \vec{x} - \vec{r}$$

$$V(x) = -Ze^2 \int \rho_{ch}(r) \frac{e^{-y/a}}{y} d\vec{r} \tag{11}$$

the first-Born approximation for a scattering amplitude $f(q)$ is given by

$$f(q) = -\frac{m}{2\pi\hbar^2} \int V(x) e^{i\vec{q}\cdot\vec{x}} d\vec{x} \tag{12}$$

Where, $q = 2k \sin(\theta/2)$ is the momentum transfer of the elastic scattering process with scattering angle. By substituting the value of $V(x)$ of equation (11), into the equation (12), we obtain the following form,

$$f(q) = \frac{mZe^2}{2\pi\hbar^2} \int \int \rho_{ch}(r) \frac{e^{-y/a}}{y} d\vec{r} e^{i\vec{q}\cdot\vec{x}} d\vec{x} \tag{13}$$

By using $\vec{x} = \vec{r} + \vec{y}$ yields,

$$f(q) = \frac{mZe^2}{2\pi\hbar^2} \int \int \rho_{ch}(r) \frac{e^{-y/a}}{y} d\vec{r} e^{i\vec{q}\cdot(\vec{r}+\vec{y})} d\vec{y}$$

$$f(q) = \frac{mZe^2}{2\pi\hbar^2} \int e^{i\vec{q}\cdot\vec{r}} \rho_{ch}(r) d\vec{r} \int \frac{e^{-y/a}}{y} e^{i\vec{q}\cdot\vec{y}} d\vec{y} \tag{14}$$

For fixed r , $d\vec{x}$ can be replaced by $d\vec{y}$. Then

$$f(q) = \frac{mZe^2}{2\pi\hbar^2} \int e^{i\vec{q}\cdot\vec{r}} \rho_{ch}(r) d\vec{r} \int \frac{e^{-y/a}}{y} e^{i\vec{q}\cdot\vec{y}} d\vec{y} \tag{15}$$

In the above equation (3.47), the integral term $\int \frac{e^{-y/a}}{y} e^{i\vec{q}\cdot\vec{y}} d\vec{y}$ is evaluated as;

$$\int \frac{e^{-y/a}}{y} e^{i\vec{q}\cdot\vec{y}} d\vec{y} = \frac{4\pi}{q^2 + (1/a^2)} \tag{16}$$

If $a \gg 1$, equation (3.48) becomes the below form,

$$\int \frac{e^{-y/a}}{y} e^{i\vec{q}\cdot\vec{y}} d\vec{y} = \frac{4\pi}{q^2}$$

Therefore, the equation (15) for the scattering amplitude $f(q)$ can be written as follow;

$$f(q) = \frac{mZe^2}{2\pi\hbar^2} \int e^{i\vec{q}\cdot\vec{r}} \rho_{ch}(r) d\vec{r} \times \frac{4\pi}{q^2}$$

and then, we get the scattering amplitude $f(q)$ is in the form of;

$$f(q) = \frac{4\pi mZe^2}{2\pi\hbar^2 q^2} \int e^{i\vec{q}\cdot\vec{r}} \rho_{ch}(r) d\vec{r} \tag{17}$$

Since, $\frac{d\sigma}{d\Omega} = |f(q)|^2$, we made by squaring of both sides to equation (17), Then we get,

$$\frac{d\sigma}{d\Omega} = |f(q)|^2 = \frac{4m^2 Z^2 e^4}{\hbar^4 q^4} \left| \int e^{i\vec{q}\cdot\vec{r}} \rho_{ch}(r) d\vec{r} \right|^2 \tag{18}$$

However, the differential scattering cross section for electron scattering by a point nucleus (Rutherford scattering) is known to be previous section, which is in the form of;

$$\left(\frac{d\sigma}{d\Omega}\right)_{\text{Rutherford}} = \frac{4m^2 Z^2 e^4}{\hbar^4 q^4} \tag{19}$$

By comparing equations (19) which is the differential scattering cross section for the target nucleus is considered as a point-charge and (18) the target nucleus is considered as with extended charge distribution. In these cases, the factor term is appeared and we can express as;

$$\left(\frac{d\sigma}{d\Omega}\right)_{\text{experiment}} = \left(\frac{d\sigma}{d\Omega}\right)_{\text{extended chargedistribution}} = \left(\frac{d\sigma}{d\Omega}\right)_{\text{Rutherford(point charge)}} |F(q)|^2$$

$$|F(q)|^2 = \frac{\left(\frac{d\sigma}{d\Omega}\right)_{\text{Experiment}}}{\left(\frac{d\sigma}{d\Omega}\right)_{\text{Ruther(point-charge)}}} \tag{20}$$

The form factor is in the form of

$$F(q) = \int e^{i\vec{q}\cdot\vec{r}} \rho_{ch}(r) d\vec{r} \tag{21}$$

If the normalization for form factor is chosen to be $F(q = 0) = 1$, the form factor can be written as;

$$F(q) = \frac{1}{Z} \int e^{i\vec{q}\cdot\vec{r}} \rho_{ch}(r) d\vec{r} \tag{22}$$

The form factor $F(q)$ is the Fourier transform of the charge density distribution and the pervious equation (9) has been verified. The form factor $F(q)$ can also be expressed as the following form,

$$F(q) = \frac{1}{Z} \int e^{i\vec{q}\cdot\vec{r}} \rho_{ch}(r) d^3\vec{r} = \frac{1}{Z} \int_{r=0}^{\infty} \int_{\theta=0}^{\pi} \int_{\phi=0}^{2\pi} e^{iqr \cos \theta} \rho_{ch}(r) r^2 dr \sin \theta d\theta d\phi \tag{23}$$

$$= \frac{2\pi}{Z} \int_{r=0}^{\infty} r^2 \rho_{ch}(r) \frac{e^{iqr} - e^{-iqr}}{iqr} dr = \frac{4\pi}{Z} \int_{r=0}^{\infty} r^2 \rho_{ch}(r) \frac{\sin(qr)}{qr} dr \tag{24}$$

$$F(q) = \frac{4\pi}{Z} \int_{r=0}^{\infty} r^2 \rho_{ch}(r) j_0(qr) dr \tag{25}$$

Nuclear Charge Density Distributions

Nuclear charged density distribution is obtained by taking the Fourier inverse of the form factor. The form factor is expressed as the form of equation (21). By multiplying the equation (21) with $\int e^{-i\vec{q}\cdot\vec{r}'} d\vec{q}$ in both sides, and then

$$\begin{aligned} \int F(q) e^{-i\vec{q}\cdot\vec{r}'} d\vec{q} &= \int \int e^{i\vec{q}\cdot\vec{r}} e^{-i\vec{q}\cdot\vec{r}'} \rho_{ch}(r) d\vec{r}d\vec{q} \\ &= \int \int d\vec{r}d\vec{q} e^{i\vec{q}\cdot(\vec{r}-\vec{r}')} \rho_{ch}(r) = \int d\vec{r} (2\pi)^3 \delta(\vec{r}-\vec{r}') \rho_{ch}(r) \\ \int F(q) e^{-i\vec{q}\cdot\vec{r}'} d\vec{q} &= (2\pi)^3 \rho_{ch}(r') \\ \rho_{ch}(r) &= \frac{1}{(2\pi)^3} \int F(q) e^{-i\vec{q}\cdot\vec{r}} d\vec{q} \end{aligned} \tag{26}$$

From an electron scattering experiment, the form factor can be deduced by the following

equation,
$$|F(q)|^2 = \frac{\left(\frac{d\sigma}{d\Omega}\right)_{\text{experiment}}}{\left(\frac{d\sigma}{d\Omega}\right)_{\text{Rutherford}}} \tag{27}$$

If the form factor $F(q)$ is known for all q , the inverse Fourier transform might be computed in order to get the charge density distribution, $\rho_{ch}(r)$ from the following equation

$$\rho_{ch}(r) = \frac{1}{(2\pi)^3} \int_{q=0}^{\infty} F(q) e^{-i\vec{q}\cdot\vec{r}} d\vec{q} \tag{28}$$

However, this is impossible because the form factor can be measured only in a limited range of momentum transfer “ q ”. Thus, the simplest analysis is to construct a model of the charge distribution. Such models have parameters which can be adjusted until the calculated form factor provides the best fit to the available experimental measurements.

$$F(q)|_{\text{calculated}} = \frac{4\pi}{Z} \int_{r=0}^{\infty} r^2 \rho_{ch}^{\text{model}}(r) \frac{\sin(qr)}{qr} dr. \tag{29}$$

Results and Discussion

Charge Density Distribution Parameters and Form Factor for 3pG Model

The charge density distribution parameters for 3pF (three parameters Fermi) model can be obtained from the reference data of Atomic and Nuclear Tables 36. [H.De.Vries, C. W. De Jager, & C. De Vries, (1987)]. We used the charge density distributions for the 3pF model as $\rho_{ch}(r) = \rho_0(1 + wr^2/c^2)/(1 + \exp((r - c)/z))$ and for form factor $F(q)|_{\text{calculated}} = \frac{4\pi}{Z} \int_{r=0}^{\infty} r^2 \rho_{ch}^{\text{model}}(r) \frac{\sin(qr)}{qr} dr$. Then we constructed the form factor and charge density distribution profiles by the help of GFORTRAN CODE Program for that 3pF model using the reference data Table.1, these profiles are shown in figure 1 and 2. In this numerical calculation, number of integration steps N is taken to be 2000, step interval $dr = 0.005$. To find the charge density distribution parameters for the 3pg model, we first looked for the difference value of the charge density distribution parameters between the 3pf and 3pg models of another nucleus which were already known in references paper. Based on the value of the difference obtained, we considered the appropriate values to fit the charge density distribution parameters for the desired 3pg model. It was estimated that the program was run over 2,000 times with various possible values. From our multiple observations, we record the closest possible values was listed in table. Among these obtained values, we choices one of the best parameters set to use the set of the charge density distribution parameters for the 3pg model.

After that we have fitted the charge density distribution parameters for 3pG model that is three parameters Gaussian model by using the formula, $\rho_{ch}(r) = \rho_0(1 + wr^2/c^2)/(1 + \exp((r^2 - c^2)/z^2))$ and we fitted these parameters based on 3pF profile as reference. We have shown best set of fitting parameters in Table 2. We plotted the Figure (4.3) to (4.4) by the used of our best set fitted data. And we compared these 3pG profiles which is used our fitted data set with already known 3pF profiles for both density distribution and form factor. From the comparison of these figures, we get the corresponding fitted parameters for 3pG model.

Finally, we can clearly say that our finding parameters are good in agreement to use as a charged density distribution parameter for 3pG model; because from the figure 3 to 4, the reference and fitted curve are the same as a single line in the momentum transfer range of 3fm for both charge density distribution and charge form factor.

Table.1 Reference charge density distribution parameters for 3pF model of silicon isotope

Nucleus	C	Z	W
	Radius Parameter	Skin Thickness Parameter	Adjustable Parameter
$^{30}_{14}Si$	3.252	0.553	-0.078

Table.2 Finding out the charge density distribution parameters for 3pG model of silicon isotope

Nucleus	C	Z	W
	Radius Parameter	Skin Thickness Parameter	Adjustable Parameter
$^{30}_{14}Si$	2.731	2.034	0.199

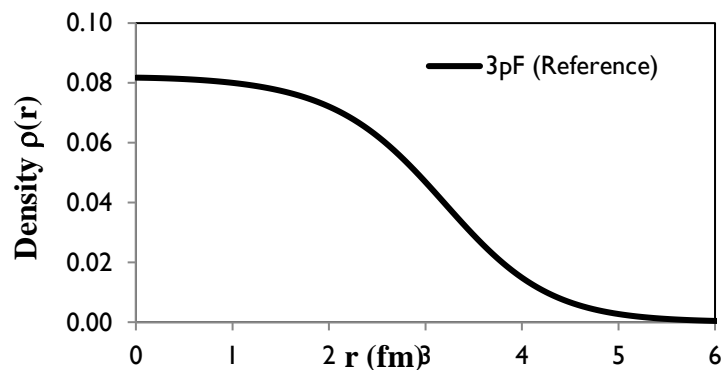


Figure 1: Charge density distribution for 3pF model of $^{30}_{14}Si$ versus the radius

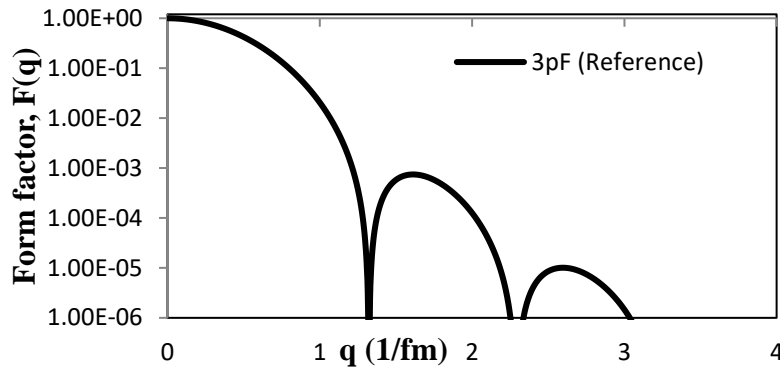


Figure 2: Charge form factor for 3pF model of $^{30}_{14}\text{Si}$ versus the momentum transfer

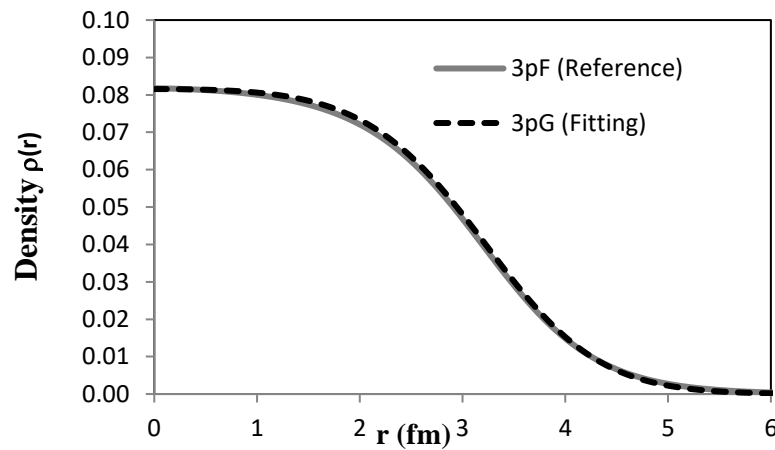


Figure 3: Comparison of the charge density distribution for reference 3pF model (solid curve) and 3pG model (dash curve) of silicon isotope $^{30}_{14}\text{Si}$

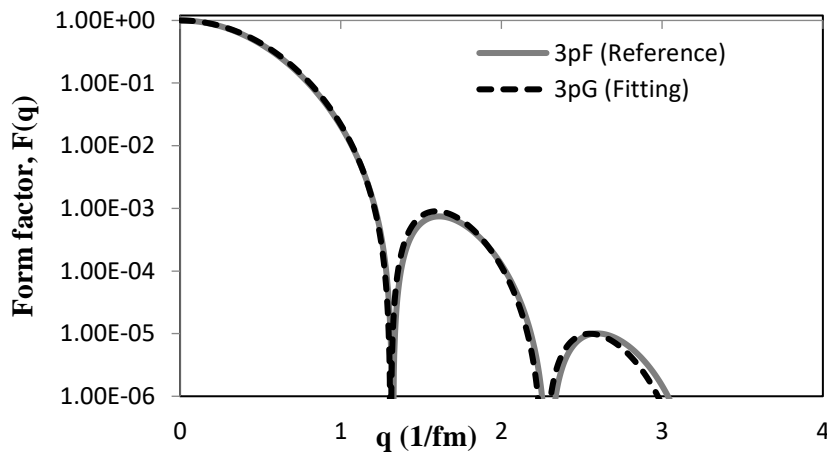


Figure 4: Comparison of charge form factor for reference 3pF model (solid curve) and 3pG model (dash curve) of silicon isotope $^{30}_{14}\text{Si}$

Acknowledgements

The authors would like to express our sincere thanks to Dr Thida Win, Professor and Head of Department of Physics, Shwebo University for her permission to do this research. We are deeply indebted to Professor Dr Khin Swe Myint, Rector (Rtd), Emeritus Professor, Department of Physics, University of Mandalay for all her enthusiastic discussion, collaboration and encouragement. Furthermore, I would like to express my gratitude towards my family for their understanding and moral encouragement.

References

- Angeli. L. & K.P Marinova, (2013) Atomic Data and Nuclear Data Tables.
- H.De.Vries., C. W. De Jager, & C. De Vries, (1987) Nuclear Charge-Density-Distribution Parameters From Elastic Electron Scattering. Atomic Data and Nuclear Data Tables.
- Schneuwly.R., H.Vuilleumier & J.L Walter, et.al, (1974) Charge Distribution parameters, Isotope shifts.
- Williams.W.S.C, (1991) Nuclear and Particle Physics.
- Zettili.N, (2009) Quantum Mechanics Concept and Application, Second Edition, John Willy & Son, Ltd.

PREPARATION AND CHARACTERIZATION OF $\text{Al}_2\text{O}_3/\text{SiO}_2/\text{Si}$ TUNNEL DIODE

Zaw Win¹

Abstract

Aluminum oxide (Al_2O_3) moisture less powder was formed by mixing aluminum nitrate nonahydrate ($\text{Al}(\text{NO}_3)_3 \cdot 9\text{H}_2\text{O}$) and glycine ($\text{C}_2\text{H}_5\text{NO}_2$) via auto combustion method. X-ray diffraction (XRD) and Scanning Electron Microscope (SEM) techniques were used to examine the structure and microstructural properties of Al_2O_3 powder. The structure of $\text{Al}_2\text{O}_3/\text{SiO}_2/\text{Si}$ cell exhibited the schottky barrier height and could not indicate the tunnel diode nature. Thus, the P_2O_5 insertion layer was added onto the SiO_2 layer. Phosphorus (P_2O_5) diffusion was made on the $\text{SiO}_2/\text{p-Si}$ (100) substrate and annealed at 550°C for 1 h to form $\text{p}^+ \text{p}$ design. The SEM was employed to observe the surface morphology and thickness of P_2O_5 layer. The Al_2O_3 sol-solution was deposited onto $\text{P}_2\text{O}_5/\text{SiO}_2/\text{Si}$ substrate by spin coating technique. The microstructure and film thickness of Al_2O_3 layer were also examined by SEM. The charge conduction mechanism of Al_2O_3 film was identified by C^{-2} -V characteristics. The change in peak current and the valley current with respect to annealing temperatures were studied.

Keywords: XRD Analysis of Al_2O_3 Powder and SEM Analysis of $\text{P}_2\text{O}_5/\text{Si}$ Layer

Introduction

A tunnel diode is a type of semiconductor diode that is capable of very fast operation, well into the microwave frequency region, by using the quantum mechanical effect called tunneling. Tunnel diode is p-n junction device that exhibits negative resistance. That means when the voltage is increased the current through it decreases. They are used in frequency converters and detectors. They have negative differential resistance in part of their operating range, and therefore are also used as oscillators, amplifiers and in switching circuits using hysteresis. Aluminum is one of the most important materials because of its high strength and modulus, resistance to attacks from molten metals and non-oxide materials, chemical inertness in both oxidizing and reducing atmospheres up to 1000°C , and good electrical insulation. Aluminum also has high melting point ($t_m > 2040^\circ\text{C}$) and low thermal conductivity (10-18 W/ (mK)). An important potential application of alumina is as fiber reinforcement of metals, ceramics and resins.

Experimental Procedure

Samples Preparation

P-type silicon with (100) orientation was cleaned by standard silicon cleaning process. First of all, Phosphorus (P_2O_5) was dissolved in methoxyethanol ($2\text{-CH}_3\text{OCH}_2\text{CH}_2\text{OH}$) and deposited onto p-Si (100) substrates by spin coating technique. It was annealed at 550°C for 1h to form $\text{p}^+ \text{p}$ design. Aluminum nitrate [$\text{Al}(\text{NO}_3)_3 \cdot 9\text{H}_2\text{O}$] and glycine ($\text{C}_2\text{H}_5\text{NO}_2$) were used as starting chemicals with analytical grade. Aluminum nitrate nonahydrate and glycine (1:3) were mixed and a small amount of ammonium hydroxide (NH_4OH) was added to the solution to change the neutral solution. During the process, the solution was stirred and heated at 60°C for 8 h. Next, it was aged in air atmosphere for 12 h and jelly-like solution was formed. To get the dried gel, the jelly-like solution was dried at 90°C for 1h and dried gel was formed. It was poured into crucible and heated at 400°C for 30 min. Thus, Al_2O_3 powder was obtained and it was annealed at 1100°C for 3 h for move crystalline fine and moisture-less. The Al_2O_3 powder and $2\text{-CH}_3\text{OCH}_2\text{CH}_2\text{OH}$ solvent were mixed and refluxed at 110°C for 3h. After air cooling, transparent Al_2O_3 sol solution was formed and ready to deposit onto $\text{p}^+ \text{p}$ substrate. It was coated onto $\text{p}^+ \text{p}$ substrate by single wafer spin

¹ Physics Department, Yadanabon University

processor. To change from coating layer into oxide film, they were annealed at 500 oC, 600 oC and 700 oC for 1 h. Figure (1) shows the flow chart of preparation for AL₂O₃ precursor solution

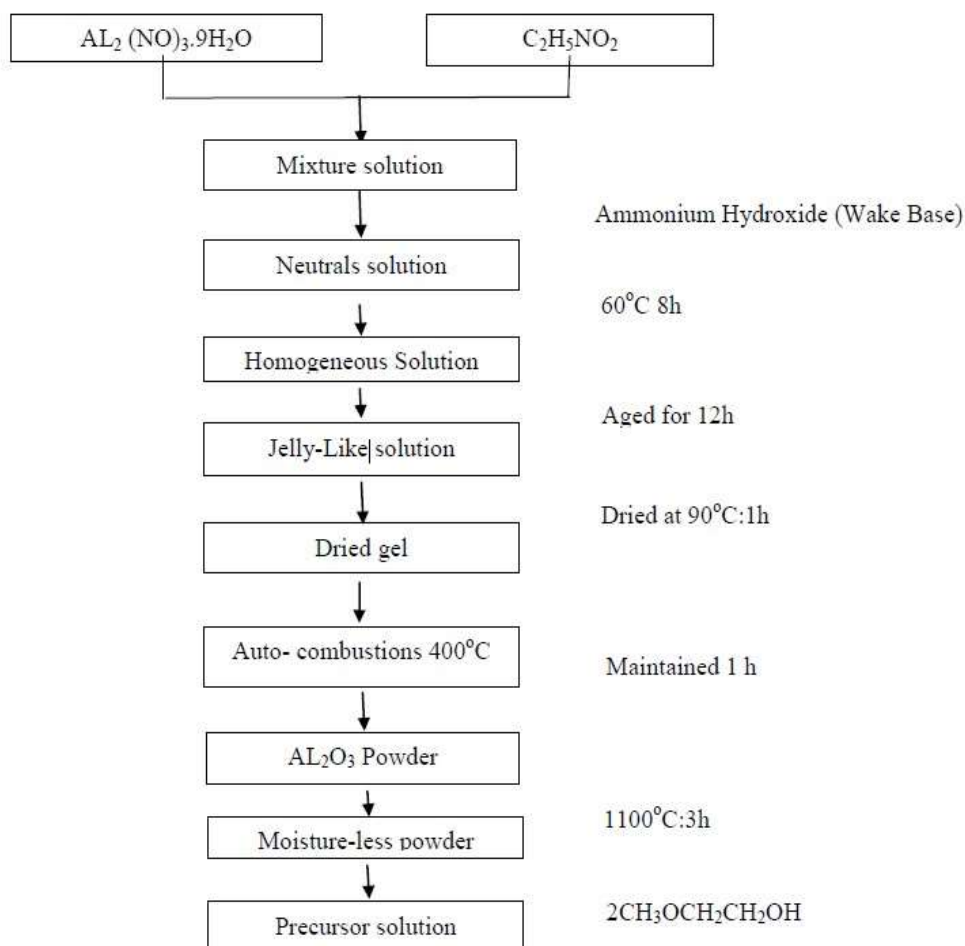


Figure 1. Flow chart of preparation for AL₂O₃ precursor solution

Results and Discussion

XRD Analysis of Al₂O₃ Powder

XRD analysis was employed to study the crystal structure and crystallographic properties of Al₂O₃ powder. The observed XRD profile was shown in Fig 2. The standard/reference XRD spectrum was 78-2427>Al₂O₃ library file (JCPDS). There was eleven peaks on observed XRD spectrum. Nine of eleven were matched well with that of standard spectrum. The crystal structure was examined to be hexagonal symmetry. The crystallite size of the (hkl) plane formed on observed XRD profile was calculated and collected in Table 1. The mean crystallite size (nanoparticle size) was found to be 70.3 nm. The lattice parameters (a-axis and c-axis) and hexagonality (lattice distortion) (lattice strain) (lattice micro strain) (c/a) were also evaluated and quoted in Table 2. The mean a-axis, c-axis and c/a were 4.7 Å, 12.99 Å and 2.73, respectively.

Microstructural Properties of Al₂O₃ powder

The grain morphology at Al₂O₃ powder was examined by scanning electron microscopy (SEM). Fig 3 showed the SEM photograph of Al₂O₃ powder. From the figure, it was found that it exhibited elongated shape with average grain size estimated by well-known bar code system about 2.02 μm. It was found a porous microstructure and low dense. Oxide layer (P₂O₅ layer) (insulating layer) (buffer layer) was thermally formed on p-Si substrate (550 oC for 1 h). The surface morphology of P₂O₅ layer was shown in Fig 4 and Fig 5 indicated the cross-sectional view of P₂O₅layer. The layer thickness was found to be 0.70 μm.

Microstructural Properties of Al₂O₃ film

Figure 6 (a-c) showed the SEM photographs of Al₂O₃ ultrafine powders at different annealing temperatures. As the detail analysis of SEM image, it was found that flat and non-cracked. This image consisted of circular features known as rosette structure in microstructure. The temperatures dependent of grain size for Al₂O₃ film were 0.6 μm, 0.5 μm, and 0.43 μm, respectively. It was found that grain sizes were more uniform at the increasing temperature 500 oC, 600 °C and 700 °C. Both microstructures were oriented toward right side and uniform grain distributions were clearly observed. The grain size with respect to the annealing temperature was plotted in Fig 7. The film thickness was found to be 36.9 μm, 29.9 μm and 24.0 μm for the Al₂O₃ / P₂O₅/SiO₂/Si film at 500 °C, 600 °C and 700 °C. The grain size with respect to the annealing temperature was plotted in Fig 8. The cross - sectional SEM image of Al₂O₃ / P₂O₅ /SiO₂/Si film was given in Fig 9 (a-c).

1/C₂-V Characteristics

To examine the film qualification of MIS tunnel diode, C-2-V characteristics were essentially observed. Fig 10 (a-c) gave C-2-V characteristics of MIS structure. This curve obeyed the Mott-Schottky relationship C-2-V characteristics were considered at negative bias condition because the built-in-voltage (the voltage across the space charge layer) must be positive. Thus, the built-in-voltage was obtained by extrapolating the C-2-V linear relationship. Table 3 showed the some important parameters of MIS tunnel diode.

I-V characteristics of Si- based Tunnel Diode

The change in current as a function of DC applied voltage for tunnel diode was plotted as Figure 11. Three distinct regions were formed on I-V curve. The current was not allowed to flow at zero bias. There was no remarkable forward current through the junction at the low voltage region. It might be due to the potential barrier was still very high. The direct tunneling current started growing at 0.03 V because the electrons in the conduction of the n-region would tunnel to the empty state of the valence in p-region. Therefore, the direct tunnel current could flow at the junction from 0.03 V to 0.165 V ~ 0.195 V. At the second state, the tunnel current decreased with increase in DC applied voltage. Thus, the region was called NDR (negative differential resistance) region because it exhibited the negative slope and varied wit $R = -1/\text{slope}$. At the third state, the diffusion current could easily flow at the junction and it increased growing with increasing dc applied voltage. For I-V curve, it was observed that the tunnel current varied with DC voltage as following equation.

$$I_{\text{tunnel}} = \frac{V}{R_0} \exp \left[\left(-\frac{V}{V_0} \right)^m \right] \quad (1)$$

Table 4 showed current and voltage characteristics of Si-based tunnel diode at different temperatures. Figure 12 (a) showed the change in peak current and valley current as a function of different annealing temperature. From the figure, it was found that the peak current and voltage gradually increased with an increase in annealing temperature in Table 5. Annealing temperature dependence of peak voltage and valley voltage of fabricated tunnel diode was described in Figure 12 (b) and collected in Table 6. The variation nature of this graph was examined to be reversed in that of peak and valley current. This fact indicated that the formation of tunnel diode.

Table 1. Crystallite size of different peaks

Different peaks	G (nm)
(012)	45.7
(104)	80.1
(110)	98.7
(113)	75.6
(202)	77.7
(024)	99.2
(116)	70.7
(211)	52.9
(122)	70.9
(214)	67.3
(300)	37.4
Means crystalline size	70.3

Table 2. a-axis, c-axis and c/a of some observed peaks

Different peaks	a-axis (Å)	c-axis (Å)	c/a
024	4.76	12.87	2.70
110	4.71	13.22	2.80
202	4.75	12.99	2.73
113	4.76	12.89	2.70
Means values	4.74	12.99	2.73

Table 3. Some important diode parameters

Temp (°C)	N _a (cm ⁻³)	N _d (cm ⁻³)	W (×10 ⁻⁷ cm)	V _{bi} (V)	φ (eV)
500	1.26E+22	2.47E+04	4.80	0.366	3.08E-01
600	4.34E+21	4.31E+03	8.21	0.293	2.63E-01
700	4.02E+21	6.64E+02	8.58	0.402	2.14E-01

Table 4. Current and voltage characteristics of Si-based tunnel diode at different temperatures

Voltage (V)	Current(μA)	Voltage(V)	Current(μA)	Voltage(V)	Current(μA)
0	2.77	0.02	0.87	0.03	0.24
0.03	14.10	0.04	10.95	0.06	7.80
0.06	27.28	0.08	21.25	0.09	15.22
0.13	30.47	0.14	24.13	0.15	17.79
0.20	30.32	0.21	24.15	0.22	17.98
0.26	24.47	0.27	19.69	0.28	14.91
0.33	15.94	0.33	13.13	0.34	10.32
0.40	6.72	0.40	6.09	0.41	5.46
0.46	2.23	0.47	1.17	0.47	0.11
0.53	1.84	0.53	2.78	0.53	3.73
0.60	4.09	0.60	5.22	0.60	6.35

Table 5. Peak current and valley current at different temperatures

Temperature °C	Peak current (μA)	Valley current (μA)
700	30.47	2.23
600	24.15	1.17
500	17.98	0.11

Table 6. Peak voltage and valley voltage at different temperatures

Temperature °C	Peak voltage (V)	Valley Voltage (V)
700	0.16	0.46
600	0.17	0.47
500	0.19	0.47

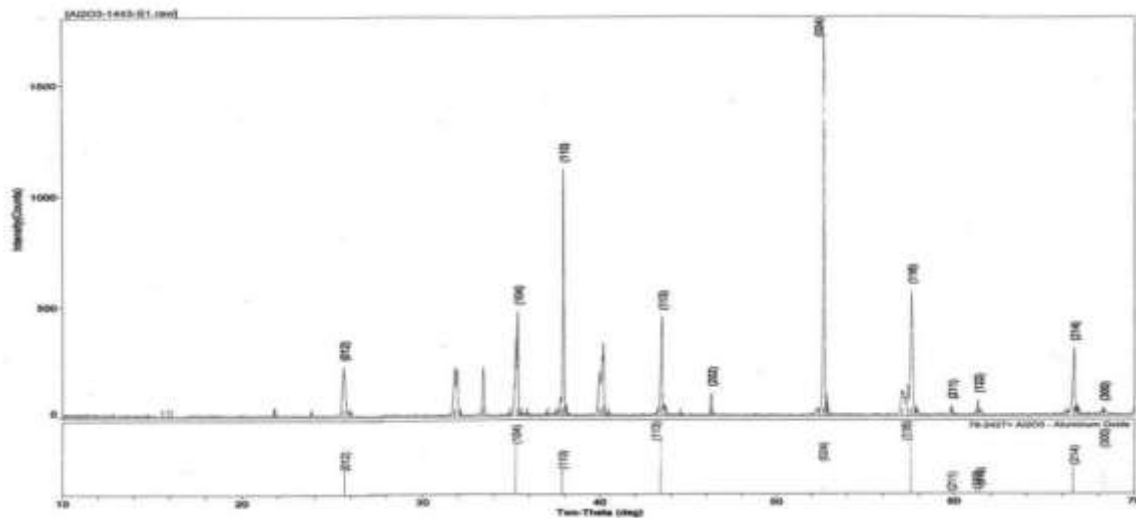


Figure 2. The XRD spectrum of Al₂O₃ ultra-fine powder



Figure 3. SEM photograph of Al₂O₃ powder

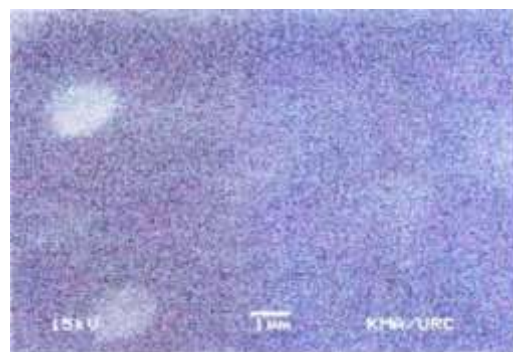


Figure 4. The surface morphology of P₂O₅ layer

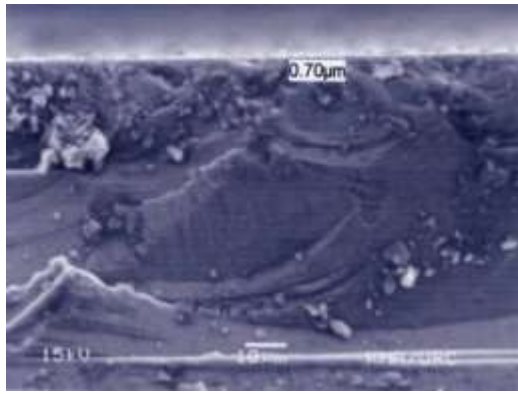


Figure 5. The cross-sectional view of P_2O_5 layer

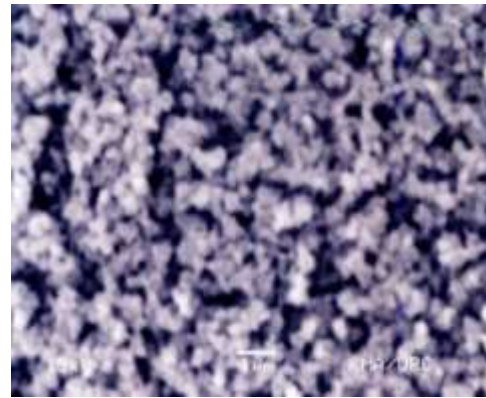


Figure 6 (a) SEM image of Al_2O_3 film at 500 °C

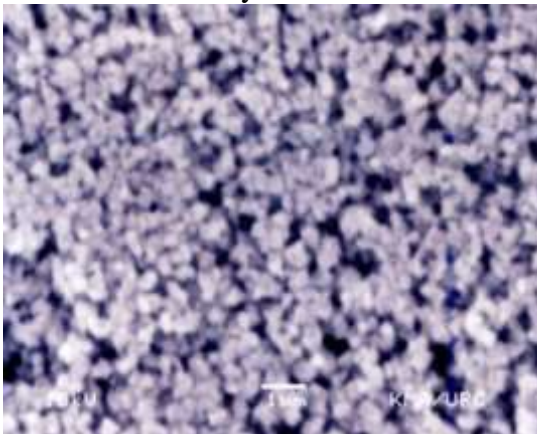


Figure 6 (b). SEM image of Al_2O_3 film at 600 °C

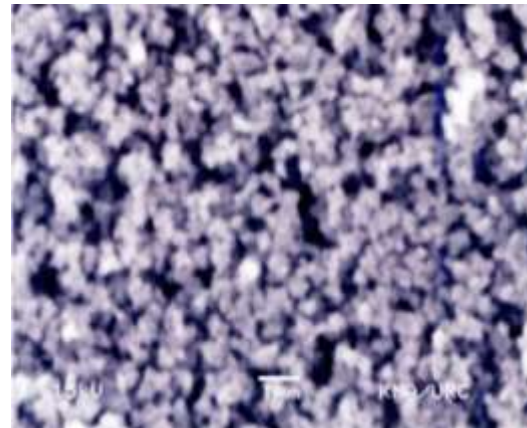


Figure 6 (c). SEM image of Al_2O_3 film at 700 °C

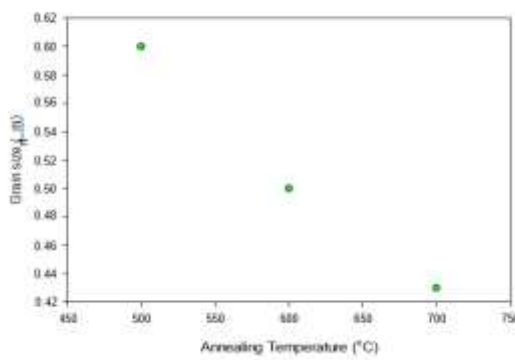


Figure 7. Annealing temperature dependence of grain size of Al_2O_3 film

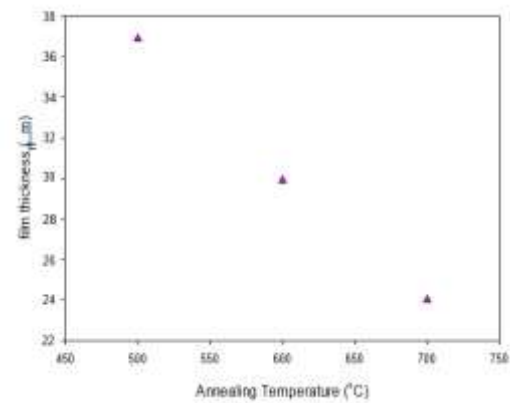


Figure 8. Annealing temperature dependence of grain size of Al_2O_3 film

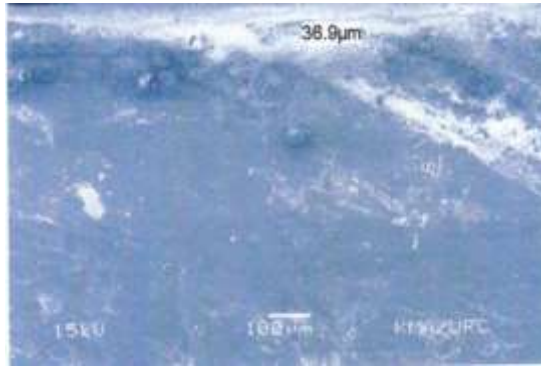


Figure 9 (a). The cross-sectional view of Al₂O₃ layer at 500 °C

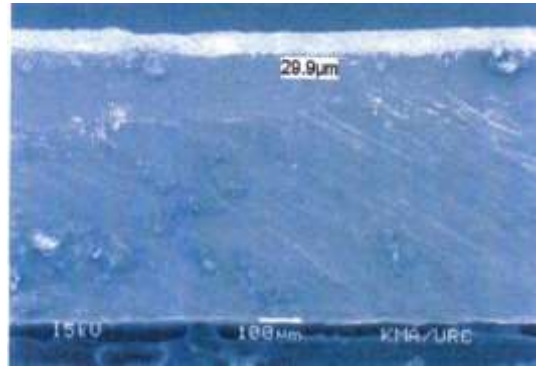


Figure 9 (b). The cross-sectional view of Al₂O₃ layer at 600 °C

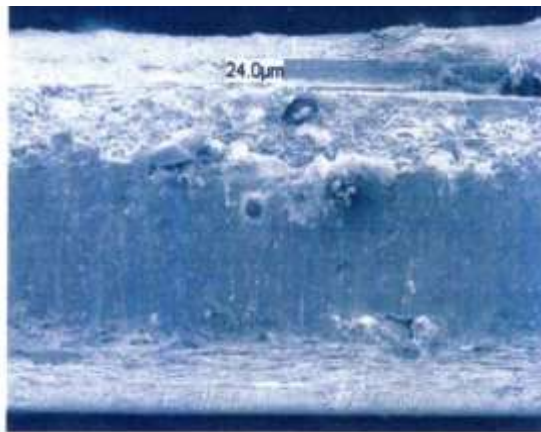


Figure 9 (c). The cross-sectional view of Al₂O₃ layer at 700 °C

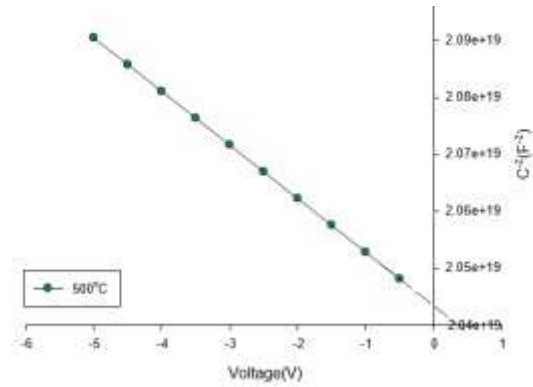


Figure 10 (a). 1/C²-V Characteristic of Si-based tunnel diode at 500 °C

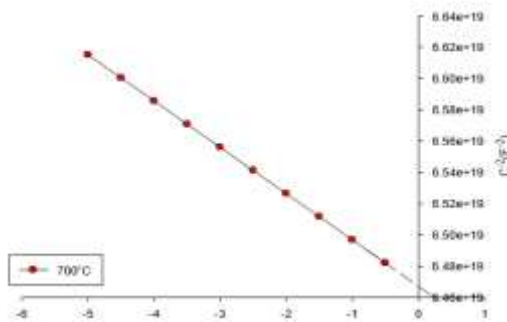


Figure 10 (b). 1/C²-V Characteristic of Si-based tunnel diode at 600 °C

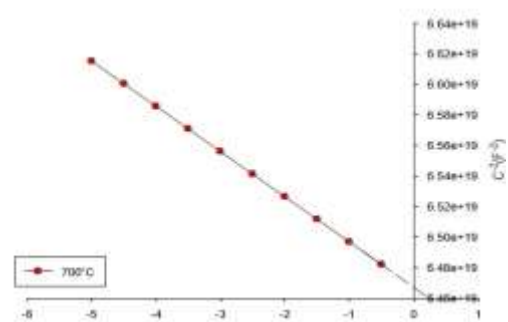


Figure 10 (c). 1/C²-V Characteristic of Si-based tunnel diode at 700 °C

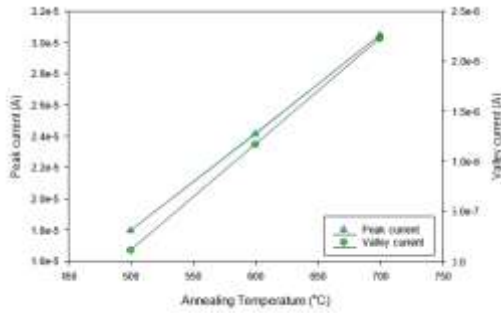


Figure 11. I-V Characteristics of Si based tunnel diode with AL₂O₃ layer at different annealing temperatures

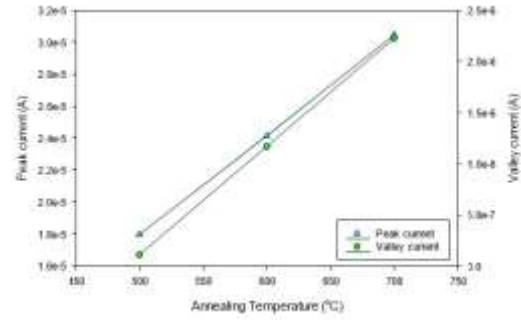


Figure 12 (a). The change in Peak current and Valley current as a function of different annealing temperatures

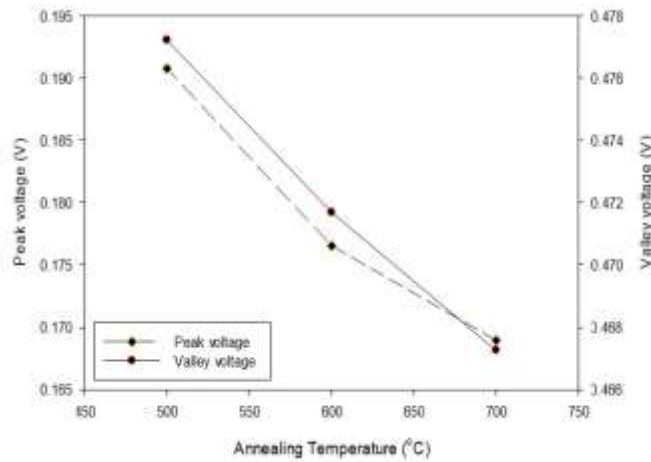


Figure 12 (b). The change in Peak voltages and Valley voltages as a function of different annealing temperatures

Conclusion

As a result of XRD, the defect – free and prime- grade pattern was formed with hexagonal symmetry. The lattice distortion was determined to be 2.70 Å and lattice match was 98% to compared with Al₂ O₃ standard (c/a =2.73 Å). Two extra peaks were formed on XRD spectrum, and it might be attributed to the secondary oxide formation. The most intense peak was observed to be (024) plane and indicated the polycrystalline nature of Al₂ O₃. Thus, auto combustion method was quite suitable for Al₂O₃ powder preparation. It also confirmed the moisture- less powder of Al₂O₃.

As a result of powder analysis by SEM, homogeneous and uniform grains were formed. The grain size was examined to be 2.02 μm and it was porous structure. Therefore, it was concluded that the auto combustion route was quite feasible for ultrafine and moisture less powder fabrication. From the result of microstructure for P₂O₅ layer, it was clear that insulation layer was formed on p-Si (100) substrate at 1100 °C. The film thickness was found to be 0.70 μm. As a result of SEM investigation for Al₂O₃ film, the image consisted of circular features known as rosette structure in microstructure. The temperature dependent of grain size for Al₂O₃film were 0.6, 0.5 μm and 0.43 μm respectively. It was found that grain size was more uniform at the increasing temperature 600 °C and 700 °C. The

film thickness was found to be 36.9 μm , 29.9 μm and 24.0 μm for the $\text{Al}_2\text{O}_3/\text{P}_2\text{O}_5/\text{SiO}_2/\text{Si}$ film at 500 $^\circ\text{C}$, 600 $^\circ\text{C}$ and 700 $^\circ\text{C}$. The values were observed to be within the range of accepted value for "Thin Film".

As a result of charge conduction mechanism, C-2-V linear relationship was observed. It indicated the homogeneity of Al_2O_3 film. All built-in voltages were observed to be positive value and confirmed the p-type conductivity of silicon substrate. The smallest degree of depletion layer width was found at annealing temperature 500 $^\circ\text{C}$. In addition, C-2 was directly proportional to W (depletion layer width). Thus, the Al_2O_3 layer was absolutely formed on SiO_2/Si substrate at given annealing temperature. The experimental data resulted from this work indicated that the fabrication route and measurement system were quite feasible for low-cost tunnel device option. The growth mechanism used in this work was observed to be technically simple and easily adaptable. These results are much interesting for developing, application and optimizing in term of an improved device fabrication.

Acknowledgements

The authors thank to Dr Tint Moe ThuZar, Rector, Yadanabon University for her motivation to have research-oriented mindset. The authors also thank to Pro-Rector Dr U Khin Myot, Pro-Rector Dr Myint Myint Oo and Pro-Rector Dr Khin Maw MawSoe, Yadanabon University, for their permission to do this paper. The authors also thank to Dr Khin Thida, Professor and Head of Physics Department, Yadanabon University, for her encouragement and valuable suggestion. The authors also acknowledge Dr Sandar Min, Professor of Physics Department, Yadanabon University, for her valuable advice and excellent supervision.

References

- Application Note 1369-1 2003 Solutions for Measuring Permittivity and Permeability with LCR Meters and Impedance Analyzers, Agilent Literature Number 5980-2862EN
- Debasish S et al 2006 "Synthesis and characterization of sol-gel derived ZrO_2 doped Al_2O_3 nano powder." (India: Ceramic International)
- Technical Overview 2003 Agilent 85071E Materials Measurement Software, Agilent literature number 5989-0222EN

<https://www.Tunnel Diode.com> _

ANALYSIS ON MODIFIED ULTRASONIC DISTANCE METER USING ULTRASONIC SENSOR, ESP32 AND PLX_DAQ SOFTWARE

Chit Su Aung¹, Ei Ei Mon², Su Nandar Htet³

Abstract

Most of researchers and hobbyists who measure the distance between observer and object are used the ultrasonic sensor and then, they determined the distance by using the speed of sound wave of 340 ms^{-1} . They assumed that the speed of sound is constant at any time and at any local weather situations. But, in the point of view of Physics, the speed of sound is not constant and it depends on some parameters of weather conditions such as temperature and humidity. In this research, the distance between the observer and the obstacle is observed by programming with constant speed of sound as well as with the speed of sound depending on the temperature and humidity. The ultrasonic sensor, DHT22, OLED and ESP32 are mainly used to determine the distance. The calculation of the current speed of sound is based on the temperature and the humidity obtained from DHT22. The distance measured with constant speed of sound and that with calculated speed of sound are displayed on the OLED. The values of distance measured are directly uploaded to Excel spreadsheet using PLX_DAQ software. The comparison of distance measured with constant speed of sound and that with the speed of sound varied due to temperature and humidity is observed on Excel.

Keywords: ESP32, ultrasonic sensor, DHT, OLED, speed of sound, PLX_DAQ.

Introduction

Ultrasonic sensor HC_SR04 can measure the distance between observer and object. For this ability, it can be used in robotic avoidable vehicles, car parking system, in-out counter and so on. Most of hobbyists and inventors used ultrasonic sensor HC_SR04 to measure the distance. In determining the distance, the speed of sound is used to calculate the distance. Most of them assume that the speed of sound is constant at anywhere and at any time. For the aspect of Physics, the speed of sound is dependent on some weather conditions. The speed of sound can be varied with temperature and humidity which are changed in time to time. The more precise value of distance can be obtained by using the calculated speed of sound at present temperature and humidity. DHT22 is a sensor which can produce the accurate temperature and humidity. The speed of sound is calculated by knowing these two parameters. ESP32 is a series of low-cost, low-power microcontroller with integrated Wi-Fi and dual-mode Bluetooth. The ESP32 consists of dual-core microprocessor, built-in antenna, switches, power amplifier, low-noise receive amplifier, filters, and power-management modules. The obtaining the temperature and the humidity from DHT22, the getting time of flight from HC_SR04, converting it to the distance and the displaying data on OLED are processed by ESP32 using C++ language. The block diagram of the system is illustrated in (figure 1).

¹ Department of Physics, Kyaukse University

² Department of Physics, Kyaukse University

³ Department of Physics, Kyaukse University

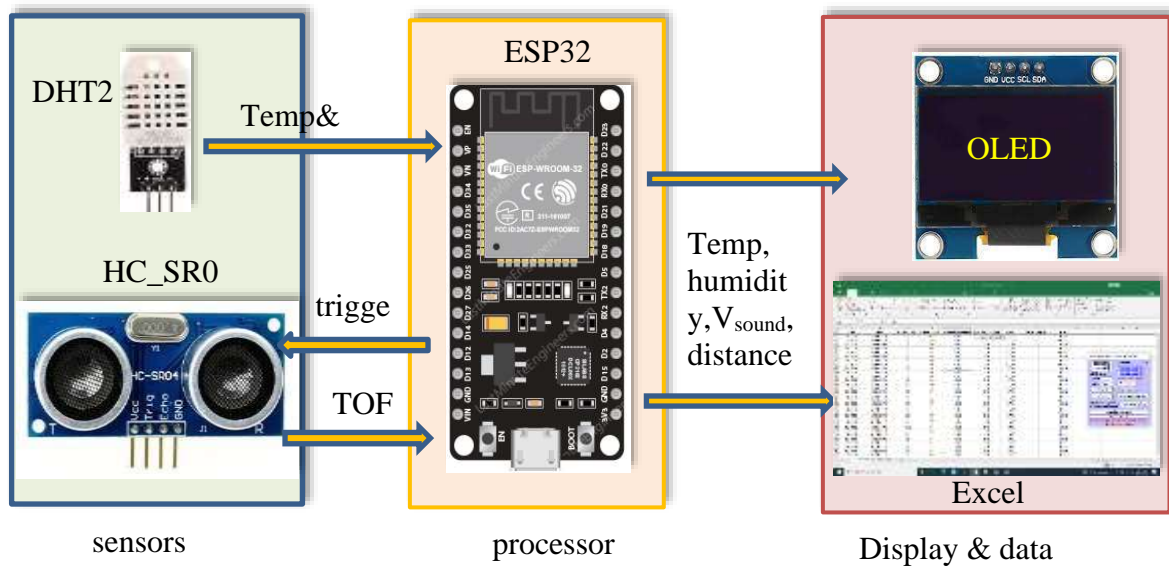


Figure 1. The block diagram of ultrasonic range measuring system

Materials and Method

DHT sensor can produce the temperature and humidity which are used to calculate the speed of sound. When HC_SR04 ultrasonic sensor is received the trigger signal from ESP32, it transmits ultrasonic pulses and receives the reflected sound. The time duration is received by ESP32 and it is converted to the distance. These measurable quantities are displayed on the OLED display.

Ultrasonic Sensor HC_SR04

Ultrasonic wave is a high-pitched sound wave whose frequency exceeds 20kHz that is beyond the audible range of human hearing. Ultrasonic sensor HC_SR04 composes of two ltrasonic transducers: transmitter and receiver. Transmitter produces the ultrasonic wave of 8 pulses at 40kHz as soon as the trigger pin of HC_SR04 is HIGH at 10µs. Meanwhile, the echo pin goes HIGH and waits for the reflected ultrasonic wave to receive. When the reflected ultrasonic is received, echo pin goes LOW state. ESP32 receives the output pulse whose width is proportional to distance in front of it. This gives the time of flight (TOF) in microsecond (µs) which can be obtained by using “pulseIn” instruction of C++. Ultrasonic sensor HC_SR04 shown in (figure 2) can measure the non-contact range between 2cm and 400cm (about 13 feet) with 3mm accuracy. The working principle is illustrated in (figure 3). The pin assignment of Ultrasonic sensor HC_SR04 is tabulated in table 1. [1]



Figure 2. Ultrasonic sensor

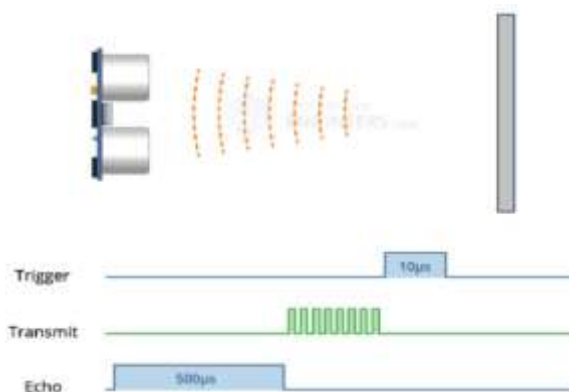


Figure 3. The working principle of Ultrasonic sensor

Table 1. Pin assignment of Ultrasonic sensor HC_SR04

Pin Name	ESP32
VCC	Connected to Vin
GND	Connected to ground.
TRIG	Pin 5 of ESP32
ECHO	Pin 18 of ESP32

ESP32

ESP32 development board composed of Tensilica Xtensa dual-core 32-bit LX6 microprocessor. This processor operates at **80 to 240 MHz** adjustable clock frequency and performs at up to **600 DMIPS** (Dhrystone Million Instructions Per Second). ESP32 integrates Wi-Fi transceiver and dual mode Bluetooth capabilities. It can not only connect to a Wi-Fi network and interact with internet but also it can setup an own network. It composes of 448KB of ROM, 520 KB of SRAM and 4MB of flash memory which are sufficient to implement web pages, JSON / XML (JavaScript Objects notation /Extensible Markup Language) data and everything used in IoT devices. ESP-WROOM-32 also contain a 4 MB SPI Flash IC, a 40 MHz Crystal Oscillator, PCB Antenna and some discrete passive components to make a working system. The pinout of a typical ESP-WROOM-32 Module shown in (figure 4). [2]

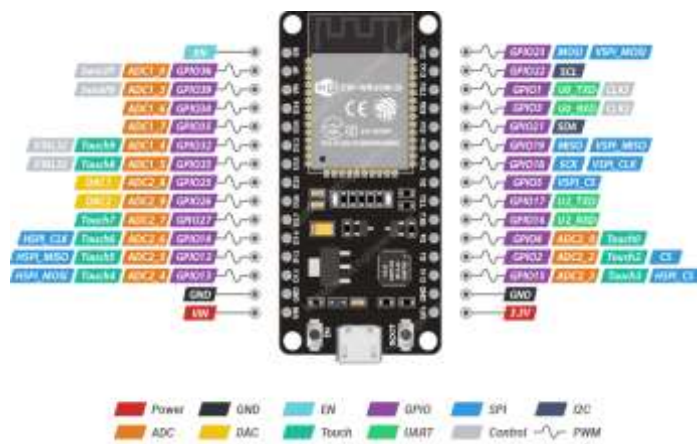


Figure 4. ESP32 module and its pin assignment

DHT22

DHT22 can measure temperature and humidity in terms of digital signal output. DHT22 includes a material whose resistance is varied with humidity and an NTC thermistor. It connects to a 32-bit ESP32 microcontroller so that its output has precise values, fast responding time and anti-interference ability. Among other temperature and humidity sensors, it is reliable and cost effective. The communication and synchronization between ESP32 and DHT22 sensor implement with Single-bus data format. Each temperature and humidity value consists of decimal and integral parts. One complete communication is about 4ms. A complete data transmission is **40bit**, and the sensor sends **higher data bit** first. The form of Data format is 8bit integral RH data + 8bit decimal RH data + 8bit integral T data + 8bit decimal T data + 8bit check sum. ESP32 transmits the data to OLED and uploads to Excel via PLX_DAQ software, if the check-sum is equal to the



Figure 5. DHT22 sensor

sum of 8bit integral RH data, 8bit decimal RH data, 8bit integral T data and 8bit decimal T data. As soon as ESP32 sends a start signal, DHT22 sends a response signal of 40-bit data that include the relative humidity and temperature information to ESP32. Overall communication process is shown in (figure 6). [3,4]

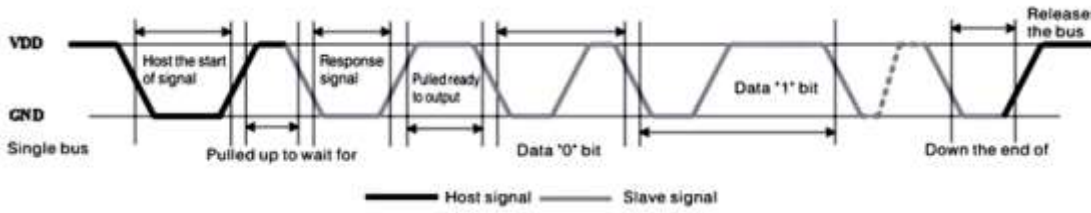


Figure 6. Overall Communication Process between DHT and MCU

OLED

OLED stands for Organic Light Emitting Diode, or Organic LED. It is a display technology consisting of OLED panels that emit their own light when an electric current is passed through them. As a result, OLEDs are super-light, have a true contrast ratio, wide color, deep color saturation and wide viewing angle. Although there are several types of OLED displays available in the market, the SH1106 1.3-inch OLED display in (figure 7) is used in this research. The main component of all different types of OLED displays is an SH 1106 controller which uses I2C or SPI protocol to communicate with the microcontrollers. The OLED performs faster in SPI communication but it is popular with I2C communication because of the lower number of pins. The OLED displays are available in various size, color, and shape but are coded in a similar way. Adafruit_GFX library and Adafruit_SH110X library are required for 1.3-inch OLED display. [5,6]



Figure 7. I2C OLED

Variation of Speed of Sound

The speed of sound depends on how faster the vibrational energy propagate in the medium. For this fact, the derivation of the speed of sound takes into account the state of medium such as temperature, humidity. According to the kinetic gas theory, the speed of sound in gas (air) is;

$$v = \sqrt{\frac{\gamma RT_K}{M}}$$

Where, R= gas constant = 8.31 joule/mol K, $\gamma=1.4$, $M=0.02897$ kg/mol for air. If temperature is $T_K= 20^\circ\text{C} = 293$ K, speed of sound is 343 m/s.

$$v = \sqrt{\frac{273\gamma R}{M}} \sqrt{\frac{T_K}{273}} = 331.4 \sqrt{\frac{T_K}{273}} = 331.4 \sqrt{1 + \frac{T_C}{273}} = 331.4 + (0.6 \times T_C)$$

The speed of sound also depends on humidity. The density of humid air is less than the density of dry air. According to the equation of, $v = \sqrt{\frac{\gamma P}{\rho}}$ the speed of sound increases in the humid air. The speed of sound can be approximated as follow;

$$v = \{331.4 + (0.6 \times T_c)\} + \{0.0124 \times \text{relative humidity} (\%)\} [7]$$

Operation

There are two main sections to measure the distance using ultrasonic sensor HC_SR04; hardware and software section. ESP32, DHT22 and OLED are used as hardware components. In software section, Arduino IDE and PLX_DAQ software are utilized. DHT library and SH110X OLED library are included in the code. Library for HC_SR04 sensor does not use in program. Knowing the operation of HC_SR04 sensor, code is written.

Hardware Preparation

Ultrasonic range meter is constructed by using ESP32, DHT22, OLED and ultrasonic sensor HC_SR04. Vcc, data output and ground of DHT22 are connected 3.3V, D4 and gnd of ESP32. Vcc, ground, serial clock (SCL) and serial data (SDA) of OLED are connected to 3.3V, gnd, D22 and D21 of ESP32. Vcc, trigger, echo and gnd of HC_SR04 are wired to Vin, D5, D18 and gnd of ESP32. The circuit connection as shown in (figure 8). The schematic circuit diagram drawn by EasyEDA software and its PCB layout design are shown in (figure 9).

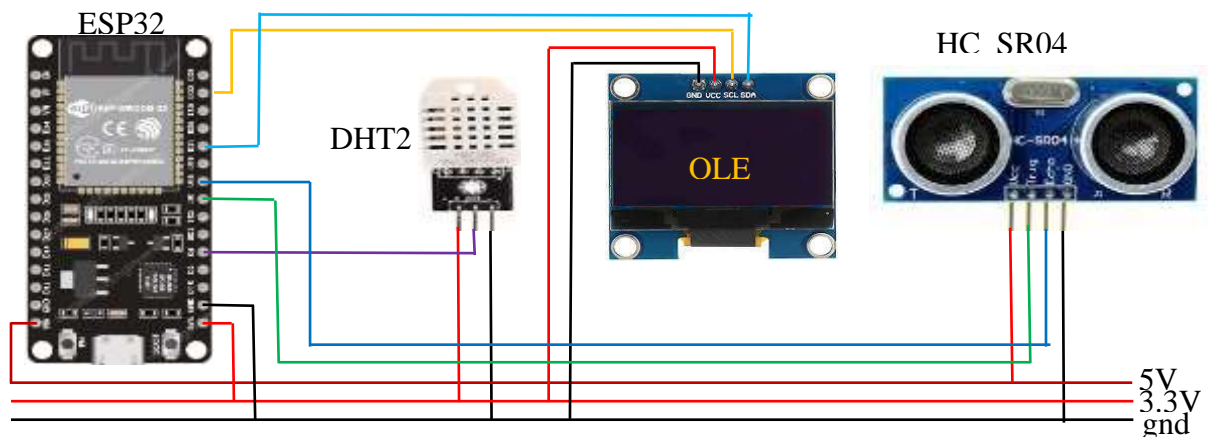


Figure 8. Circuit connection of Ultrasonic range meter



Figure 9. Schematic circuit and PCB layout using EasyEDA software

Software Explanation

Many programming environments such as Arduino IDE, espressif IDF, micropython, Javascript, Lua and etc. can be used with ESP32. In this research, Arduino IDE and C++ language are used. Firstly, the libraries of DHT and SH110X OLED are included. The variables used in code, configurations of pin and baud rate (data transfer rate between ESP32 and PC) are defined. DHT library and OLED library are initialized and then, the table heading for Excel spreadsheet is prepared. ESP32 obtains the values of temperature and humidity from DHT22 sensor. Based on these values, the velocity of sound is calculated with the equation of $v = \{331.4 + (0.6 \times T_c)\} + \{0.0124 \times \text{relative humidity} (\%)\}$. After that, ESP32 sends the $10\mu\text{s}$ trigger pulse to HC_SR04 ultrasonic sensor to produce 8-pulse of 40kHz. Simultaneously, echo pin is HIGH. As soon as the reflected pulse reaches the echo pin, it goes LOW. This time of flight (ToF) or duration in microsecond is noted by using `pulseIn()` function. The distance is calculated by $s = (\text{duration} \times \text{speed of sound}) / 2$. Here, the object distance in front of source is calculated with constant speed of sound of 340m/s and with the variable speed of sound which is function of temperature and humidity. Temperature, humidity, speed of sound, and two calculated distances are displayed on OLED. At the same time, the current date-time, temperature, humidity, speed of sound, two types of distance with % error are directly uploaded to Excel spreadsheet using PLX_DAQ software. Data can be refreshed with optional period. In this research, refreshing time is 2 seconds. [8,9,10]

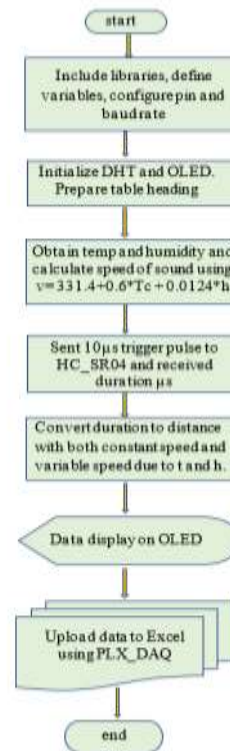


Figure 10. Flowchart of range meter

Results

The ultrasonic range meter is designed and constructed as shown in figure 11(a). Firstly, the object is placed at a distance of 1foot in front of meter in figure 11(b). The distance is measured by both UNI-T laser distance meter and the ultrasonic range meter as shown in figure 11(c). And then, the temperature, humidity, speed of sound, distances measured with constant speed, the distance measured with speed due to temperature and humidity and their respective errors with current date and time are uploaded to Excel spreadsheet via PLX_DAQ software. The uploaded Excel sheet is illustrated in (figure 12).

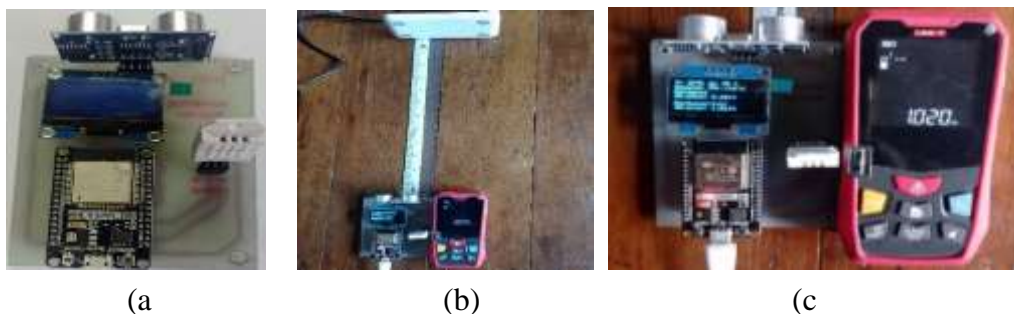


Figure 11. Ultrasonic range meter and distance measuring

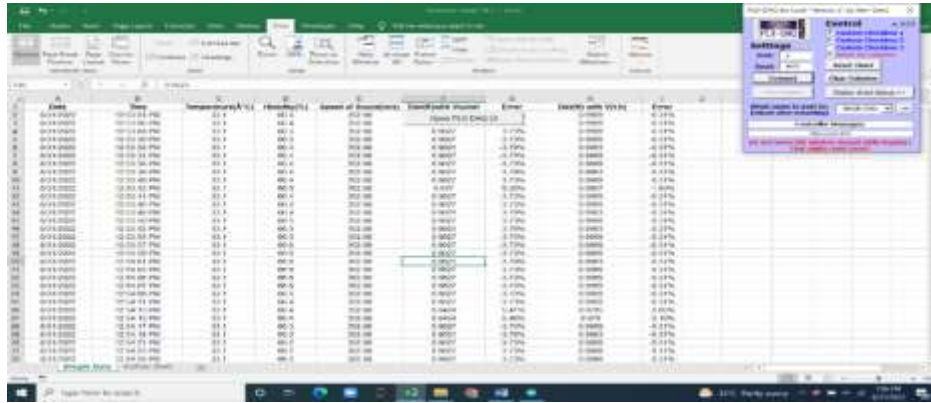


Figure 12. The data on Excel spreadsheet

The distance can be measured up to 10 feet. The (figure13) shows the various distances measured by both UNI-T laser distance meter and ultrasonic range meter. The comparison of distance measured with constant speed of sound and the distance with the speed of sound due to temperature and humidity as shown in (figure 14).



Figure 13. Comparison of distance measured by both meters



Figure 14. Comparison of distance measured with constant speed and varied speed of sound

Discussion

Firstly, the object is placed 1 foot in front of the HC_SR04 sensor using ruler. The distance is measured in two points of view. One is the distance measurement by using ultrasonic range meter while another is the distance measurement by using UNI-T laser distance meter which can measure up to 60m. In ultrasonic distance measurement, there are two methods used to measure distance. That is- the distance is measured with constant speed of sound and the distance is measured with varying speed of sound due to temperature and humidity. Using constant speed of sound of 340 m/s and measuring 1 ft distance, the minimum distance measured is 0.9454 ft and maximum distance 0.9627 ft with minimum percentage error is -3.79% and maximum percentage error is -5.46%. Using varying speed of sound and measuring 1 ft distance, the minimum distance measured is 0.979 ft and maximum distance 0.9969 ft with minimum percentage error is -0.31% and maximum percentage error is -2.10%. These measurements are carried out at the temperature 33.1°C and relative humidity 66% approximately. At these conditions, the approximated speed of sound is 352 m/s. The speed of sound is 340 m/s at the temperature of 20°C roughly. Therefore, distance measured with constant speed of sound has more percentage error. Higher temperature and humidity are, the more error is in measuring with constant velocity of 340 m/s. In this research, data refreshed time is 2 seconds that means data is measured each 2 seconds. It may be more précised by measurements taking 10 times and calculating the average values. As the HC_SR04 ultrasonic sensor transmits eight pulses at 40kHz, the receiver can distinguish its transmitted pulse from ambient noise. During the measurement carries out, the ambient sound intensity is minimum 24.6 dB, maximum 78dB and average 39.1dB as shown in (figure 15). As it is low intensity, it cannot affect the measurement.



Figure 15. Ambient sound

Conclusion

HC_SR04 ultrasonic sensor is reliable in terms of accuracy and overall usability but there are some limitations in using it. The distance between the sensor and obstacles can be measured 2cm to 400cm (about 13 ft) in factory issues. But, in this research, the distance can be measured within 10 feet. It is not suitable to measure the small object which is at distant location. HC_SR04 sensor is difficult to detect the object which has soft and irregular surface. There are some variations of distance measurement due to the variation of speed of sound. The surface of the object should be perpendicular to the line of sound propagated. If not, the sound is not reflected back to the receiver. Although, there are many limitations of HC_SR04 ultrasonic sensor, it is used in many innovations such as avoidable robot, water levelling, in- out counter, typical radar system. According to the researched results, HC_SR04 ultrasonic sensor is used by attaching the DHT sensor for more precise distance measurement.

Acknowledgements

My first and large appreciation reflects to Professor Dr Khin Nyo Win, Head of Department of Physics, Kyaukse University, for her marvelous guidance and encouragement. My gratitude is extended to her generous participation in constructive feedback, kind support during my service.

I greatly appreciate Professor Dr Myat Myo Myo Aye, Department of Physics, Kyaukse University, for her kind support of hardware required in this research, constructive guideline and excellent encouragement.

Many thanks to all of my colleagues in our department for their time, advice and mutual support. Last, but not least, my heartfelt thanks go to my parent for their tremendous support and hope.

References

- <https://lastminuteengineers.com/arduino-sr04-ultrasonic-sensor-tutorial>
<https://www.electronicshub.org/esp32-pinout>
<https://components101.com/sensors/dht11-temperature-sensor>
<https://nerdyelectronics.com/working-of-dht-sensor-dht11-and-dht22>
<https://www.explainthatstuff.com/how-oleds-and-leps-work.html>
<https://microcontrollerslab.com/oled-esp32-arduino-ide>
<https://pressbooks.online.ucf.edu/osuniversityphysics/chapter/17-2-speed-of-sound>
<https://inegm.medium.com/quick-start-to-simple-daq-system-using-plx-daq-excel-arduino-d2457773384b>
Rui Santos, (2020) “ESP 32 troubles shooting guide” Random Nerd Tutorial Lab, Porto, Portugal
Rui Santos, (2020)” Learn ESP32 with Arduino IDE” Random Nerd Tutorial Lab, Porto, Portugal

SEASONAL DETERMINATION OF RADON CONCENTRATION IN SOIL SAMPLES FROM KALAIN GOLD MINE AT BAGO REGION

Hein Nay Zar Wann¹, Yin Maung Maung²

Abstract

Soil gas Radon, ²²²Rn, concentration was measured in kalin gold mine of Shwe Kyin Township at Bago Region. Seasonal determination of radon concentration in soil samples were tested by using RAD 7 radon technique detector. Three different seasons (summer, rainy and cold) in each level of five different depths (2.5 ft, 5 ft, 7.5 ft, 10 ft and 12.5 ft) in the same place were taken for soil gas measurement, starting from the ground surface. Based up on results, the cold season has the most radon contents in three seasons. The measured results were accepted by International Commission on Radiological Protection (ICRP) standard. The results obtained from this study are not dangerous for workers in that area.

Keywords- gold mine, soil, Radon concentrations, cold season and RAD 7

Introduction

Radon is formed in the ground from the radioactive decay of uranium-238, which is present in small quantities in all rocks and soils. Radon is a naturally occurring radioactive noble gas. The soil and rocks feature also control the prevalence of radon [K.B.A. Ahmad, 2010]. In an outdoor, air flow is reducing its stronger quickly dissipate radon. It can move freely through cracks or gaps in soils and bedrock. Radon which reaches the open air is rapidly diluted to harmless concentrations [O.O. Joshau, L. Macheke, 2013]. Radon -222 gas, commonly called radon is colourless, odourless and tasteless and therefore undetectable by human senses. Radon can only be detected or measured with special detectors. Two methods can be used for measuring of radon concentrations as short-term (Active) and long-term (Passive) methods [P.A.a.M. Colgan, A.T, 2009]. In this research, RAD 7 radon detector short-term (Active) method was used to determine the radon concentrations of soil samples from Kalain Gold Mine, Shwe Kyin Township and Bago Region.

Material and Methods

Radon

Radon (²²²Rn) is a chemically noble gas. The atomic number of radons is 86. Although it is a colourless gas, the half-life of ²²²Rn is 3.82 days [Benter & Yinon, 2005]. Basic information of radon is shown in table 1. Radon (²¹¹Rn) to (²²²Rn) isotopes and their half-life were listed in table 2. The atomic structure of radon is shown in table 3 and radon electron configuration (Bohr Model) as shown in figure 1 [Brill A.B, 1994].

¹ Department of Physics, Pakokku University

² Department of Physics, University of Yangon

Table 1. Basic information's of radon

Symbol	Rn
Atomic number	86
Atomic mass	222.0 amu
Melting point	- 71.0 °C (202.15 K, -95 °F)
Boiling point	- 61.8 °C (211.35 K, -79.24 °F)
Number of protons/ electrons	86
Number of neutrons	136
Classification	Noble gas
Crystal structure	Cubic
Density at 293K	9.73 g/cm ³
Colour	colourless

Table 2. Isotopes

Isotopes	Half-life
Rn-211	14.6 hours
Rn-212	24.0 minutes
Rn-217	0.6 milliseconds
Rn-218	35.5 milliseconds
Rn-219	3.96 seconds
Rn-220	55.61 seconds
Rn-222	3.82 days

Table 3. Atomic structure of radon

Number of energy levels	6
First energy level	2
Second energy level	8
Third energy level	18
Fourth energy level	32
Fifth energy level	18
Sixth energy level	8

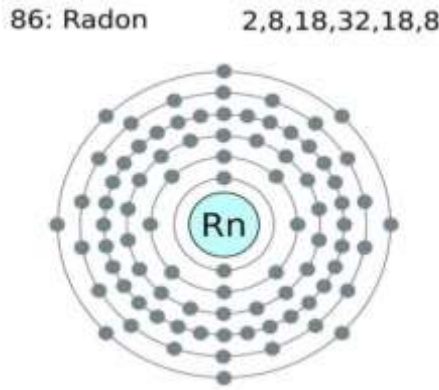


Figure 1. Radon Electron Configuration (Bohr Model)

Table 4. Unit of Measuring Radon Level

Type of Device	Units Used	Conversion
Devices that measure concentrations of radon gas	Becquerel’s per cubic metre (Bq/m ³) (Canada)	1Bq = 1 dis / s
	picocuries per litre (pCi/L) (United States)	1pCiL ⁻¹ = 37 Bqm ⁻³ 200 Bqm ⁻³ = 5.4 pCiL ⁻¹

A Safe Level of Radon Gas

Guideline values of action levels of radon concentration in different countries as shown in table 5. Action levels of radon concentration in different countries were generally mentioned as four circumstances by ICRP's record [(ICRP) in USA]. There is no action required for the concentration volume which was lower than 200Bqm⁻³ as shown in table 5 [ICRP 46(3-4)].

Table 5. Action levels of radon concentration in different countries

Country	Action Level (Bqm ⁻³)
United Kingdom	200
Ireland	200
Israel	200
Norway	200

Sample Collection

The RAD 7 detection was performed in soil samples at Kalain gold mine at 284 ft above sea level. The samples are collected at 17° 50' 46.08" north latitude, 96° 57' 46.80" east longitude and Kalian gold mine with GPSMAP 62 S as shown in figure 2. Soil samples were collected from various depths, recoding their depths with long tape measurement as shown in figure 3.

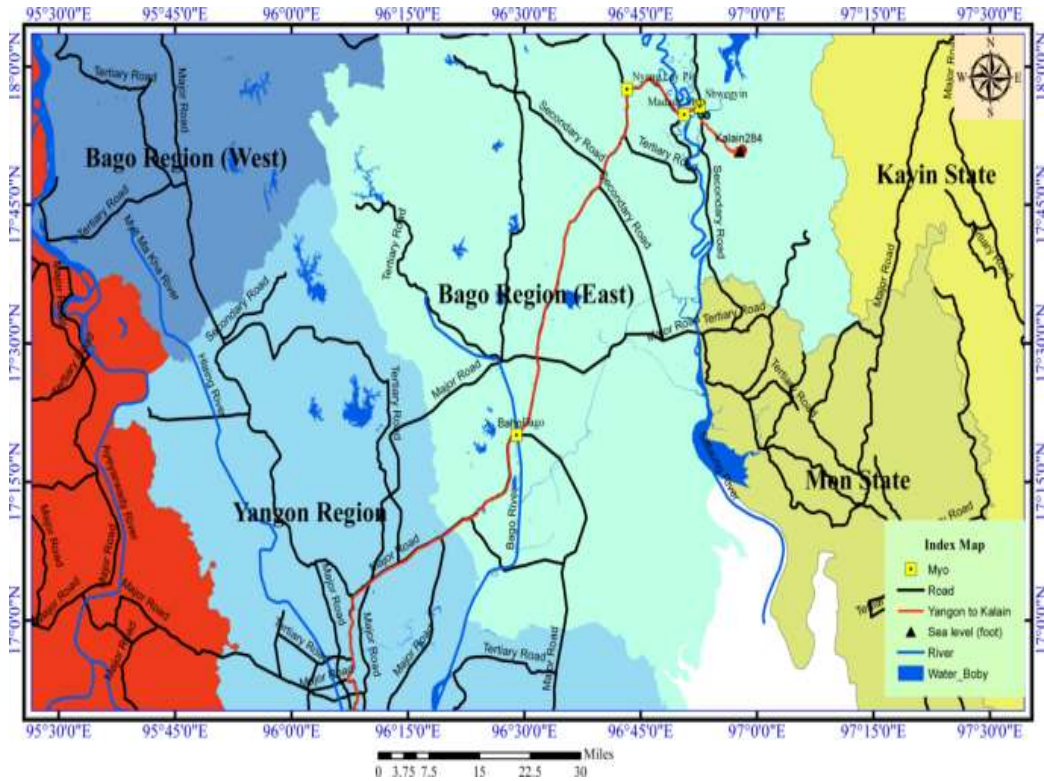


Figure 2 Location map of Kalain Gold Mine from Yangon Region



Figure 3 Kalain gold mine at Shwe Kyin Township

Measurement Procedure

Radon Soil gas measurement

After taking arrangement consists of RAD 7(Active Method) professional Durrige and small drying tube filled with fresh (blue) descendant ($CaSO_4$) positioned vertically, soil gas sample plastic can was filled through sampling point. The soil gas probe should be inserted into the soil sample up to depth about 15cm. Make sure that there is a reasonable seal between the probe shaft and the lid of can, so that ambient air does not descend around the probe and dilute the soil gas sample. Soil gas is normally so high in radon that it is not necessary to use long cycle

times to gain precision. Five minutes' cycle times (purge 5 minutes, pumping 5 minutes, waiting 5 minutes and counting 5 minutes) are sufficient. In total, each set of readings included four 5-minute cycles that took half hour. Running the test and interpretation of the data were also taken out [Ali K. Hasan, Ahmed R. Shaltakh, 2011]. Soil samples were placed into the small tube inlet, and passed through the inlet filter after small drying tube and then took out the results from its clear wide monitor as shown in figure 4.



Figure 4 DurrIDGE RAD 7 Radon Monitor

The RAD 7 detector (Active Method) converts alpha radiation directly to an electric signal and has the possibility of determining electronically the energy of each particle, which allows the identification of the isotopes (^{218}Po , ^{214}Po) produced by radiation, so it possible to instantaneously distinguish between old and new radon, radon from thorn and signal from noise. The schematic diagram of the radioactive natural decay series of Uranium- 238 is shown in figure 5 [S. Girigisu, 2012].

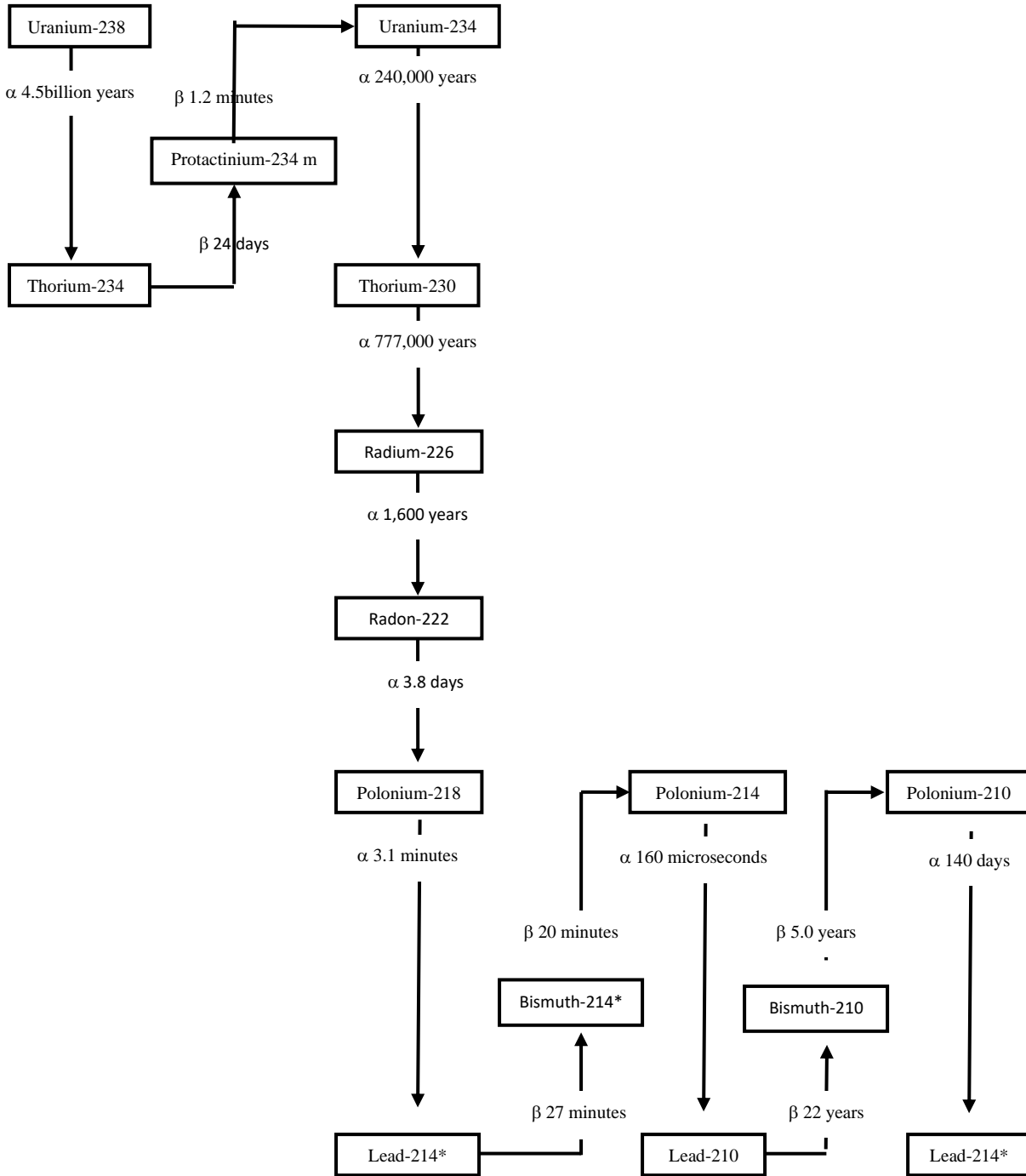


Figure 5 Radioactive Natural Decay Series of Uranium- 238

Results and Discussion

For radon concentration measurement, passive method does not require external power to operate and active method requires power to function (i.e., batteries, DC adaptors or electricity from outlet). In active method, RAD7 radon gas detector will measure the radon concentrations in soil samples at the end of the half hour period. After the determination of the soil sample was used RAD7 detector, coming out five different results for three seasons. It could be easily note that radon concentration was showing maximum at 5ft depth and minimum at 12.5ft depth. These different results data were also described with (chart) in figure 7 and below table 6, table 7 and table 8. As shown in table 6, the radon concentrations of Kalain gold mine in Summer Season

higher than that of Kalain gold mine in Rainy Season as shown in table 7. Among the three seasons, the Cold Season has the most radon concentration of Kalain gold mine than the others as shown in table 8. No action is required for the concentration volume which was lower than 200 Bqm⁻³ that had been defined by International Commission on Radiological Protection (ICRP) standard.

Table 6 Specific activity of Soil samples different depths in Summer Season at Kalain Gold Mine by RAD 7

Samples No:	Depth	Specific Activity (Bqm ⁻³)
1	76.2 cm (2.5 ft)	24.60 ± 2.70
2	152.4 cm (5 ft)	36.51 ± 2.90
3	228.6 cm (7.5 ft)	16.40 ± 1.04
4	304.8 cm (10 ft)	10.90 ± 0.57
5	381 cm (12.5 ft)	8.20 ± 2.00

Table 7 Specific activity of Soil samples different depths in Rainy Season at Kalain Gold Mine by RAD 7

Samples No:	Depth	Specific Activity (Bqm ⁻³)
1	76.2 cm (2.5 ft)	16.40 ± 2.44
2	152.4 cm (5 ft)	24.60 ± 2.68
3	228.6 cm (7.5 ft)	15.30 ± 0.54
4	304.8 cm (10 ft)	8.84 ± 0.75
5	381 cm (12.5 ft)	8.16 ± 1.98

Table 8 Specific activity of Soil samples different depths in Cold Season at Kalain Gold Mine by RAD 7

Samples No:	Depth	Specific Activity (Bqm ⁻³)
1	76.2 cm (2.5 ft)	25.70 ± 1.49
2	152.4 cm (5 ft)	49.20 ± 3.19
3	228.6 cm (7.5 ft)	16.40 ± 1.41
4	304.8 cm (10 ft)	13.10 ± 0.68
5	381 cm (12.5 ft)	12.30 ± 1.33

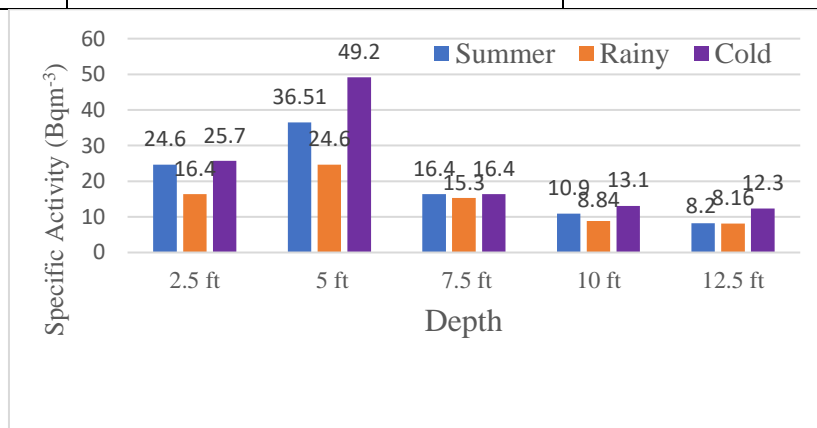


Figure 7 The radon concentrations of soil samples three season at kalain gold mine by RAD 7

Conclusion

The purpose of this research is focused on the public health point of view why radon is believed to be the second largest cause of lung cancer, after that of smoking. According to the results, it was evidently shown that maximum and minimum concentration of radon in soil samples is found in depths of 5ft and 12.5ft respectively. The maximum radon concentration obtained at 5 ft by all seasons. For the depths less than 5 ft the recoil radon prevalence moves more easily to the air, so the activity should be less. In the depths more than 5 ft the rocks soil grains constituted more compact with small or without pore space. The recoil radon at those depths should be embedded in the grains, and then the radon activity may decrease. In order to agree with results acquired at larger depths by actual practice methods, the radon emanation coefficients for different soil samples should be modified. No action may be required for maximum concentration in 5 ft depth by three seasons was less than 200 Bqm^{-3} that had been defined by International Commission on Radiological Protection (ICRP) standard. So, it did not seriously effect on people at Kalain gold mine. However, we have to continuously and widely study on radon concentration and it is very important in future for human health dealing with unseen-able radioactive leaking such as radon.

Acknowledgements

I would like to extend our thanks to Dr Htun Win, Professor (Head) and Dr Win Myint Kyu, Professor, Department of Physics, Pakokku University for their encouragement to conduct this research.

I am greatly indebted to my Supervisor, Professor Dr Yin Maung Maung, Head of Department of Physics and University of Yangon for his kind permission and guidance to carry out this research work.

I also deeply thank to my Cosupervisor, Dr Kyi Thar Myint, Professor (Retired), Department of Physics, West Yangon University for her valuable advice and guidance in carrying out this research.

We would like to thank all people who encouraged and supported us during the undertaking of this work.

References

- Ali K. Hasan, Abdul.R.H.Subber and Ahmed R. Shaltakh, 2011, "Measurement of Radon Concentration in soil gas using RAD7 in the environs of Al-Najaf Al-Ashraf city-Iraq" *Advace in Applied Science Research*, 2(5):273-278.
- A.Smith, S. Pournis and P. Barretto, 1976, "Radon methods in uranium".
- Benter & Yinon, 2005 *Chemical Element and Radon* 73
- Brill A.B. 1994, *the Journal of Nuclear Medicine* 23
- Canadian Nuclear Safety Commission, 2012, "Radon and Health".
- ICRP: The 2007 recommendations of International Commission on Radiological Protection (ICRP) in USA.
- ICRP, 2017 *Occupational Intakes of Radionuclides: Part 3. ICRP Publication 137, Ann. ICRP* 46(3-4).
- K.B.A. Ahmad, 2010, "Determination of Heavy Metal Concentration in Top Surface and Sub-surface Soil around ULU TUALANG Closed Landfill, Temerloh Pahang", Faculty of Chemical & Natural Resources Engineering University, Malaysia
- O.O. Joshau, I.O. Anthony, M.M. Nquobile, L. Macheke, 2013, "Investigating the Concentrations of Different Elements in Soil and Plant Composition from a Mining Area"
- P.A.a.M. Colgan, A.T, 2009, "Radon Monitoring and Control of Radon Exposure, in Radiological Protection Institute of Ireland".
- S. Girigisu, 2012, "Assessments of radiological levels and Elemental Concentration in soil from Awwal and Bagega gold mining sites in Kebbi and Zamfara States, Nigeria"

SOUND-ABSORBING PROPERTIES OF WASTE SCRAPED TIRE RUBBER FIBER REINFORCED POLYVINYL ALCOHOL FILMS AS RUBBER AEROGEL

Khin Sandar Lin¹, Chan Nyein Aung², Lwin Maung³

Abstract

Poly vinyl alcohol (PVA) based polymers are being widely used in additive manufacturing because of their physical characteristics such as low weight, flexibility, thermally and electrically insulation. The morphological characterization of pure PVA film and scraped tire rubber fiber (STRF) reinforced PVA films were investigated by the digital optical microscope (x1000). The average size of air bubble of PVA film and STRF reinforced PVA films are about $1.9E-8$ mm² and $7.06E-8$ mm². The chemical functional group of pure PVA film and 5 w/v%, 10 w/v%, 15 w/v%, 20 w/v% waste scraped tire rubber fiber reinforced PVA films were examined by the Fourier Transform Infrared Spectroscopy (FTIR) in the range of wave number from 4000 to 450 cm⁻¹. The resultant FTIR transmittance spectra were matched with chemical functional group of PVA and scraped tire rubber fiber (STRF). The acoustic absorption coefficient of pure PVA film and waste scraped tire rubber fiber (STRF) reinforced PVA films were investigated in the range of audio frequency 200 Hz to 2 kHz.

Keywords: PVA, scraped tire rubber fiber (STRF), acoustic properties, optical microscope, FTIR, STRF composite PVA films

Introduction

Nowadays PVA based polymers are being widely used in additive manufacturing. Poly (vinyl alcohol) PVA is a water-soluble synthetic polymer. It has the idealized formula $[CH_2CH(OH)]_n$. Polyvinyl alcohol has a melting point of 180 to 190°C. Poly vinyl alcohol is a hydrophilic semi-crystalline polymer produced by polymerization of vinyl acetate to poly vinyl acetate (PVAc), and subsequent hydrolysis of PVAc to PVA. Commercial PVA is available in highly hydrolyzed grades (degree of hydrolysis above 98.5%) and partially hydrolyzed ones (degree of hydrolysis from 80.0 to 98.5%). The content of hydrolysis or the content of acetate groups in PVA affects its chemical properties, solubility and crystal growth ability.

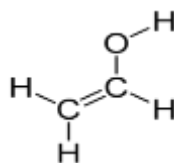


Figure 1 Molecular Structure of Poly vinyl alcohol (PVA)

Polymeric scraped tire rubber fiber (STRF) is one of the byproducts derived from the processing of used vehicle tires. Presently, significant quantities of STRF are generated annually in most developed countries of the world. However, and unfortunately, STRF been an amalgam of crumb rubber, steel and other particles, its reusability has been limited. Hence, STRF is mainly used as a fuel source in kilns or landfilled. Sulfur vulcanization of rubber is the most commonly used chemical process, by which cross-links are formed between rubber polymer chains by heating, thereby enhancing the physical properties of vulcanizes. Thus, as a consequence of vulcanization, a typical tire rubber contains about 1.52–1.64% sulfur and other chemical

¹ Department of Physics, Yangon University

² Department of Physics, Yangon University

³ Department of Physics, Patheingyi University

constituents such as 81.2–85.2% carbon, 7.22–7.42% hydrogen, 1.72–2.07% oxygen and 0.31–0.47% nitrogen, nitrogen oxides (NO_x), Sulfur dioxide (SO₂), carbon monoxide (CO) and polycyclic aromatic hydrocarbon (PAH) are emitted during scrap tire combustion. The sulfur gases are also produced during scrap tire pyrolysis. Toxic hydrogen sulfide gas was also observed as a major byproduct of scrap tire pyrolysis. Therefore, to avoid the inherent environmental pollution associated with the combustion of waste car tire rubber, it is imperative that alternative benign and value-added applications for STRF be developed.

By adding the scraped tire rubber fiber (STRF) to the PVA film, the sound absorption, electrically insulation and thermal insulation properties of PVA film can be enhanced because of their good properties such as low weight, flexibility, highly absorption and thermally insulated.

Materials and Experimental Methods

Materials

Poly Vinyl Alcohol (PVA, molecular weight of 186,000 g/mol, Sigma Aldrich, Germany) was purchased and used without further purification. The waste car tire was collected from the car workshop and cleaned to scrap the rubber filament from the waste vulcanized rubber car tire. Deionized water was used in the preparation of the blending PVA films.

Sample Preparation

The waste car tire was collected and washed in water by using iron brush. The scrap tire rubber fibers were scraped from the washed pieces of the waste car tire by the iron brush rotor machine and put the scraped tire rubber fibers into the pure water to separate the rubbers and the iron dust, metal pieces of the tire by the floating method. The floating scraped tire rubber fibers were filtered and dried in the oven at 150°C for 2 hr. Finally, the remaining iron dust in the scraped tire rubber fibers were eliminated by the magnet to get purified scraped tire rubber fiber (STRF).

Preparation of the Waste Scraped Tire Rubber Fibers (STRF) Reinforced (PVA) Films

The 2 g of PVA were dispersed in 10ml of deionized water and was stirred for 20 min at 80°C with 500 rpm to get the transparent and homogeneous 20 w/v% PVA solution. The 20 w/v% PVA solution was poured into the ceramic mold to cast the pure PVA film by solution-casting method and the resultant PVA film was dried at 60 °C in the desiccator to synthesize pure PVA film. The 0.5 g of the scraped tire rubber fiber (STRF) were slightly added into the homogenous 20 w/v% PVA solution and was stirred for 20 min at 80°C with 500rpm. The resultant rubber fiber mixed PVA solution was casted into ceramic mold by the solution casting method to get the 5 w/v%, STRF reinforced PVA film. The 10 w/v% and 15 w/v%, 20 w/v% STRF reinforced PVA films were also prepared by the use of 1 g 1.5 g and 2g of the scraped tire rubber fiber (STRF) as the above solution-casting method. The resultant STRF reinforced PVA films were dried and kept at 60°C in the desiccator. Figure 2 shows sample preparation processes of the scraped tire rubber fiber.

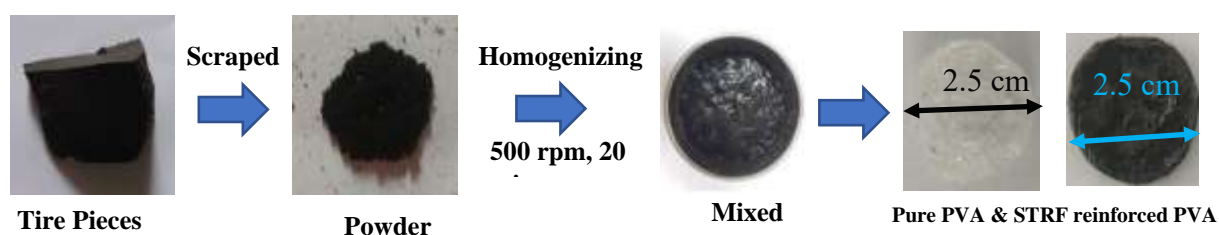


Figure 2. Sample preparation processes of the scraped tire rubber fiber

Morphological Characterizations

The morphological characterization of pure PVA film was investigated by the Transicom Singapore 300 LCD digital microscope (x1000). The average size of air bubble of pure PVA film and STRF reinforced PVA films were examined by the use of the Fiji image analysis software.

Chemical Functional Group Analysis by FTIR Method

The chemical functional group of pure PVA film and 5 w/v%, 10 w/v%, 15 w/v%, and 20 w/v% waste scraped tire rubber fiber reinforced PVA film were examined by the Fourier Transform Infrared Spectroscopy (FTIR). The pure PVA films and the waste scraped tire rubber fiber reinforced PVA films were obtained as 4 mm thickness films and analyzed by the FTIR using Transmittance Mode. FTIR spectra were obtained in the range of wavenumber from 4000 to 450 cm⁻¹ using FTIR spectrometer Perkin Elmer, 109976, USA. The FTIR spectra were normalized and major vibration bands were associated with chemical functional groups.

Acoustic Absorption Analysis

The acoustic absorption coefficient of pure PVA film and waste scraped tire rubber fiber (STRF) reinforced PVA films were investigated in the range of audio frequency 200 Hz to 2 kHz by the use of the oscilloscopic analysis. The frequency generator, oscilloscope and sound transmission tube were served to examine the acoustic absorption coefficient of sample PVA and STRF composite PVA films. The acoustic absorption coefficient measurement setup is depicted as in the Figure 3 and 4. The acoustic absorption coefficients of the samples were calculated as the following relation.

$$\alpha = 1 - \frac{I_{\text{Transmission}}}{I_{\text{incident}}} \tag{1}$$

α = acoustic absorption coefficient

I_{incident} = Intensity of incident sound wave, I_0

$I_{\text{Transmission}}$ = Intensity of transmitted sound wave, I

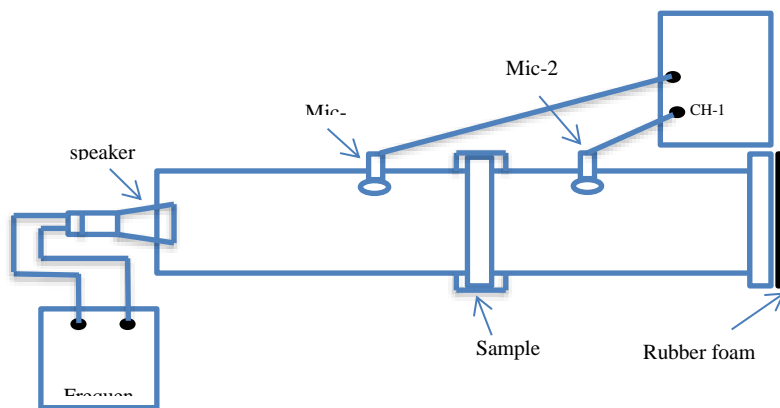


Figure 3. Acoustic absorption coefficient measurement setup



Figure 4. Measurement of Acoustic absorption coefficient

Results and Discussion

The morphological characterization of pure PVA film by the optical microscope shows the roughness surface and the air bubble formation of the PVA film as in the optical micrograph in figure. The average size of air bubble of PVA film and STRF reinforced PVA films are about are 1.9E-8mm² and 7.06E-8mm².



Figure 5. Optical Micrograph of pure PVA and SCRF reinforced PVA Films

FTIR Analysis of Waste Scraped Rubber Fiber (SCRF) Reinforced PVA Films

The Fourier Transform Infrared Spectroscopy (FTIR) analysis of pure PVA films indicated the chemical functional group of PVA film as in the Figure 6 and Table 1. The FTIR transmittance spectra of the 5 w/v%, 10 w/v%, 15 w/v% and 20 w/v%, scraped tire rubber reinforced PVA film are shown in the Figure 7 and the chemical functional group of scraped tire rubber reinforced PVA films is as in the Table 2. The peak number 4,5,6 and 7 and 8 of the FTIR transmittance spectra of the 5 w/v% scraped tire rubber reinforced PVA film in the Figure 7 correspond to the waste scraped tire rubber fiber and other peak numbers are represented PVA. The resultant FTIR transmittance spectra were matched with chemical functional group of PVA and the scraped tire rubber fiber.

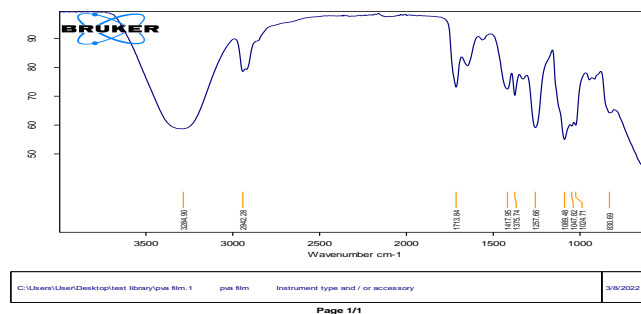


Figure 6. FTIR transmittance spectra of pure PVA film

Table 1 Chemical functional groups of FTIR spectra of pure PVA film.

Peak Number	Wave Number (cm ⁻¹)	Functional Group
1	3284.90	O-H stretching
2	2942.28	C-H stretching
3	1713.84	C=O stretching
4	1417.95	CH ₃ -O bending
5	1375.74	C-H bending
6	1257.66	C-O stretching
7	1089.48	C=O-C stretching
8	1047.82	C-O stretching
9	1024.71	C-O stretching

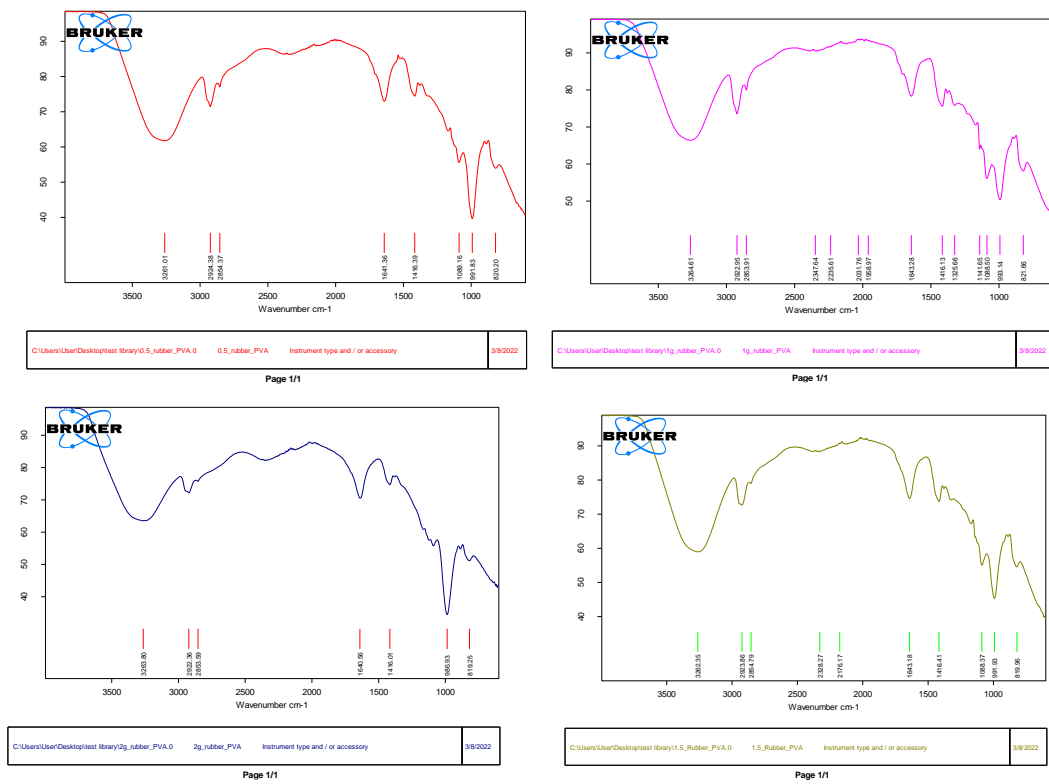


Figure 7. FTIR transmittance spectra of 5 w/v%, 10 w/v%, 15 w/v%, 20 w/v%, scraped tire rubber reinforced PVA films

Table 2 Chemical functional groups of FTIR spectra of 5w/v%, 10 w/v%, 15 w/v%, 20 w/v% scraped tire rubber fiber (STRF) reinforced PVA films

Peak Number	Wave Number (cm ⁻¹)	Functional Group
1	3261.01	O-H stretching
2	2924.38	C-H stretching
3	2854.37	C-H stretching
4	1641.36	[-C=C] bending
5	1416.39	[=CH ₂] bending
6	1089.16	SiO ₂
7	1377.66	[-CH ₃] bending
8	991.83	P-O-C stretching
9	821.66	C=C-H stretching

Sound-Absorbing behavior of waste scraped rubber fiber (SCRF) reinforced PVA films

The oscilloscopic analysis of the acoustic absorption coefficient of pure PVA film and waste scraped tire rubber fiber (STRF) reinforced PVA films were shown in the Table-3,4,5,6 and 7. The frequency dependency of the acoustic absorption coefficient of the PVA film and the waste scraped tire rubber fiber (STRF) reinforced PVA films were depicted as in the Figure 8.

Table 3 Acoustic absorption coefficients of pure PVA film in the range of audio frequency 200 Hz to 2 kHz

Frequency	I ₀ (V)	I (V)	α
200Hz	1.7	0.38	0.78
300Hz	1.6	0.4	0.75
400Hz	1.3	0.4	0.7
500Hz	1.5	0.52	0.65
600Hz	1.8	1.1	0.39
700Hz	2	1.4	0.3
800Hz	2	1.1	0.45
900Hz	1.75	0.6	0.65
1kHz	1.2	0.25	0.79
1.5kHz	0.36	0.032	0.91
2kHz	0.35	0	1

Table 4 Acoustic absorption coefficients of 5 w/v% SCRF reinforced PVA Film in the range of audio frequency 200 Hz to 2 kHz

Frequency	I ₀ (V)	I (V)	α
200Hz	0.68	0.034	0.95
300Hz	0.6	0.044	0.94
400Hz	1.5	0.088	0.94
500Hz	2.4	0.1	0.95
600Hz	2.4	0.1	0.95
700Hz	2.4	0.07	0.97
800Hz	2	0.036	0.98
900Hz	1.4	0.024	0.98
1kHz	1	0.014	0.98
1.5kHz	0.32	0.003	0.90
2kHz	0.22	0.002	0.90

Table 5 Acoustic absorption coefficients of 10 w/v% SCRF reinforced PVA Film in the range of audio frequency 200 Hz to 2kHz

Frequency	I ₀ (V)	I (V)	α
200Hz	0.48	0.017	0.96
300Hz	1	0.04	0.96
400Hz	1.4	0.084	0.94
500Hz	1.75	0.068	0.96
600Hz	2.6	0.056	0.97
700Hz	3.2	0.050	0.98
800Hz	2.3	0.028	0.98
900Hz	1.6	0.018	0.98
1kHz	1.2	0.09	0.92
1.5kHz	0.36	0.002	0.99
2kHz	0.24	0	1

Table 6 Acoustic absorption coefficients of 15 w/v% SCRF reinforced PVA Film in the range of audio frequency 200 Hz to 2kHz

Frequency	I ₀ (V)	I (V)	α
200Hz	0.72	0.014	0.98
300Hz	0.96	0.04	0.95
400Hz	1.25	0.035	0.97
500Hz	1.6	0.049	0.96
600Hz	2.4	0.064	0.97
700Hz	2.3	0.062	0.97
800Hz	2.1	0.046	0.97
900Hz	1.5	0.026	0.98
1kHz	1.15	0.012	0.98
1.5kHz	0.36	0.002	0.99
2kHz	0.24	0	1

Table 7 Acoustic absorption coefficients of 20 w/v% SCRF reinforced PVA Film in the range of audio frequency 200 Hz to 2kHz

Frequency	I_0 (V)	I (mV)	α
200Hz	0.3	2	0.99
300Hz	0.9	22	0.97
400Hz	1	40	0.96
500Hz	1.55	12	0.99
600Hz	3	19	0.99
700Hz	3	28	0.99
800Hz	2	14	0.99
900Hz	1.6	9	0.99
1kHz	1.1	7	0.99
1.5kHz	0.34	6	0.98
2kHz	0.26	5	0.98

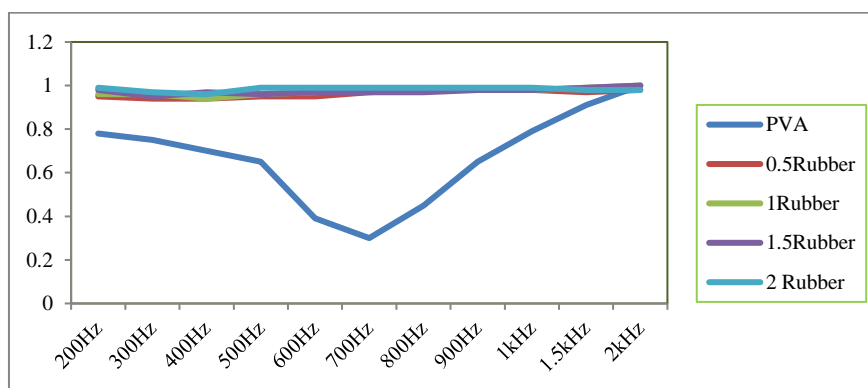


Figure 8 Acoustic Absorption Coefficient of pure PVA film and the waste scraped tire rubber fiber (STRF) reinforced PVA films as the function of the audio frequency in the range of audio frequency 200 Hz to 2 kHz

Conclusion

The waste scraped tire rubber fiber (STRF) reinforced PVA films have greater Acoustic absorption coefficient than the pure PVA film. The acoustic absorption coefficient of pure PVA layer is varied as the function of the acoustic frequency. The pure PVA layer has maximum acoustic absorption coefficient at the acoustic frequency 2 kHz and has minimum acoustic absorption coefficient at 700 Hz. All of the PVA acoustic absorber have large acoustic absorption coefficient at high frequency, 2 kHz due to their resonant frequency nature. This research has shown that the waste scraped tire rubber fiber (STRF) reinforced PVA films can be used as the Acoustic absorber to reduce sound pollution of the environment and may be one of the solutions for the waste car tire rubber recycling.

Acknowledgements

I would like to express appreciation to acting Rector Dr Than Htun, Patheingyi University for his encouragement and kind permission to undertake the present research. I also would like to express my profound thanks to Dr Yin Maung Maung, Head of Department of Physics, Yangon University, Dr Min Maung Maung, Professor and Dr Chan Nyein Aung, Associate Professor, Department of Physics, Yangon University for their kind permission to carry out this work, their encouragement and help during this work.

References

- Chen JH, et al (2001), "On the pyrolysis kinetics of scrap automotive tires." J Hazard Mater B84:43–550.
- Isayev AI, et al (1996) "*Appl. Polym. Sci.*, 59, 803–813.
- Levendis YA, et al (1996) "Comparative study on the combustion and emissions of waste tire crumb and pulverized coal". Environ Sci Technol 30:2742–2754.
- Li Y, et al "*Polym. Environ*". 2012, 20, 372–380.
- Murena F (2000) Kinetics of sulphur compounds in waste tyres pyrolysis. J Anal Appl Pyrol 56:195–205. R. R. N. Jones, et al "*Chemical Applications of Spectroscopy*". New York: Interscience, 1956.
- S. Ramarad, et al (2015), "Waste tire rubber in polymer blends: A review on the evolution, properties and future," *Progress in Material Science*, Volume 72, 100-140.
- Tang L, et al (2004) "An investigation of sulfur distribution during thermal plasma pyrolysis of used tires". J. Anal Appl Pyrol 72:35–40.
- T. Wang, et al (2004), "Polymer International" 53-911.
- Zhang X (2007), et al, "*Appl. Polym.*", 103, 4087–4094.

THE PROPAGATION OF A PARTICLE IN THE ONE-DIMENSIONAL INFINITE SQUARE-WELL BY USING THE PATH INTEGRAL FORMALISM

Khin Myat Thet Wai¹, Hla Hla Maw², Thet Thet Wai³

Abstract

Path integral was invented by Feynman as an alternative formulation of quantum mechanics. Feynman formulation of quantum mechanics using the so called path integral is arguably the most elegant. The path formulation of quantum field theory represents the transition amplitude (corresponding to the classical correlation function) as a weighted sum of all possible histories of the system from the initial to the final state. In this work, the full propagation for the propagation of a particle in the one dimensional infinite square well by using the path integral formalism will be obtained by using Feynman's path integral approach. Visualization of key results is implemented by Mathematica.

Keywords: Feynman path integral, Propagator, Kernel

Introduction

The path integral formalism, which was invented by the US physicist Richard Feynman, is a tool for calculating such quantum mechanical probabilities. Feynman's recipe, applied to a particle travelling from A to B. The resulting sum tells us the probability of detecting the particle that started out at A at the location B at the specified time. Physicists called such a sum over all possibilities a path integral or sum over histories. In quantum mechanics and quantum field theory, the propagator is a function that specifies the probability amplitude for a particle to travel from one place to another in a given period of time, to travel with a certain energy and momentum. The propagator can be written as a sum over all possible paths between the initial and final points.

Path integral provided a unified view of quantum mechanics, field theory and statistical physics and is nowadays an irreplaceable tool in theoretical physics. Feynman showed that Dirac's quantum action was, for most cases of interest, simply equal to the classical action, appropriately discretized. This means that the classical action is the phase acquired by quantum evolution between two fixed endpoints. Amplitude computed according to Feynman principles will also obey the Schrodinger equation for the Hamiltonian corresponding to the given action. Since the relation between Feynman's formulation and classical mechanics is very close, the path integral formalism often has the important advantage of providing a much more intuitive approach.

Theoretical background

The Time-Evolution Operator

The time evolution from time t_0 to t of a quantum mechanical state is described by a linear operator $\hat{U}(t, t_0)$. Thus a ket at time t that started out at t_0 being the ket is

$$|\alpha(t)\rangle = \hat{U}(t, t_0)|\alpha\rangle \quad (1)$$

The time evolution operator $\hat{U}(t, t_0)$, which also is known as a propagator, satisfies three important properties:

¹ Department of Physics, Dagon University

² Department of Physics, Dagon University

³ Department of Physics, Dagon University

(1) The time evolution operator should do nothing when $t = t_0$

$$\lim_{t \rightarrow t_0} \hat{U}(t, t_0) = 1 \quad (2)$$

(2) The propagator should preserve the normalization of state kets. That is, if $|\alpha\rangle$ is normalized at t_0 it should also be normalized at later time t . This leads to the requirement

$$\langle \alpha | \alpha \rangle = \langle \alpha(t) | \alpha(t) \rangle \quad (3)$$

Which implies

$$\hat{U}^\dagger(t, t_0) \hat{U}(t, t_0) = 1 \text{ (or)}$$

$$\hat{U}^\dagger(t, t_0) = \hat{U}^{-1}(t, t_0) \quad (4)$$

(3) The propagator should satisfy the composition property

$$\hat{U}(t_2, t_0) = \hat{U}(t_2, t_1) \hat{U}(t_1, t_0) \quad (5)$$

Which means that in order to evolve a state from t_0 to t_2 we might as well first evolve the state from t_0 to t_1 and then evolve the state from so obtained from t_1 to t_2 .

Formally, we can evolve a wave function forward in time by applying time-evolution operator.

For time-independent Hamiltonian, $|\psi(t)\rangle = \hat{U}(t)|\psi(0)\rangle$, where time-evolution operator (“the propagator”):

$$\hat{U}(t) = e^{-i\Delta H t / \hbar} \quad (6)$$

Follows from time-independent Schrodinger equation,

$$\hat{H}|\psi\rangle = i\hbar\partial_t|\psi\rangle \quad (7)$$

By inserting the resolution of identity, $I = \sum_i |i\rangle\langle i|$,

Where $|i\rangle$ are eigenstates of \hat{H} with eigenvalue E_i ,

$$|\psi(t)\rangle = e^{-i\Delta H t / \hbar} \sum_i |i\rangle\langle i|\psi(0)\rangle = \sum_i |i\rangle\langle i|\psi(0)\rangle e^{-iE_i t / \hbar} \quad (8)$$

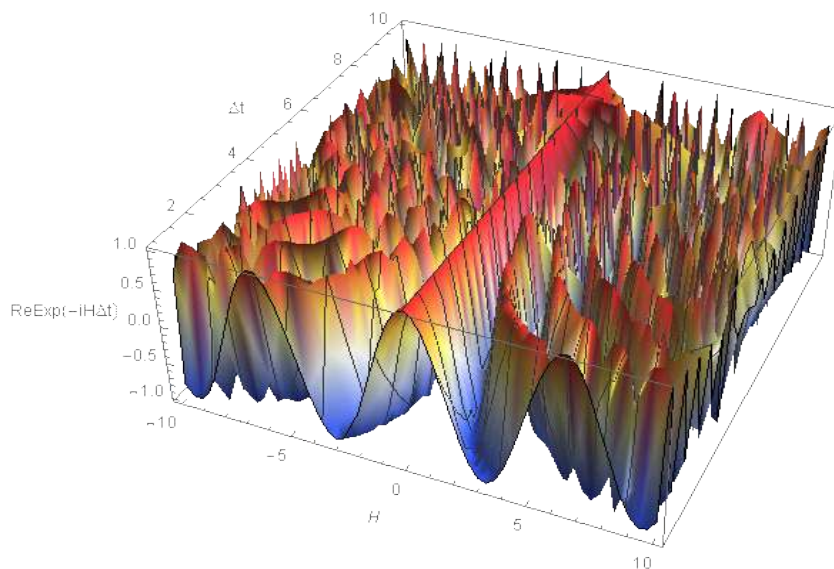


Figure 1. Real part $\text{Exp}(-iH\Delta t)$ in term of H and Δt

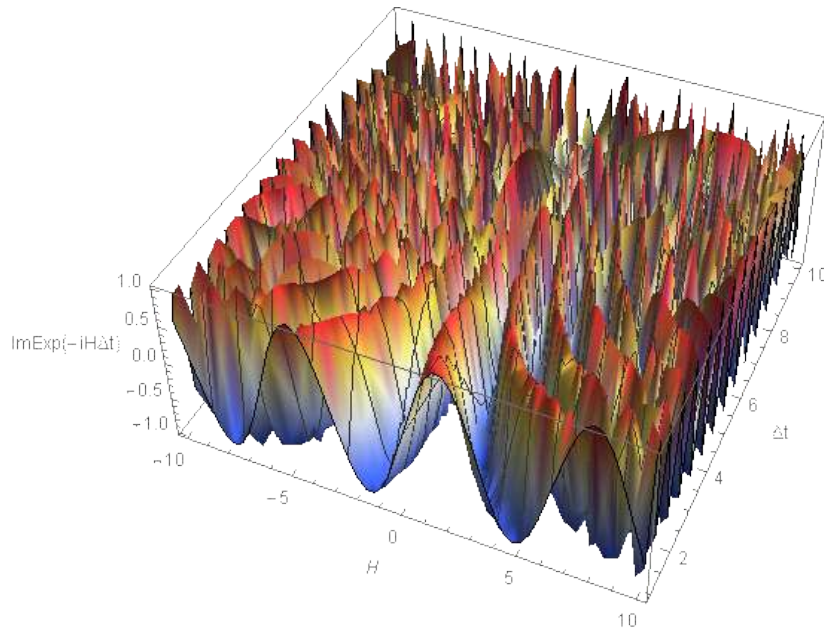


Figure 2. Imaginary part $\text{Exp}(-iH\Delta t)$ in term of H and Δt

Definition of the Propagator

Mathematical form of the propagator. The summation carried out between all the arrows in the initial wavefunction and each single detection event approximates the integral in which the propagator function K is usually employed for a continuous wavefunction,

$$\psi(xb, tb) = \int K(b, a) \psi(xa, ta) dx_a \tag{9}$$

Here the label ‘a’ refers to a point in the initial wavefunction, while the label ‘b’ applies to a point on a later wavefunction. The free-particle propagator K has specific expression.

The paths are sliced into finite number of segments between time interval δt ; each of which has two end points $\{x(t)\}$. Each path are assigned an action (L) corresponding to the position function $x(t)$. The corresponding probability amplitude for each path is given by

$$A(x) = e^{iS(x)/\hbar} \tag{10}$$

The Action Integral

In physics, action is an attribute of the dynamics of a physical system from which the equations of motion of the system can be derived through the principle of stationary action. Action is a mathematical functional which takes the trajectory, also called path or history, of the system as its argument and has a real number as its result. Generally, the action takes different values for different paths.

Action is a part of an alternative approach to finding such equations of motion. The action is typically represented as an integral over time; take along the path of the system between the initial time and the final time of the development of the system:

$$S = \int_{t_1}^{t_2} L dt \tag{11}$$

Where the integrand L is called the Lagrangian. For the action integral to be well-defined, the trajectory has to be bounded in time and space.

Action has the dimensions of [energy]. [time], and its SI unit is joule-second, which is identical to the unit of angular momentum.

In classical mechanics, the input function is the evolution $q(t)$ of the system between two times t_1 and t_2 , where q represents the generalized coordinates. The action $S[q(t)]$ is defined as the integral of the Lagrangian L for an input evolution between the two times:

$$S[q(t)] = \int_{t_1}^{t_2} L[q(t), \dot{q}(t), t] dt \quad (12)$$

Where the endpoints of the evolution are fixed and defined as $q_1 = q(t_1)$ and $q_2 = q(t_2)$.

The action principle can be extended to obtain the equations of motion for fields, such as the electromagnetic field and gravitational field. The trajectory (path in space time) of a body in a gravitational field can be found using the action principle.

The equation of motion between two times t_1 and t_2 should minimize the action integral

$$S = \int_{t_1}^{t_2} L(\dot{q}(t), q(t)) dt \quad (13)$$

Assuming that $q(t_1)$ and $q(t_2)$ are fixed, then the function $q(t)$ between t_1 and t_2 should minimize S , the action. Taking the first variation of equation (13),

$$\begin{aligned} \delta S &= \delta \int_{t_1}^{t_2} L(\dot{q}, q) dt = \int_{t_1}^{t_2} L(\dot{q} + \delta\dot{q}, q + \delta q) dt - \int_{t_1}^{t_2} L(\dot{q}, q) dt \\ &= \int_{t_1}^{t_2} \delta L(\dot{q}, q) dt \\ &= \int_{t_1}^{t_2} \left(\delta\dot{q} \frac{\partial L}{\partial \dot{q}} + \delta q \frac{\partial L}{\partial q} \right) dt = 0 \end{aligned} \quad (14)$$

In order to take variation into the integrand, we have to assume that $\delta L(\dot{q}, q)$ is taken with constant time.

At constant time, \dot{q} and q are independent variables. Using integration by parts on the first term,

$$\begin{aligned} \delta S &= \delta q \frac{\partial L}{\partial \dot{q}} \Big|_{t_1}^{t_2} - \int_{t_1}^{t_2} \delta q \frac{d}{dt} \left(\frac{\partial L}{\partial \dot{q}} \right) dt + \int_{t_1}^{t_2} \delta q \frac{\partial L}{\partial q} dt \\ &= \int_{t_1}^{t_2} \delta q \left[-\frac{d}{dt} \left(\frac{\partial L}{\partial \dot{q}} \right) + \frac{\partial L}{\partial q} \right] dt = 0 \end{aligned} \quad (15)$$

The first term vanishes because $\delta q(t_1) = \delta q(t_2) = 0$ because $q(t_1)$ and $q(t_2)$ are fixed.

Since $\delta q(t)$ is arbitrary between t_1 and t_2 we must have-

$$\frac{d}{dt} \left(\frac{\partial L}{\partial \dot{q}} \right) - \frac{\partial L}{\partial q} = 0 \quad (16)$$

The above equation is called the Lagrange equation, from which the equation of motion of a particle can be derived. The derivative of the Lagrangian with respect to the velocity \dot{q} is the momentum

$$p = \frac{\partial L}{\partial \dot{q}} \quad (17)$$

The derivative of the Lagrangian with respect to the coordinate q is the force. Hence,

$$F = \frac{\partial L}{\partial q} \quad (18)$$

The above equation of motion is then

$$\dot{p} = F \quad (19)$$

The solution of the equations of motion for a given initial condition is known as a trajectory of the system.

The Propagation of a Particle in the One-Dimensional Infinite Square-Well by Using the Path Integral Formalism

$$S = \int_{t_1}^{t_2} dt [L(\dot{x}) + \frac{\partial L}{\partial \dot{x}} |_{\dot{x}} \dot{y} + \frac{1}{2} \frac{\partial^2 L}{\partial \dot{x} \partial \dot{x}} |_{\dot{x}} \dot{y}^2] \tag{20}$$

$$S = S_{cl} + \frac{m}{2} \int_{t_1}^{t_2} dt \dot{y}^2 \tag{21}$$

And thus, for the kernel:

$$K(x_2, t_2; x_1, t_1) = e^{\frac{iS_{cl}[\bar{x}]}{\hbar}} \int_{y(t_1)=0}^{y(t_2)=0} [dy(t)] \exp \left[\frac{i}{\hbar} \int_{t_1}^{t_2} dt \frac{m}{2} \dot{y}^2 \right] \tag{22}$$

The classical action for a free particle,

$$S_{cl} = \frac{m}{2} \frac{(x_2 - x_1)^2}{t_2 - t_1} \tag{23}$$

Eqn:(22) thus yields for the kernel:

$$K(x_2, t_2; x_1, t_1) = \exp \left[\frac{i}{\hbar} \frac{m}{2} \frac{(x_2 - x_1)^2}{t_2 - t_1} \right] \int_{y(t_1)=0}^{y(t_2)=0} [dy(t)] \exp \left[\frac{i}{\hbar} \int_{t_1}^{t_2} dt \frac{m}{2} \dot{y}^2(t) \right] \tag{24}$$

the value of the path integral is only a function of the time difference, i.e.,

$$A(t_2 - t_1) = \int_0^0 [dy(t)] \exp \left[\frac{i}{\hbar} \int_{t_1}^{t_2} dt \frac{m}{2} \dot{y}^2 \right] \tag{25}$$

$$K(x_2, t_2; x_1, t_1) = A(t_2 - t_1) \exp \left[\frac{i}{\hbar} \frac{m}{2} \frac{(x_2 - x_1)^2}{t_2 - t_1} \right] \tag{26}$$

for $t_1 = t_2 (\equiv t)$:

$$A(t) = e^{-\frac{i\pi}{4}} \sqrt{-\frac{m}{2\pi i \hbar t}} = \sqrt{\frac{m}{2\pi i \hbar t}} \quad , \quad \left(\frac{1}{\sqrt{i}} = e^{-\frac{i\pi}{4}} \right) \tag{27}$$

the phase in such a manner that

$$K(x_2, t; x_1, 0) = \sqrt{\frac{m}{2\pi i \hbar t}} \exp \left[\frac{i}{\hbar} \frac{m}{2} \frac{(x_2 - x_1)^2}{t} \right] \tag{28}$$

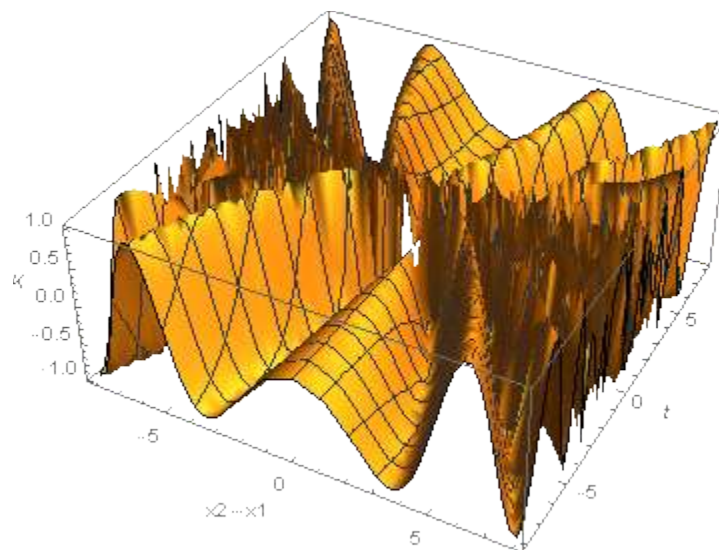


Figure 3. Imaginary part of K

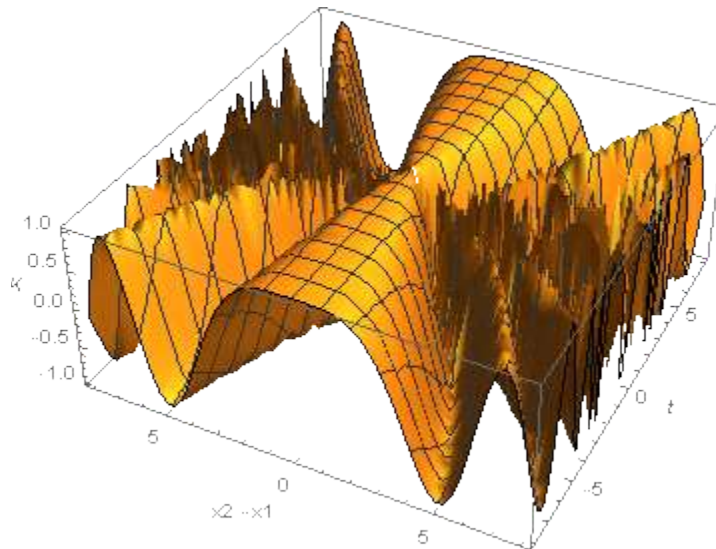


Figure 4. Real part of K

the propagator of the free particle

$$K(x_2, t_2; x_1, t_1) = \sqrt{\frac{m}{2\pi i \hbar (t_2 - t_1)}} \exp \left[\frac{i m (x_2 - x_1)^2}{\hbar 2 (t_2 - t_1)} \right] \quad (29)$$

$$= \sqrt{\frac{m}{2\pi i \hbar (t_2 - t_1)}} e^{\left(\frac{i}{\hbar}\right) S_{cl}}$$

$$\int_{y(t_1)=0}^{y(t_2)=0} [dy(t)] \exp \left[\frac{i}{\hbar} \int_{t_1}^{t_2} dt \frac{m}{2} \dot{y}^2(t) \right] = \left(\frac{m}{2\pi i \hbar (t_2 - t_1)} \right)^{\frac{1}{2}} \quad (30)$$

In three dimensions:

$$K(r_2, t_2; r_1, t_1) = \left(\frac{m}{2\pi i \hbar (t_2 - t_1)} \right)^{\frac{3}{2}} \exp \left[\frac{i m (r_2 - r_1)^2}{\hbar 2 (t_2 - t_1)} \right] \quad (31)$$

For future purpose the above boundary condition in mind,

$$\lim_{t \rightarrow 0} K(x_2, t; x_1, 0) = \delta(x_2 - x_1) \quad (32)$$

the Schrodinger wave function for a free particle which was emitted at $x_1 = 0$ at time $t_1 = 0$ and at (x, t) is described by the probability amplitude $\psi(x, t)$,

$$\psi(x, t) = K(x, t; 0, 0) = \sqrt{\frac{m}{2\pi i \hbar t}} \exp \left[\frac{i m x^2}{\hbar 2 t} \right] \quad (33)$$

$$\psi(x, t) = \sqrt{\frac{m}{2\pi i \hbar t}} \times \exp \left\{ \frac{i}{\hbar} \left[\underbrace{m \left(\frac{x_0}{t_0} \right) x}_{p_0} - \underbrace{\frac{m}{2} \left(\frac{x_0^2}{t_0^2} \right) t}_{E_0} \right] \right\} \quad (34)$$

$$\psi(x, t) \cong \sqrt{\frac{m}{2\pi i \hbar t}} \times \exp \left[\frac{i}{\hbar} (p_0 x - E_0 t) \right] \quad (35)$$

$$\exp \left[i \left(\frac{2\pi}{\lambda} x - \frac{v}{2\pi} t \right) \right] = \exp \left[\frac{i}{\hbar} (p x - E t) \right] \quad (36)$$

$$K(x, t; p, 0) \equiv \chi_{p, 0}(x, t) \int_{x'=-\infty}^{+\infty} dx' K(x, t; x', 0) \underbrace{\chi_{p, 0}(x', 0)}_{\equiv K(x', 0; p, 0)} \tag{37}$$

$$(K(x, 0; p, 0) \equiv) \chi_p(x, 0) = \frac{1}{\sqrt{2\pi\hbar}} e^{\left(\frac{i}{\hbar}\right)xp} \tag{38}$$

$$\chi_p(x, t) = \frac{1}{\sqrt{2\pi\hbar}} \exp \left[\frac{i}{\hbar} \left(xp - \frac{p^2}{2m} t \right) \right] \tag{39}$$

a particle with momentum p and energy $(p) = \frac{p^2}{2m}$.

In three dimensions:

$$\chi_p(x, t) = \frac{1}{(2\pi\hbar)^{\frac{3}{2}}} \exp \left[\frac{i}{\hbar} r \cdot p - \frac{i}{\hbar} \frac{p^2}{2m} t \right] \tag{40}$$

So for the free propagator in momentum,

$$K(p_2, t; p_1, 0) = \delta(p_2 - p_1) \exp \left[-\frac{i}{\hbar} \frac{p_1^2}{2m} t \right] \tag{41}$$

With this form for K we can, conversely, return to real space:

$$\begin{aligned} &K(x_2, t; x_1, 0) \\ &= \int \frac{dp}{2\pi\hbar} e^{\left(\frac{i}{\hbar}\right)(x_2-x_1)p} \exp \left[-\frac{i}{\hbar} \frac{p^2}{2m} t \right] \end{aligned} \tag{42}$$

$$\begin{aligned} K_L(x_f, t_f; x_i, t_i) &= \sqrt{\frac{m}{2\pi i \hbar (t_f - t_i)}} \left\{ \exp \left[\frac{i}{\hbar} \frac{m}{2} \frac{(x_f - x_i)^2}{(t_f - t_i)} \right] - \exp \left[\frac{i}{\hbar} \frac{m}{2} \frac{(-x_f - x_i)^2}{(t_f - t_i)} \right] \right\} \\ &= K(x_f, t_f; x_i, t_i) - K(-x_f, t_f; x_i, t_i) \end{aligned} \tag{43}$$

$$K_L(x_f, t_f; x_i, t_i) = \sum_{r=-\infty}^{+\infty} (-1)^r K(x_r, t_f; x_i, t_i) \tag{44}$$

And obtain for propagator,

$$K_L(x_f, t_f; x_i, t_i) = \frac{i}{L} \sum_{n=-\infty}^{+\infty} \exp \left[-\frac{i}{\hbar} E_n (t_f - t_i) \right] \times \exp[-ik_n x_i] \sin(k_n x_f) \tag{45}$$

The appearance of the δ -function implies energy and momentum quantization:

$$E_n = \frac{1}{2m} \frac{\pi^2 \hbar^2}{L^2} n^2 \quad , \quad k_n = \frac{\pi n}{L} \tag{46}$$

So final result reads ($t_f > t_i$),

$$K_L(x_f, t_f; x_i, t_i) = \frac{2}{L} \sum_{n=1}^{\infty} \exp \left[-\frac{i}{\hbar} E_n (t_f - t_i) \right] \sin(k_n x_i) \sin(k_n x_f) \tag{47}$$

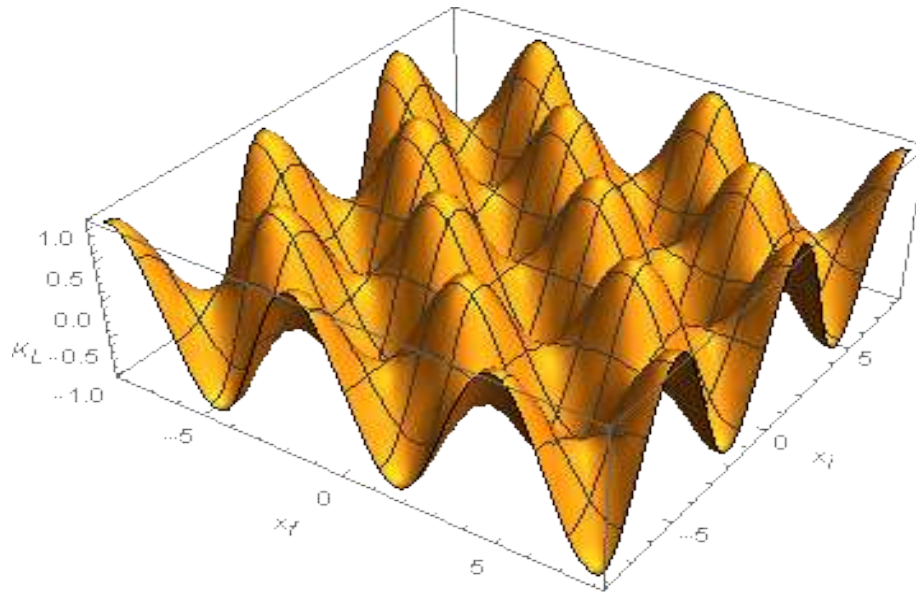


Figure 5. 3D visualization figure of K_L with x_i and x_f

Results and Discussion

From the some basic properties of the kernel, the retarded propagator satisfies

$$\left[i\eta \partial_{x_f} - \hat{H}(x_f, p_f = (\eta/i) \partial_{x_f}, t_f) \right] K_r(x_f, x_i; t_f - t_i) = i\eta \delta(t_f - t_i) \delta(x_f - x_i)$$

Thus the retarded propagator is a Green's function for the Schrodinger equation.

For time-evolution operator the generator expression for a time-dependent Hamiltonian involves

the time-ordered exponential is
$$U(t_f, t_i) = T \left(e^{-i/\eta \int_{t_i}^{t_f} dt \hat{H}(t)} \right)$$

The another key property of the time-evolution operator is

$$U(t_f, t_i) = U(t_f, t) U(t, t_i) \quad t_i < t < t_f$$

The evolution from time t_i to t_f is the same as evolution from t_i to t , following by evolution from t to t_f .

The action is functional because it takes a function as argument and returns a number. Particles always follow a path of least action. By varying (minimizing the variance of) the action, the path actually followed by a particle can be determined. There are an infinite number of paths connecting the two fixed points. This means that there are an infinite number of paths for the particle to follow between these two points. The actual path that the particle follows is the path of least action. The path of least action represents a minimum.

The principle of least action gives rise to the Euler-Lagrange equations. Hence the Lagrangian satisfies the Euler-Lagrange equation independently for each coordinate. The probability amplitude for the evolution of the system from the initial state $|q_0\rangle$ to the final state $|q_N\rangle$ is proportional to a weighted sum over all classical paths kinematically allowed, where each path is weighted with iS (with S being the classical action corresponding to the path). The larger is N , the number of intermediate steps, the better is the approximation of the classical action with the discrete sum of equation.

From the knowledge of the solution of the Schrodinger equation for a generic non-relativistic system, the wave function $\psi(\vec{q}, t)$ is equivalent to the knowledge of the Green function of the Schrodinger equation with a particle initial condition.

According to Feynman’s formulation of quantum mechanics, the particle explores all possible paths between fixed initial and final events. The action along these many paths plays a fundamental role.

It can be seen that from the path integral formalism, the propagator in the constant field is

$$K(x_2, t_2; x_1, t_1) = \left[2\pi i k(x_2) k(x_1) \int_{x_1}^{x_2} \frac{dx}{k(x)^3} \right]^{-\frac{1}{2}} \times \exp \left[i \int_{x_1}^{x_2} dx k(x) - \frac{i}{\eta} E_{cl} (t_2 - t_1) \right]$$

Conclusion

In this paper the path integral expression for the propagator in quantum mechanics, especially the free particle and particle in the one-dimensional infinite potential well were derived. From the calculations, it can be clarified that all paths contribute in a sense the quantum particle takes all paths and the amplitudes for each path add according to the usual quantum mechanical rule for combining amplitudes. By this path integral formalism, the propagator can be written as a sum over all possible paths between the initial and final points. Each path contributes $\exp\left[\frac{iS}{\hbar}\right]$ to the propagator. In this work, it can be seen that path integral formalism are vividly described and important physical interpretations concerning the free particle have been given. The time evolution of the state is visualized in terms of Hamiltonian (H) and the time (Δt). It gives us the nature of sharply attenuated wave patterns. 3D visualization of K_L with x_i and x_f shows the sinusoidal wave patterns. Real and imaginary parts of kernel K is visualized in terms of space (x_2-x_1) and time t . It shows the random wave patterns.

Acknowledgements

First of all, my special thanks to Dr U Win, Professor and Head of Department of Physics, Dagon University, for his warmly support and permission to carry out this paper.

I also would like to express my gratitude and sincere thanks to Dr San San Swe, Dr Thet Mar Win and Dr Nilar Shwe, Professors, Department of Physics, Dagon University, for their kind permission to conduct this work.

I am deeply grateful to Daw Hla Hla Maw, Associated Professor, Department of Physics, Dagon University, for her understanding, guidance and advice throughout this work.

References

D.Bauch, (1985), “The Path Integral for a Particle Moving in a δ -function potential”, *Nuovo Cim.*85B, 118.
 F.W.Wiegel, (1986), “Introduction to Path-Integral Methods in Physics and Polymer science”, World Scientific Singapore.
 L.S.Schulman, (1987), “Techniques and Applications of Path Integration”, Wiley, New York (hereafter known as “my book”).
 M.G.Gultwiller, A.Inomata, J.R. Klauder and L.Streit, (1986), “Path Integrals from meV to MeV, World Scientific”, Singapore.
 V. Sa-yakanit, M. Nithisoontorn and W. Svitra kook, (1985), “Path-Integral Theory of The Plasmaron”, *Physica Scripta* 32,334.
 V. Sa-yakanit and H.R.Glyde, (1985), “Path Integral Approach to the Theory of Heavily Doped Semiconductors, this volume”.

MEASUREMENTS OF RADON CONCENTRATIONS OF SHWEKU TANKE PAGODA AT PAKOKKU TOWNSHIP IN MAGWAY REGION, MYANMAR

Hnin Hnin Ei¹

Abstract

In this research paper, radon concentrations from two places of Shweku Tanke Pagoda at Pakokku township in Magway region have been estimated by using alpha sensitive two CR-39 detectors (SSNTDs). Radon track densities, radon concentrations and annual effective doses were carried out from these two detectors at 18th March from 15th July, 2022. The radon concentrations were observed $15.78 \pm 8.63 \text{ Bqm}^{-3}$ and $16.41 \pm 10.615 \text{ Bqm}^{-3}$ from two locations in these Pagoda. The radon concentrations from two places were found that lower than the recommended WHO (2009) reference level of 100 Bqm^{-3} . The annual effective dose from two locations were observed $0.27 \pm 0.148 \text{ mSvyr}^{-1}$ and $0.28 \pm 0.18 \text{ mSvyr}^{-1}$ which were lower than the International Commission on Radiological Protection (ICRP) recommendation of 5 mSvyr^{-1} . The radon concentrations from the two places of Shweku Tanke Pagoda were found within the safe limit.

Keywords: radon concentrations, CR-39, SSNTDs, annual effective dose

Introduction

Shweku Tanke Pagoda is one of the historical pagodas in Myanmar. It is situated at Pakokku city in Pakokku township, Magway Region. It was built by King Alaungsithu at 454 eras. Tanke or Tangee (ornamental backdrop of throne) of standing Buddha image from Shweku Tanke Pagoda is world famous wood carvings sculpture. It was carved prominent sculptor by U Kan Gyi in 1908. The height of the Tanke is twelve feet and ten inches, length five feet and ten inches, cubic thickness is eight inches. It was carved with the best wood yamanaythar (Khin Nu Swe, 2016). In this research work, the investigations of radon concentrations of Shweku Tanke Pagoda were measured in Pakokku city at Pakokku Township in Magway division.

Radiation is the energy that transport either in the form of electromagnetic waves or particles. Basically, radiation can be classified into two types. The first type is ionizing radiation such as (X-ray, gamma ray, alpha and beta particles) that contains high energy to transport electrons from atoms and molecules in the cell. The harmful result of ionizing radiation is biological damage to Deoxyribose Nucleic Acid (DNA) or other parts of the body. Even low doses of radiation, there is a higher risk of cancer. The second type is non-ionizing radiation such as (radio waves, micro waves, Ultra violet Ray (UV), Infrared Ray (IR) and visible light).

Radiation includes an important sector of our daily life as the world is naturally radioactive. Radioactive materials are present in earth crust, the floors and walls of the building and in the food. Radioactive elements are being occurred naturally from the radon gases in the air we breathe, in the muscles, the bones and the tissue of the human bodies.

The atoms are unstable and changes in the atoms of another element through ionizing radiation process. This process is known as radioactivity which means the spontaneous decay and transformation of unstable atomic nuclei accompanied with the emission of nuclear particles or photons. Exposure to natural radiation occurs in two ways. For the first time by gamma ray and radon exhalation. Gamma radiation rises from ^{40}K , ^{238}U and ^{232}T , thus exposing the entire body to that radiation while radon leads to internal dose exposure. Half of the total annual effective dose received by the population stems from radon and its decaying products There are many factors that contribute to indoor radon. These factors are the construction of terrestrial, internal or external building materials, soil characteristics, water supply, ambient air, environmental

¹ Department of Physics, Pakokku University

standards (temperature, atmospheric pressure, precipitation). There are four radioactive decay series, Uranium, Actinium, Thorium and Neptunium. Radon (^{222}Rn) gas is obtained from these decay chain of ^{238}U , ^{235}U , ^{232}Th and ^{237}Np (Irving Kaplan et al, (1954). Radon is colourless, odourless and is an alpha emitter that decays with a half-life of 3.82 days into a series of radon progeny.

In order to measure the radon concentration, Solid State Nuclear Track Detectors (SSNTDs) CR-39 was used. Solid State Nuclear Track Detectors are dielectric materials or solid insulator such as mica, glass synthetic plastics etc., which record and permanently store the trajectory of fast-moving charged particles in the form of submicroscopic trails of continuous damage called "latent tracks". These nuclear tracks formed are identified by using optical microscope.

This research is to measure the radon concentrations of Shweku Tanke Pagoda by using CR-39 SSNTDs detector. In this research, two detectors S1 and S2 were placed in Shweku Tanke Pagoda at 20th March to 17th July in 2022 as shown in the figure (1).

This research will support the data of the radon concentrations of the selected places of Shweku Tanke Pagoda at Pakokku city in Magway region. The information of this research will be benefit for the people from this region.

REPUBLIC OF THE UNION OF MYANMAR



MAGWAY DIVISION



Figure 1. Shweku Tanke Pagoda in Pakokku Township



Figure 2. Location map of Shweku Tanke Pagoda in Pakokku Township



Figure 3(a). CR-39 detector S1 under the Buddha Image



Figure 3(b). CR-39 detector S2 in front of the main building



Figure 4(a). The etching photograph of CR-39 detector

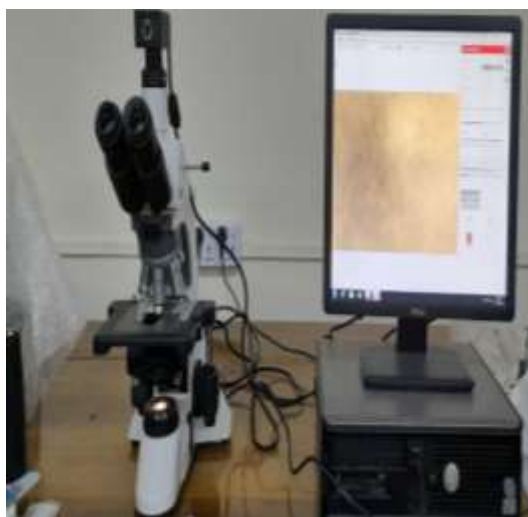


Figure 4(b). Photograph of optical microscope

Materials and Methods

Study Area

The two detectors were placed in the main building of Shweku Tanke Pagoda in 9th quarter of Pakokku city which is situated between 21° 20' 21.89" North latitude and 95° 04' 13" East longitude. Location of the places of Shweku Tanke Pagoda were shown in figure 2.

Study Period

The study period is 18th March from 17th July, 2022. The exposure time of the detectors is 120 days.

Sample Preparation

The two detectors were cut into small pieces of size 1cm x 1cm each. The first detector S1 were placed under the throne of the Buddha image and the second detector S2 were placed on the wall in front of the main building of the Shweku Tanke Pagoda as shown in the figure 3(a)

and figure 3(b). After 120 days, the two detectors were removed from the two places. 6N NaOH solution will be needed to prepare. Firstly, 24g of NaOH was weighted in the balance and put in 100mL of empty beaker. Distilled water were poured into this beaker with NaOH to reach the 100mL scale point and stirred with a glass rod to dissolve NaOH. The NaOH solution were poured into another empty glass beaker. The beaker with NaOH solution was heated on a stove with temperature controller. When the temperature reached at 70°C, one of the radon exposed CR 39 detector was put into the beaker for 6 hours and 30 minutes. During etching period, the temperature was kept constant with accuracy $70 \pm 1^\circ\text{C}$ for 6 hours and 30 minutes as shown in figure 4(a). After it was etched, the detector was washed with distilled water thoroughly until the surface of the detector became cleaning from etchant. Finally, the detector was dried in open air to avoid scratching from the detector After drying the detector, it was placed under optical microscope (Olympus B202 BX51) as shown in figure 4(b) from Universities' Research Center with digital camera and a display system to count the tracks produced by alpha particle of the detector. The tracks of the detector were viewed 20 times to reduce the statistical error. Another detector was also made like this procedure.

Materials and Methods

The two detectors CR-39 were used to investigate the radon concentrations of Shweku Tanke Pagoda from Pakokku township.

Solid State Nuclear Track Detectors Technique

The selected CR-39 detector is made of polyallyl diglycol carbonated with a thickness of 1.5mm. Solid State Nuclear Track Detectors (SSNTDs) technique is the technique of measuring the number of particles by observing their tracks in certain organic and inorganic materials has been used for the study of nuclear physics. SSNTDs techniques is based on the damage created in a solid along the path of a heavily ionizing particle such as an alpha particle or a fission fragment. The damage along the path called a track can be seen an ordinary optical microscope after etching with suitable chemicals. The visible tracks are counted either by direct observation with the help of automated instruments. (Durrani et al., (1997)

CR-39 Track Detector

CR-39 is Allyl Diglycol Carbonate (ADC) is a plastic polymer commonly used in the manufacture of eyeglass lenses. CR-39 is made by polymerization of diethyleneglycol bis allylcarbonate(ADC) in presence of diisopropyl peroxydicarbonate initiator. CR-39 plastic has an index of refraction of 1.498. An alternative use includes a purified version that is used to measure neutron radiation, type of ionizing radiation in neutron dosimetry. In the radiation detection application, CR-39 is used as a solid state nuclear track detector to detect the presence of ionizing radiation. Energetic particles colliding with the polymer structure leave a trail of broken chemical bonds within the CR-39. Before etching, photographs are taken of the biological sample with the affixed CR-39 detector, with care taken to ensure the prescribed location marks on the detector are noted. After etching process, automated or manual scanning of the CR-39 is used to physically locate the ionizing radiation recorded, which can be mapped to the position of the radionuclide within the biological sample.

Track Detection Technique

Solid state nuclear track detectors technique is fundamentally similar to cloud chamber and ionization chamber techniques. The passage of heavily ionization nuclear particles through most insulating solids creates narrow paths of intense damage trails on an atomic scale. The size

of the latent tracks is very small about 50 Å and therefore track etching technique has to be used to enlarge the size of the tracks. The etched tracks in the detector are permanent and these tracks can easily be seen visually by using the optical microscope. (Price P B et al., 1975)

Microscopic Observation

The nuclear track formed are identified by using Olympus Bx51 optical microscope. The optical microscope with Bx51 digital camera attached was used in this research work. The tracks formed were viewed under different magnifications as the display monitor. The visible area containing tracks in an SSNTD will vary depending upon the magnification. Also, in a given SSNTD, the size of tracks formed depend upon the energy of irradiating particles and etch conditions.

Nature of the Damage

Most tracks are ionization produced defects by the results of the interaction of charge particle with the electrons attached to atoms in the detector. The magnitude of the damage from ionization and excitation processes along a particle trajectory can be determined. (Harald Enge et al., (1987).

Alpha Track Density

The technique of SSNTD is based on the damage created in an insulating solid along the path of a heavily ionizing particle such as alpha particle. The damage along the path called a track can be seen with optical microscope. The visible tracks were counted either by direct observation by a human or with the help of automated instruments. Within viewing optical image analysis with 20 times, the average value of the track density with statistical error were calculated by counting number of tracks using Arithmetic mean and standard error method with the help of Microsoft Excel. The alpha track density in solid state nuclear track detector is the number of net alpha track per unit area in equation 1 (Fareed M et al., IJSR (2018).

$$\text{Track density} = \frac{\text{Number of Net Tracks}}{\text{Area of Counting}} \quad (1)$$

Chemical Etching

Chemical etching was carried out in a thermostatically controlled bath at temperature ranging from 70±1°C. The etching time was one and half hours. The etchants which have been most commonly used for plastic detectors are aqueous alkaline solutions of 6N NaOH solution. 240 g of NaOH was added into 1 L of distilled water. Size of the track depends upon the concentration of etching solution, etching time and temperature. Each detector was placed in the beaker with NaOH solution and heated 70 ± 1°C with temperature-controlled stove as shown in the figure 4(a). After heating in one and half hours, the detector was removed and washed with distilled water to remove the etching residue from each pit. After being washed with distilled water, the detector was dried in air for twelve hours. Then the detector was counted under an optical microscope. The etched track diameter was typically a few micrometers in size and larger in size after prolonged etching.

Calibration Factor of Radon Concentration

According to number the alpha tracks as shown in the figure 5(a) and figure 5(b), the radon concentrations were calculated by using the number of tracks. The calibration factor was obtained from the inter-laboratory comparison exercises carried out at the national level by the Environmental Assessment Division of BARC, Mumbai. Calibration factor 0.065Bqm⁻³ were

used to estimate the radon concentrations of the detectors. The annual effective doses 0.072 mSv y^{-1} were carried out using publication (ICRP1993). (Moe Win et al., 2014)

Result and Discussion

The track densities in different places of detectors were shown in table (1), the radon concentrations of the two different places were shown in table (2), the annual effective dose in different places were shown in table (3). Comparison of the track densities for different places were shown in figure (6), Comparison of radon concentrations of two places were shown in figure (7). Comparison of the annual effective dose in two places were shown in figure (8). The track densities, radon concentrations and annual effective dose of detector S1 was lower than the detector S2 in the main building of the Shweku Tanke Pagoda.

In this research work, the radon concentrations were observed $15.78 \pm 8.63 \text{ Bqm}^{-3}$ and $16.41 \pm 10.615 \text{ Bqm}^{-3}$ from two locations in these Pagoda. The radon concentrations from two places were found that lower than the recommended WHO (2009) reference level of 100 Bqm^{-3} . The annual effective dose from two locations were observed $0.27 \pm 0.148 \text{ mSvyr}^{-1}$ and $0.28 \pm 0.18 \text{ mSvyr}^{-1}$ which were lower than the International Commission on Radiological Protection (ICRP) recommendation of 5 mSvyr^{-1} .

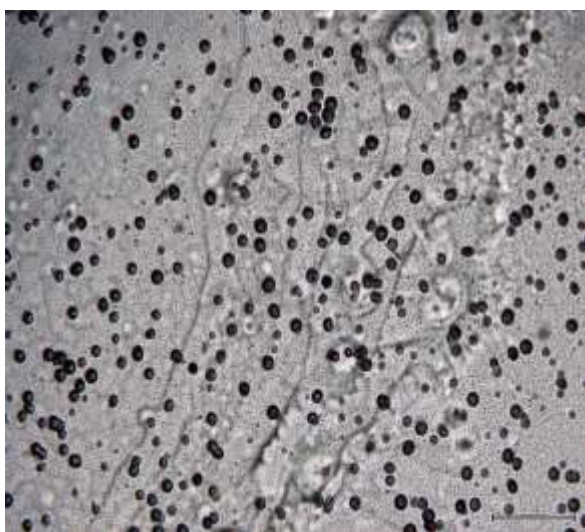


Figure 5(a). Photomicrograph of detector S1 **Figure 5(b).** Photomicrograph of detector S2

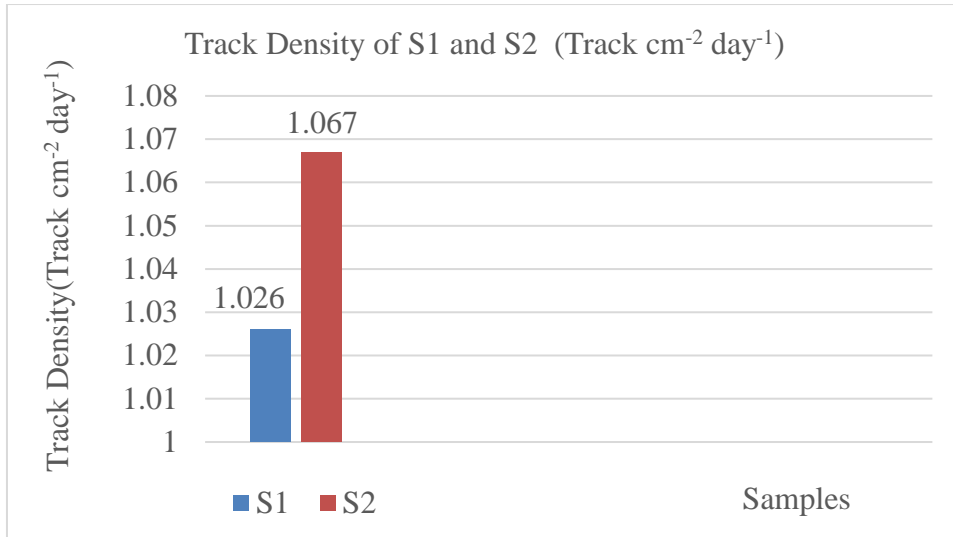


Figure (6). Comparison of the track densities for two places

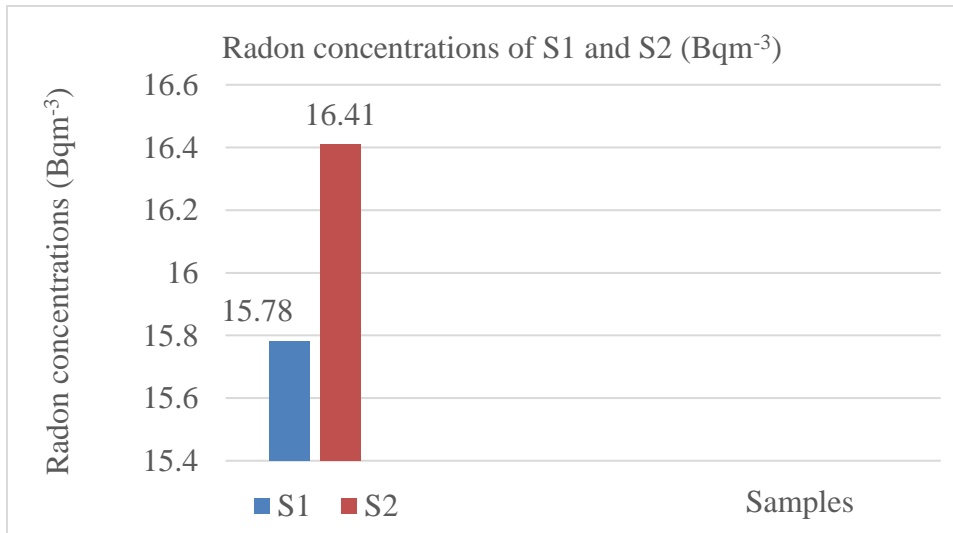


Figure (7). Comparison of radon concentrations for two places

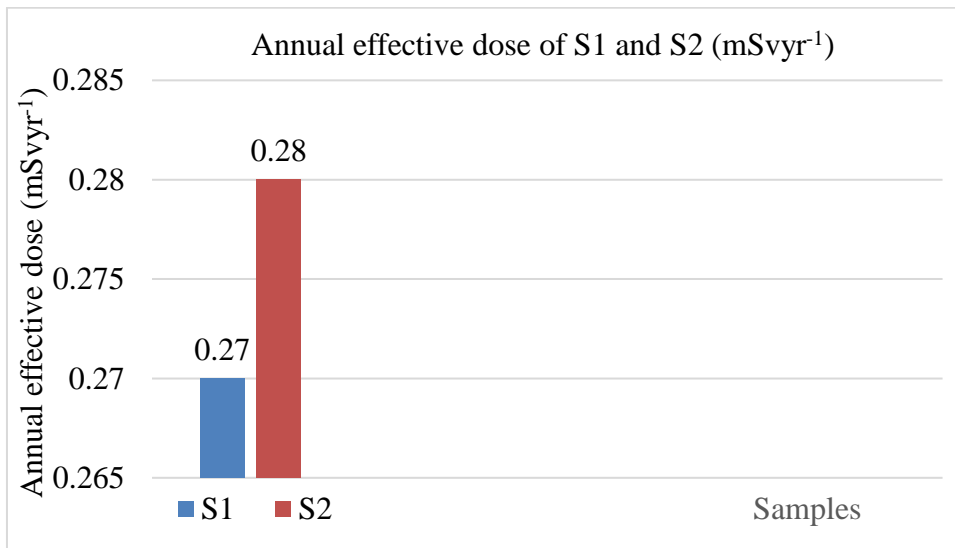


Figure (8). Comparison of the annual effective dose for two places

Table (1). Track Density of the detectors

No	CR-39 Detector	Average Track Density (Track cm ⁻² day ⁻¹)
1	S1	1.026±0.561
2	S2	1.067±0.69

Table (2). Radon Concentrations of the detectors

No	CR-39 Detector	Radon Concentrations (Bqm ⁻³)
1	S1	15.78±8.63
2	S2	16.41±10.615

Table (3). Annual Effective dose of the detectors

No	CR-39 Detector	Annual Effective Dose (mSvyr ⁻¹)
1	S1	0.27±0.148
2	S2	0.28±0.18

Conclusion

The radon concentrations of sample S1 from the wall under the throne of Buddha image were seen that lower than the radon concentration of sample S2 from the wall in front of the main building. The air ventilation of the place from sample S1 is better than the place from the sample S2. The radon concentrations from the two places of Shweku Tanke Pagoda were found within the safe limit. Although the radon concentrations were within the acceptable limit, radon concentration measurements will be needed to measure seasonally. The data of my research work will be useful data for the people from this region.

Acknowledgements

I would like to express my gratitude to Rector Dr Tin Tun Aung, Pro Rector Dr Win Win Ei and Pro Rector Dr Khin Khin Htoot, Pakokku University for their interest and encouragement for my research work. Then I wish to express my profound gratitude to Professor and Head Dr Htun Win, Professor Dr Win Mar and Professor Dr Win Myint Kyu, Pakokku University for their kind provision of the research facilities and valuable encouragement. I am deeply grateful to Professor and Head Dr Yin Maung Maung, Professor Dr Min Maung Maung and Assistant Lecturer Dr Hnin Hlwar Nu, Department of Physics, University of Yangon for supporting the materials CR39 and the informations of this research work.

References

- Durrani S A, Llic R, (1997) "Radon Measurement by Etched Track Detector: Application in Radiation Protection", Singapore: World Scientific.
- Fareed M. Mohammed, Khalid Hadi Mahdi, Shakir M. AL-Jobori, Bilal Kareem Enzi (2018) "Determination of Indoor Radon Concentrations in Some Buildings at Tikrit University by using CR-39 Detector" *Journal of Science and Research (JSR)*, vol7, pp1679-1687.
- Harald Enge, (1987) "Introduction to Nuclear Physics" Addison-Wesley Publishing Company.
- Irving Kaplan, (1954) "Nuclear Physics" Second Edition (Narosa: Publishing House)
- Khin Nu Swe (2016) "A Study of the Art-Work of Pakokku Shweku Tanke Pagoda from the Standpoint of Imitation of Essence Theory" *Pakokku University Research Journal*, vol7, pp 62-71.
- Price P B, Walker P M, (1975) "Nuclear Tracks in Solid: Principles and Applications" (Berkeley: University of California).
- Moe Win (2014) Radon Concentration Measurement in Water from Meiktila University, Using Solid State Nuclear Track detectors. M.Sc. Thesis Physics Department, Meiktila University (Unpublished)
- <https://www.fornsic.com/applications.com/radon.htm>
- <https://www.hse.gov.uk/radiation/ionising/radon.htm>
- <https://www.neha-nrpp.org/index.php>
- <https://www.physics.isu.edu/radinf/natural.htm>
- <https://www.radonleaders.org/index.php>

RAINBOW NUMBERS WITH INDEPENDENT CYCLES IN $K_{m,n}$ DEPENDING ON RAINBOW BIPARTITE GRAPHS*

Oothan Nweit¹, Kyawt Kyawt Aye², Pann Zar Nyo³

Abstract

An edge-colored graph G is called a rainbow graph if all the colors on its edges are distinct. Let Γ be a family graph of an edge-colored graph G such as $\Gamma \subseteq G$. The rainbow graph denoted by $rb(G, \Gamma)$ is related to the anti-Ramsey number $AR(G, \Gamma)$. The anti-Ramsey $AR(G, \Gamma)$, introduced by Erdős et al., is the maximum number of colors in an edge coloring graph of G without rainbow copy of any graph in G . Evidently, $rb(G, \Gamma) = AR(G, \Gamma) + 1$, $rb(G, \Gamma)$ is the rainbow number of Γ in any edge coloring graph G .

In this paper, we consider the existence of rainbow number with independent cycles in the complete bipartite graphs, denoted by $K_{m,n}$, order m and n with bipartitions (M, N) . For this result, we endeavor to construct the complete bipartite graphs on the multi-graphs without independent cycles. Denote that the rainbow number $rb(K_{m,n}, \Omega_2)$ for $m \geq n \geq 5$. Let Ω_2 denote the family of graphs containing two independent cycles. The rainbow number $rb(K_{m,n}, \Omega_2)$ is the minimum number of colors such that $\Omega_2 \subseteq K_{m,n}$, then any edge coloring of $K_{m,n}$ with at least distinct c colors contains a rainbow copy of Ω_2 . Without loss of generality, we obtain the result for any $m \geq n \geq 5$, $rb(K_{m,n}, \Omega_2) = 3m + n - 2$. Finally, we hope the main result will be supported at the fiber optic communications network in real life for our country.

Keywords: rainbow graph, rainbow number, independent cycles, edge-colored graph.

Introduction

Now we currently study edge colorings with rainbow numbers to do our paper completely. Here, first we introduce that an edge-colored graph is a graph that its edges have been colored somehow with distinct colors, we can denote it as rainbow edge-colored graph.

Again, we introduce the rainbow numbers for independent cycles in an edge-colored graph. We studied (Bondy & Murty, 1976) terminology and notation to consider finite and simple graphs. (Bondy & Murty, 1976) is completely fulfilled for us to study the basic points in finite and simple graphs. Let Γ be a family of graphs and G be an edge coloring graph and K_n be a complete graph. To determine the rainbow numbers $rb(K_n, \Gamma)$ for our conditions, first we studied anti-Ramsey number $AR(K_n, \Gamma)$. The anti-Ramsey number was introduced by Eros, Simonovits and Sos in the 1970s (Erdős et al., 1973). They showed that these are closely related to *Turan number*, $ex(K_n, \Gamma)$ which means that takes one edge of each color in an edge coloring of K_n , one can show that $AR(K_n, \Gamma) \leq ex(K_n, \Gamma)$. Γ consists of a single graph H , we can write $AR(K_n, \Gamma)$ and $ex(K_n, \Gamma)$. Here, we studied the anti-Ramsey number for a cycle conjectured in (Erdős et al., 1973) by Erdos et al. that $AR(K_n, C_3) = n - 1$ and then the anti-Ramsey number for cycles, $AR(K_n, C_k)$, was determined for $k \leq 6$ in (Alon, 1983; Erdős et al., 1973). Continuously, we studied that the rainbow numbers for cycles, $rb(K_n, C_3) = n$ in (Chartrand & Zhang, 2009). We studied that rainbow numbers for matching in plane triangulation in (Jendrol et al., 2014).

The rainbow numbers is related to the anti-Ramsey numbers that equivalently, $rb(G, H) = AR(G, H) + 1$. Therefore, in our paper to search rainbow numbers, we make anti-Ramsey number focused. Denote by Ω_k the family of multi-graphs that contain k vertex disjoint

¹ Department of Mathematics, Sittway University

² Department of Mathematics, Sittway University

³ Department of Mathematics, Sittway University

* Best Paper Award Winning Paper in Mathematics (2022)

cycles, vertex disjoint cycles are said to be independent cycles. The family of multi-graph does not belong to Ω_k is denoted by $\overline{\Omega}_k$, it is clear that is just the family of forests. It is proved in (Jin & Li, 2009) that anti-Ramsey number $AR(K_n, \Omega_2) = 2n - 2$ for $n \geq 6$. Using the extremal structures theorem for graphs in $\overline{\Omega}_2$ (Bollobas, 1978), we determine that rainbow number $rb(K_{m,n}, \Omega_2)$ for $m \geq n \geq 5$.

Rainbow Bipartite Graphs without Independent Cycles

2.1 Extremal structures theorem for graphs without independent cycles

First, we present extremal structures for the graphs which do not contain two independent cycles.

Theorem 2.1 (Bollobas, 1978) Let G be a multi-graph without two independent cycles. Suppose that $\delta(G) \geq 3$ and there is no any vertex contained in all the cycles of G . Then one of the following six assertions holds (see Figure 1).

- (1) G has three vertices and multiple edges joining every pair of the vertices.
- (2) G is a K_4 in which one of the triangles may have multiple edges.
- (3) $G \cong K_5$.
- (4) G is K_5^- such that some of the edges not adjacent to the missing edge may be multiple edges.
- (5) G is a wheel whose spokes may be multiple edges.
- (6) G is obtained from $K_{3,p}$ by adding vertices or multiple edges joining vertices in the first class.

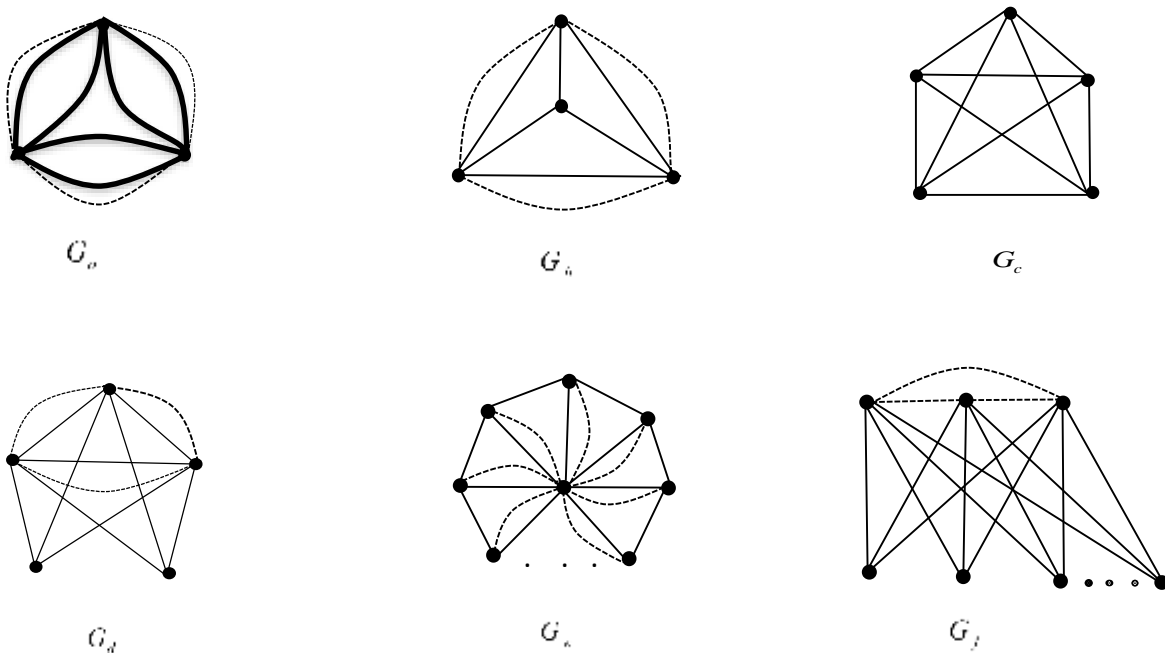


Figure 1: The graphs without independent cycles

Theorem 2.2 (Bollobas, 1978) A multi-graph G does not contain two independent cycles if and only if either it contains a vertex x_0 such that $G - x_0$ is a forest, or it can be obtained from a subdivision G_0 of a graph listed in Figure 1 by adding a forest and at most one edge joining each tree of the forest to G_0 .

In general, we have the following result.

Lemma 2.3 Let $m \geq n$ and G be a simple bipartite graph of order m and n with size q without two independent cycles. If G contains a vertex x_0 such that $G - x_0$ is a forest, then $q \leq 2m + 2n - 3$

By Theorem 2.1, we have the following lemma.

Lemma 2.4 Let $m \geq n$ and G be a simple bipartite graph of size q with m and n vertices in each partite set. Suppose that G can be obtained from a subdivision G_0 of a graph listed in Figure 1 by adding a forest and at most one edge joining each tree of the forest to G_0 . Then one of the followings holds.

- (1) G_0 is a subdivision of G_a , and then $q \leq 2m + n - 2$.
- (2) G_0 is a subdivision of G_b , and then $q \leq 2m + n - 1$.
- (3) G_0 is a subdivision of G_c , and then $q \leq m + n + 5$.
- (4) G_0 is a subdivision of G_d , and then $q \leq 2m + n$.
- (5) G_0 is a subdivision of G_e , and then $q \leq 2m + n - 2$.
- (6) G_0 is a subdivision of G_f , and then $q \leq 3m + n - 3$. Furthermore, the equality holds if and only if G can be obtained from $K_{3,p}$ by adding edges or the multiple edges joining vertices in the first class.

Proof: We prove the lemma by the induction on $m + n$. When $m + n \leq 5$, the lemma holds obviously. Assume that the lemma holds for the graph of order less than $m + n$. Now consider the graph G . Let $G = (M, N; E)$ with $|M| = m$, $|N| = n$ and then $m \geq n$.

Case 1. G_0 is a subdivision of G_a .

Suppose that G_a is a multi-graph containing three vertices such as u, v, w . Take a vertex $x \in G$. If $\delta(G) \leq 1$, then $|V(G - x)| = m + n - 1$. Let $\delta(G) = 0$. Considering the cases $x \in M$ or $x \in N$, we have

$$|E(G)| = |E(G - x)| \leq \max \{2(m - 1) + n - 2, 2m + (n - 1) - 2\} = 2m + n - 3 < 2m + n - 2,$$

as desired.

If $\delta(G) = 1$, by the same reason we have

$$|E(G)| = |E(G-x)| + 1 \leq \max \{2(m-1) + n - 2 + 1, 2m + (n-1) - 2 + 1\} \\ = 2m + n - 2,$$

as desired again.

So let $\delta(G) \geq 2$. By the Theorem 2.2 and then since G_a is a multi-graph and $\delta(G) \geq 2$, all vertices of $G - \{u, v, w\}$ lie on (multi)-edges between u, v, w . Now, considering the possible vertices belonging to M and N , we distinguish the following subcases.

Subcase 1.1 $u, v, w \in N$.

There are at most m (multi)-edges in G_0 . Here, each vertex of M is of degree two. Hence, we have that $q \leq 2m$ and we are done.

Subcase 1.2 $u \in M$ and $v, w \in N$.

There are at most $m - 1$ (multi)-edges in G_0 . Here, u is degree of n and each vertex of $M - u$ is of degree two. Hence, we obtain that $q \leq 2(m-1) + n = 2m + n - 2$ and we are done.

Subcase 1.3 $u, v \in M$ and $w \in N$.

Here, there are at most $n - 1$ (multi)-edges in G_0 . Here, w is degree of m and each vertex of $N - w$ is of degree two. Hence, we obtain that $q \leq 2(n-1) + m = 2n + m - 2$ and we are done.

Subcase 1.4 $u, v, w \in M$.

There are at most n (multi)-edges in G_0 . Here, each vertex of N is of degree two. Hence, we can deduce that $q \leq 2n$ and we are done. /

Furthermore, these cases such as **Case 2.** G_0 is a subdivision of G_b , **Case 3.** G_0 is a subdivision of G_c , **Case 4.** G_0 is a subdivision of G_d , and **Case 5.** G_0 is a subdivision of G_e can be proved by the similar analysis as above and we omit the details.

Then, we continue to prove the following.

Case 6. G_0 is a subdivision of G_f .

Given that $G_f \cong K_{3,p}$ by adding edges or the (multi)-edges joining vertices in the first class. To say $G_f \subseteq G$. Denote by $G_f = (U, V : E)$. So, let $U = \{u, v, w\}$ be the first class of G_f and then $V = \{x_1, x_2, \dots, x_p\}$ be the second class of G_f . Take a vertex $x \in G$. If $\delta(G) = 0$, then $|V(G-x)| = m + n - 1$. Considering the cases $x \in M$ or $x \in N$.

$$|E(G)| = |E(G-x)| \leq \max \{3(m-1) + n - 3, 3m + (n-1) - 3\} = 3m + n - 4 < 3m + n - 3,$$

as desired.

If $\delta(G) = 1$, by the same reason we have

$$|E(G)| = |E(G-x)| + 1 \leq \max \{3(m-1) + n - 3 + 1, 3m + (n-1) - 3 + 1\} = 3m + n - 3,$$

as desired again.

So let $\delta(G) \geq 2$. Since G_f is a multi-graph and $\delta(G) \geq 2$, all vertices of $G \setminus (U, V)$ lie on (multi)-edges among the vertices of U . Now, considering the possible vertices u, v, w belonging to M and N , it is enough reason to provide confirmation. So, we distinguish the following subcases.

Subcase 6.1 $u, v, w \in N$

Here, if $V \subseteq M$, there are at most $m - p$ (multi)-edges in G_0 . It is obviously that there are at least one vertex of $M \setminus N$ on any (multi)-edges. Here, we need to consider the number of vertices of p , since G is a bipartite graph,

$$\sum_{x \in M} d(x) = \sum_{y \in N} d(y)$$

$$2(m - p) + 3p \geq 2(n - 3) + 3p.$$

Therefore, $m \geq n + p - 3, 3 \leq p \leq n \leq m$.

Continuously, in details we determine the number of vertices in V , so let $V = V_x \cup V_{p-x}$ such that x -vertices in V_x and $0 \leq x \leq p$. Now, we consider the possible vertices in V_x and V_{p-x} belonging to M and N so we again distinguish the following sub-subcases.

Sub-subcase 6.1.1 $V_x \subseteq N$ and $V_{p-x} \subseteq M$.

Here, we have at most $m - p + x$ (multi)-edges in G_0 . Each vertex of $M \setminus V_{p-x}$ is of degree two and each vertex of V_{p-x} is three. Hence, we have that

$$q \leq 2(m - (p - x)) + 3(p - x) = 2m + p - x \leq 2m + n \text{ (since } 0 \leq x \leq p \leq n)$$

and done.

Sub-subcase 6.1.2 $V_x \subseteq M$ and $V_{p-x} \subseteq N$.

Here we have at most $m - x$ (multi)-edges in G_0 . Each vertex of $M \setminus V_x$ is of degree two and each vertex of V_x is three. Hence, we have that

$$q \leq 2(m - x) + 3x \leq 2m + p \leq 2m + n$$

and done.

Here, if $V \subseteq N$, there are at most m (multi)-edges in G_0 and each vertex of M is of degree two. Hence, we have that $q \leq 2m$ and done.

Subcase 6.2 $u, v, w \in M$.

Here, if $V \subseteq N$, there are at most $n - p$ (multi)-edges in G_0 . It is obviously that there are at least one vertex of $M \setminus V_p$ on any (multi)-edges. Here, we need to consider the number of vertices of p . Since G is a bipartite graph,

$$\sum_{x \in M} d(x) = \sum_{y \in N} d(y)$$

$$2(m - 3) + 3p \leq 2(n - p) + 3p.$$

Since $m \geq n$, so $m \leq n - p + 3, p \leq 2$.

Here, also we distinguish in details the number of vertices in V by the same reason as above subcase, so we have the following sub-subcases.

Sub-subcase 6.2.1 $V_x \subseteq N$ and $V_{p-x} \subseteq M$.

Here, we have at most $n - x$ (multi)-edges in G_0 . Each vertex of $N \setminus V_x$ is of degree two and each vertex of V_x is three. Hence, we have that

$$q \leq 2(n - x) + 3x \leq 2n + p$$

and done.

Sub-subcase 6.2.2 $V_x \subseteq M$ and $V_{p-x} \subseteq N$.

Here, we have at most $m - p + x$ (multi)-edges in G_0 . Each vertex of $N \setminus V_{p-x}$ is of degree two and each vertex of V_{p-x} is three. Hence, we have that

$$q \leq 2(n - p + x) + 3(p - x) = 2n + p - x \leq 2n + p$$

and done.

Here, if $V \subseteq M$, then there are at most n (multi)-edges in G_0 and each vertex of N is of degree two. Hence, we have that $q \leq 2n$ and done.

Subcase 6.3 $u, v \in N$ and $w \in M$

Here, if $V \subseteq M$, there are at most $m - p - 1$ (multi)-edges in G_0 . By the summing of degree,

$$\begin{aligned} \sum_{x \in M} d(x) &= \sum_{y \in N} d(y) \\ 2(m - p - 1) + n + 3p &\geq 2(n - 2) + 2p \\ 2m &\geq n - 2 + p. \end{aligned}$$

So, $n + 2 \leq p \leq m - 1$

Here, also we distinguish in details the number of vertices in V by the same reason as above subcase. So, we have the following sub-subcases.

Sub-subcase 6.3.1 $V_x \subseteq N$ and $V_{p-x} \subseteq M$.

Here, $0 \leq x \leq p$, we have at most $m - p + x$ (multi)-edges in G_0 . Each vertex of $M \setminus (V_{p-x} + w)$ is of degree two and each vertex of V_{p-x} is three and w is of degree n . Hence, we have that

$$q \leq 2(m - p + x - 1) + 3(p - x) + n = 2m + n + p - x - 2 \leq 3m + n - 3$$

and done.

Sub-subcase 6.3.2 $V_x \subseteq M$ and $V_{p-x} \subseteq N$.

Here, we have at most $m - x - 1$ (multi)-edges in G_0 . Each vertex of $M \setminus (V_x + w)$ is of degree two and each vertex of V_x is three and w is of degree n . Hence, we have that

$$q \leq 2(m - x - 1) + 3x + n = 2m + n + x - 2 \leq 2m + n + p - 2 \leq 3m + n - 3$$

and done.

Here, if $V \subseteq N$, then we obtain the same result as above. So, we omit the details.

Subcase 6.4 $u \in N$ and $v, w \in M$.

Here, if $V \subseteq N$, then there are at most $n - p - 1$ (multi)-edges in G_0 . By the sum degree,

$$\sum_{x \in M} d(x) = \sum_{y \in N} d(y)$$

$$2(m-2)+2p \leq 2(n-p-1)+m+3p$$

$$2n \geq m-2+p.$$

So, $m+2 \leq p \leq n-1$.

Here, also we distinguish in details the number of vertices in V by the same reason as above subcase. So, we have the following sub-subcases.

Sub-subcase 6.4.1 $V_x \subseteq N$ and $V_{p-x} \subseteq M$.

Here, $0 \leq x \leq p$, we have at most $n-x-1$ (multi)-edges in G_0 . Each vertex of $N \setminus (V_x + w)$ is of degree two and each vertex of V_x is three and w is of m . Hence, we have that

$$q \leq 2(n-x-1) + m + 3x = 2n + m + p - x - 2 \leq 3n + m - 3$$

and done.

Sub-subcase 6.4.2 $V_x \subseteq M$ and $V_{p-x} \subseteq N$.

Here, we have at most $n-p+x-1$ (multi)-edges in G_0 . Each vertex of $N \setminus (V_{p-x} + w)$ is of degree two and each vertex of V_{p-x} is three and w is of degree m . Hence, we have that

$$q \leq 2(n-p+x-1) + 3(p-x) + m = 2n + m + p - x - 2 \leq 2n + m + p - 2 \leq 3n + m - 3$$

and done.

Here, if $V \subseteq M$, then we obtain the same result as above. So, we omit the details.

This completes the proof.

More precisely, from the lemma above, we have the following theorem.

Rainbow graphs with independent cycles in $K_{m,n}$

Let Ω_2 be a family of the two independent cycles in a given graph G , then an edge coloring c of $K_{m,n}$ is induced by G and assigns one additional color to all the edges of \overline{G} . Clearly, G is a spanning subgraph of $K_{m,n}$, an edge coloring of $K_{m,n}$ induced by G has $|E(G)|+1$ colors. Let G be a complete bipartite graph with bi-partitions $M \cup N$ and $|M|=m$ and $|N|=n$, without loss of generality, in the following result we always assume $m \geq n$.

Theorem 3.1 For any $m \geq n \geq 5$, $rb(K_{m,n}, \Omega_2) = 3m + n - 2$.

Proof: We shall prove the theorem by contradiction. In this theorem, we consider the family of graphs with two rainbow independent cycles, i.e., rainbow member of Ω_2 in any complete bipartite graph $K_{m,n}$ with bipartition $M \cup N$ and $|M|=m$ and $|N|=n$, without loss of generality, $m \geq n$.

Now, we consider **the Lower bound**.

Here, we present an edge coloring of $K_{m,n}$ as follows. Take a copy of $K_{3,m}$ in $K_{m,n}$ and color its edges by distinct colors. For each vertex in $N \setminus V(K_{3,m})$, all the edges incident to it are colored by its own color. So, we get edges incident to it are colored by its own color. So, we get a

$(3m + n - 3)$ -edge coloring of $K_{m,n}$. Clearly, there is not any rainbow graph with two independent cycles. Then $rb(K_{m,n}, \Omega_2) \geq 3m + n - 2$.

Now, we consider **the Upper bound**.

In order to the upper bound, here we only need to show that any $(3m + n - 2)$ -edge coloring c of $K_{m,n}$ always contains a rainbow subgraph belonging to the family Ω_2 . By contradiction, we assume that $K_{m,n}$ does not contain any rainbow subgraph in Ω_2 . Take a rainbow spanning subgraph G of $K_{m,n}$, which is of size $(3m + n - 2)$. That is to say that G contains exactly one edge of each color. By the induction hypothesis, $G \notin \Omega_2$.

From Theorem 2.1, Lemma 2.4, we have that G can be obtained from a subdivision G_0 of a graph listed in Figure 1 by adding a forest and at most one edge joining each tree of the forest to G_0 . Since $|E(G)| = 3m + n - 2$, from by Lemma 2.4, G is not a subdivision of G_a, G_b, G_c, G_d, G_e and G_f . Clearly, the number of edges of them is less than $3m + n - 2$. Therefore, this is contradiction.

This completes the proof.

Conclusion

In the current paper, we studied different problems in edge colorings. In particular, we studied rainbow numbers in bipartite graphs with multiple edges and minimum color numbers for rainbow graphs with independent cycles in complete bipartite graph.

Acknowledgements

This work was supported by Department of Mathematics, Sittway University and Myanmar Academic of Arts and Science. The authors are very grateful to the referees for helpful comments and suggestions.

References

- Alon, N., (1983) "On a conjecture of Erdős, Simonovits and Sos concerning anti-Ramsey theorems" [J], *J.Graph Theory.*, vol.1: pp.91-94.
- Axenovich, M., T. Jaing, and A. Kiindgen, (2001) "Bipartite anti-Ramsey numbers of cycles" [J], *J.Graph Theory.*, vol.47: pp.9-28.
- Babu, J., L.S. Chandran, and K. Vaidynathan, (2015) "Rainbow matchings in strongly edge-colored graphs" [J], *Discrete Math.*, vol.338: pp.1191-1196.
- Bollobas, B., (1978) *Extremal Graph Theory* [M]. Academic Press, New York.
- Bondy, J. A., and U. S. R. Murty, (1976) *Graph Theory with Applications* [M]. Macmillan, London and Elsevier, New York.
- Chartrand, G., and P. Zhang, (2009) *Chromatic Graph Theory*, Chapman and Hall.
- Erdős, P., M. Simonovits, and V.T. Sos, (1973) "Anti-Ramsey theorems", *Colloq. Math.Soc. Janos Bolyai.* Vol.10, Infinite and Finte Sets, Keszthely (Hungary)., pp.657-665.
- Jendrol, S., I. Sciermeyer, and J.H. Tu, (2014) "Rainbow numbers of matchings in plane triangulations" [J], *Discrete Math.*, vol. 331(28): pp. 158-164.
- Jin, Z.M., and X.L. Li, (2009) "Anti-Ramsey numbers for graphs with independent cycles"[J], *Electron. J.Combin.*, 16: #R85.

PREDICTION AND VISUALIZATION OF MENTAL HEALTH PATTERNS USING MACHINE LEARNING TECHNIQUES*

Shwe Sin Ei¹, Thet Thet Hlaing², Soe Mya Mya Aye³

Abstract

Mental health includes emotional, psychological, and social well-being. As the coronavirus pandemic has spread across the world, the public health crisis has brought with it considerable impact on social and economic. Besides physical health, the psychological impacts of COVID-19 also pose significant risks to mental-wellbeing as the greater levels of stress, depression and anxiety in people. In this paper, patterns of mental health were discovered using public data by machine learning approach. The main contribution of this paper is to provide awareness and nature of mental health to determine the factors that influence mental health across people's lifespans (e.g. genetics, cognition, demographics). This research use three machine learning classifiers: decision tree, random forest and k-nearest neighbour (KNN). The experimental results found that Random Forest classifier achieves the best accuracy.

Keywords: Mental Health, Machine Learning, Decision tree, Random forest, K-nearest neighbour

Introduction

Nowadays, the impact of modern age life style, mental illnesses have become more common in life. Depression, anxiety, stress and suicide are all more prevalent, year by year. Around 1-in-7 people globally (11% to 18%) have one or more mental or substance use disorders. Mental health is vital at every stage of life, not only from childhood to adulthood but also for old people, in every age.

Mental health can happen to all kinds of people from all kinds of works life, young or old, rich or poor. Good mental wellbeing doesn't mean a person is always happy or unaffected by external experiences. Mental health affects how people think, feel, and act. The impact of poor mental health creating tension, uncertainty, stress and sometimes significant changes in how people live their lives. Mental health awareness is so important that it can help you to understand your symptoms, get access treatment and perhaps you can overcome mental unhealthy conditions.

The information technologies offer a lot of opportunities for communication and social networking. In medical field, machine learning is widely used and it helps in mental health research and practice. With the help of advances technology, doctors can get a huge amount of information at a rapid rate. Machine learning in AI analyze these data and this allows data patterns are correctly discovered. Machine learning techniques aided quick and scalable analysis of complicated data as well as accurate predictions can be made.

In this paper, three machine learning classifiers: decision tree and random forest and k-nearest neighbors (KNN) were applied for research. Among these algorithms, decision tree and random forest are popular machine learning algorithms which belongs to the supervised learning technique. It can be used for both classification and regression problems in machine learning. Random Forest can predict the output with high accuracy and decision trees can perform classification without requiring much computation. K-nearest neighbors (KNN) is one of the simplest machine learning algorithms based on supervised learning technique. It can be used for classification as well as regression problems.

¹. Department of Computer Studies, University of Yangon

². Department of Computer Studies, University of Yangon

³. Department of Computer Studies, University of Yangon

* Best Paper Award Winning Paper in Computer Science (2022)

The paper is organized as follows. Section 2 describes the related works to clarify more on the approach. In Section 3, we describe the materials and method use in identifying the pattern of mental health. Section 4 describes the implementation of the system and finally, Section 5 describes results and future work.

Materials and Methods

Data source

This dataset is survey in 2014 from Kaggle which measures attitudes towards mental health and frequency of mental health disorders in the Tech workplace.

The original dataset has 1260 records and 27 variables. This research utilized 1260 records involving 8 selected variables. The sample dataset was as shown in table 1.

Table 1: Dataset of selected features of Mental Health

Sr. No.	Age	Gender	Self Employed	Family History	Work Interferes	Coworkers	Supervisor	Treatment
1	37	Female	Yes	No	Often	Some	Yes	Yes
2	44	Male	Yes	No	Rarely	No	No	No
3	32	Male	No	No	Rarely	Yes	Yes	No
4	31	Male	Yes	Yes	Often	Some	No	Yes
5	31	Male	No	No	Never	Some	Yes	No
6	33	Male	No	Yes	Sometimes	Yes	Yes	No
7	35	Female	No	Yes	Sometimes	Some	No	Yes
8	39	Male	No	No	Never	No	No	No
9	42	Female	No	Yes	Sometimes	Yes	Yes	Yes
10	23	Male	No	No	Never	Yes	Yes	No
:	:	:	:	:	:	:	:	:
:	:	:	:	:	:	:	:	:
:	:	:	:	:	:	:	:	:
1259	46	Female	No	No	Never	No	No	No
1260	25	Male	No	Yes	Sometimes	Some	No	Yes

Patterns in machine learning

A pattern is a series of data that repeats in a recognizable way. Pattern recognition is a process of finding regularities and similarities in the dataset. Machine learning technique classifies data based on statistical information or knowledge gained from patterns and their representation. In this study, the patterns of influencing factors on mental health are visualized by using matplotlib, data visualization and graphical plotting library of python.

Machine learning methods

Machine learning is a subfield of artificial intelligence. The concept of machine learning is that the computer program can learn and adapt to new data without human intervention. Machine learning involves a group of computational algorithms that can perform classification, pattern recognition and prediction. There are different types of machine learning Algorithms such as supervised learning, unsupervised learning, semi-supervised learning and reinforcement Learning.

Decision Tree Algorithm

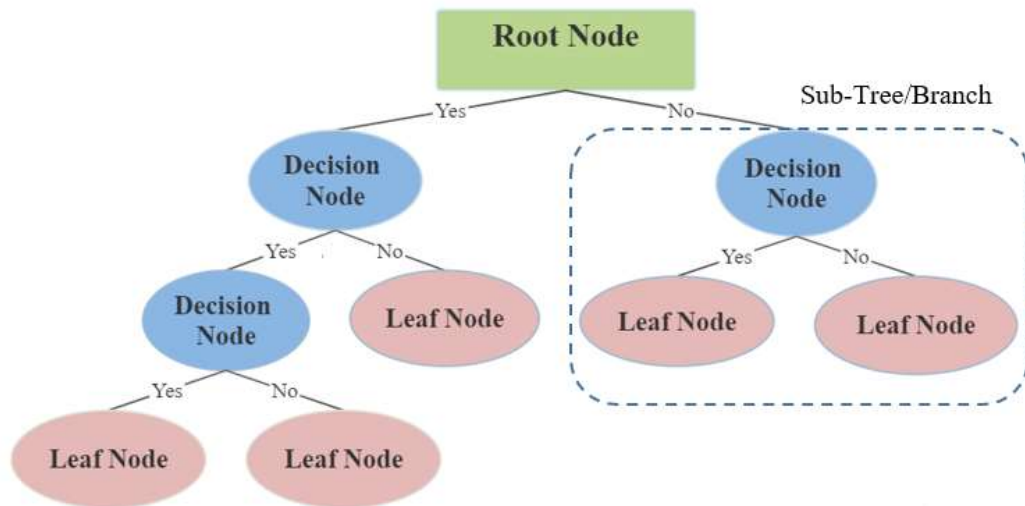


Figure 1: Decision Tree Structure

Decision Tree Algorithm which is also called ‘CART’ used for both classification and regression problems. It uses supervised machine learning technique. Because of its tree-structured classifier, it is called decision tree and it starts with the root node, which expands on further branches.

In a Decision tree, there are two nodes, decision node and leaf node. Decision nodes are used to make decision whereas Leaf nodes are the output of those decisions. A decision tree simply works, asks a question and based on the answer (yes/no), it is further split into branches and sub trees.

Random Forest Algorithm

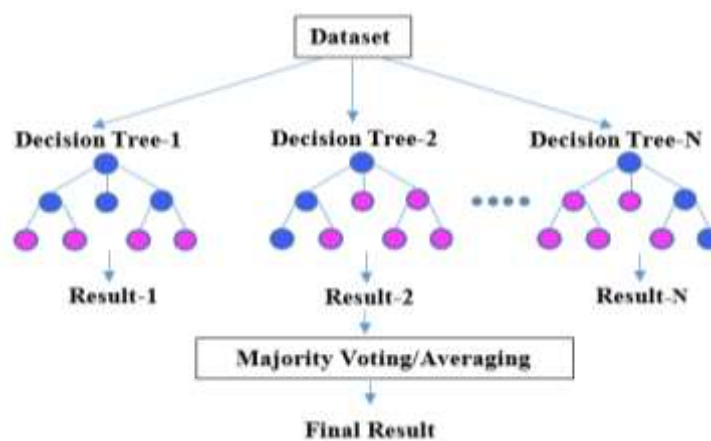


Figure 2: Random Forest Structure

Random Forest is a well-known machine learning algorithm that uses supervised learning techniques. Random Forest is a classifier that combines a number of decision trees on different subsets of a dataset to create a forest and feeds random features from the input dataset to them.

One of the most important features of the Random Forest Algorithm is that it can handle both categorical variables and continuous variables. The random forest uses the majority votes of predictions from each tree in the forest and it produce the final output of predictions. The greater the number of trees leads to the more accuracy of result can be produced and it prevents from over fitting.

K-Nearest Neighbour (KNN) Algorithm

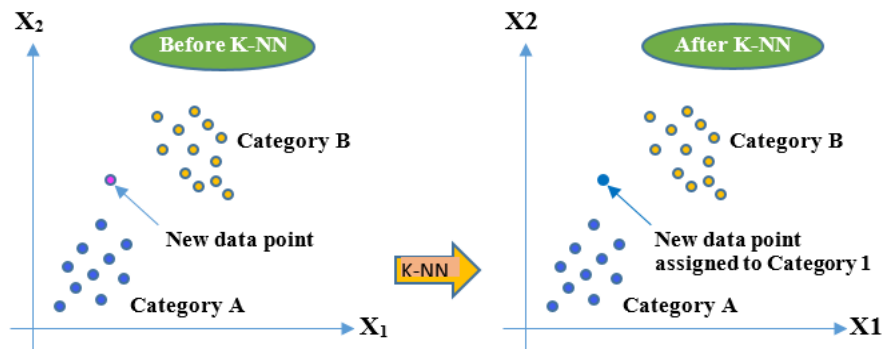


Figure 3: K-Nearest Neighbour Classifier

The K-Nearest Neighbors (KNN) algorithm is a simple supervised machine learning algorithm that can be used to solve both classification and regression problems. In pattern recognition, the KNN algorithm is a method for classifying objects based on closest training examples in the feature. Aleem Shumaila and Huda Noor ul [2022] said this rule simply retains the entire training set during learning and assigns to each query a class represented by the majority label of its K-Nearest Neighbors in the training set.

It is a major classical machine learning algorithm that focuses on the distance from new unclassified/ unlabeled data points to existing classified/labeled data points. For classification problems, a class label is assigned on the basis of a majority vote that means the label that is most frequently represented around a given data point is used.

Implementation and Results

In developing the system, Python programming language is used in Spyder Platform which is an open source cross-platform integrated development environment (IDE) for scientific programming in the Python Language. The dataset that we used in our research is from Kaggle.com. In this study, we will implement the decision tree, random forest and K-Nearest Neighbors algorithms using Python's Scikit-Learn library.

Experimental Setup

The experiments were implemented on 8 selected attributes containing 1260 instances. The dataset was imported first from Kaggle and data cleaning i.e., removing duplicate records, incorrect and incomplete data in dataset was done. Then, the dataset was split into two separate datasets, train and test datasets for input dataset (features) and output dataset (target). The attributes description of datasets are as shown in table (2).

Table 2: Mental Health Dataset Description

No	Attribute Names	Description
1.	Age	18 ~ 70
2.	Gender	Male/Female/Queer
3.	Remote work	Do you work remotely (outside of an office) at least 50% of the time?
4.	Family history	Do you have a family history of mental illness?
5.	Work interfere	If you have a mental health condition, do you feel that it interferes with your work?
6.	Coworkers	Would you be willing to discuss a mental health issue with your coworkers?
7.	Supervisor	Would you be willing to discuss a mental health issue with your direct supervisor(s)?
8.	Treatment	Have you sought treatment for a mental health condition?

Workflow Diagram of a Proposed System

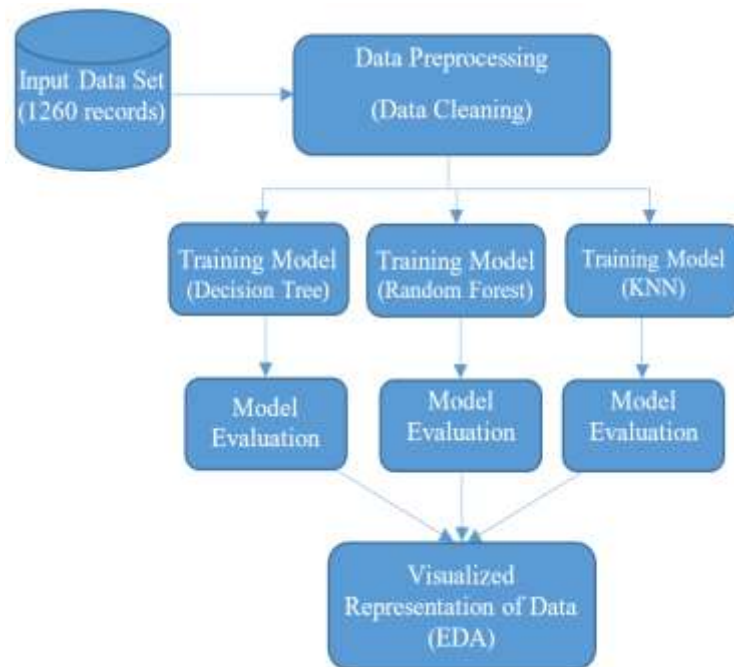


Figure 4: Workflow Diagram of a Proposed System

The work flow of the proposed system starts with input of dataset. The input data contains 8 attributes and 1260 employee records. In the first step, the data processing is done to clean the raw data. In the second step, three different classification algorithms in machine learning: Decision tree, Random forest and K-Nearest Neighbors are chosen and the model are trained. In the third step, models are evaluated to test the accuracy of each model. At the last stage, EDA data are displayed in the form of graphs and charts.

Building Models

In supervised learning, algorithms learn from labeled data. Classification techniques are used to determine which class is yes and no. In this study, three classification models are built using supervised machine learning techniques called decision tree classifier, random forest classifier and k-nearest neighbors classifier. So, these classifiers are imported from scikit-learn library which is the machine learning library in python as shown in figure (5). Decision trees were generated using CART algorithm. After decision tree generation, Random Forest was performed. Then, KNN classifier was imported from scikit-learn and create a model.

```
#Load Dataset
mh = pd.read_csv('survey.csv')
# Modeling
from sklearn.tree import DecisionTreeClassifier
from sklearn.neighbors import KNeighborsClassifier
from sklearn.metrics import accuracy_score, recall_score, plot_roc_curve
from sklearn.ensemble import RandomForestClassifier
# Splitting Data
from sklearn.model_selection import train_test_split, StratifiedKFold, cross_val_score
# Tuning
mh.drop(columns=['Timestamp', 'Country', 'state', 'comments'], inplace = True)
mh.rename({'self_employed' : 'Self_Employed', 'family_history' : 'Family_History',
          'treatment' : 'Treatment', 'work_interfere' : 'Work_Interfere',
          'remote_work' : 'Remote_Work', 'coworkers' : 'Coworkers', 'supervisor' : 'Supervisor',
          }, inplace = True , axis = 1)
mh['Age'].replace([mh['Age'][mh['Age'] < 15]], np.nan, inplace = True)
mh['Age'].replace([mh['Age'][mh['Age'] > 100]], np.nan, inplace = True)
```

Figure 5: Code Segments of Developing Classification Models

Afterwards, the models are trained on two separate datasets to train and test. The dataset is divided into training dataset and testing dataset, 70-80% of the dataset is used for the training and 20-30% is used for the testing. Evaluation of the models show that the best results are obtained if dataset is divided into 20% for testing, and the remaining 80% for training. The training dataset is used to train the machine learning models and the testing dataset is used to test the trained model. Our models will learn patterns on the data to make predictions whether an employee willingly to take treatment or not. The scores of different models are measured to evaluate and compare their accuracy. The k=5-fold Cross Validation was adopted for the training datasets and test datasets. The accuracy of the models were calculated using Confusion Matric and compared the performances of the models using recall, standard deviation, mean and cross validation scores as shown in figure (6).

```

def model_evaluation(model, metric):
    model_cv = cross_val_score(model, X_train, y_train, cv = StratifiedKFold(n_splits = 5), scoring = metric)
    return model_cv

tree_pipe_cv = model_evaluation(tree_pipe, 'recall')
knn_pipe_cv = model_evaluation(knn_pipe, 'recall')
rf_pipe_cv = model_evaluation(rf_pipe, 'recall')

for model in [tree_pipe, rf_pipe, knn_pipe]:
    model.fit(X_train, y_train)

score_cv = [tree_pipe_cv.round(5),
            rf_pipe_cv.round(5), knn_pipe_cv.round(5)]
score_mean = [tree_pipe_cv.mean(), rf_pipe_cv.mean(), knn_pipe_cv.mean()]
score_std = [tree_pipe_cv.std(), rf_pipe_cv.std(), knn_pipe_cv.std()]
score_recall_score = [recall_score(y_test, tree_pipe.predict(X_test)),
                      recall_score(y_test, rf_pipe.predict(X_test)), recall_score(y_test, knn_pipe.predict(X_test))]
method_name = [ 'Decision Tree Classifier', 'Random Forest Classifier', 'K Nearest Neighbour']
cv_summary = pd.DataFrame({
    'method': method_name,
    'std score': score_std,
    'recall score': score_recall_score,
    'mean score': score_mean})
cv_summary
print(cv_summary)

```

Figure 6: Code Segments to calculate Accuracy and Performance of Models

Exploratory Data Analysis (EDA)

Visualization of the discovered patterns is important in order to communicate information efficiently using graphs, charts and tables. In this paper, different machine learning algorithms such as Decision Tree, Random Forest and K-Nearest Neighbors are used to identify the key features of mental health patterns that lead to mental health problems in working environment. Exploratory Data Analysis based on the selected features are shown in figure (7).

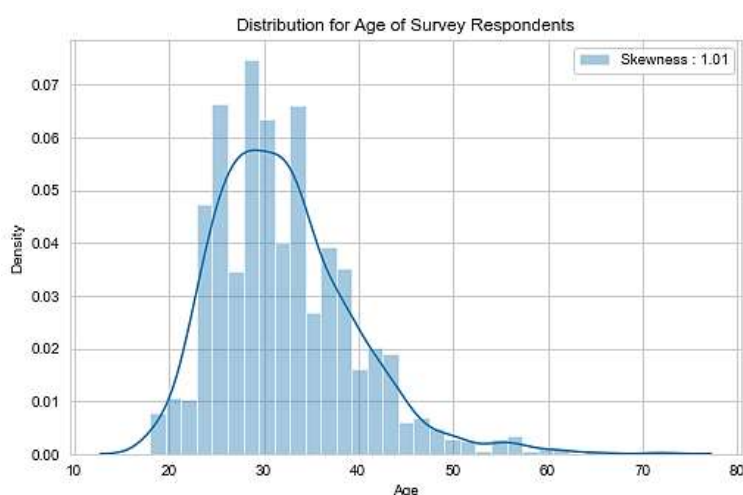


Figure 7: Density of respondents by age

From figure (7), age pattern indicated that most of the employees that fill the survey around the end 20s to early 40s.

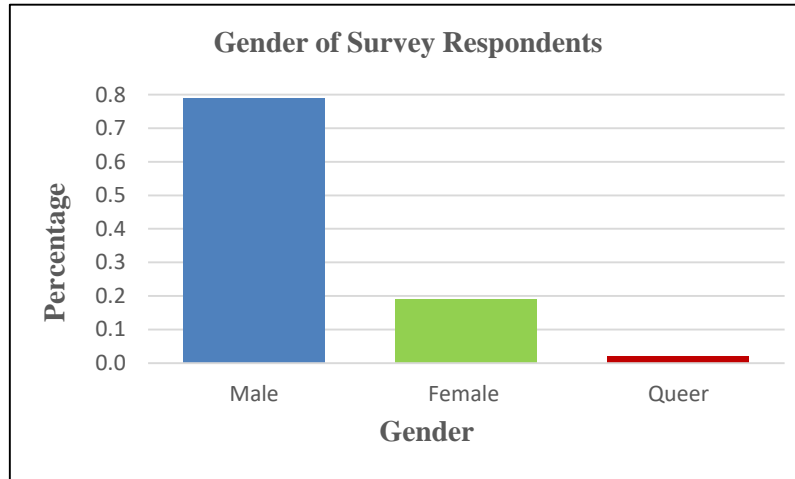


Figure 8: The respondents by Gender

According to gender pattern in figure (8), it was found that male are higher rate of respondents almost 79% of respondents are male.

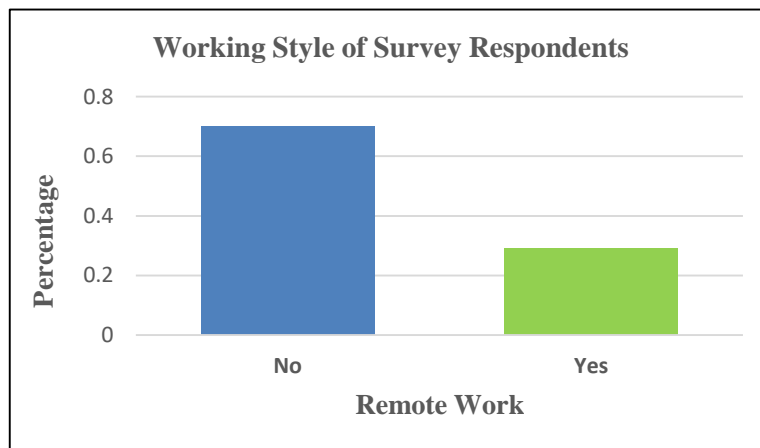


Figure 9: The working style of respondents

According to working style pattern in figure (9), around 70% of respondents don't work remotely, which means the biggest factor of mental health disorder came up triggered on the workplace.

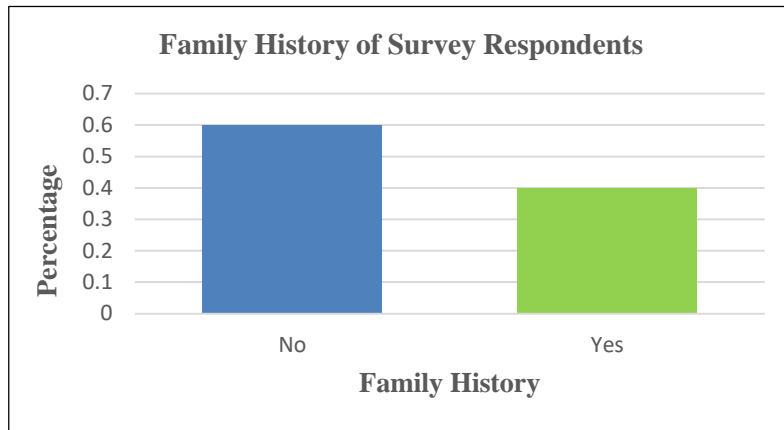


Figure 10: Family History of survey respondents

Figure (10) describes the ‘family history of survey respondents by percentage’. According to the patterns, 40% of respondents who say that they have a family history of mental illness.

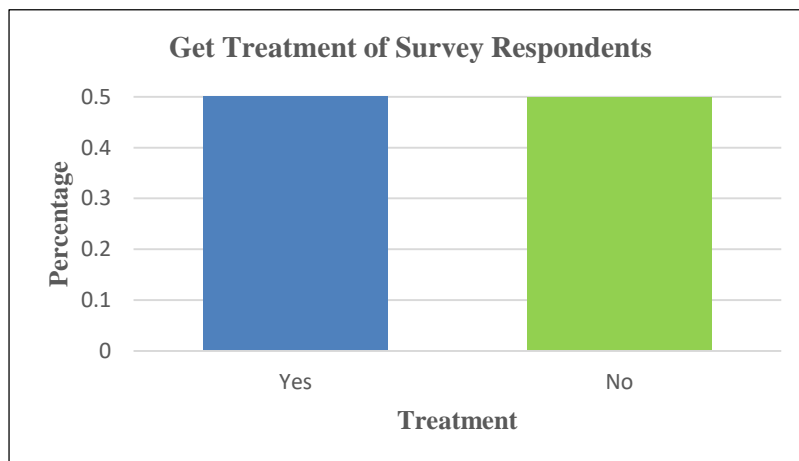


Figure 11: Percentage of getting treatments

Figure (11) describes the ‘Percentage of getting treatments’. It was found that the percentage of respondents who want to get treatment is 50%.

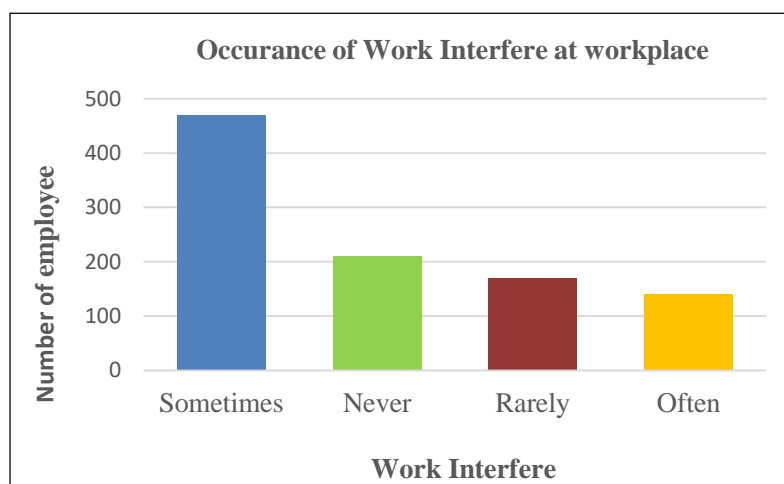


Figure 12: Mental Health that makes work interfere at workplace by percentage

In the above figure (12) shows that the ‘occurrence of work Interfere at workplace by Percentage’, about 78% of respondents have experienced interference at work with a ratio of rarely, sometimes, and frequently.

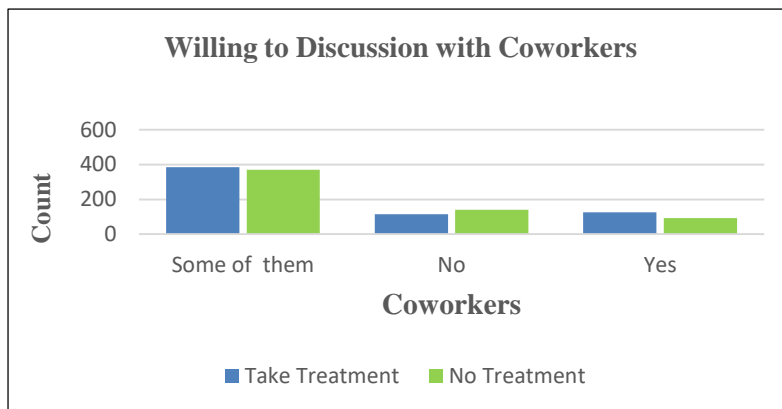


Figure 13: Respondents who are willing for discussion with coworkers.

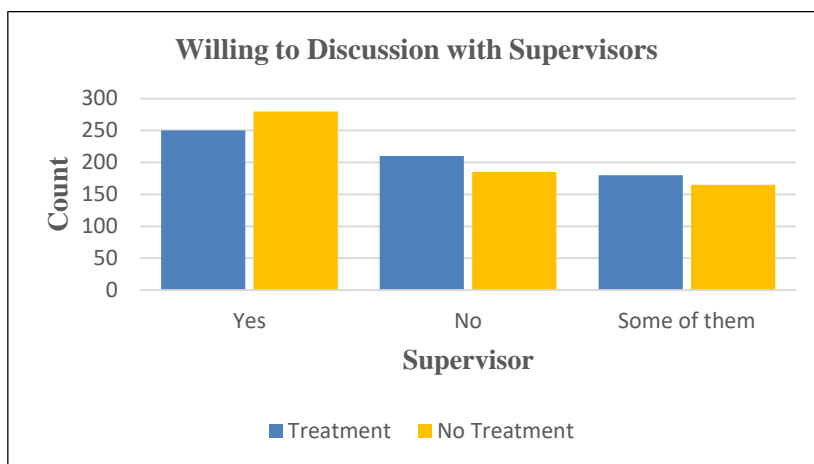


Figure 14: Respondents who are willing for discussion with supervisors.

The above figure (13) and (14) shows ‘the number of poor mental health people who are willing to discuss with coworkers and supervisors’. According to a pattern released by exploratory data analysis, most people with mental health conditions are more inclined to make discussions with their superiors than coworkers.

Model Evaluation

Evaluating a model is the core part of creating an effective model. After building machine learning models by using Random forest, Decision tree and K-Nearest Neighbors algorithms, next accuracy of the models are measured to make improvements and continue until achieving a desirable accuracy.

The measurement scores described in table (3) are obtained by running the code of program of three different machine learning classifiers and results are as shown in figure (15).

```
In [3]: runfile('D:/mental_health/04Allscore_edit.py', wdir='D:/mental_health')
      method  std score  recall score  mean score
0 Decision Tree Classifier  0.033664      0.617801      0.679451
1 Random Forest Classifier  0.018375      0.706806      0.762297
2 K Nearest Neighbour      0.027498      0.612565      0.589588
      method  cv score
0 Decision Tree Classifier [0.64444, 0.64045, 0.69663, 0.73034, 0.68539]
1 Random Forest Classifier [0.77778, 0.77528, 0.73034, 0.75281, 0.77528]
2 K Nearest Neighbour     [0.63333, 0.60674, 0.58427, 0.5618, 0.5618]
```

Figure 15: Standard deviation, Recall, Mean and CV scores of three Classifiers

Table 3: Accuracy Measurement Table for the model comparisons

Method	Standard score	Recall score	Mean score	CV score
Decision Tree	0.033664	0.617801	0.679451	[0.64444, 0.64045, 0.69663, 0.73034, 0.68539]
Random Forest	0.018375	0.706806	0.762297	[0.77778, 0.77528, 0.73034, 0.75281, 0.77528]
K-Nearest Neighbors	0.027498	0.612565	0.589588	[0.63333, 0.60674, 0.58427, 0.5618, 0.5618]

Standard score: Standard score is the number of standard deviations by which the value of a raw score (i.e., an observed value or data point) is above or below the mean value of what is being observed or measured.

Recall score: The recall measures the model's ability to detect positive samples. The higher the recall, the more positive samples detected.

Mean score: Mean score is to measure the accuracy of the model.

CV score: Cross-validation (CV) is used to estimate the skill of a machine learning model on unseen data.

Discussion

The objective of this study is to provide awareness of potential mental health and to discover the factors influencing on mental health among socio-demographics data and information on the occupations. The experimental results of three machine learning classifiers are shown in this paper and Random Forest classifier achieves the highest accuracy with 76% and K-Nearest Neighbors classifier is the lowest accuracy with 58% and that of Decision Tree classifier is 67%.

Based on Exploratory Data Analysis (EDA), data visualization makes better data-based decisions on the relation between mental health and associated factors. A histogram shows that most of the survey respondents are around 20s to early 40s and the distribution of ages indicates that to have younger employees. There is no statistically significant difference of ages between respondents that get treatment and no treatment. According to gender, almost 79% of respondents are male as the Tech work space and a queer is less than 2%. It was also found that 40% of respondents who say that they have a family history of mental illness, the plot shows that they significantly want to get treatment rather than without a family history. Relation with mental health and work interference, it was found that about 78% of respondents have experienced interference at work and mental health conditions sometimes become interfere at work is about

45%. The respondents result of question, 'Would you be willing to discuss a mental health issue with your coworkers and Supervisors', 18% of respondents who say yes to discuss it with coworkers, 60% of them want to get treatment and 40% of respondents who say yes to discuss with supervisor, only 55% of them want to get treatment. Based on survey respondents shown on graphs, generally mental health disorder came up triggered on the workplace, consequently it was found that mental health is closely related to the type of working style.

Conclusion

In this study, different machine learning algorithms such as Decision Tree, Random Forest and K-Nearest Neighbors were applied for classification, and identified factors associated with mental health patterns. This study found that Random Forest Model has the best accuracy among the three prediction models using Machine Learning Techniques. Exploratory Data Analysis (EDA) are used to analyze the data using visual techniques. Dataset for this study was from kaggle.com containing 1260 employee records with 8 selected attributes for this paper.

Acknowledgements

I would like to give my warmest thanks to Professor Dr. Thet Thet Hlaing, Department of Computer Studies, University of Yangon for guiding me through all the stages of doing my research. I would like to express my special thanks to Professor Dr. Soe Mya Mya Aye, Head of Department of Computer Studies, University of Yangon for her kind permission to carry out this research. My thanks for my gratitude to U Zaw Win Htun, Principal of Myanmar Mercantile Marine College for giving me a chance to do this research.

References

- Aleem, S., Noor ul Huda, Rashid Amin, Samina Khalid, Sultan S. Alshamrani and Abdullah Alshehri, (2022) "Machine Learning Algorithms for Depression: Diagnosis, Insights, and Research Directions", <https://doi.org/10.3390/electronics11071111>.
- Das, J., Quy-Toan Do, Jed Friedman and David McKenzie, (2009) "Mental Health Patterns and Consequences: Results from Survey Data in Five Developing Countries", *The World Bank Economic Review*, Vol. 23, No. 1, pp 31-55.
- Gold, A., Danny Gross, Abdul Latif Jameel, (2022) "Deploying Machine Learning to Improve Mental Health", MIT News, <https://news.mit.edu>.
- Kaur, P., Ravinder Kumar and Munish Kumar, (2019) "A Healthcare Monitoring System Using Random Forest and Internet of Things (IoT)", *Multimedia Tools Applications* 78, 19905–19916.
- Mind (2017) "Understanding mental health problems: Introduction of Mental Health Problems", Booklet, <https://www.mid.org.uk>.
- Shafiee, S. M., Sofianita Mutalib, (2020) "Prediction of Mental Health Problems among Higher Education Student Using Machine Learning", *International Journal of Education and Management Engineering*, 10(6):1-9.
- Thieme, A., Danielee Belgrave and Gavin Doherty, (2020) "Machine Learning in Mental Health: A Systematic Review of the HCI Literature to Support the Development of Effective and Implementable ML Systems", *ACM Trans. Human Computer Interaction*. Vol. 27, No. 5, Article 34, pp 1-53.
- Vaishnavi, K., U Nikhitha Kamath, B Ashwath Rao and N V Subba Reddy, (2022) "Predicting Mental Health Illness using Machine Learning Algorithms", *Journal of Physics: Conference Series*, AICECS 2021.

EXPLORING THE BIG DATA ANALYTICS TOOLS FOR STRUCTURED AND UNSTRUCTURED DATA

Kyaw Kyaw Min¹, Pwint Phyu Khine², Soe Mya Mya Aye³

Abstract

Today, as technologies advance, so does the data usage. This makes many organizations need to handle a lot of data creating huge data collection which affects all sectors. A larger amount of data assumingly could give a better output however manipulating such amount of data with different structures becomes a challenge. A specific generation of analytical tools is increasing in use to handle such an increase in the data, structured and unstructured data. With appropriate big data analytical tools, an organization or individual can manipulate large amounts of diverse data to solve specific problems. The major objectives of the research are to analyze some popular big data analytics tools for structured and unstructured data using case studies to support better analytics.

Keywords: Big Data, Big Data Analytics

Introduction

Big data can be defined as datasets in which a large amount of volume requires more advanced and sophisticated technologies to obtain, store, transform, manage, and analyze for extracting useful valuable information. According to Waller & Fawcett (2013) define big data as datasets that are too large for traditional data processing systems and therefore require new technologies to process them. Sabharwal and Shah Jahan Miah (2021), describe it as the traditional enterprise machine-generated data and social data. The extraction of valuable information from a large amount of data is called big data analytics. Big data analytics is the process used to examine a large amount of different structured datasets to extract most of the useful information to uncover unknown correlations, hidden patterns, market trends, customer preferences and which help organizations to make better business decisions.

The first three characteristics of big data are volume, velocity, and variety. Additional characteristics of big data are variability, veracity, visualization, and value. Understanding the characteristics of Big Data is the key to learning its usage and application properly. Among Big Data characteristics, Variety is one of the study aspects which can further be classified into structured data, and unstructured data. Big data is defined as a huge volume of structured and unstructured data. Semi-structured data is considered to be included in unstructured data although another opinion is to consider semi-structured data as standalone data.

The need of storing and analyzing these kinds of diverse data is a big challenge. Big data challenges encompass data collection, data storage, data analysis, search, sharing, transfer, and querying, updating, information, and data source as data are differ in structures, types, sources and tools and techniques to handle them. According to Katal (2013), its main functionalities are to provide different corporate to enhance quicker access and smart decision in the importance of database management. As data variety differ, so are the tools used for big data analytics. Big data analytics tools help organizations and businesses in saving time and cost providing faster and better insights to make decisions. With appropriate big data analytical tools, an organization or

¹ Department of Computer Studies, University of Yangon

² Department of Computer Studies, University of Yangon

³ Department of Computer Studies, University of Yangon

individual can obtain, store, transform and analyze large amounts of data to solve specific problems. The major objectives of the research are to understand some of the most popular Big Data Analytics Tools used for Structured and Unstructured Data, and to analyze some case studies using these tools to support better analytics. This research describes the characteristics of three software tools for big data analytics based on data variety characteristics-SPSS for structured data, Tableau for semi-structured and Python for unstructured data.

Types of Big Data

Regardless of effort to store and analyze traditional data, most big data is unstructured (or) not structured in nature, which requires different techniques and tools to store, process, and analyze. The structured data and unstructured data which differ based on data variety specific characteristics are described detail in Table 1.

Table 1: Example of Structured and Unstructured Data

Structured Data	Unstructured data
Highly organized information Define how they will be stored with rigid data types and structures	Data with different specific structure that could not be stored in a traditional row and column format.
Mostly relational structure with Entity relationship (Tables as schema, rows as records, columns as fields) e.g. transaction data, traditional RDBMS (Relational Database Management System)	Semi-structured data e.g. data files such as spreadsheets in CSV (Column Separated Values), location (Longitude, Latitude), log files, XML files. Unstructured data e.g. (Images, audio, videos, log files, etc.)
Databases, data warehouses	Data lakes, non-relational databases
Predetermined Formats with fixed structures for creating a model defined data type and some restrictions on the data.	An array of different formats with undefined data structures

To analyze the unstructured data advanced analytical knowledge is needed. Sometimes, it is very tough to manage and analyze completely due to different forms of inherent structures. Semi-structured data is a form of structured data that does not conform to the formal structure of data models associated with relational models or other forms of data tables. This semi structured data has been added to unstructured data in the research.

Big Data Analytics

Big data analytics is a process of inspecting, differentiating, and transforming data with different data structure characteristics to extract useful information. Big data analytics has emerged as an important tool for supporting managerial decision-making. Jeble et al (2018) suggests that big data discovery efforts can reveal previously unknown findings which can result in insights that are helpful for managerial decision-making. Khan and et al (2014) have presented that Big Data Analytics is a strategy used to analyze huge information sets containing various qualities of information.

Three Levels of Big Data Analytics

Data analytics addresses information obtained through observation, measurement, or experiments about an occurrence of interest. Data analytics aims to extract as much information as possible that is relevant to the subject under consideration. Further, classified the entire field of big data analytics can be classified into the three-level based on the depth of analysis -

- (a) descriptive analytics- to use data to understand past and present
- (b) predictive analytics- to analyze current and historical facts to make predicting future events
- (c) prescriptive analytics- to use optimization techniques and suggests what should be done to optimize results, it addresses decision making and efficiency

Big Data Analytics Tools

There are different types of Big Data Analytics tools available under data analytics that help to improve the process such as data analysis, data cleansing, data mining, data visualization, data integration, data storage, and management. It is essential to know about which data analytical tools match the best for given data. There were nearly more than a hundred tools available to perform various steps of analytics such as SPSS, Spark, Talend, Khime, Tableau, PowerBI, Python, R, Julia, Hadoop, Hive, Sqoop, Mahout, Storm, Teradata, HBase, SAS, RapidMiner, and so on. Selecting a tool from the vast number of existing tools is a challenging task. When choosing analytical tools to use, it is useful to grasp the dimension of the software's market share and popularity.

To demonstrate the different dataset usage, two datasets are used. Employee Dataset Real World Dataset for Civil Service Academy (Lower Myanmar) Trainees For Structured Data and Semi-Structured Data), and Olivetti faces dataset from the scikit-learn library For Unstructured Data. Location such as city from real world employee dataset is used to demonstrate the Semi-structured data usage.

There are various analytics tools for analytics such as low-cost light weight spreadsheets such as excel. Data Analytics is the process of analyzing datasets to draw results, based on information they get. It is popular in commercial industries, scientists, and researchers to make a more informed business decision. There are many Big Data Analytics Tools for Structured Data such as SPSS, SAS, Khime, RapidMiner and so on. Big data analytical tools for unstructured data are more diverse and complex. Tools such as Tableau, PowerBI for esthetic analytical visualization, Programming tools such as Python, R, Julia for complex and advanced data analytics, Hadoop for file processing, Pig, Sqoop for data transfer, Hive for data warehouse and management, and so on. With big data, more commercialized or open-source tools are needed to use for analytics. Commercialized tools such as SPSS, Tableau, etc. are developed specially for the analysis of big amount of data. Open source tools could offer the advanced data analytics due to their resourceful libraries. The process of Big Data analytics helps organizations to better understand the information which is present within the sets of data. This research is conducted particularly based on three big data analytical tools, namely SPSS for structured data, Tableau for semi-structured data, and Python as unstructured data analytics.

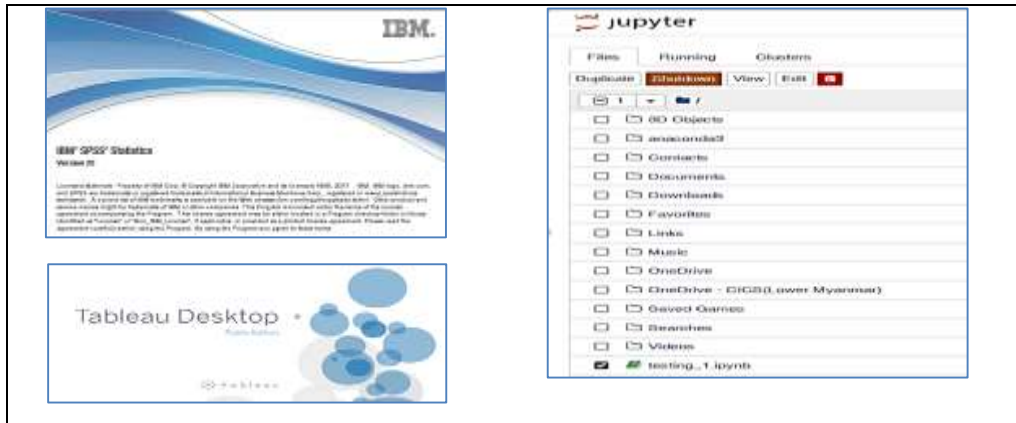


Figure 1: Big Data Analytics Tools “SPSS, Tableau and Python”

Big Data Analytics Tools for Structured Data

SPSS

SPSS (Statistical Package for the Social Sciences) from IBM Statistics, is a software package used for the analysis of statistical data. The origin of SPSS is in the field of social sciences; however, its use has further expanded into a wide variety of science for the analysis of data. SPSS become a popular data analytics platform especially for structured data. The most widely used powerful algorithms such as Decision Tree, K-Nearest Neighbor, even some neural network algorithms have been included in in-built solutions.

Data Processing for SPSS

Scaling including normalizing and transforming data such as binning could easily performed in SPSS. It is also possible to perform dimensionality reduction although data must be conformed with the rigid relational structure. As a use case for to perform data Processing in SPSS, real-world dataset of employee information who attended the Central Institute of Civil Service - Lower Myanmar for a period of time is used. E.g. variable Gender (Sex) into Male or Female (Binary). Table 2 describes some of the variables (fields) that are preprocessed for further analysis. Scaling including normalizing and transforming data such as binning could easily be performed in SPSS. Possible to perform dimensionality reduction although data must be confirmed with the rigid relational structure. The relevant data fields required for analyzing are first categorized such as variable Gender (Sex) into Male or Female (Binary). Table 2 describe some of the variables (fields) that are preprocessed for further analysis.

Table 2: Type the Field on Data View in SPSS

No	Variable Name	Type	Note
1	Sex	Categorical (Binary)	Male=0, Female=1
2	Age Group	Categorical (Numeric)	21-25 = “1”, 26-30 = “2”, 31-35 = “3”, 36-40 = “4”, 41-45 = “5”, 45+ = “6”
3	Qualification	Categorical	Bachelor = “1”, Honest = “2”, Master = “3”, M.Res = “4”, Ph.D = “5”, Diploma = “6”, Other = “7”
4	Rank	Ordinal	Officer = “1” Head of Branch = “2” Assistant Manager = “3” Assistant Engineer = “4” Head of Workshop = “5” Coaching Officer = “6”

SPSS provide Data View for data values, and variable view for data definitions. Qualification should be ordinal data. However, there is an assumption a degree holder might have related or unrelated diploma degree. Therefore, data is categorized as nominal (categorical data). Rank is ordinal data although there may have some other values with different name such as officer(administration) and assistant lecturer (university) has the same ordinal value. Figure 2 explore some features (variables) in above dataset as case study. Average age of the trainees is around the age of 30 i.e. regardless of rank, trainees in this age are more willing to get the diploma Figure 2(a). Scatter plot for fields Age, Qualification, Department are used to visualize each employee as a dot on three-dimensional predictor space to explore the dataset. Male and female employees are represented with blue and red dot color respectively. It indicates that females are more interested in getting the diploma for career advancement Figure 2(b).

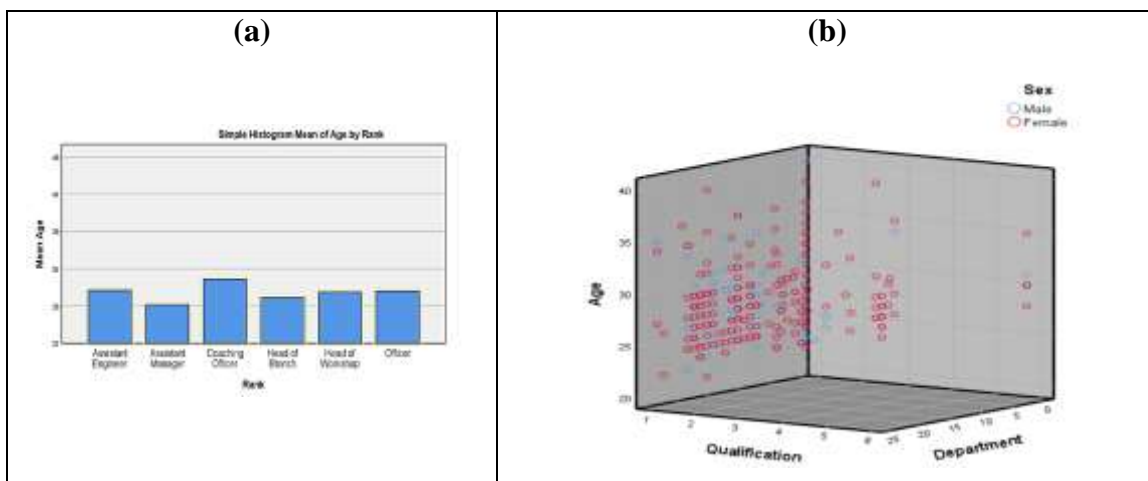


Figure 2: Exploratory analysis for structured data in SPSS

Big Data Analytics Tools for Unstructured Data

Data Analytics is the process of analyzing datasets to draw results, based on information they get. It is popular in commercial industries, scientists, and researchers to make a more informed business decision. There are many Big Data Analytics Tools for Unstructured Data such as Python, R, Julia, Power BI, including tools from Hadoop ecosystems such as Hadoop, Hive, Pig, Spooq, other big data analytic tools such as Spark, Mahout, and so on. Among them, Python, a very widespread use for big data analytic and management is explored.

Python

Python is a computer programming language often used to build websites and software, automate tasks, and conduct data analysis. Python is a general-purpose language, meaning it can be used to create a variety of different programs and isn't specialized for any specific problems. Python can be considered a tool, analyze structured data, semi structured and unstructured data. Programming knowledge is required to use python. In addition, in-depth understanding is also required. However, the most used algorithms can be included in the famous python machine learning and data visualization libraries and can be used with a few lines of code providing required flexibility. For example: Data preprocessing for analysis in python is described in following figure 4. Unstructured text data could easily be encoded for further analysis.

```

from sklearn.preprocessing import OneHotEncoder, LabelEncoder
lbl = LabelEncoder()
enc = OneHotEncoder()
qualitative = ['officer', 'Head of Branch', 'Assistant Manager', 'Assistant Engineer',
              'Head of Workshop', 'Coaching Officer']
labels = lbl.fit_transform(qualitative).reshape(6,1)
print(enc.fit_transform(labels).toarray())

[[0. 0. 0. 0. 0. 1.]
 [0. 0. 0. 1. 0. 0.]
 [0. 1. 0. 0. 0. 0.]
 [1. 0. 0. 0. 0. 0.]
 [0. 0. 0. 0. 1. 0.]
 [0. 0. 1. 0. 0. 0.]]

```

Figure 4: data preprocessing in python

The weakness of both SPSS and Tableau is their inability to handle with unstructured data. To demonstrate the use case of unstructured data, Olivetti face dataset from scikit-learn library is used. Data Visualization could be done easily by importing necessary libraries to classify an image. First, Python handle unstructured data image dataset by interpreting the image data into data set with numerical values. Unstructured image data is transformed, processing, and refined to be able to use for training. Dataset containing the image is simply split into training set and test set to analyze the face of an image. Then, randomized Principal Component Analysis algorithm is used in training of the data.


```

1: from skimage.io import imread
2: from skimage.transform import resize
3: from matplotlib import pyplot as plt
4: import matplotlib.cm as cm

import numpy as np
from sklearn.datasets import fetch_olivetti_faces

dataset = fetch_olivetti_faces(shuffle=True, random_state=101)
train_faces = dataset.data[:350,:]
test_faces = dataset.data[350:,:]
train_answers = dataset.target[:350]
test_answers = dataset.target[350:]
print(dataset.DESCR)

from sklearn.decomposition import RandomizedPCA
n_components = 25
R_pca = RandomizedPCA(n_components=n_components,
                      whiten=True, random_state=101).fit(train_faces)
print ('Explained variance by %i components: %0.3f' %
      (n_components, np.sum(R_pca.explained_variance_ratio_)))
compressed_train_faces = R_pca.transform(train_faces)
compressed_test_faces = R_pca.transform(test_faces)

```

Figure 5: Image face dataset import program in python

After data is trained, unstructured image data can be interpreted and visualized easily. However, these visualizations could be impossible or difficult in SPSS and tableau. The demonstration is done as follow. First, a script is written to find a face from test data set that is most similar in the trained data. The image is searched in the training dataset set. Necessary image processing steps are performed in both the training set and test set such as changing into the greyscale image to reduce the inference of color in determining the similarity. The most similar image from the train set is retrieved as a result.

```

import matplotlib.pyplot as plt
plt.subplot(2, 2, 1)
plt.axis('off')
plt.title('Unknown face '+str(photo)+' in test set')
plt.imshow(test_faces[photo].reshape(64,64),
           cmap=plt.cm.gray, interpolation='nearest')
for k,m in enumerate(most_resembling[:3]):
    plt.subplot(2, 2, 2+k)
    plt.title('Match in train set no. '+str(m))
    plt.axis('off')
    plt.imshow(train_faces[m].reshape(64,64),
              cmap=plt.cm.gray, interpolation='nearest')
plt.show()

```




Figure 6: Image classification program in python

Results and Discussion

This paper first describes the literature review of big data, data variety based on structured and unstructured data, the nature of data analytics, and introduce different big data tools. Big Data Analytics Tools is one of the most important tools to support decision-making in every organization, business, and Research field. The success of an organization is critically linked to effective analytics. These Big Data Analytics Tools provide effectiveness and are essential for all organizations and businesses.

Table 3: Comparison of Big Data Analytics Tools

Tools	Data Variety	Processing	Skill Requirements
SPSS	Structured Data	Batch processing, Standalone	Statistics, Data Visualization, Domain knowledge
Tableau	Structured, Semi-structured	Batch, and Online Analytical, Both Standalone and Crowd sourced	Data Analytical Skill, Statistics, Understanding of SQL and NoSQL data stores
Python	Structured, Semi-structured, Unstructured	Could support all degrees of processing-batch, complex event processing, near real time, real-time, Stream processing. Required advanced knowledge	Programming Skill, Data Science, Database knowledge- both SQL and NoSQL, Statistical Knowledge, Understanding of Advanced algorithms and data structures

Analytics Tools for Structured data explored. In SPSS, Structured Data Field can be analyzed to get the required results. SPSS provides data analysis for descriptive and exploratory statistics providing easy data transformation, analysis, and visualization. However, it is rigid and could only support batch processing. Tableau can support both structured data and unstructured data (semi-structured data). Tableau support online processing by allowing distributed computing. Python, a programming language, can also be used as a tool for big data analytics although it requires the advanced understanding of data structures and algorithms. There are other data analytical oriented programming languages such as R and Julier which also provide famous mathematical, statistical, data analytical and data visualization. Table 3 describes the comparison of above explored three data analytical tools -SPSS, Tableau, and Python.

Conclusion

In this research, both real-world and pre-built datasets are used to explore the potential of big data analytics tools SPSS for structured data, Tableau for semi-structured data, and Python for unstructured data in areas such as data identification, data storage, data filtering and extraction, data analysis, and data visualization. Big Data tools can provide insights and benefits to decision-makers for better decisions in various areas.

SPSS provide structured data fields can easily analyze, however, it is rigid and could only support batch processing. Tableau can support both structured data and unstructured data (semi-structured data), and supports online processing by allowing distributed computing, however, it is limited as a preparatory analytical tool. Python, a programming language, can also be used as a tool for big data analytics and able to handle all structured, semi-structured, and unstructured data, however it requires an advanced understanding of data structures and algorithms, mathematical, statistical, data analysis, and data visualization methods.

Big data analytics is of great significance in this age of data overflow and can provide insights and benefits to decision-makers in various areas different sectors and industries, such as civil service management, healthcare, retail, telecommunication, manufacturing, etc. Future research will be conducted an in-depth look, the pros and cons of these analytics tools, and experimental analysis about the currently explored big data analytical tools. Some rapidly

renowned tool such as Power BI and other big data tools will also be explored. By using Big Data Analytics Tools, faster and better decision-making for organizations and businesses can be achieved with reduced cost and time.

Future research will be conducted with an in-depth look, at the pros and cons of these analytics tools, and experimental analysis of the currently explored big data analytical tools. Some rapidly renowned tools such as Power BI and other big data tools will also be explored. By using Big Data Analytics Tools, faster and better decision-making for organizations and businesses can be achieved with reduced cost and time.

Acknowledgments

I would like to thank Dr. Nwe Nwe Win, Professor, and Head (Retired), Department of Computer Studies, University of Yangon, for her guidance to perform this research.

I extend my wholehearted thanks to Dr. Soe Mya Mya Aye, Professor and Head, Department of Computer Studies, University of Yangon for her kind and valuable advice and help. I am also thankful to Dr. Khin Sandar Myint, Associate Professor and Daw Pwint Phyu Khine, Demonstrator, Department of Computer Studies, University of Yangon for their interest and advice given on the research.

References

- Jeble, S., Sneha Kumari, Yogesh Patil, (2018), "Role of Big Data in Decision Making", *Operation and Supply Chain Management*, Vol. 11, No. 1, 2018, pp (36-44), ISSN 1979-3561/EISSN 2759-9363.
- Katal, A., M. Wazid and R.H. Goudar, (2013), "Big Data: Issues challenges tools and Good Practices", *Sixth International Conference on Contemporary Computing (IC3)*, pp(404-409), <http://dx.doi.org/10.1109/ic3.2013.6612229>.
- Khan, N., et. al., (2014), "Big Data: survey, technologies, opportunities, and challenges", *Scientific World Journal*. doi: 10.1155/2014/712826.
- Sabharwal, R. and Shah Jahan Miah, (2021), "A new theoretical understanding of Big Data Analytics Capabilities in organizations: A thematic analysis", *Journal of Big Data* 8, Article number: 159(2021).
- Waller, M.A., Stanley E. Fawcett, (2013), "Data Science, Predictive Analytics, and Big Data", *Journal of Business Logistics*, Vol. 34, Issue 2, pp (77-84).

INSTRUCTIONS TO AUTHORS

Presentation: Manuscripts (MS) should be typed on one side of **quarto or A4 size paper**. Typing should be single spaced, with a one-inch margin all around. A CD of the paper should be submitted together with two print-outs. In general, the text should be organized according to the following outline:

- (i) Title
- (ii) Abstract
- (iii) Materials & Methods/ Premises / Hypotheses
- (iv) Results / Findings
- (v) Discussion
- (vi) Summary/ Conclusion
- (vii) Acknowledgements
- (viii) References

The body of the text should be printed in **font size 12**, and those of the Abstract, Acknowledgement and References should be printed in **font size 10**. The relative importance of the **headings** in the text should be indicated as follows:

First Order	-	CENTRE HEADING, All Capitals
Second Order	-	Centre Heading, Capitals & lower case
Side Heading	-	Capitals & lower case, not indented (bold – faced)
Run-in heading	-	Capitals & lower case, indented (bold-faced)

Title. The title should describe the contents of the article adequately and concisely and should be typed in **font size 14**.

Author's name. Capital & lower case. The designation of the first author and email (where the number of authors is more than two) and the name of the institution where the work was carried out should be given at the bottom of the title page; but academic degree of the author is not necessary.

Abstract. The main points of the paper, including its findings and conclusions, should be highlighted in the abstract; it should not contain more than 300 words. Add email address for making further contact with the author; evaluation of the paper should be typed in **font size 10**.

Keywords: Between 3-7 keywords highlighting the main points should be listed below the abstract.

References. References should be presented in alphabetical order, beginning with the surname first for the senior author and surname last for the other authors, followed by the year of publication. Examples of references are given below:

To a paper: Rabinowitz, A., Than Myint, email, Tun Khaing, and S. Rabinowitz, (1999)"Description of the Leaf Deer (*Muntiacus Putaoensis*), a New Species of Muntjac from Northern Myanmar" *Journal of Zoology*, London, vol.249, pp.427-435.

To a book: Corbet, G.B., & J.E. Hill, (1992) *The mammals of the Indomalayan Region*. Oxford, Oxford University Press.

To a thesis: May Soe Thu (1995) *Taxonomy of Offshore Fishes Caught by Bottom Trawl Operations in Myanmar Waters*. M.Sc. Thesis Zoology Department, Yangon University (Unpublished).

N.B. If the manuscript submitted is from a thesis, its format should be revised to conform to the instructions of the Myanmar Journal of Arts & Science presented here. **Pagination** should commence from the title page except when they are used to identify the affiliated instructions, and cite unpublished material. **Footnotes** should be avoided wherever possible. The MS, including illustrations and references, should **not exceed 15 pages** for Arts and related subjects and **10 pages** for Science in length. Please kindly follow this limit in your final manuscript.

**MYANMAR ACADEMY OF ARTS AND SCIENCE
EXECUTIVE COMMITTEE**

President : Dr Thet Lwin

Vice-Presidents : Dr Maung Kyaw, Dr U Win

Secretary : Dr Win Tun

Joint Secretaries: Dr Tin Maung Tun, Dr Aye Aye Khaing, Dr Tin Tin Htwe

Executive Members

Dr Myo Thant Tyn	Dr Daw Than Nwe
Dr Tin Nyo	Daw Carole Ann Chit Tha
Dr Khin Than Oo	Daw Khin Lat
Dr Hla Pe	Dr Maung Thin

Publication Committee

Dr Thet Lwin	(Chairman)	Dr Maung Kyaw	(Vice-Chairman)
Dr U Win	(member)	Dr Daw Than Nwe	(member)
Dr Tin Nyo	(member)	Daw Carole Ann Chit Tha	(member)
Daw Khin Lat	(member)	Dr Hla Pe	(member)
Dr Maung Thin	(member)	Dr Khin Than Oo	(Joint Secretary)
Dr Myo Thant Tyn	(Secretary)		

Editorial Board

Dr Maung Kyaw	(Chairman)	Dr Myo Thant Tyn	(member)
Dr Daw Than Nwe	(member)	Dr Tin Nyo	(member)
Dr Khin Than Oo	(member)	Daw Khin Lat	(member)
Dr Hla Pe	(member)	Dr Maung Thin	(member)
Dr U Win	(Secretary)	Daw Carole Ann Chit Tha	(Joint Secretary)

Coordinators for International Academies

Daw Carole Ann Chit Tha	Dr Maung Kyaw
Dr Myo Thant Tyn	Dr Daw Than Nwe
Dr Tin Nyo	Dr Tin Maung Tun
Dr Tin Tin Htwe	